

Magneto-structural correlations in molecular magnets containing the S–N motive

Dissertation for the award of the degree
'Doctor rerum naturalium' (Dr.rer.nat.)
of the Georg-August Universität Göttingen

within the doctoral program GAUSS
of the Georg-August School of Science (GAUSS)

submitted by Christina Legendre
from Paris, France

Göttingen, 2021

Thesis Committee

Prof. Dr. Dietmar Stalke, Department of Chemistry, Institute of Inorganic Chemistry, Georg-August Universität Göttingen, Germany

Prof. Dr. Jacob Overgaard, Department of Chemistry, University of Aarhus, Denmark

Prof. Dr. Vasily Moshnyaga, Department of Physics, I. Physikalisches Institut, Georg-August Universität Göttingen, Germany

Members of the Examination Board

Reviewer: Prof. Dr. Dietmar Stalke, Department of Chemistry, Institute of Inorganic Chemistry, Georg-August Universität Göttingen, Germany

Second Reviewer: Prof. Dr. Jacob Overgaard, Department of Chemistry, University of Aarhus, Denmark

Additional Reviewer: Prof. Dr. Vasily Moshnyaga, Department of Physics, I. Physikalisches Institut, Georg-August Universität Göttingen, Germany

Further members of the Examination Board

Prof. Dr. Marina Bennati, Max-Planck Institute for Biophysical Chemistry & Department of Chemistry, Georg-August Universität Göttingen, Germany

Prof. Dr. Ricardo Mata, Department of Chemistry, Institute of Physical Chemistry, Georg-August Universität Göttingen, Germany

Jun.-Prof. Anna Krawczuk, Department of Chemistry, Institute of Inorganic Chemistry, Georg-August Universität Göttingen, Germany

Date of the oral examination: 19.05.2021

Table of contents

Table of contents.....	7
Declaration	11
Note – List of publications	12
Acknowledgments.....	14
Foreword.....	19
Abbreviations	22
List of compounds 1 – SN-ligands and their alkali-metal complexes.....	25
List of compounds 2 – dysprosium SN-based compounds	26
List of compounds 3 – cobalt SN-based compounds.....	27
 Chapter One The S-N moiety: synergies, ligand synthesis, and further curiosities.....	 29
1.1. The S-N moiety: using S-N based ligands towards single-molecule magnets	30
1.2. General procedures for ligand synthesis	33
1.3. Expanding the SN family: presentation of two new compounds	36
1.3.1. The dimer $\{\text{Ph}(\text{N}^t\text{Bu})\text{S}(\text{BuNH})\}_2$ ($\{1_H\}_2$).....	36
1.3.2. $[\{\text{PhS}(\text{N}^t\text{BuH})_2\}_2][\{(\text{BuNH})\text{PhS}(\text{BuN}^t\text{LiCl}_2)\}_2]$ ($\{8_H_4\}(8_H_2\text{LiCl}_2)\}$).....	37
1.3.3. Perspectives	39
1.4. Isolation and characterization of the transient radical species $[\text{S}(\text{N}^t\text{Bu})_3]_2\text{M}_3$ ($\text{M}=\text{Li}, \text{K}$) ($\{\text{L}_2\}_2_M_3$).....	40
1.4.1. Characterization of $\{\text{L}_2\}_2_Li_3$	40
1.4.2. Isolation and characterization of $[\text{S}(\text{N}^t\text{Bu})_3]_2\text{K}_3$ ($\{\text{L}_2\}_2_K_3$)	45
1.4.2. Solid-state structure of $\{\text{L}_2\}_2_K_3$	50
1.4.5. Perspectives for $\{\text{S}(\text{N}^t\text{Bu})_3\}$ -based radical species.....	53
 Chapter Two Magneto-structural correlations in dysprosium-containing SMMs: from field induced relaxation to hysteresis.....	 55
2.1. Single-molecule magnets (SMM): Historical timeline	56
2.2. SMM: design basics, theory of magnetic anisotropy and characterization methods....	57
2.2.1. The double well potential model: how does a single-molecule magnet work?	57
2.2.2. Relaxation processes of the magnetization in SMMs	59
2.2.3. Magnetic anisotropy.....	61
2.2.4. Design of mononuclear SMMs: actual trends and challenges	63

2.2.5. Current characterization methods of SMMs	64
2.3. Dy ³⁺ : the magical ion for the design of lanthanide single-ion magnets	65
2.3.1. Dy ³⁺ : the most investigated paramagnetic lanthanide ion in molecular magnetism .	65
2.3.2. Strategies towards the design of dysprosium SMMs.....	65
2.3.3. Current challenges in dysprosium SMMs.....	66
2.4. Novel mononuclear dysprosium complexes based on the S-N motive.....	67
2.4.1. Synthesis of the mononuclear dysprosium complexes 1-3_Dy	67
2.4.2. Crystallographic analysis of 1-3_Dy	68
2.4.3. Magnetic characterization of 1-3_Dy	70
2.5. Strategies towards pseudo-linear dysprosium complexes	76
2.5.1. Synthesis of [(Ph ₂ PCH ₂ S(N ^t Bu) ₃) ₂ DyCl] (4_Dy)	76
2.5.2. Magnetic properties of [(Ph ₂ PCH ₂ S(N ^t Bu) ₃) ₂ DyCl] (4_Dy).....	78
2.5.3. Conclusion and perspectives	80
 Chapter Three Influence of main group elements in trigonal planar and magneto-structural correlations in highly distorted tetrahedral mononuclear cobalt single-ion magnets	81
3.1. Cobalt based SMMs: challenging 3d transition metals.....	82
3.2. Trigonal planar field induced cobalt SMMs.....	83
3.2.1. Synthesis of 1-2_Co	83
3.2.2. Solid-state structures of 1_Co and 2_Co	84
3.2.3. Magnetic characterization of 1-2_Co	85
3.2.4. Multiconfigurational calculations: probing the influence of the soft P-donor on the magnetic properties	88
3.2.5. Conclusion and perspectives.....	91
3.3. Distorted tetrahedral mononuclear cobalt single-ion magnets.....	92
3.3.1. Synthesis of 3-7_Co	93
3.3.2. Solid-state structures of 3-7_Co	94
3.3.3. Magnetic characterization of 3-7_Co	100
3.3.4. Multiconfigurational calculations: correlating magnetic anisotropy with the N-Co-N angle.....	114
3.3.5. Conclusion and perspectives.....	119
 General conclusion and perspectives.....	120

Chapter Four: Experimental section	121
4.1. Methods	121
4.1.1. General considerations	121
4.1.2. Single-crystal X-ray diffraction	121
4.1.3. Magnetic measurements	123
4.1.4. Computational calculations	126
4.1.5. Additional characterization methods	128
4.2. Compound synthesis and characterization	130
4.2.1. $\{\text{Ph}(\text{N}^t\text{Bu})\text{S}(\text{N}^i\text{BuNH})\}_2$ ($\{1_H\}_2$)	130
4.2.2. $[\{\text{PhS}(\text{N}^t\text{BuH})\}_2][\{(\text{N}^i\text{BuNH})\text{PhS}(\text{N}^i\text{BuN}(\text{LiCl}_2))\}_2]$ ($\{(8_H_4)(8_H_2\text{LiCl}_2)\}$)	132
4.2.3. $[\text{S}(\text{N}^i\text{Bu})_3]_2\text{K}_3$ ($\{L_2\}_2_K_3$)	133
4.2.4. $\text{Dy}(\text{PPh}_2\text{CH}_2\text{S}(\text{N}^i\text{Bu})_2)_2\text{Cl}_2\text{Li}(\text{THF})_2$ (1_Dy)	135
4.2.5. $\text{Dy}(\text{PhS}(\text{N}^i\text{Bu})_2)_2\text{Cl}_2\text{Li}(\text{THF})_2$ (2_Dy)	136
4.2.6. $\text{Dy}(\text{MeS}(\text{N}^t\text{Bu})_3)_2\text{Cl}_2\text{Li}(\text{THF})_2$ (3_Dy)	137
4.2.7. $[\{\text{Ph}_2\text{PCH}_2\text{S}(\text{N}^i\text{Bu})_3\}_2\text{DyCl}]$ (4_Dy)	139
4.2.8. $[\{\text{Ph}_2\text{PCH}_2\text{S}(\text{N}^i\text{Bu})_3\}_2\text{Dy}(\text{C}_3\text{H}_5)(\mu^2\text{-Cl}_2)\text{Dy}(\text{C}_3\text{H}_5)\{\text{Ph}_2\text{PCH}_2\text{S}(\text{N}^i\text{Bu})_3\}]$ (5_Dy) ..	140
4.2.9. $[(\text{THF})_2\text{Li}\{(\text{N}^i\text{Bu})_4\text{S}\}\text{Co}\{\text{N}(\text{SiMe}_3)_2\}]$ (1_Co)	144
4.2.10. $[\{\text{PPh}_2\text{CH}_2(\text{N}^i\text{Bu})_3\text{S}\}\text{Co}\{\text{N}(\text{SiMe}_3)_2\}]$ (2_Co)	145
4.2.11. $\text{Co}(\text{MeS}(\text{N}^i\text{Bu})_2)_2$ (3_Co)	146
4.2.12. $\text{Co}(\text{PhS}(\text{N}^i\text{Bu})_2)_2$ (4_Co)	147
4.2.13. $\text{Co}(\text{MeS}(\text{N}^i\text{Bu})_3)_2$ (5_Co)	148
4.2.14. $\text{Co}(\text{PhS}(\text{N}^i\text{Bu})_3)_2$ (6_Co)	149
4.2.15. $\text{Co}(\text{PPh}_2\text{CH}_2\text{S}(\text{N}^i\text{Bu})_3)_2$ (7_Co)	150
4.2.16. $[(\text{THF})_2\text{Li}(\mu^2\text{-Cl}_2)\text{Dy}\{(\text{THF})\text{Cl}(\text{Ph}(\text{S}(\text{N}^i\text{Bu})_2)_2)(\text{THF})\text{Cl}\}\text{DyCl}_2]$	152
4.2.17. $[(\text{THF})_2\text{Li}(\mu^2\text{-Cl}_2)\text{Dy}\{(\text{THF})\text{Cl}(\text{Ph}(\text{S}(\text{N}^i\text{Bu})_2)_2)(\text{THF})\text{Cl}\}\text{DyCl}_2]$	155
4.2.18. $[\{(\text{Ph}_2\text{S}(\text{N}^i\text{Bu})_2)_2\text{Cl}\}\text{Co}(\mu^2\text{-Cl}_2)\text{Co}\{\text{Cl}(\text{Ph}_2\text{S}(\text{N}^i\text{Bu})_2)_2\}]_2$ (C_7H_8) _x	158
4.2.19. $\text{M}(\text{Mebox})_2$ complexes ($\text{M} = \text{Mn, Fe, Co, Ni}$)	161
Annex 1: Crystallography service	171
Crystal structure of NS_1: $\text{PhC}(\text{N}^i\text{Bu})_2\text{SiSeC}_6\text{H}_4\text{PPh}_2$	173
Crystal structure of NS_2: $\text{PhC}(\text{N}^i\text{Bu})_2\text{SiZnCl}_2\text{C}_6\text{H}_4\text{PPh}_2$	175
Crystal structure of NS_3: $\text{PhC}(\text{N}^i\text{Bu})_2\text{SiAlCl}_3\text{C}_6\text{H}_4\text{PPh}_2$	176
Crystal structure of NS_4: $\text{PhC}(\text{N}^i\text{Bu})_2\text{SiGaCl}_3\text{C}_6\text{H}_4\text{PPh}_2$	177
Crystal structure of NS_5: $[\{\text{PhC}(\text{N}^i\text{Bu})_2\text{SiF}_2(\text{C}_6\text{H}_4\text{PPh}_2)_2\text{Ag}\}\{\text{AlCl}_4\}]$	178

Crystal structure of NS_6: $\text{PhC}(\text{N}^i\text{Bu})_2\text{SiP}(\text{Tip})\text{C}_6\text{H}_4\text{PPh}_2$	179
Crystal structure of NS_7: $\text{PhC}(\text{N}^i\text{Bu})_2\text{Si}^i(\text{Bu})^*-\text{B}(\text{Br})\text{Tip}$	180
Crystal structure of NS_8: $\text{PhC}(\text{N}^i\text{Bu})_2\text{Si}(\text{HMDS})^*-\text{B}(\text{Br})\text{Tip}$	181
Crystal structure of NS_9: $\text{PhC}(\text{N}^i\text{Bu})_2\text{Si}(\text{NMe}_2)^*-\text{B}(\text{Br})\text{Tip}$	184
Crystal structure of NS_10: $\text{PhC}(\text{N}^i\text{Bu})_2\text{Si}(\text{N}^i\text{Bu})-\text{B}(\text{Br}_2)\text{Tip}$	185
Crystal structure of NS_11: $\text{PhC}(\text{N}^i\text{Bu})_2\text{SiB}(\text{Tip})\text{C}_6\text{H}_4\text{PPh}_2$	186
Crystal structure of NS_12: $\text{PhC}(\text{N}^i\text{Bu})_2\text{SiB}(\text{Tip})\text{C}_6\text{H}_4\text{PPh}_2\text{Br}$	187
Crystal structure of NS_13: $\text{PhC}(\text{N}^i\text{Bu})_2\text{TipSbSi}-\text{SiSbTip}(\text{N}^i\text{Bu})_2\text{CPh}$	188
Crystal structure of NS_14: $\text{PhC}(\text{N}^i\text{Bu})_2\text{Si}(\text{HMDS})(\text{N}^i\text{Bu})\text{Si}(\text{N}^i\text{Bu})_2\text{CPh}$	189
Crystal structure of NS_15: $\text{PhC}(\text{N}^i\text{Bu})_2\text{Si}^i(\text{Bu})\text{Se}/\text{PhC}(\text{HN}^i\text{Bu})_2\text{Br}$	190
Crystal structure of NS_16: $\text{PhC}(\text{N}^i\text{Bu})_2\text{Si}(\text{PTip})_2\text{K}(\text{Et}_2\text{O})_2$	191
Crystal structure of NS_17 : $(\text{PhC}(\text{N}^i\text{Bu})_2\text{Si})_2\text{Li}_2\text{I}(\text{N}^i\text{Bu})_2\text{PhC}$	192
Annex 2: Magnetometry service	193
JK_K3: $\text{K}(\text{B}^{\text{th}}\text{H}_2\text{BoxCH})_n(\text{THF})_2\text{K}@18\text{-crown-6}$	195
NS_7: $\text{PhC}(\text{N}^i\text{Bu})_2\text{Si}^i(\text{Bu})^*-\text{B}(\text{Br})\text{Tip}$	197
JJ_1: $[\text{Cl}_2\text{Mn}(\text{N}^i\text{Bu})_2\text{S}^i(\text{BuN})_2\text{Mn}\{\text{ClLi}(\text{THF})_3\}_2]$	199
JJ_2: $[(\text{acac})\text{Co}(\text{N}^i\text{Bu})_2\text{S}^i(\text{BuN})_2\text{Co}(\text{acac})]$	201
DL_1: $\{(\text{MeBox})_2\text{Gd}(\mu^2\text{-Cl}_2)\text{Gd}(\text{Mebox})_2\}$	203
Bibliography	205

Declaration

This dissertation is submitted to the Georg-August University School of Science (GAUSS) to fulfill the requirements for obtaining a degree of ‘Doctor rerum naturalium’ in Chemistry. In this work, I present the central part of the research conducted during my PhD studies under the supervision of Prof. Dr. Dietmar Stalke at the Institute of Inorganic Chemistry of the Georg-August Universität Göttingen.

Note – List of publications

Some of the present work has been published or is under peer-review in scientific journals. The present dissertation constitutes a part of the PhD work that is inseparable from these articles, as listed below.

- I. *Synthesis and Coordination Behavior of a New Hybrid Bidentate Ligand with Phosphine and Silylene Donors* by Mohd Nazish, Mujahuddin M. Siddiqui, Samir Kumar Sarkar, Annika Münch, **Christina M. Legendre**, Regine Herbst-Irmer, Dietmar Stalke,* Herbert W. Roesky,* *Chem. Eur. J.*, 2020, 26, 1-10, [10.1002/chem.202003513](https://doi.org/10.1002/chem.202003513)
- II. *Regionales Fonds-Stipendiatentreffen in Göttingen*, **Christina M. Legendre**, Daniel Becker, *Nachr. Chem.*, 2020, 68 (6), 75a, DOI: [10.1002/nadc.20204099490](https://doi.org/10.1002/nadc.20204099490)
- III. *Exchange coupling in binuclear manganese and cobalt complexes with the tetraimido sulfate anion $[S(N^iBu)_4]^{2-}$* by Jochen Jung, **Christina M. Legendre**, Regine Herbst-Irmer, Dietmar Stalke,* *Inorg. Chem.*, 2021, 60 (2), 967–972, DOI: [10.1021/acs.inorgchem.0c03085](https://doi.org/10.1021/acs.inorgchem.0c03085) (Annex 2)
- IV. *The quest for optimal 3d orbital splitting in tetrahedral cobalt single-molecule magnets featuring colossal anisotropy and hysteresis* by **Christina M. Legendre**, Emil Damgaard-Møller, Jacob Overgaard,* Dietmar Stalke,* *Eur. J. Inorg. Chem.* 2021, online, DOI: [10.1002/ejic.202100465](https://doi.org/10.1002/ejic.202100465), #MyFavoriteEIJC (section 3.3)
- V. *Selective Route to Stable Silicon-Boron Radicals and their Corresponding Cations* by Mohd Nazish, **Christina M. Legendre**, Samir Kumar Sarkar, Daniel J. Goffitzer, Martin Diefenbach, Brigitte Schwederski, Jana Lücken, Regine Herbst-Irmer, Dietmar Stalke,* Max C. Holthausen,* Wolfgang Kaim,* Herbert W. Roesky*, *Inorg. Chem.*, 2021, online, DOI: [10.1021/acs.inorgchem.1c01438](https://doi.org/10.1021/acs.inorgchem.1c01438) (Annex 1)
- VI. *Trigonal planar iron(II) and cobalt(II) complexes containing $[RS(N^iBu)_3]^{n-}$ ($R = N^iBu$, $n = 2$; CH_2PPh_2 , $n = 1$) as acute bite-angle chelating ligands: soft P-donor proves beneficial to magnetic Co species* by Jochen Jung, **Christina M. Legendre** (co-first author), Serhiy Demeshko, Regine Herbst-Irmer, Dietmar Stalke,* *Inorg. Chem.*, 2021, 60, (13), 9580-9588, DOI: [10.1021/acs.inorgchem.1c00770](https://doi.org/10.1021/acs.inorgchem.1c00770) (section 3.2)
- VII. *Enhancing steric hindrance via ligand design in dysprosium complexes: from induced slow relaxation to zero-field SMM properties* by **Christina M. Legendre**, Regine Herbst-Irmer and Dietmar Stalke,* *Inorg. Chem.*, 2021, DOI: [10.1021/acs.inorgchem.1c00973](https://doi.org/10.1021/acs.inorgchem.1c00973) (section 2.4)
- VIII. *Isolation and properties of the long elusive ultramarine blue $[K_3\{(N^iBu)_3S\}_2]^\cdot$ radical* by **Christina M. Legendre**, A. Claudia Stüchl, Christian P. Sindlinger, Regine Herbst-Irmer and Dietmar Stalke,* *submitted*, 2021 (section 1.4)
- IX. *Benchmarking magnetic and spectroscopic properties on highly stable 3d metal complexes with tunable bisheterocyclomethanide ligands* by **Christina M. Legendre**, Daniel Lüert,

- Regine Herbst-Irmer, Dietmar Stalke,* *Dalton Trans.* **2021**, DOI: [10.1039/D1DT03230E](https://doi.org/10.1039/D1DT03230E) (section 4.2.19)
- X. *Scorpionate ligands for lanthanide single-ion magnet design: slow magnetic relaxation and butterfly hysteresis for Dy[Cl(Ph₂PCH₂S(N^tBu)₃)]₂*. by Jochen Jung, **Christina M. Legendre**, Serhiy Demeshko, Regine Herbst-Irmer, Dietmar Stalke,* *Dalton Trans.*, **2021**, DOI: [10.1039/D1DT03555J](https://doi.org/10.1039/D1DT03555J) (section 2.5)
- XI. *Stabilization of Reactive Nitrene by Silylenes without using a Reducing Metal* by Yi Ding, Samir K. Sarkar, Mohd Nazish, Daniel Lüert, P. Niklas Ruth, **Christina M. Legendre**, Shahila Muhammed, Regine Herbst-Irmer, Pattiyil Parameswaran, Dietmar Stalke,* Zhi Yang,* Herbert W. Roesky,* *Angew. Chem. Int. Ed.*, **2021** DOI: [10.1002/anie.202110456](https://doi.org/10.1002/anie.202110456) (Annex1)
- XII. *Stable 1, 2 benzene substituted C₂PBSi five-membered ring system resulted in radical and non-radical species* by Mohd Nazish, **Christina M. Legendre**, Bastian Schluschas, Brigitte Schwederski, Regine Herbst-Irmer, Dietmar Stalke,* Wolfgang Kaim,* Herbert W. Roesky*, *submitted* (Annex 1)
- XIII. *Magnetic, XRD and DOSY-NMR studies on the sodium and lanthanide bis(4-R-benzoxazol-2-yl)methanide family* by Daniel Lüert, Anne Kreyenschmidt, **Christina M. Legendre**, Regine Herbst-Irmer, Dietmar Stalke*, *manuscript in preparation*. (Annex 2)
- XIV. *Structural and magnetic investigations of single ion magnets from triimidosulfite based alkali-metal-cages* by Daniel Lüert, **Christina M. Legendre**, Regine Herbst-Irmer, Dietmar Stalke*, *manuscript in preparation*
- XV. *Various silicon-boron radicals and their reactivity* by Mohd Nazish, Yi Ding, Arun Kumar, **Christina M. Legendre**, Nico Graw, Brigitte Schwederski, Regine Herbst-Irmer, Dietmar Stalke,* Wolfgang Kaim,* and Herbert W. Roesky*, *manuscript in preparation* (Annex 2)
- XVI. *Synthesis of unsaturated R-Sb=Si-Si=Sb-R chain compounds isoelectronic to ethane-1,2-diimine* by Mohd Nazish, **Christina M. Legendre**, Nico Graw, Regine Herbst-Irmer, Dietmar Stalke* and Herbert W. Roesky*, *manuscript in preparation* (Annex 2)
- XVII. **Christina Legendre**, Dietmar Stalke, CCDC 2076511: Experimental Crystal Structure Determination, 2021, DOI: [10.5517/ccdc.csd.cc27ps7z](https://doi.org/10.5517/ccdc.csd.cc27ps7z) (Chapter 4)

Acknowledgments

A PhD is a succession of many small events happening over the course of several years. A PhD can only be successful if the right people are there at the right place and at the right moment. The field is vast, the journey is long, but the final achievement is rewarding.

I wish to begin by acknowledging my PhD advisor, Prof. Dr. Dietmar Stalke, not only because it is standard to do so, but because he offered me more than a simple PhD position and a facile access to the exhaustive equipment of the University of Göttingen. He *actually* brought me some new hope for the academic world, which is probably the most important achievement of this doctoral thesis. I thank the Fonds der Chemischen Industrie for providing financial support for my two first years of PhD. I thank the Institute of Inorganic Chemistry and the GAUSS program research fund for their further financial support for my third year of PhD and my travels abroad, respectively. I thank my thesis committee for their availability.

The first person who welcomed me at the institute as I started my PhD was Anna Kölpin: her straightforward manners and social potential immediately matched my character, and it was the beginning of a wonderful friendship. A couple of days later, I met with Dr. Serhiy Demeshko, a priceless asset to the institute. He had the will to guide and support me, essentially in magnetic measurements at the SQUID, but also at other critical occasions, which determined much of my PhD life. His accessibility, generosity and unalterable patience made him a wonderful teacher and friend. I could not have achieved half of this work without Serhiy. Another important contributor to this work is Emil Damgaard-Møller (from Jacob Overgaard's group in Aarhus), who showed me the potential underlying in some of my cobalt complexes.

But let me first acknowledge the Stalke group's members: my lab partner Nico, a wonderful person and a skillful chemist, welcomed me in his nice and ordered lab. While listening to the greatest music playlists ever, he looked after me for each Schlenkline experiment and gave me invaluable advice for *pretty much everything*. Thank you, Nico, for this great time together! The magnetism team – Jochen, Daniel – quickly worked me through my new doctoral topic. We were not only sharing research interest but also one glovebox. It still worked out thanks to lots of patience, regardless of our 'non-German' organizational skills. Johannes was often doing chemistry at the other box, and we shared great conversations, besides training for hand-free talking and multitasking. Christian (*tse-pe-stern*) often joined us for French speaking/singing sessions, which seriously impacted our productivity in these moments. I also had great chats with Xiaobai at the glovebox. But the Stalke group is not only a hard-working group: their members also love to challenge themselves at any opportunity, including *baby-foot*, darts, BBQ, Rage Cage!, QUIZZ Night, and occasionally weird games invented for WoDuR purposes, such as throwing beer capsules into a water bucket as fast as possible... well, whatsoever. In this (at the beginning) mainly male-populated group, the girls – Anne, Annika, Helena, and me – often had to demonstrate additional skills to compensate the lack of beard – apparently mandatory for better recrystallization attempts. Anne, our NMR expert, can speak extremely fast, especially while eating turnip. Our expert in advanced diffraction experiences and caretaker of the instruments

(with Peter) is Helena. She is also a specialist to place the badminton birdie in particularly annoying places. I'd like to further thank her to get me into the fitness club after work to enjoy sport and sauna. We also spent great moments together, either in the lab to refine bizarre crystal structures (no need to mention from whom) or – and that is better by far – to watch old Soviet movies. Thank you also for showing me the charming Melsungen. The other electron charge density expert, Annika, continuously cheered everyone up, probably partly because she was in charge of the 'sweet groceries' – the job I took over after her graduation. She was undoubtedly the *posey* girl of the AK and I hope we were able to cheer her up as well when she needed to. Thank you, Nico, Helena, Niklas, Annika, for valuable crystallography advice. Thank you, Peter for taking care of the diffractometers and making sure that our *old ladies* managed to collect the data of all our crystals. Thank you, Tobias E., for keeping good care of our vast collection of chemicals and for ordering everything we needed as quickly as possible. Enormous thanks to Heike for her administrative job, making my PhD tasks easier and enabling me to smoothly go through the documents of work trips and shipments. Important members of the group also include (does it!) the people from the Sindlinger's group: Tobias H. and Christian. Both are infinitely helpful, witty, and bringing in important scientific input for synthesis. I would also like to particularly thank Christian for his great introduction course to practical DFT calculations. Since October 2020, Anna joined the faculty staff (and our kitchen!). She is an amazingly open and funny person; thanks Anna and Bruno for the joyful moments all together enjoying fondue and raclette. Many thanks to my bachelor students for co-researching molecular magnets with me: Per & Anatoly. Huge thanks to Prof. Dr. Jacob Overgaard and to his highly skilled student (Dr.!) Emil, who patiently taught me everything he could about computations during these two wonderful weeks in Aarhus! Many thanks to Dr. Lennard K., the rest of the MolMag group and of the institute of chemistry for the warm welcoming and the nice atmosphere.

Back to Gö: I would like to particularly thank Dr. Claudia Stückl now, for her wonderful patience despite constant changes in my official and financial status at the university. Additionally, her skills in EPR resulted in my beautiful spectrum in chapter 1. Many thanks to Dr. Christian Würtele for teaching me crystallography and refinement, I will remember his surprised looks when I'd bring the 1,000th crystal of the week to the diffractometer already on Wednesday. The *Hausmeister*, Bernd, Ha-Jo and his team, Annika were always here to chat, help, repair anything we'd break and organize the great AC hiking tours every year. Additional thanks to Sheida, Richt, Alyssa, Giuseppe, Jeff, Massi, Guillermo, Max F., Seb F. (SJFK on publications please!) & Niyaz for nice chats, help with instruments or occasional beers. In the Moshnyaga group – the so-called MAD group – I want to thank Vitaly, Philipp and Kai for taking care of the SQUID and making the sharing of the instrument so smooth and easy.

For our social activities outside of the lab, many thanks to Anne, Nico, Tobias H., Johannes, Timo, Helena, Annika, Jochen, Xiaobai for these great times together balancing the work hours. Special thanks go to the theater team as well - Claudia, Anna, Kathi, Pierre- for interactive and cultural Thursdays. Speaking Russian almost every day often cheered me up, when interacting with various members of the 'Slavic community', including Anna, Serhiy, Vasily, Vitaly, Alex, Helena, Rita. Huge thanks to the *Mädels* for our all-girls evenings: Kathi, Claudia, and Anna;

these times with you were absolutely crazy and wonderful! Thanks to Max and his parents Bruno and Eurydice, whom I owe my first trips to Kassel. Many thanks to my friends who endured my complaints about the PhD: the *C club* – Céline, Charlotte, Caroline and Nathalie –, Loirín, for being who you are, the MBA girls – Fede, Tracy, Inès, Laurane, Fanny –, Eva, whose early friendship influenced my choice of studies, Coralie, Tim, Cecilia, Faustine, Marie-Laura, Natacha, Verena, Ania, Alice T., Dana & Miguel (for my chemical and drinking education overseas), Lydya, my neighbors Rudi & Inge, Galatée, and many more... Thanks to Regina, René, Nicolas, Clémence, Philéas, Valentin, Catherine, Jean-Marc, Charlotte and Helmut for wonderful family gatherings in the heart of France and the escapades to Rostock. Special huge thanks to Niki & Rudolf, because TitForTat, and to Joachim S. for his great guidance and inspiring discussions. Before starting my PhD, Göttingen was not foreign to me for several reasons. I would just mention one here: Adelebsen is the key to many things...and thank you all SchöSchuSchü: Marie, Christian, Sabine, Uli, Walter, Flo, Nica, *Großmutti* Erika, and *Großvati* Hans for wonderful sunny days full of *Apfelmuß* and laughs since I'm fifteen.

It is now time to thank my family. They obviously supported me a lot and I cannot be enough grateful to them for it. Even if the distance between Göttingen and Paris is 797,4 km and even if it takes almost 7 hours by train to reach the French capital, they picked up on almost anything that happened in Göttingen (and in Michigan), for the better and the worse. Papa and Maman have always been here for me, since the very beginning, supporting me unconditionally. They always asked me to “look for *blue* crystals, as these are the most beautiful”! My siblings Nathalie, Nicolas, and Cyril, and my brother-in-law Benjamin, who are all non-chemists, are the funniest and always had some interesting not science-related interpretations about my results. Merci à vous tous, heureusement que vous étiez là ! From some more afar (2 123,3 km), my Russian relatives were there for me as well: Nikolai, Nina, Dima, Ioulia, Aliona, Natasha, Philip, Kyrill, Liza and Piotr, as well as Tiotia Tania, Diadia Boria, Oleg, especially for wonderful holiday far, far away from work! *Огромное спасибо всем!* From even farther (6 694 km), the Becks – Jennifer, Don, Mitchell, and Ellie – opened me their hearts and home in hard times. Besides giving me unlimited generosity and love, they also taught me how to design a Gold Ruberg Machine for Science Olympiads, to play several board games and cook the most delicious chili on Earth. Thank you to all my ‘extended’ family members! Last but not least: for almost four years, Pierre has been a very special person to me. He has been here for both sunny and stormy days, and his love and support helped me during these great, yet challenging years. I do not even know how to express my gratitude and tell you, my husband Pierre, how lucky I am that you are beside me every day. The PhD experience is surely something important, but my life experience with you, which will continue on for many, many years, is simply and immensely more treasurable. Merci, mon Pierre.

And it is probably time to end this section, before it surpasses the length of my *actual* dissertation.

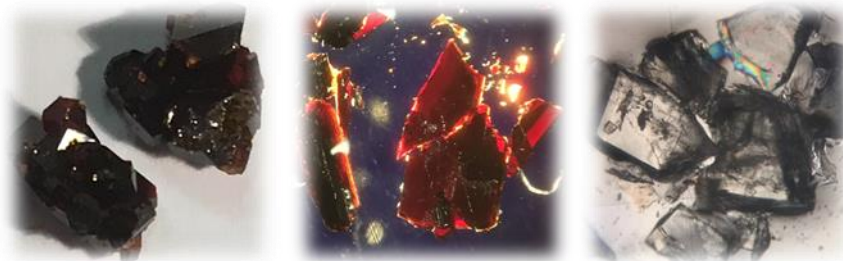
To my grandparents Marie, Natalya, Pierre, and Vladimir

*Пишите, пишите...*ⁱ

ⁱ Алиса Фрейндлих in *Служебный роман*, 1977, СССР

Foreword

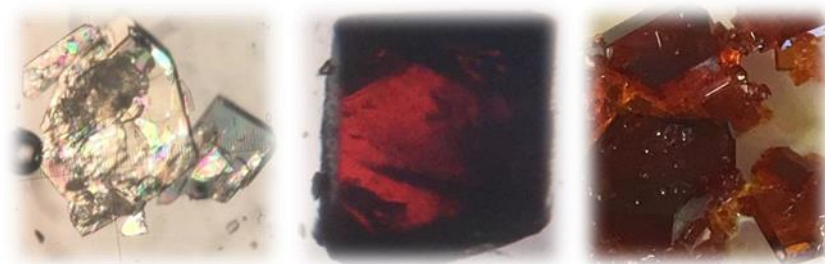
Since Ancient Times, the search of divine perfection in Nature, or the aspiration to sacralize Nature, has driven humanity towards understanding the order of things and of the elements. In particular, it resulted in a fascination for colorful, highly symmetric things, such as magnificent crystalline gemstones, or octahedral-shaped black stones with attracting properties. Although our understanding for these curiosities has grown, our thirst for knowledge is far from being replenished. Curiously, the admiration for the geometric colorful stones has remained constant over time. Some of these apparently useless rare stones has become highly expensive over time or even unaffordable. Equally fascinated by these wondrous stones, I would herein like to share my own enthusiasm and curiosity. It is probably an intrinsic feature of humankind, something that one cannot entirely explain. One motivation for a chemist to join an inorganic chemistry lab is to acquire the knowledge of crystallizing ‘things’ and experience the excitation and joy of creating a new molecule, following its transformation unto a macroscopic colored crystal, akin to our ancestors’ most secret manufacturing processes.



Creating a new thing implies choosing the right building blocks; for a chemist, it means choosing the right elements. Thereupon, ancient civilizations did more chemistry than we commonly think. Our ancestors were already professional in nitrogen and sulfur chemistry. Although only isolated around 1772, nitrogen as ammonium chloride was already used in early agriculture as a fertilizer. Persian alchemists knew how to prepare strong acids, notably the *aqua regia* in order to dissolve solid gold. Reactivity was one of the multiple facets of alchemy, but unusual colors of stones were undoubtedly even more fascinating. Lapis-lazuli, a naturally occurring semi-precious blue stone, was mined in Afghanistan as early as 7 000 BC. Considered a sacred stone in Ancient Mesopotamia and Egypt, it represented, through its mysterious association of colors, the complexity of the universe and the power of the Ancient Gods. Its intense blue color is nowadays known to come from the atomistic combination of three sulfur atoms hosting a free radical. Sulfur itself exists under several forms that cover most of the rainbow palette, for example as bright yellow native brimstone melting into a red liquid with emission of a blue flame.



Even more mysterious minerals were discovered and used in previous civilizations as stones with special ‘powers’, as they could ‘move things without contact’. For example, some stones were associated with the attributes of various ancient deities, such as the falcon god Horus or the monstrous Typhon. The stones would bring luck, happiness, or protect against demons and heal wounds. Around the sixth century BC, Ancient Greeks found that some of these wondrous stones can attract iron. These dark magnetic stones, or *stones of Magnes*, son of Zeus, came from the Ancient Magnesia region (either in Thessaly or in Ancient Anatolia). The local tribe of the Magnetes named these minerals *magnetite*, or sometimes *black magnesia*, after their region. Meanwhile in East Asia, both Chinese and Indian people discovered magnetites as well, exploiting their properties for navigation and for healing. Later on, in Europe, they were used as compasses by sailing merchants and therefore better known as *lodestone* – the *leading stone*. The magnetite was also sometimes named the *cornerstone*, or the *seed of the discovery* of the Americas. In modern times, clarifications concerning the molecular constitution of these special rocks were finally possible. Ironically, these stones called magnesia draw their magnetic properties from ferrimagnetic iron oxide $\text{Fe}^{2+}\text{Fe}_2^{3+}\text{O}_4$, and not from magnesium or manganese as the name may suggest. Magnetites are naturally occurring magnets magnetized by strong magnetic fields caused by lightning bolts.



Physical magnetic properties gained more interest over time as knowledge grew and enabled more ‘control’ of these properties for technological applications. Around 1600, Court physician Gilbert first distinguished electric and magnetic bodies (especially the difference between magnetic attraction and electrostatics) and identified Earth itself as a magnet. He also drew the first magnetic attraction and repulsion laws through the magnetic poles (precursor of Maxwell’s equations) and described the influence of temperature on magnetism (precursor of Curie’s law). Scientists early understood that electricity and magnetism, although different, are rarely dissociable, and the word *electromagnetism* appeared as early as 1641. The relationship between electric and magnetic phenomena became evident through the works of Ørsted in 1819, who discovered that a circular electric current generates an axial magnetic field. The discovery of the electron at the end of the XIXth century by Thomson allowed to correlate the two phenomena even stronger together, as the electron is the particle responsible for both.

Through the incorporation of advanced modern theories from physics, in combination with synthetic chemistry, magnetism has always been investigated. It became possible to study magnetism in the solid state as well as the liquid state. Unpaired electrons were found to play a key role in the magnetic properties. Deeper understanding of the matter allowed to foresee the potential applications of materials and molecules with these excitable, free electrons. It further appeared that the physical properties of such materials can be influenced by external stimuli such

as pressure, light or temperature. Notably, the early 1930s witnessed the discovery by Cambi of the spin-crossover phenomena in small molecules, which is still nowadays a broad topic of the scientific community. Later on, in 1991, a known molecular cluster, $[\text{Mn}_{12}\text{O}_{12}(\text{OAc})_{16}(\text{H}_2\text{O})_4]$, was found to display unusual magnetic properties, and, more extraordinarily, to retain its magnetization upon the removal of the external magnetic field. Such compounds were named ‘single-molecule magnet’ – the term was then coined in 1996.

Single-molecule magnets (SMMs) in 2021 represent a fully dedicated research area. Possible industrial applications include magnetic refrigeration, spintronics for high-end devices, high-density data storage and quantum computing. Mastering the synthesis and deposition of single-molecule magnets on surfaces will thus open a vast field of novel materials answering the current technological needs. The complexity of SMM engineering, however, increased as knowledge has been generated, which is a reason why industrial applications are delayed. The first challenge concerns the operating temperature of these molecules: they are showing their remarkable magnetic properties only at super-cool temperatures (He-level), which is impracticable for industrial processes. Secondly, they can retain their magnetization for only a short amount of time (at best some months while hard drives last more than ten years), which does not suffice for data storage applications. Finally, most of the SMMs are air and moisture-sensitive, which makes it challenging to deposit them on surfaces, and even more to address them individually. Further research is necessary to deeper understand how SMMs function and how to overcome their current drawbacks. To fundamentally understand the properties of a SMM, one needs to isolate the molecule in its purest form: as a crystal. The pictures represented here are photographs of some crystals (under the optical microscope) synthesized in this work. They have various colors, various shapes: they show the complexity of the analysis of matter.



The present work aims to investigate monometallic cobalt and dysprosium complexes containing the S-N motive and put their potential as competitive SMMs into perspective. To this purpose, experimental and computational methods are combined to study the best structural conditions that give optimal magnetic properties. The magneto-structural correlations unveiled in this work should help steer further studies towards better performing SMMs.

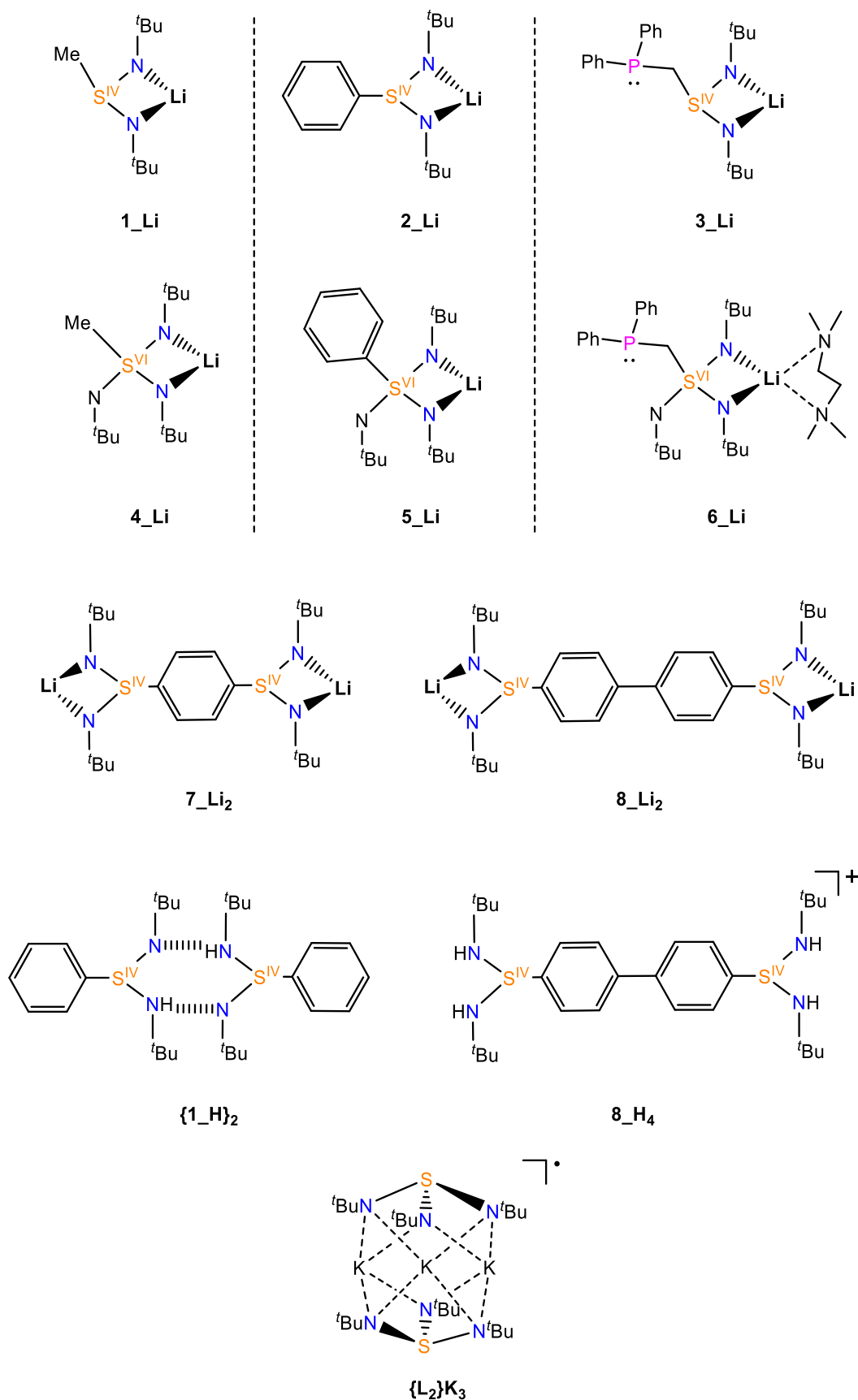
Abbreviations

ac	alternating current
An	actinides (Th-Lr)
AILFT	<i>ab initio</i> Ligand Field Theory
B	magnetic field, magnetic flux density
B3LYP	hybrid functional Becke, 3-parameter, Lee–Yang–Parr
CAM	Coulomb Attenuating Method
CASSCF	Complete Active Space Multiconfiguration Self Consistent Field
CCDC	Cambridge Crystallographic Database Centre
δ	chemical shift (ppm)
D	zero-field splitting (ZFS) parameter
dc	direct current
DCM	dichloromethane
DFT	Density functional theory
DKH	Douglas-Kroll-Hess basis set
E	rhombic zero-field splitting parameter (usually given as E/D)
emu	electromagnetic unit
EPR/ESR	Electron Paramagnetic Resonance/Electron Spin Resonance
Et ₂ O	diethylether (ether)
g	Landé magnetic factor
H	magnetic field strength (magnetizing field)
\hat{H}	Hamiltonian operator
HF	Hartree-Fock
HMDS	Hexamethyldisilazane or bis(trimethylsilyl)amide
I	nuclear spin
IR	infrared (spectroscopy)
J	magnetic exchange coupling constant

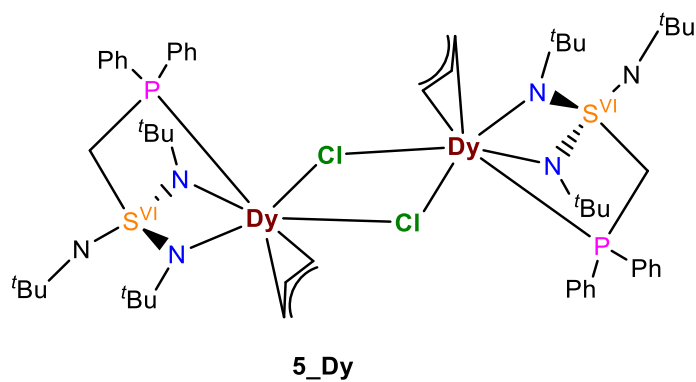
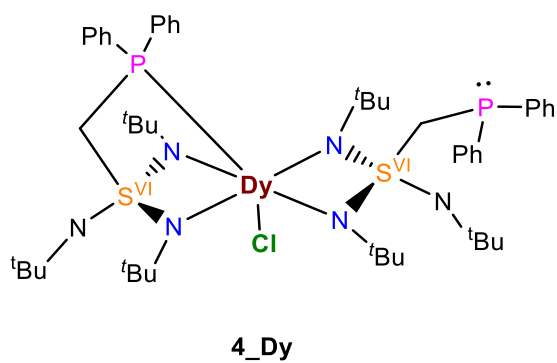
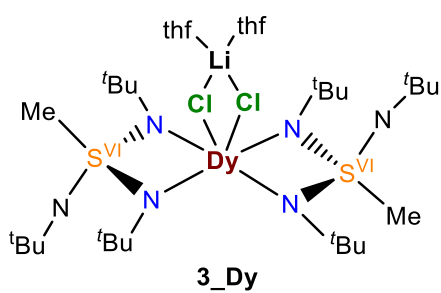
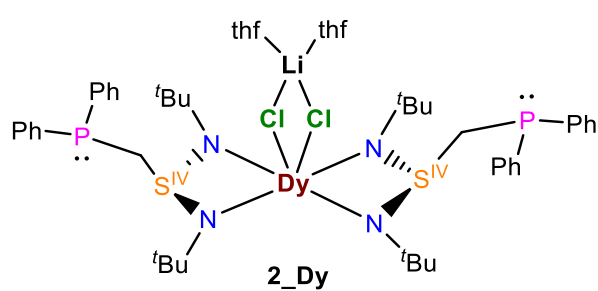
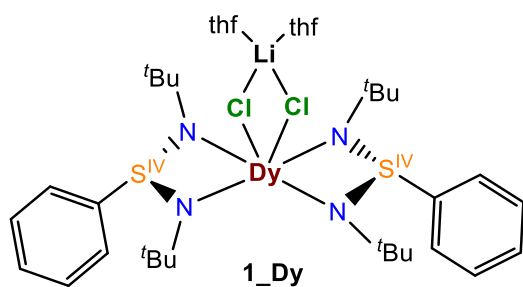
J	magnetic quantum number for lanthanide ions, total angular momentum (spin + orbital)
k_B	Boltzmann's constant
KD	Kramers' doublet
L	orbital angular momentum
LIFDI	Liquid Introduction Field Desorption Ionization
Ln	lanthanides (Ce-Lu), also referred to as 4f-elements
μ_B	Bohr magneton (magnetic moment of an electron)
μ_{eff}	effective magnetic moment
Me	methyl
MPMS	Magnetic Properties Measurement System
MS	Mass Spectrometry
M_S/M_J	magnetic quantum number or magnetic state
ν (Hz, cm^{-1})	frequency (usually given in Hertz for magnetic measurements and in inversed centimeters for spectroscopic measurements)
NEVTP2	second order n-electron valence state perturbation theory
NMR	Nuclear Magnetic Resonance
OAM	Orbital Angular Momentum
Oe	Oersted
PI	paramagnetic impurity
Ph	phenyl
ppm	part per million
QTM	Quantum Tunneling of the Magnetization
S	electronic spin, spin angular momentum
SCF	Self-Consistent Field
SC-XRD	Single-Crystal X-Ray Diffraction
SMM/SIM	Single-Molecule Magnet/Single-Ion Magnet
SOC	Spin-Orbit Coupling
SQUID	Superconducting Quantum Interference Device

T (K or °C)	temperature
τ	relaxation time
^t Bu	tert-butyl
TD-DFT	time-dependent density functional theory
THF	tetrahydrofuran
TIP	Temperature Independent Paramagnetic (parameter)
TMEDA	tetramethylethylenediamine
TMS	trimethylsilyl or tetramethylsilane (NMR reference only)
U_{eff}	effective thermal energy barrier to spin reversal
UV-vis	Ultraviolet-visible (spectroscopy)
VTVH	variable temperature variable field
χ	magnetic susceptibility
ZFS	Zero Field Splitting

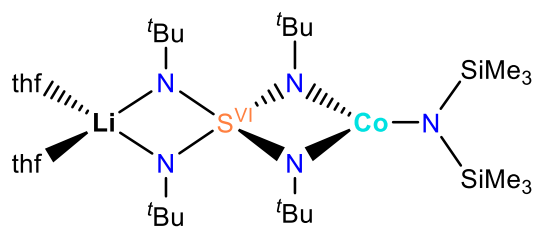
List of compounds 1 – SN-ligands and their alkali-metal complexes



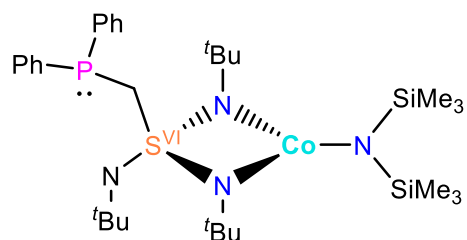
List of compounds 2 – dysprosium SN-based compounds



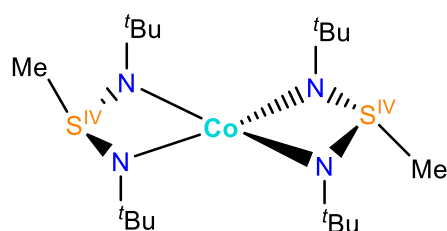
List of compounds 3 – cobalt SN-based compounds



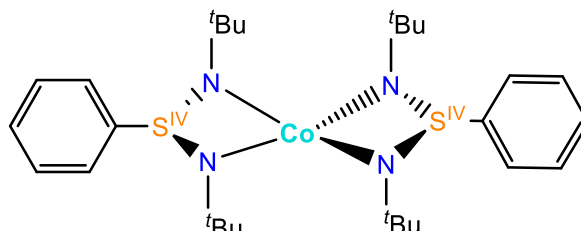
1_Co



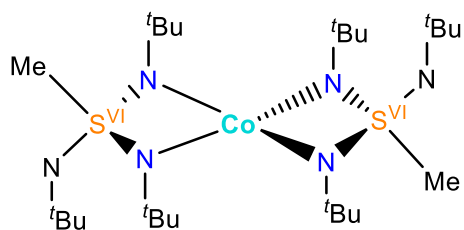
2_Co



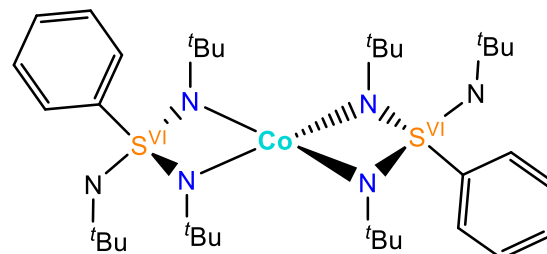
3_Co



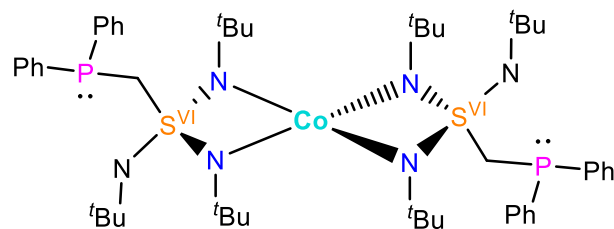
4_Co



5_Co



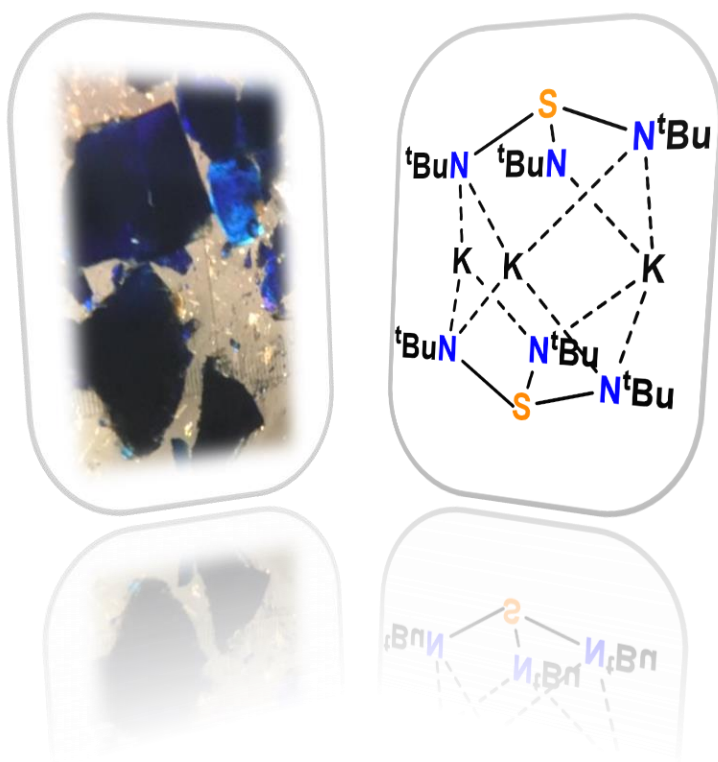
6_Co



7_Co

Chapter One

The S-N moiety: synergies, ligand synthesis, and further curiosities



1.1. The S-N moiety: using S-N based ligands towards single-molecule magnets

The association of sulfur with nitrogen to form S-N based compounds dates back to 1835, as a novel cage compound, namely $[S_4N_4]$, was discovered.¹ This explosive, thermochromic tetra-sulfur tetranitride is the most important binary sulfur nitride and is the precursor to many S-N compounds.²⁻⁴ It is available from the reaction of sulfur monochlorine with ammonia. The S-N bonds in $[S_4N_4]$ are easily thermally cleavable and it can give metal-like polymers of sulfur nitride $(SN)_x$ upon heating. Such polymers display anisotropic electrically conductive properties as well as superconducting properties at very low temperatures.^{5,6} Many parent compounds can be generated from $[S_4N_4]$, including sulfur tetraimide $[S_4(NH)_4]$ through reduction with tin chloride or dithionite. Their reactivity towards halogens, alcohols, p- and d-group metals (forming $M(SN)_x$ compounds, with $M = Fe, Co, Ni, Pd, Pt, x = 4$ or $M = Cu, Ag, Hg, Pb, x = 2$, or $M = Tl, x = 3$) were extensively studied and later reviewed by Goehring in 1956.^{3,7} Additionally, in the same year, Goehring and Weis reported the synthesis of sulfur diimide from SCl_4 and *n*-butylamine in ether at low temperatures.⁸ Subsequent distillation was necessary to isolate the pure yellowish liquid as $(n-BuN)_2S$ (sulfur in oxidation state +IV). A similar procedure was published in 1965 by Clemens, Bell and O'Brien.⁹ In their case, they used SCl_2 and *t*-butylamine as starting materials, which resulted in better stabilized sulfur diimides. In 1970, at the University of Göttingen, Glemser and Wegener¹⁰ prepared the first sulfur (+VI) triimide from $Li(N(TMS)_2)$ and NSF_3 in 10% yield. It was followed by a modified procedure published by Lidy and Sundermeyer¹¹ in 1974, starting from $NaN(TMS)_2$ and OSF_4 to give the same $(TMS_2N)_3S$ in 56% yield. The synthetic procedures, however, gave relatively low yields and were hazardous, mainly due to the use of reactive and dangerous OSF_4 and NSF_3 gases as sulfur sources.^{12,13} The sulfur-nitrogen chemistry had to wait until 1998, when Fleischer and Stalke¹⁴⁻¹⁶ reported a new route to sulfur (+VI) triimides.¹⁷ Achieved *via* oxidation with bromine, it involved a lithium triimidosulfite (sulfur in the oxidation state +IV) intermediate species.¹⁴ Albeit toxic and corrosive, the use of liquid bromine is less hazardous than those of thionyl tetrafluoride and of thiazyl trifluoride. The discovery of this easier, more accessible synthesis route boosted sulfur-nitrogen organometallic chemistry.

Collecting experimental data on S-N compounds provided interesting metric details regarding the S-N chemical bond. Several SN compounds were probed through charge density experiments with highly resolved SC-XRD.¹⁸⁻²¹ The careful analysis of the S-N bond(s) gave proof to support theoretical debates concerning sulfur hypervalency.^{16,20,22,23} A recent example, the compound $(tBuN)_2S(tBuNH)_2$, analogous to sulfuric acid demonstrates the polarized character of the S-N bonds (presence of the lone pairs on the nitrogen atoms with no distortion towards the S-N bond).²¹ (**Figure 1.1.1**) The parent sulfur ylides compounds $(R_2C)S(NR)_x$ ($x = 2, 3$ and $R = tBu$ or Me) were similarly investigated via experimental charge density.^{23,24} Comparable trends were found, ruling out sulfur hypervalency in both types of compounds, regardless of the sulfur oxidation state. Additional characterization methods such as IR, UV-vis, and advanced NMR spectroscopies further documented these novel S-N compounds in coordination chemistry.

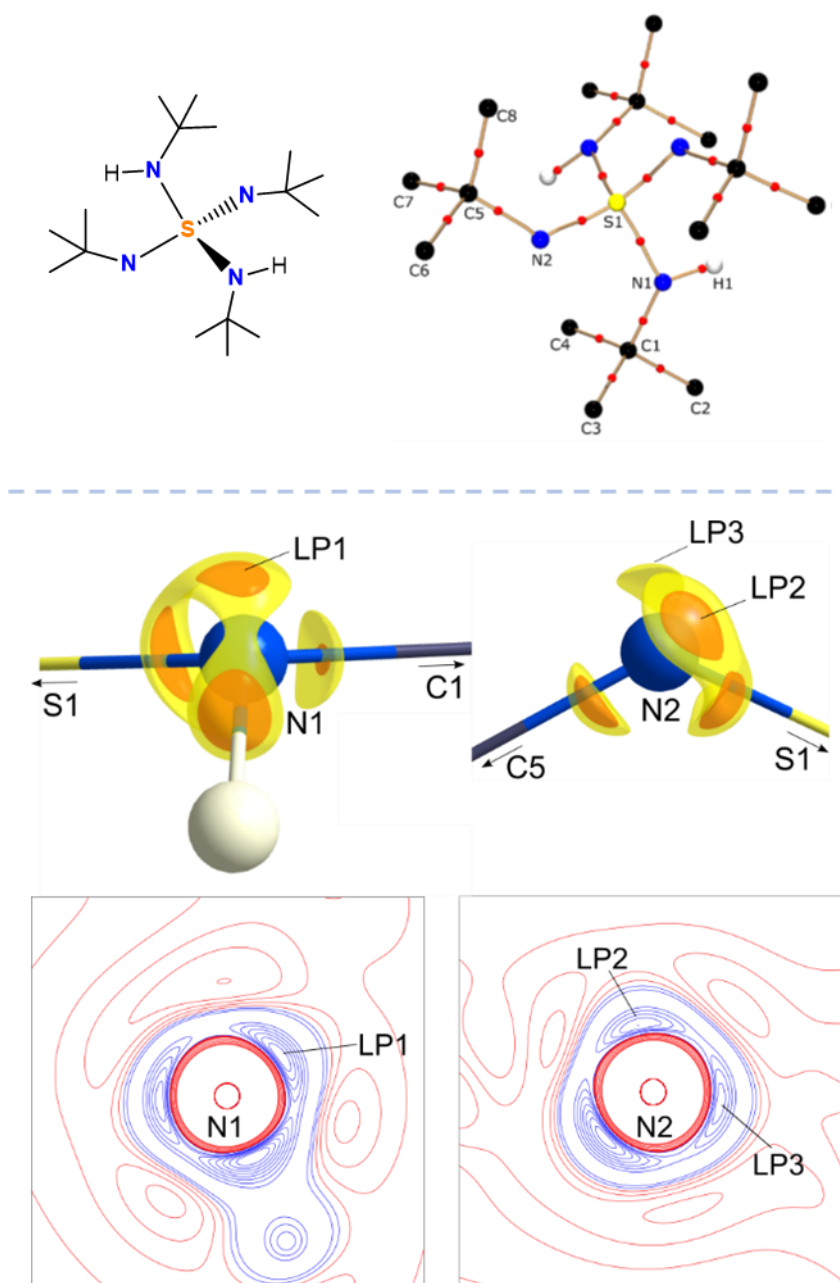


Figure 1.1.1: (top) Molecular representation of $(t\text{BuN})_2\text{S}(t\text{BuNH})_2$, the imido-analog to sulfuric acid, upon charge density analysis. The bonding paths are in gold, with the bond critical point (BCP) in red. (bottom) Laplacian of the electron density at isolevel of $-52 \text{ e}\text{\AA}^{-5}$ (orange) and $-35 \text{ e}\text{\AA}^{-5}$ (yellow) at N1 and N2 in $(t\text{BuN})_2\text{S}(t\text{BuNH})_2$ and contour plots of charge concentrations in the H1-N1-LP1 and LP2-N2-LP3 plane. Contours are drawn at ± 1 , to $135 \text{ e}\text{\AA}^{-5}$, blue contours show negative values, red values show positive values.²¹ (LP = lone pair).

Thereafter, Stalke *et al.*²³⁻³³ and Roesky *et al.*³⁴ designed several novel SN organic compounds, mainly used as ligands for further coordination with s -³⁵⁻³⁹, p -^{34,37,40}, d -⁴¹⁻⁴³ and, more recently, f -block metals. Upon coordination, the obtained complexes can be used for different purposes,^{18,19} including reactivity to access new Grignard reagents,^{36,44} redox activity,¹⁴ O_2 sensing,⁴⁵

fluorescence,³⁷ and magnetism.^{42,46} A succinct overview of some of the existing SN ligands and associated complexes is presented in **Figure 1.1.2**.

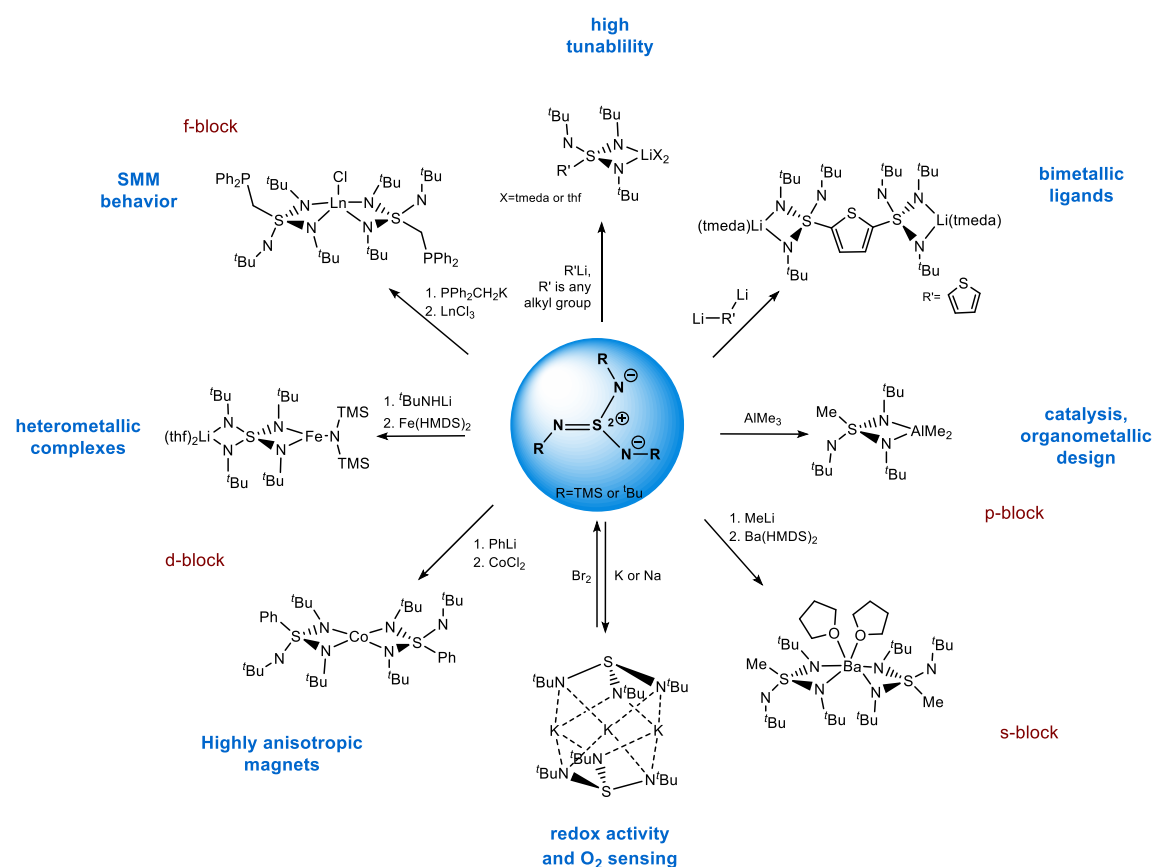


Figure 1.1.2. Overview of the versatile chemistry and potential applications of the SN family.

Amongst the variety of complexes that can be obtained with the SN motive, it became tempting to probe the SN synergy towards SMM applications.^{47–54} Indeed, this combination of sulfur with nitrogen as two antagonist atoms is suitable towards the design of SMMs. First, the sulfur atom provides flexibility while the donating nitrogen retains its hardness, resulting in an adaptable, ubiquitous ligand. Secondly, the SN moiety constitutes a versatile and galore tunable platform, which allows a particularly meticulous control of the ligand design.^{16,24,55} The obtained ligands thus display small structural variations. They are therefore well-suited candidates for comprehensive studies regarding correlations between structural and physical properties.^{24,55} Thirdly, the central sulfur atom can be further oxidized and/or substituted with alkyl groups containing other p-block elements, such as phosphine derivatives.^{56,57} This enables the investigation of the influence of p-block elements on the magnetic properties. Finally, the ditopic ligands of the SN family seem suitable for the synthesis of binuclear – and even multinuclear – structures, in order to study magnetic couplings, heavy p-block/d-block synergies and to access multidimensional SMMs.^{37,58} Altogether, SN ligands are therefore well suitable building blocks for single molecule magnets.⁴² Armed with these optimistic considerations, their challenging synthesis will now be described in detail.

1.2. General procedures for ligand synthesis

The main results of this thesis are based on the *t*-butylamine SN derivatives, which is why we shall focus on them in the present section. The synthesis proceeds as follows:

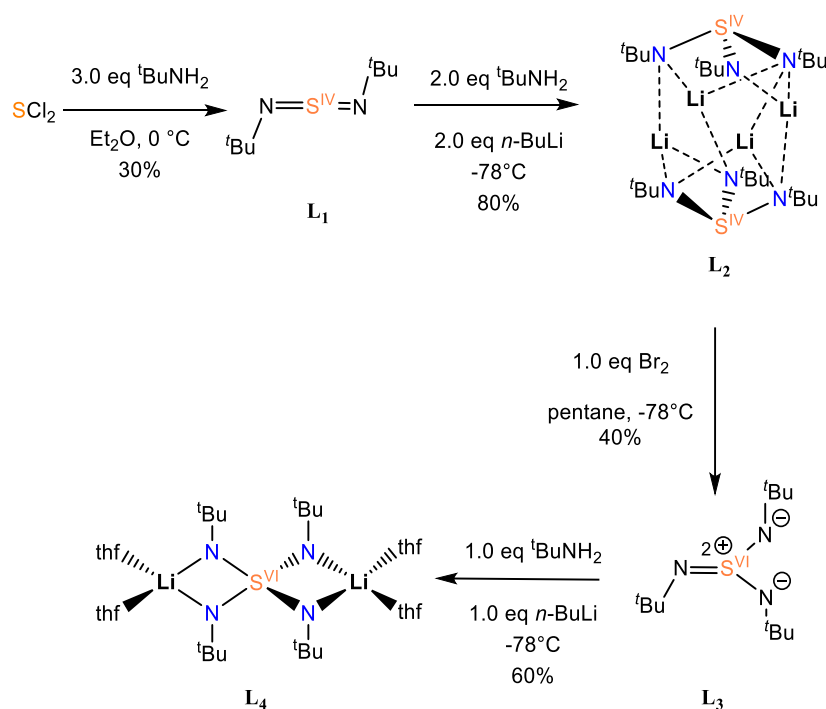


Figure 1.2.1: Synthesis route to **L**₁, **L**₂, **L**₃ and **L**₄ from SCl₂

Commonly used as a sulfur source in organometallic synthesis, sulfur dichlorine is firstly obtained from elemental sulfur and chlorine gas.⁵⁹ Under a saturated chlorine gas flow, the reaction flask will warm up to 120°C and the yellow solid sulfur will slowly evolve into a cherry-red solution, without the use of a solvent. A distillation purification step is mandatory before further use.ⁱⁱ The freshly distilled sulfur dichlorine then reacts with *tert*butyl-amine in ether at 0°C to form sulfur diimine (**L**₁) and *tert*butyl-ammonium chloride as a by-product.⁹ Upon filtration of the white salt, the resulting oily yellow product is then purified twice by vacuum distillation. The sulfur diimine (N^{*t*}Bu)₂S (**L**₁) is obtained as a volatile, slightly yellow liquid. Sulfur is in the oxidation state +IV. This SN compound **L**₁ will be the cornerstone of all further ligand synthesis of this work. To achieve compound **L**₂, ^{*t*}BuNLi is prepared in situ from ^{*t*}BuNH₂ and *n*-BuLi at -78°C in toluene. The subsequent slow addition of **L**₁ gives the trisubstituted triimidosulfate lithium salt [Li₂(N^{*t*}Bu)₃S]₂ (**L**₂), which recrystallize as colorless needles from the reaction mixture at -25°C. To improve the yield, reducing the mother liquor and setting it up for recrystallization is recommended.¹⁴ **L**₂ can be further oxidized with Br₂ in pentane to obtain (N^{*t*}Bu)₃S (**L**₃).¹⁵ The reaction must be carried out within 24 hours, otherwise decomposition of the product **L**₃ or very poor yields may be expected. Upon addition of liquid bromine at -78°C to the pentane solution of **L**₂, the solution color evolves from colorless to intense blue to green to orange to white. The reaction is finished when the reaction flask contains a white creamy-like mixture (formation of a

ⁱⁱ Fresh distillation is required due to the existing equilibrium $2 \text{ SCl}_2 \rightleftharpoons \text{S}_2\text{Cl}_2 + \text{Cl}_2$

precipitate). Upon filtration through celite, the filtrate is collected, and the solvent reduced. Since the product is volatile, it is recommended to use a cooling bath and a vacuum controller to avoid subliming the product at this step. When a brownish liquid is left, a proper vacuum sublimation can be started, for which heating up to +150°C should suffice. It works best while using nitrogen as inert gas in order to have a better control on the vacuum. Indeed, the product is gathered in a Schlenk trap cooled with liquid nitrogen, which creates an equilibrium between liquid and gaseous nitrogen (if argon is used instead of nitrogen, it might start liquefying). The trap is placed between the sublimation apparatus and the vacuum controller. Upon collection of the product, the trap is subsequently washed with a minimal amount of anhydrous pentane and the resulting solution is transferred to a Schlenk flask. If necessary, the volume is reduced to a few mL, as the product is highly soluble in pentane. Colorless block-shaped crystals of **L**₃ are obtained after a few hours in the freezer at -35°C from the concentrated pentane solution. Compound **L**₃ now possesses a sulfur atom in the +VI oxidation state. The subsequent reaction of **L**₃ with ^tBuNLi (prepared in situ as described for **L**₂) in THF allows to tetra substitute the sulfur atom with four equivalent N^tBu groups, yielding compound **L**₄, which recrystallizes as colorless blocks from the reaction solution at -35°C.¹⁵ Similar reaction routes allow access to a plethora of SN based ligands.^{15,24,33,36,37,57,58} The synthesis of the ligands relevant to this work is shortly depicted in the following **Figures 1.2.2, 1.2.3 and 1.2.4**. The ligands **1_Li**, **2_Li** and **3_Li** synthesized from **L**₁ (**Figure 1.2.2**) are usually obtained in high yields and are soluble in organic solvents, including pentane and hexane. This allows a better subsequent separation of lithium halide salts upon metalation. The ligands **7_Li**₂ and **8_Li**₂ (**Figure 1.2.3**) can also be obtained via the same synthesis route and the same work-up, starting with dilithiumphenyl and dilithiumbiphenyl, respectively.⁵⁸

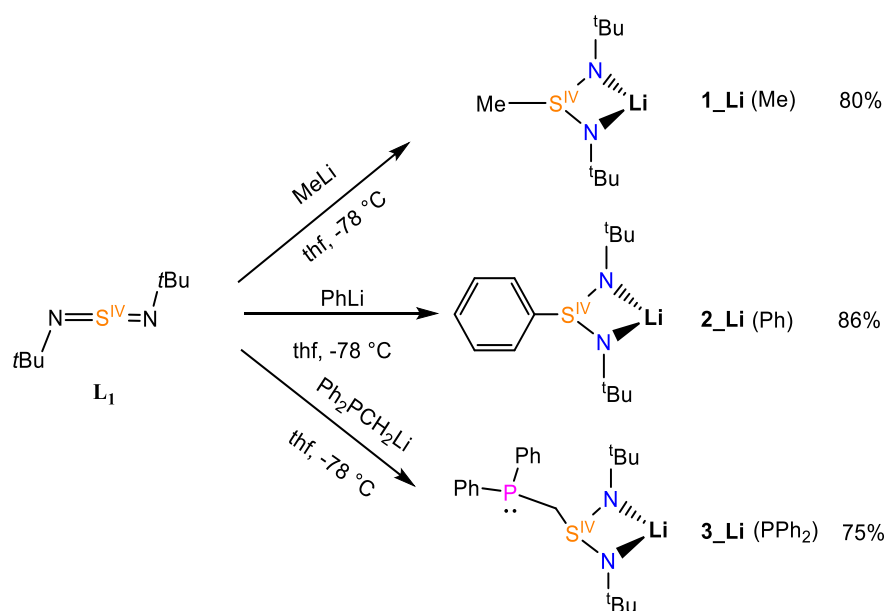


Figure 1.2.2: Synthesis of ligands **1_Li**, **2_Li** and **3_Li** from **L**₁.

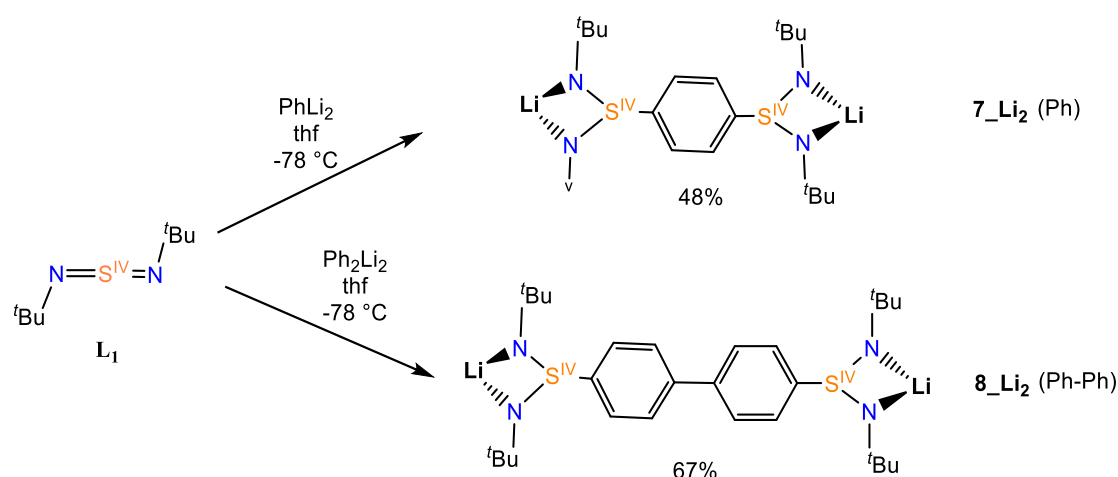


Figure 1.2.3: Synthesis of **7_Li₂** and **8_Li₂** from **L₁**

From **L₃**, ligands with the sulfur atom in the oxidation state +VI can be obtained by the addition of an alkyllithium reagent. As described for **L₄**, the overall synthesis of such ligands requires several steps from **L₁** to the desired product, resulting in relatively poor yields. Additionally, they are usually more difficult to isolate as pure crystalline material and are less soluble in non-polar solvents than the ligands obtained from **L₁**. Crystalline products are standardly obtained from concentrated THF solutions layered with pentane. Metalation reactions often require a subsequent filtration through celite. Nevertheless, the ligands with the sulfur atom in the oxidation state +VI, such as **4-6_Li** shown in **Figure 1.2.4**, possess several advantages compared to their S(IV) analogs.^{23,24}

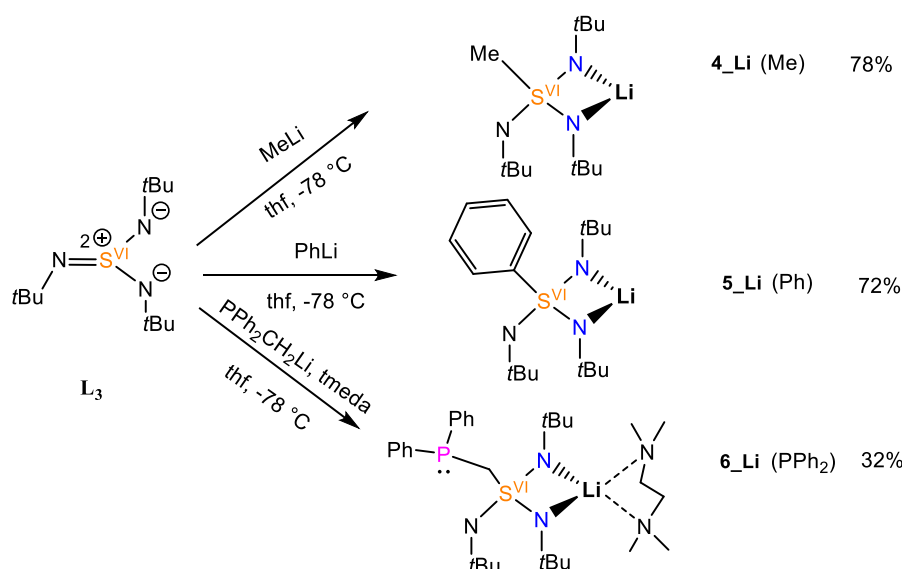


Figure 1.2.4: Synthesis of ligands **4_Li**, **5_Li** and **6_Li** from **L₃**

Firstly, they are more robust against oxidation if exposed to oxygen. Secondly, the fourth substitution on the sulfur atom seems to better stabilize their corresponding metal complexes. Finally, smaller acute N-M-N bite angles are accessible for the S(VI) ligand series. Tiny variations of this particular structural parameter have drastic influence on the physical properties, which

will be further discussed in **Chapters 2 and 3**. The access to both ligands with sulfur in the oxidation state +IV and +VI results in fruitful comprehensive studies to draw correlations between their structural and physical properties. Other SN compounds with interesting redox properties may be obtained from **L₂** or **L₃**, as reported elsewhere.^{14,60}

Notably, three new compounds of the SN family – the protonated species **{1_H}_2** obtained from **2_Li**, the salt species **{(8_H₄)(8_H₂LiCl₂)}** containing **8_Li₂** ligand and a radical **{L₂}_2K₃** – were successfully synthesized and characterized. These novel compounds are presented in the next two sections **1.3 and 1.4**.

1.3. Expanding the SN family: presentation of two new compounds

1.3.1. The dimer **{Ph(N^tBu)S(PhNH)}₂ (**{1_H}_2**)**

{1_H}_2 can be obtained from **2_Li** upon reaction with H₃N^tBuCl in pentane at room temperature (**Figure 1.3.1**). Upon stirring for a day, the clear colorless solution turns yellowish and a precipitate forms. The unreacted materials and lithium chloride are removed by filtration through celite. Volatiles are removed *in vacuo*, the crude product is then dissolved in pentane and filtered again. The product is soluble in non-polar solvents (benzene, hexane, and pentane) as well as polar solvents. The ¹H-NMR analysis in deuterated THF confirms the protonation, as an additional broad peak is then detectable at $\delta = 4.35$ ppm, in good agreement with the typical amine proton chemical shift range and shape.

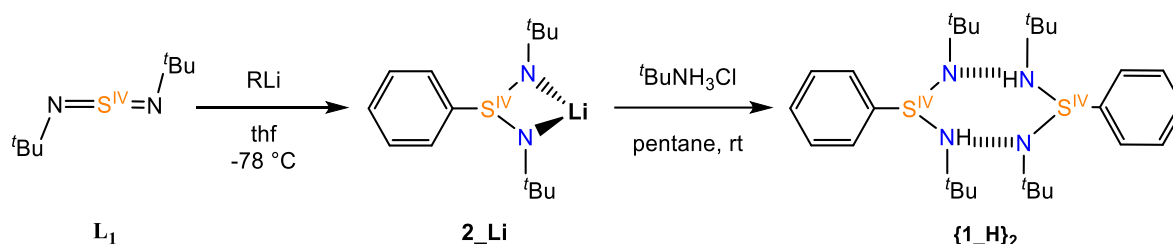


Figure 1.3.1: synthesis route from **L₁** to **{1_H}_2**

Colorless block-shaped crystals suitable for X-ray diffraction analysis are grown over a week from a concentrated clear filtered pentane solution of the crude product at **-35 °C**. It crystallizes in the monoclinic space group **P2₁/c** with two molecules in the asymmetric unit. In the solid-state, it dimerizes through hydrogen bonds (**Figure 1.3.2**) and the two molecules are ideally antiparallel to each other. The packing shows a perpendicular arrangement of each dimer to the next ones. The S-N bonds lengths range from 1.5839(10) to 1.6776(11) Å. The bond distances between the sulfur atom and the protonated nitrogen atoms are longer than the other two S-N distances by 0.1 Å, similar to (tBuN)₂S(tBuNH)₂. This could be explained by some double bond character for the shorter S-N bonds, while the other two are single bonds. The sulfur atoms adopt a trigonal pyramidal geometry with a distance of 0.657 Å to the (N, C_{Ph}, N) plane. The two hydrogen bond distances are 2.209(15) Å and 2.251(15) Å, slightly shorter than the typical hydrogen bond length for a S=N-H donor.⁶¹ A DOSY-NMR in THF reveals that the compound does not conserve its dimerized association in solution (see **4.2.1**). In the solid-state, the dimeric structure is probably stabilized by the hydrogen bonds as well as the phenyl groups arranged anti-parallelly. The

shortest distance between the phenyl groups is of 5.651 Å, which may speak for weak parallel offset π - π interactions.⁶²

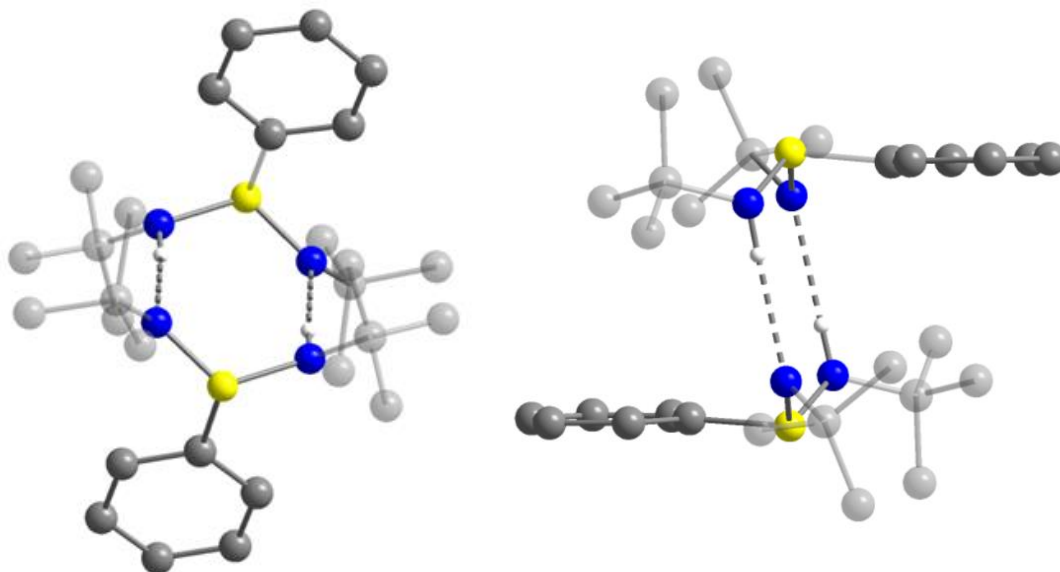


Figure 1.3.2. Crystal structure and asymmetric unit of $\{1_H\}_2$ in two different views. Sulfur, nitrogen and carbon atoms are represented in yellow, blue and grey, respectively. Hydrogens located on carbon atoms are omitted for clarity. Dashed lines represent N-H hydrogen bonds.

1.3.2. $[(\text{PhS}(\text{N}^t\text{BuH})_2)_2][\{(\text{BuNH})\text{PhS}(\text{BuNLiCl}_2)_2\}] \{(8_H_4)(8_H_2\text{LiCl}_2)\}$

In a similar manner, the reaction of 8_Li_2 , obtained from **I**,⁵⁸ with two eq. of $\text{H}_3\text{N}^t\text{BuCl}$ in THF yields the salt $[(\text{PhS}(\text{N}^t\text{BuH})_2)_2][\{(\text{BuNH})\text{PhS}(\text{BuNLiCl}_2)_2\}]$, further abbreviated $\{(8_H_4)(8_H_2\text{LiCl}_2)\}$, as depicted in **Figure 1.3.3**.

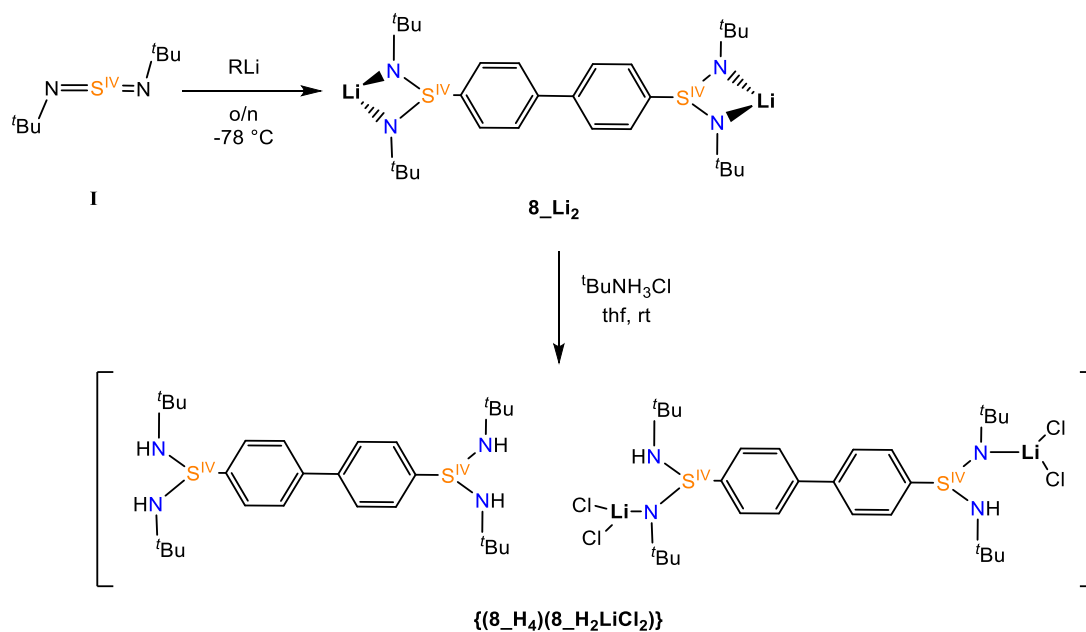


Figure 1.3.3: Synthesis route to $\{(8_H_4)(8_H_2\text{LiCl}_2)\}$ from **I** via 8_Li_2

In this case, however, the reaction takes place in THF, as the ligand **8_Li** is completely insoluble in toluene and only slightly soluble in THF. When combining both reagents in THF, the solution turns yellow and clear, indicating that a reaction is taking place. After a couple of minutes, the solution becomes cloudy and a white precipitate forms, presumably LiCl. Upon stirring for several hours, the mixture is filtered, and the resulting clear yellow solution is reduced. The crude product is then recrystallized from a THF solution layered with pentane (1:5) at -35°C .

Colorless block-shaped crystals of $\{(\mathbf{8_H_4})(\mathbf{8_H_2LiCl_2})\}$ suitable for X-ray analysis are obtained from the slow diffusion of pentane into concentrated THF solutions. The compound crystallizes in the tetragonal space group $P\bar{4}2_1c$. The tetra-protonated ligand (**8_H₄**) co-crystallizes with the bi-protonated lithium chlorine adduct **8_H₂LiCl₂**, which is probably the intermediate during the formation of **8_H₄** (**Figure 1.3.4**). The asymmetric unit only contains half of each subunit, as well as a disordered THF molecule. The two subunits **8_H₄** and **8_H₂LiCl₂** are stacked parallelly to each other, allowing parallel face-centered π - π interactions between the phenyl rings (distant of 7.165 Å from each other).⁶² Noteworthy, the LiCl_2^+ coordination is located in between the two sub-units. This suggests that the negatively charged chlorine atoms may weakly interact with the hydrogen atoms (distance range of 2.27 – 2.41 Å).

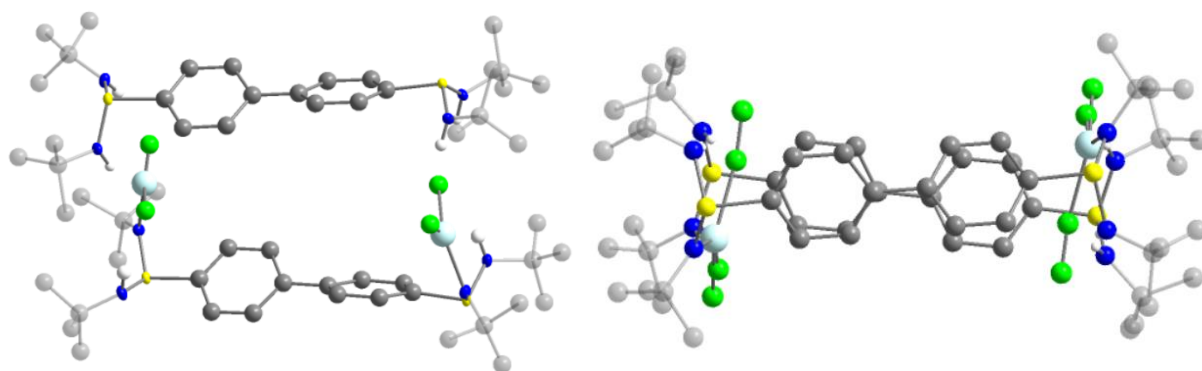


Figure 1.3.4: crystal structure of $\{(\mathbf{8_H_4})(\mathbf{8_H_2LiCl_2})\}$ in top and side views. The doubly protonated cation co-crystallizes with its mono-protonated species carrying LiCl_2 as a counter ion. Chlorine, sulfur, nitrogen, carbon, lithium and the amine hydrogens are represented in green, yellow, blue, grey, light blue and white, respectively. Other hydrogens are omitted for clarity.

In the subunit **8_H₄**, the S-N distances are found almost equivalent of 1.614(4) and 1.610(4) Å. On the contrary, the subunit **8_H₂LiCl₂** contains two longer S-N bond of 1.663(5) and two shorter S-N bond of 1.577(4) Å, reminiscent of the bond lengths found in **{1_H₂}**. In both complexes, hydrogen bonding plays a significant role in these structural variations. Furthermore, the sulfur atoms are in a trigonal pyramidal environment with distances to the (N, C_{Ph}, N) plane of 0.635 Å in **8_H₄** and of 0.661 Å in **8_H₂LiCl₂**. These slight variations may be due to the electron-withdrawing effect arising from the LiCl_2^- unit coordinated on the nitrogen atom in **8_H₂LiCl₂**. The structure packing is dense (**Figure 1.3.5**) and reveals that the intermolecular distances between two phenyl rings can be as short as 3.05 Å, which definitely speaks for the presence of strong π - π stacking between the ligand phenyl rings.⁶²

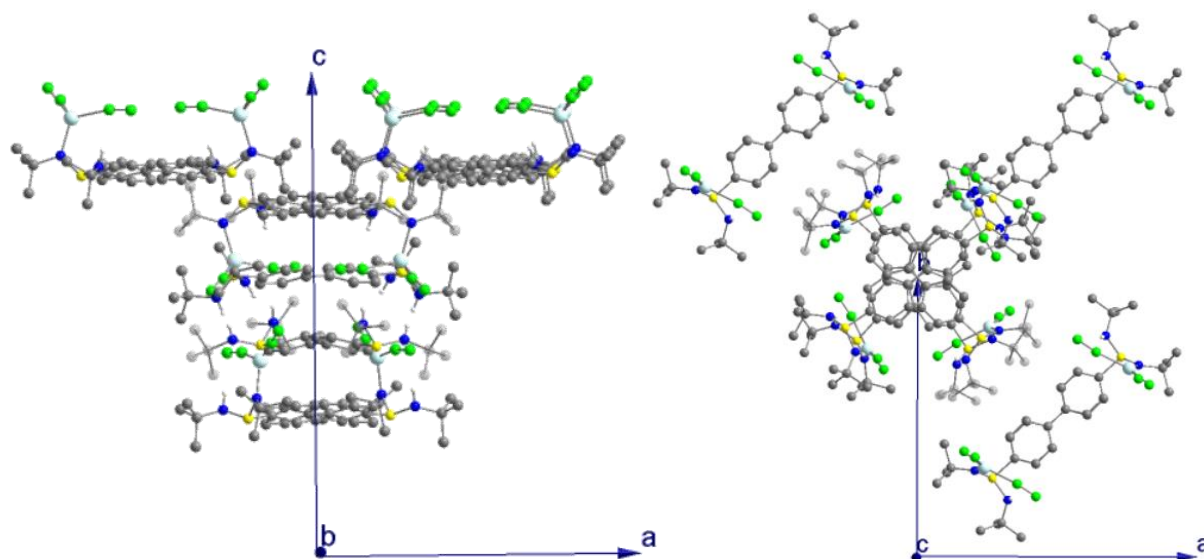


Figure 1.3.5. Views along the *b* (left) and *c* (right) axes of the structure packing for compound $\{(8_H_4)(8_H_2LiCl_2)\}$.

1.3.3. Perspectives

Since its crystal structure does not show disorder and has a high resolution by a standard X-ray diffraction experiment, the compound $\{1_H\}_2$ represents an interesting candidate for charge density analysis in order to better assign the influence of the protonation on the S-N bond lengths. The crystal structure of $\{(8_H_4)(8_H_2LiCl_2)\}$ shows that the product of the corresponding reaction consists of a mixture of two compounds, with one presumably being the intermediate to the second one. The compound 8_H_2 can probably be accessed in high yields and isolated if more equivalents of $tBuNH_3Cl$ are employed or upon screening the reaction conditions. Both $\{(8_H_4)(8_H_2LiCl_2)\}$ (or 8_H_4 only if accessible) and $\{1_H\}_2$ can then be used as starting materials for further reactivity towards metal complexes in order to avoid the use of the lithium reagent 2_Li or 8_Li_2 with metal halide salts. It can be used as such with $M(HMDS)_x$ salts ($M = d\text{-metal}$, $x = 2$ or $M = Ln$, $x = 3$) or deprotonated back with potassium or sodium sources. Thereafter, the subsequent difficult (or sometimes even impossible) separation of a metalation product from the lithium halide by-product is avoided. This hypothesis will be further discussed in **chapter 2** for the synthesis of dysprosium complexes and in **chapter 3** for obtaining trigonal planar asymmetric cobalt complexes.

1.4. Isolation and characterization of the transient radical species

$[\text{S}(\text{N}^t\text{Bu})_3]_2\text{M}_3$ ($\text{M}=\text{Li}, \text{K}$) ($\{\text{L}_2\}_2\text{M}_3$)

1.4.1. Characterization of $\{\text{L}_2\}_2\text{Li}_3$

Remarkably, the exposure of $[\text{Li}_4\{(\text{N}^t\text{Bu})_3\text{S}\}_2]$ (L_2) to oxygen leads to the observation of an intense deep blue color, reminiscent of the lapis-lazuli pigment, the ultramarine blue. Further exposure to air or reaction with iodine gives colorless solutions in minutes, from which the respective oxidation products $[\{\text{S}(\text{N}^t\text{Bu})_3\}_2\text{Li}_3\{\text{Li}(\text{THF})\}]$ and $[(\text{THF})_3\text{Li}_3(\mu_3\text{-I})\{(\text{N}^t\text{Bu})_3\text{S}\}]$ were isolated and characterized by X-ray diffraction (**Figure 1.4.1**). However, the transient blue species itself, as observable in **Figure 1.4.1**, was never isolated. A solution of L_2 exposed to O_2 was investigated by EPR spectroscopy in 1996.¹⁴ The EPR spectrum showed the coupling of the electron with three ^{14}N nuclei ($I = 1$, hyperfine coupling, gives a septet) and with two ^7Li nuclei ($I = 3/2$, super-hyperfine coupling, gives a septet if fully resolved). Based on the EPR spectrum and inspired by the X-ray structures of the colorless oxidation products, Stalke *et al.* then proposed a structure containing two lithium ions located between two cap-shaped $\text{S}(\text{N}^t\text{Bu})_3$ ligands.^{14,60} The stability of such a species, however, was never further probed by DFT calculations.

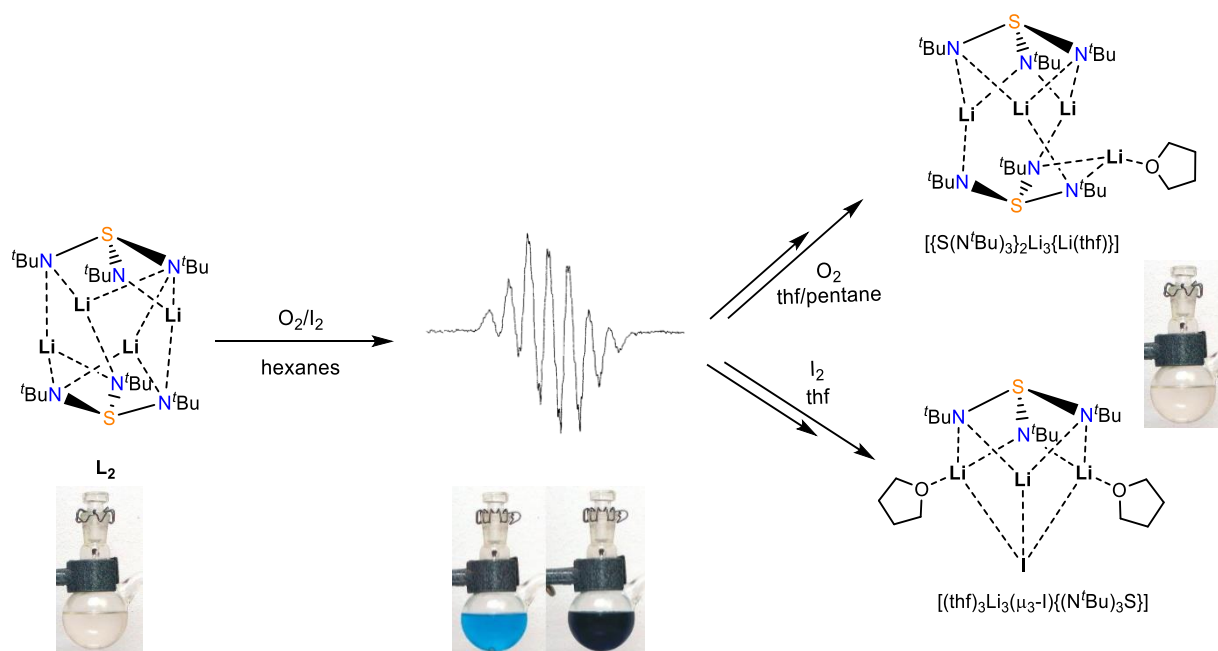


Figure 1.4.1. Scheme of the oxidation of $[\text{Li}_4\{(\text{N}^t\text{Bu})_3\text{S}\}_2]$ (L_2) with O_2 or iodine. Colorful solutions of the intermediate radical species upon addition of O_2 are shown under the corresponding EPR spectrum measured in hexanes at rt. Pictures and EPR spectrum reproduced from previous work.¹⁴

A better resolved EPR spectrum was measured two years later¹⁷ and revealed that not two, but three lithium atoms must be present in the structure and must couple with the unpaired electron (**Figure 1.4.2**).

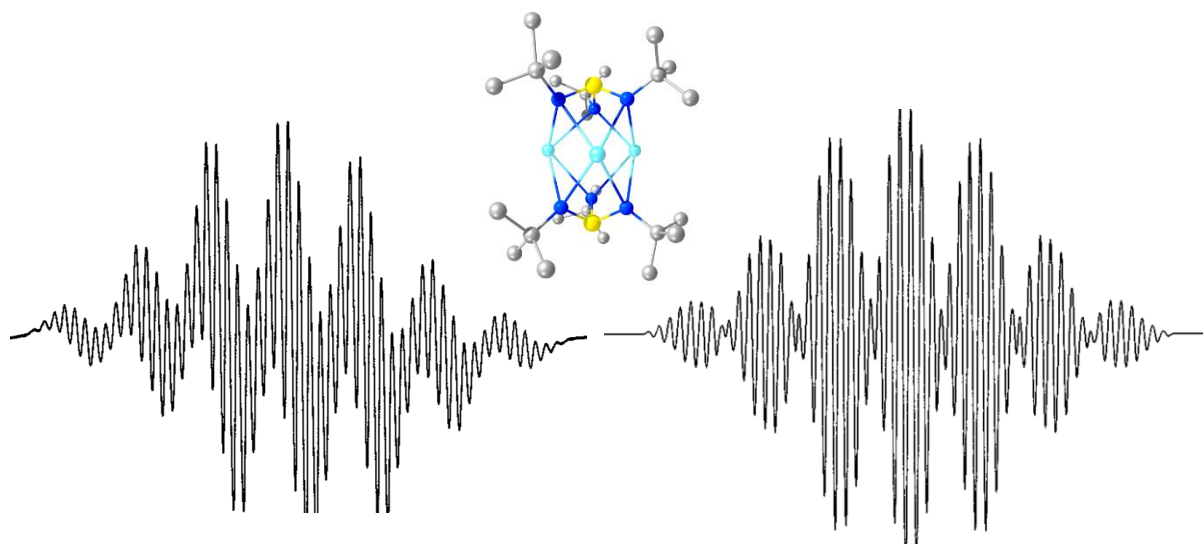


Figure 1.4.2. EPR spectrum of $\{L_2\}_2Li_3$ in hexanes at rt. The hyperfine splitting gives a septet ($a = 8G$, intensity ratio 1:3:6:7:6:3:1) confirming interaction with three equivalent ^{14}N nuclei ($I = 1$). The super-hyperfine coupling (decet with $a = 0.8G$) corresponds to the interaction with three equivalent 7Li nuclei ($I = 3/2$). The signal's center is at 3487 G.¹⁷ (The simulated EPR spectrum on the right gave the same pattern.) Proposed crystal structure based on the EPR spectrum analysis Yellow, dark blue, grey and light blue spheres correspond to sulfur, nitrogen, carbon and lithium atoms respectively. Hydrogens are omitted for clarity.

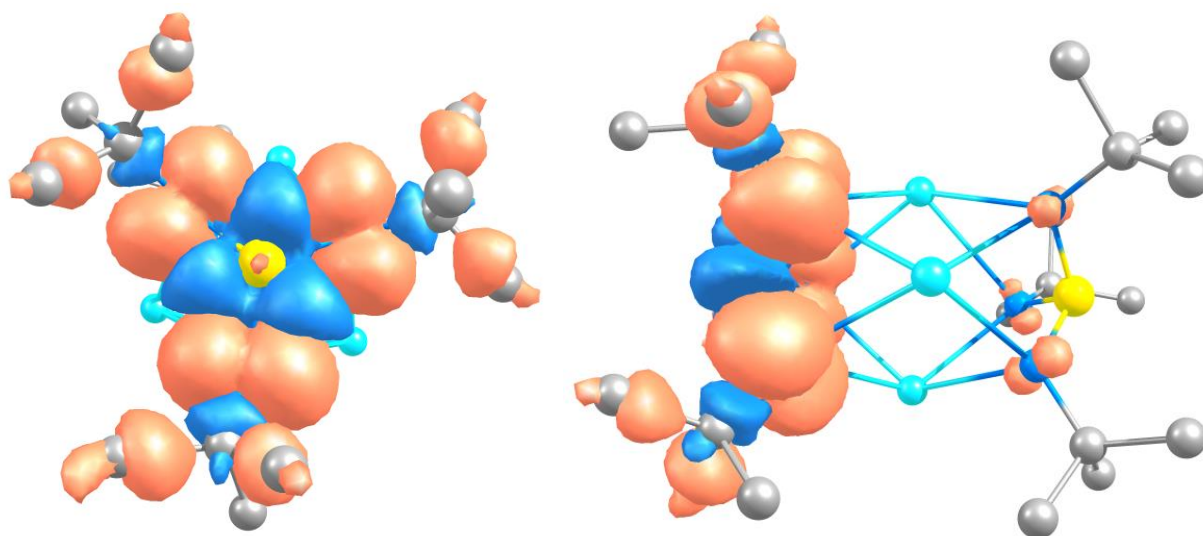


Figure 1.4.3. Calculated spin density plots for $\{L_2\}_2Li_3$. Positive and negative densities are depicted in orange and blue, respectively (isosurfaces at 0.005 level). Both top-down (left) and side views (right) are depicted for better clarity. Hydrogens are omitted for clarity.

The visualization of the spin density calculated on a theoretical structure is consistent with the hyperfine coupling of the free electron with three nitrogen atoms of one capping ligand (**Figure 1.4.3.**). Interestingly, no positive spin density is detected on the central sulfur atom, although the transfer of electron density is probably going through it. This may suggest that the electron transfer is occurring very fast between the three nitrogen atoms.

Unfortunately, the elusive lithium radical species, further abbreviated $\{\text{L}_2\}_2\text{Li}_3$, could never be further characterized by X-ray diffraction.^{14,60} At the time, the repeated attempts to grow crystals of $\{\text{L}_2\}_2\text{Li}_3$ for X-ray analysis were unsuccessful, probably because of its high sensitivity to oxygen or simply because of its inability to crystallize due to the small lithium ions compared to the ligand size. Alternatively, the transient radical species always further reacted with traces of oxygen to give fully oxidized products, preventing the effective isolation of $\{\text{L}_2\}_2\text{Li}_3$. Reactions in other solvents yielded different color changes (in THF, the solution turns red) and the subsequent crystallization was found similarly challenging.^{14,60} Nevertheless, the lithium radical species is herein revisited and further characterized by UV-vis spectroscopy (Figure 1.4.4).

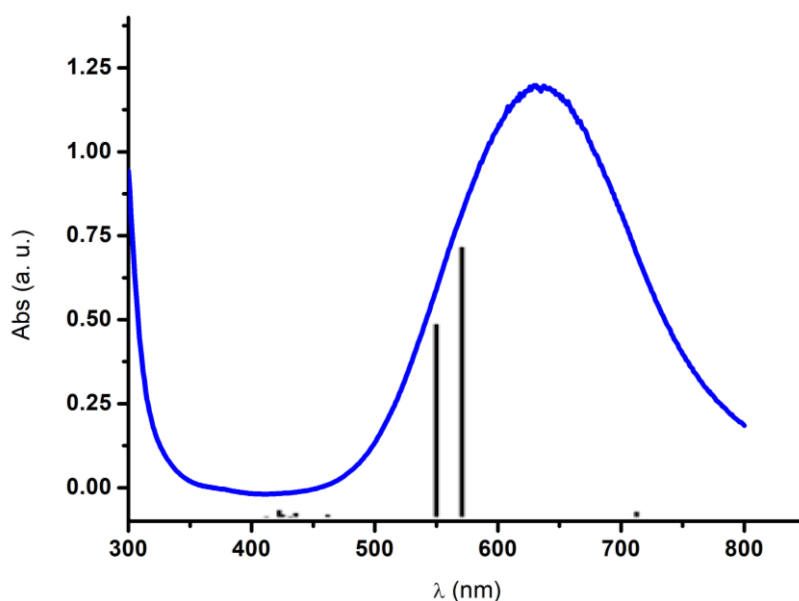


Figure 1.4.4. Absorption spectrum of $\{\text{L}_2\}_2\text{Li}_3$ at maximal absorbance. The experimental data is represented with a blue solid line and the calculated absorption peaks are represented as black lines.

A time dependent UV-vis measurement of L_2 upon exposure to air was carried out. The colorless compound L_2 was dissolved in toluene and the solution was transferred to a Schlenk cuvette with a stir bar. A reference spectrum acquisition confirmed the absence of colorful species before the start of the reaction. The Schlenk cuvette was unsealed, and the solution thus exposed to air while stirring to allow homogeneous O_2 diffusion into the sample. A broad absorption band appeared with a maximum at $\lambda_{\text{max}} = 633$ nm, whose amplitude grew during the first 7 minutes of the reaction. Afterwards, the peak intensity diminished completely, and the solution turned colorless after approx. 5-6 min. The corresponding spectra are plotted in **Figure 1.4.5**. The time-dependent absorbance at the peak's maximal intensity $\lambda_{\text{max}} = 637$ nm is plotted below. The present vis spectroscopy characterization gives access to new features of $\{\text{L}_2\}_2\text{Li}_3$. First, it confirms the formation of a colorful species absorbing at $\lambda_{\text{max}} = 633$ nm (**Figures 1.4.4** and **1.4.5**). The broad absorption band spreads from 550 nm to 750 nm, responsible for the blue color of the solution. Secondly, it suggests that $\{\text{L}_2\}_2\text{Li}_3$ decomposes rapidly while further exposed to air, surviving about ten minutes. This may explain the difficulty to isolate and recrystallize $\{\text{L}_2\}_2\text{Li}_3$.

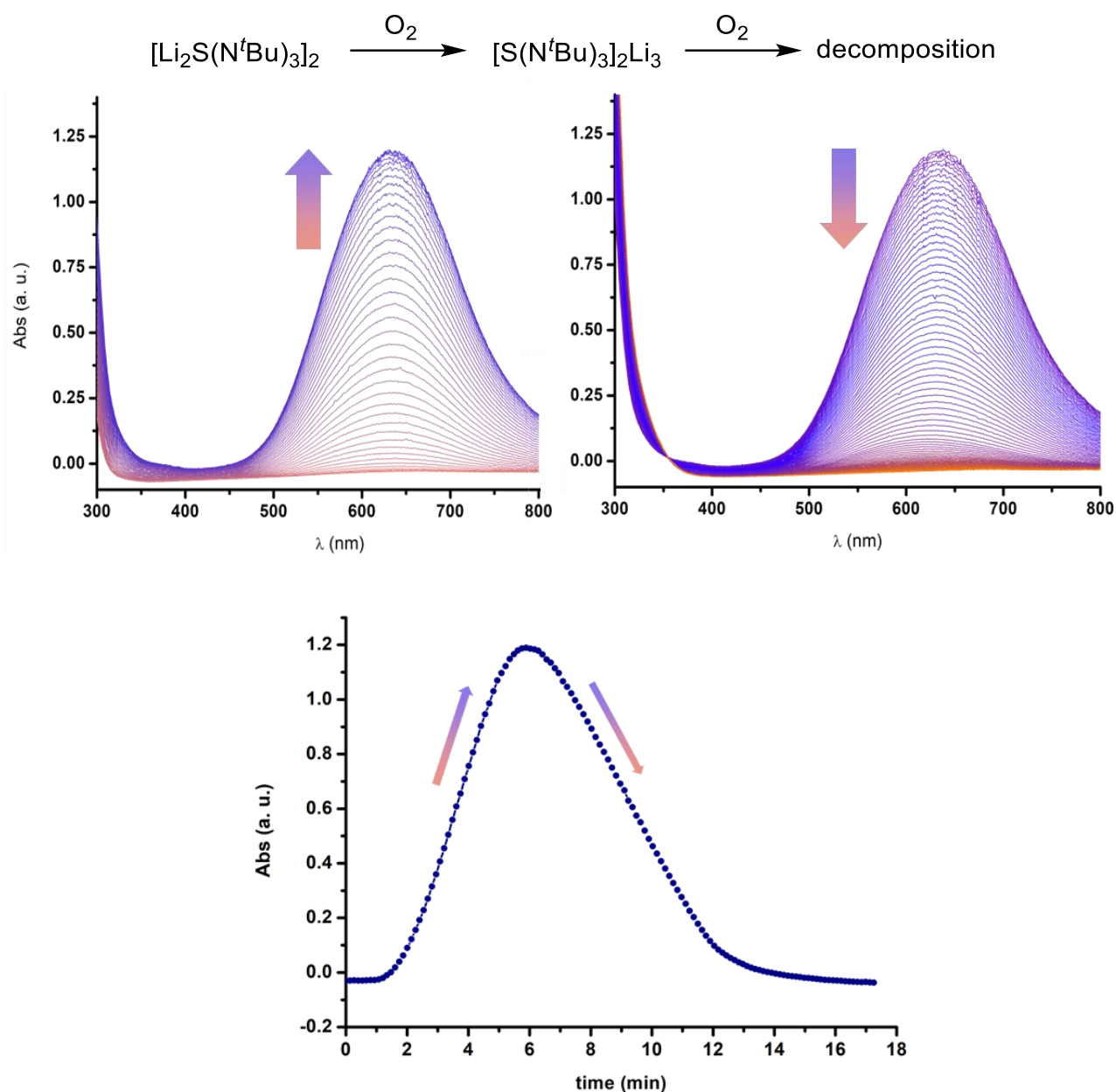


Figure 1.4.5. (top) time-dependent vis spectra of L_2 upon exposure to air. Formation of $[\text{L}_2]_2\text{Li}_3$ (left) and subsequent decomposition (right) with increasing amount of O_2 , in toluene, at RT. (bottom) time-dependency of the absorbance at 635 nm.

Theoretical TD-DFT calculations on $[\text{S}(\text{N}^t\text{Bu})_3]_2\text{Li}_3$ further show that nine different absorptions are responsible for the spectrum depicted in **Figure 1.4.6**. The bands with the highest intensity are located at $\lambda = 566$ nm and 548 nm. The associated TD-DFT plots for these wavelengths show that these absorptions correspond to the transfer of electron density from one nitrogen atom to its nearest two nitrogen atoms of the same capping ligand. The fact that the most intense bands are due to the delocalization of the free electron on the three nitrogen atoms of the same capping ligand is in good agreement with the hyperfine coupling with three ^{14}N nuclei in the EPR spectrum.

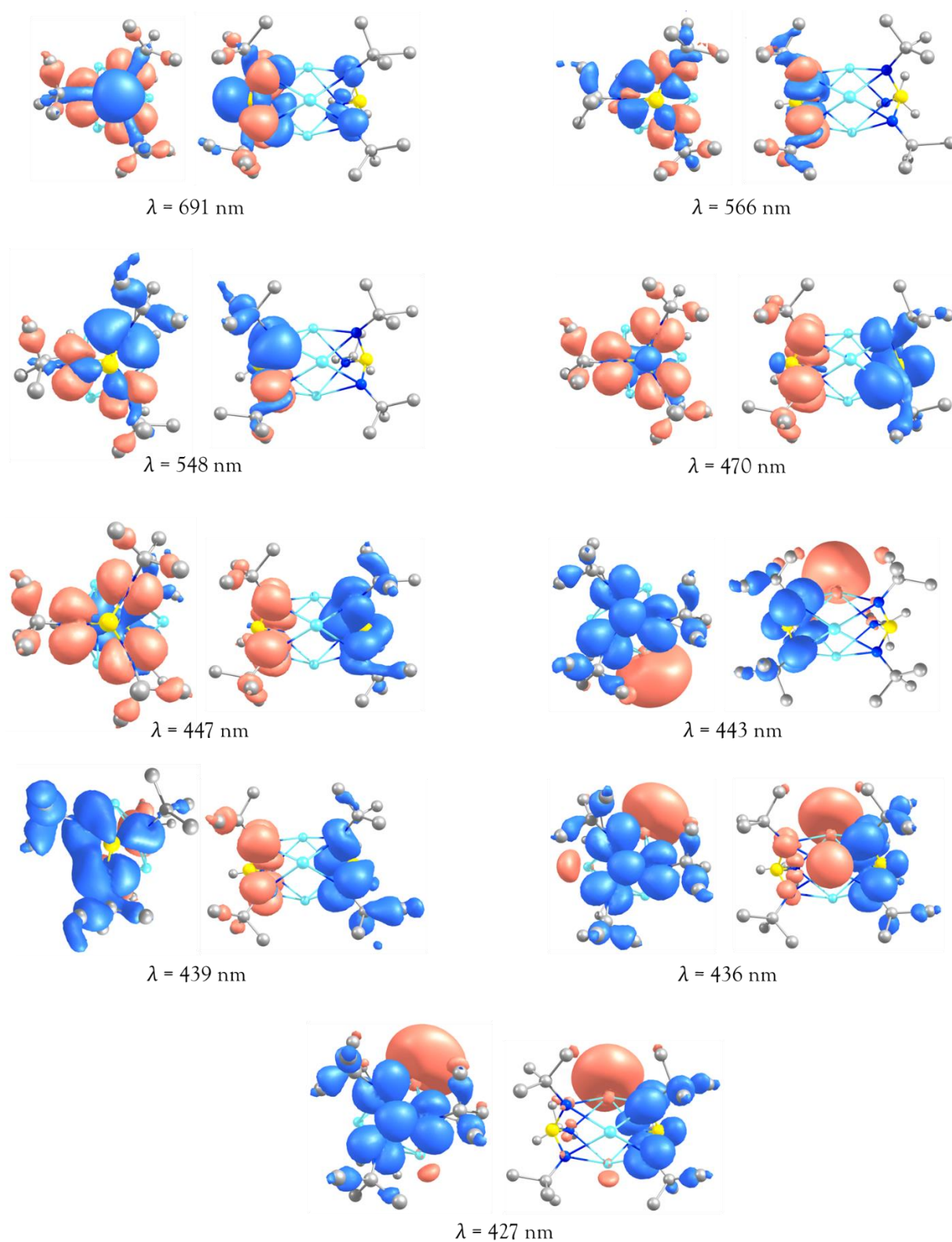


Figure 1.4.6. TD-DFT difference density plots for 9 states responsible for the absorption in the vis range of $\{L_2\}_2\text{-Li}_3$. Top and side views are shown for better clarity. Positive and negative densities are depicted in orange and blue, respectively (isosurfaces at 0.001 level)

The other absorption bands are at least 100 times less intense and are due to the following electron density transfers:

- from the sulfur atom to the three nitrogen atoms of the same capping ligand ($\lambda = 691$ nm and 470 nm)
- from the three nitrogen atoms of one capping ligand to the three nitrogen atoms of the other capping ligand ($\lambda = 691, 470, 447, 439, 436$ nm)
- from the three nitrogen atoms of one capping ligand to the two lithium atoms ($\lambda = 443, 436, 427$ nm, weakest absorption)

1.4.2. Isolation and characterization of $[\text{S}(\text{N}^t\text{Bu})_3]_2\text{K}_3$ ($\{\text{L}_2\}_2\text{-K}_3$)

In order to circumvent recrystallization issues that might arise from the size of the lithium atoms, the potassium analog compound $[\text{S}(\text{N}^t\text{Bu})_3]_2\text{K}_3$ ($\{\text{L}_2\}_2\text{-K}_3$) was further aimed at. This parent compound is as elusive as $\{\text{L}_2\}_2\text{-Li}_3$ and another synthesis route had to be probed to replace the lithium atoms by potassium atoms. Since the metal transfer from Li to K is uneasy in L_2 , the following way was preferred: L_2 is first oxidized with Br_2 and then the obtained L_3 is reduced back with high-purity potassium, giving $\{\text{L}_2\}_2\text{-K}_3$ as a dark blue powder in acceptable yields (30%) (Figure 1.4.7).

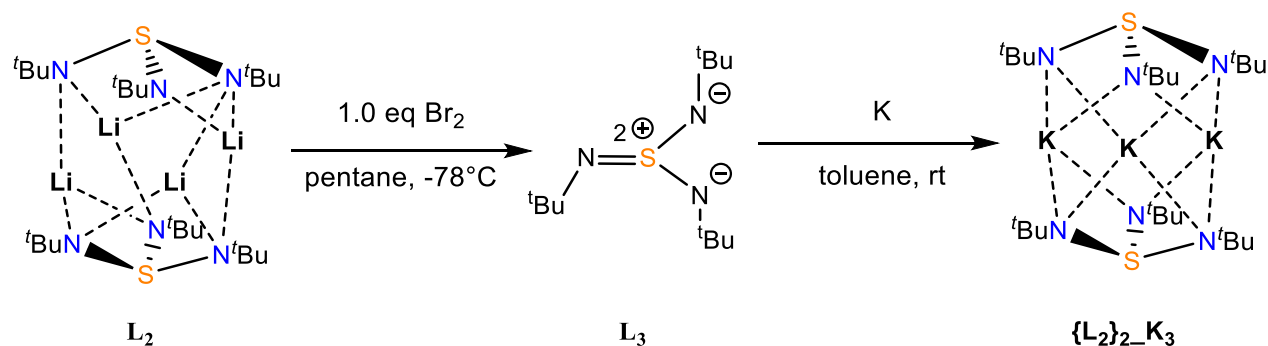


Figure 1.4.7. Synthesis route to $\{\text{L}_2\}_2\text{-K}_3$ from L_2 . The proposed structure is similar to $\{\text{L}_2\}_2\text{-Li}_3$.

The synthesis is carried out in an argon glovebox. A 10 mL vial is prepared with potassium metal corresponding to 1.5 molar eq to L_3 . 1eq of L_3 is separately dissolved in a minimal amount of toluene and added to the reaction vial. The solution immediately turns baby blue, indicative of the reaction's start. Upon further stirring, the surface of the potassium metal rapidly turns dark blue. Upon 1h of intense stirring, the metal is tritured to release all the blue product into the solution. Upon filtration, the solution is dried under *vacuo* to give the product as a dark blue powder. The product $\{\text{L}_2\}_2\text{-K}_3$ is soluble in THF, toluene and pentane. To improve the yield, a delicate trituration of the potassium metal during the reaction could free some metal surface for further reaction. It should however be avoided to release the blue product into the solution during the reaction, as diluted solutions are highly instable. This would result in loss of color and precipitation of an unidentified white powder. A potassium mirror may be a more practical solution, although dilution issues may still arise.

Further characterization of $\{\text{L}_2\}_2\text{K}_3$ was performed by EPR spectroscopy. EPR results indicate the presence of an unpaired electron, as shown in **Figure 1.4.8**.

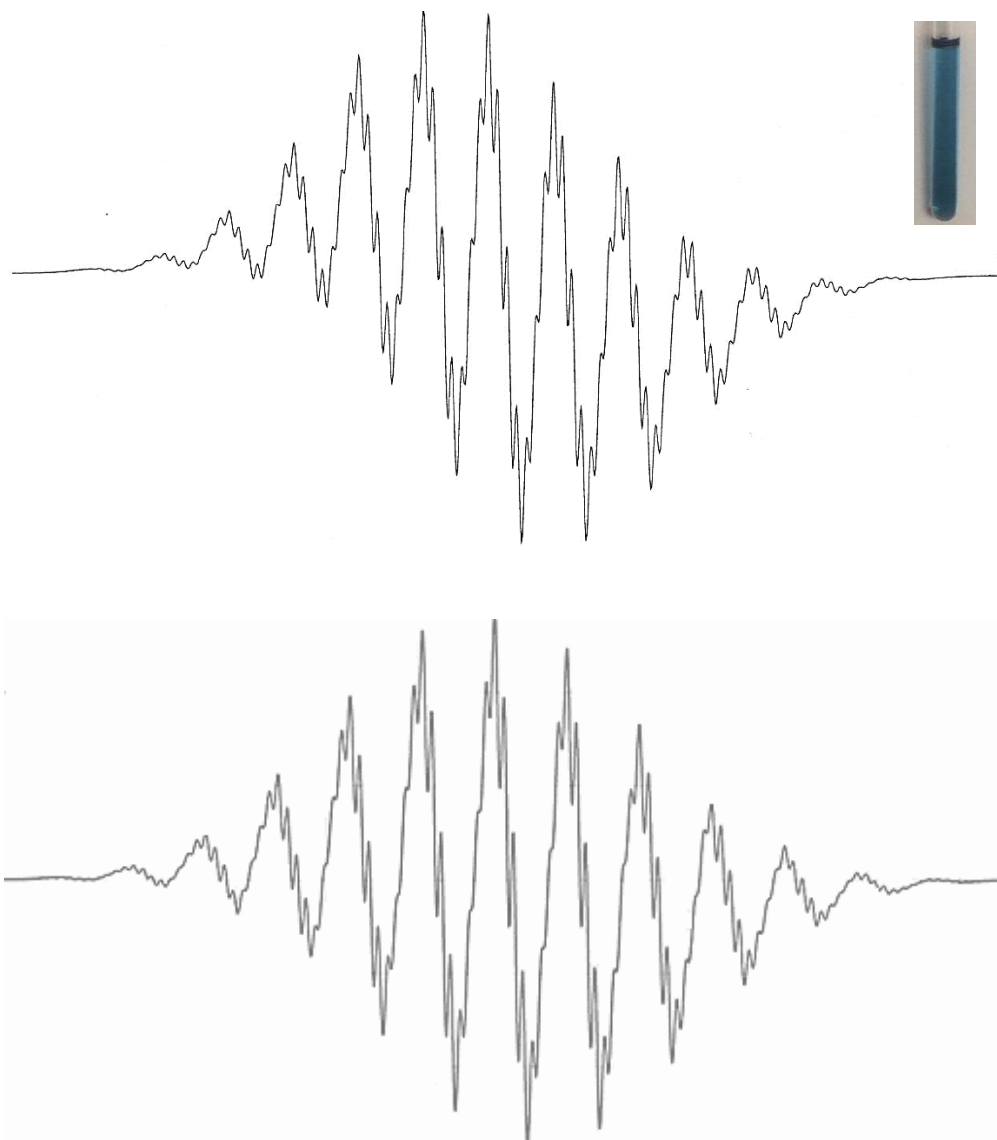


Figure 1.4.8. (top) EPR spectrum of $\{\text{L}_2\}_2\text{K}_3$ in toluene at rt. Picture of the diluted sample prepared for the EPR measurement. (bottom) Simulated spectrum. Both spectra are centered at 3356.5 G.

The center of the spectrum is located at 3356.5 G, with the g factor being 2.022 (2.0023 for the free electron). This corresponds to an energy difference of $\Delta E = 0.32 \text{ cm}^{-1}$ between the two $\pm \frac{1}{2}$ M_S states. The analysis of the hyperfine coupling reveals the following: in solution, the unpaired electron couples with the six ^{14}N nuclei ($I = 1$), resulting in 13 main lines ($m = 2I \times 6 + 1 = 13$, with intensity ratio 1 : 6 : 21 : 50 : 90 : 126 : 141 : 126 : 90 : 50 : 21 : 6 : 1, hyperfine constant $a = 2.618 \text{ G}$). Additionally, the super hyperfine coupling of the unpaired electron could be induced by either the three ^{39}K nuclei ($I = 3/2$, natural abundance of 93.7%), or the two sulfur ^{33}S nuclei ($I = 3/2$, low abundance of 0.75%), giving 10 or 7 smaller lines on each of the 13 main lines,

respectively ($m = 2I \times 3 + 1 = 10$ for K and $m = 2I \times 2 + 1 = 7$ for S, with $a = 0.379$ G). The resolution here allows to identify seven lines, suggesting a superhyperfine coupling with the sulfur nuclei. However, further theoretical calculations are required to unambiguously assign the origin of the superhyperfine coupling since spectrum resolution issues might result in misinterpretation. First, the natural abundance of ^{33}S is much lower than ^{39}K . Second, compared to $\{\text{L}_2\}_2\text{Li}_3$, the present compound $\{\text{L}_2\}_2\text{K}_3$ would have some differences:

- (1) The unpaired electron couples with all six nitrogen nuclei, instead of only three in $\{\text{L}_2\}_2\text{Li}_3$
- (2) The super-hyperfine coupling is generated by either the two ^{33}S nuclei or the three alkali metals as in $\{\text{L}_2\}_2\text{Li}_3$.

While (1) is strongly supported by experimental evidence, (2) is less straightforward to validate. Nevertheless, both the experimental and simulated EPR spectra are in good agreement with the proposed structure for $\{\text{L}_2\}_2\text{M}_3$, regardless of the alkali metal nature and, more importantly, regardless of the superhyperfine coupling with S or K, due to resolution issues. Different than $\{\text{L}_2\}_2\text{Li}_3$, standard theoretical calculations with the orca software for $\{\text{L}_2\}_2\text{K}_3$ and ADF calculations show that the spin density gathers on the two capping ligands, as depicted in the spin density plots (**Figure 1.4.9**). This is however only true on a symmetry enforced structure, while calculations on the coordinates directly obtained from X-ray analysis yield the same results than for $\{\text{L}_2\}_2\text{Li}_3$.

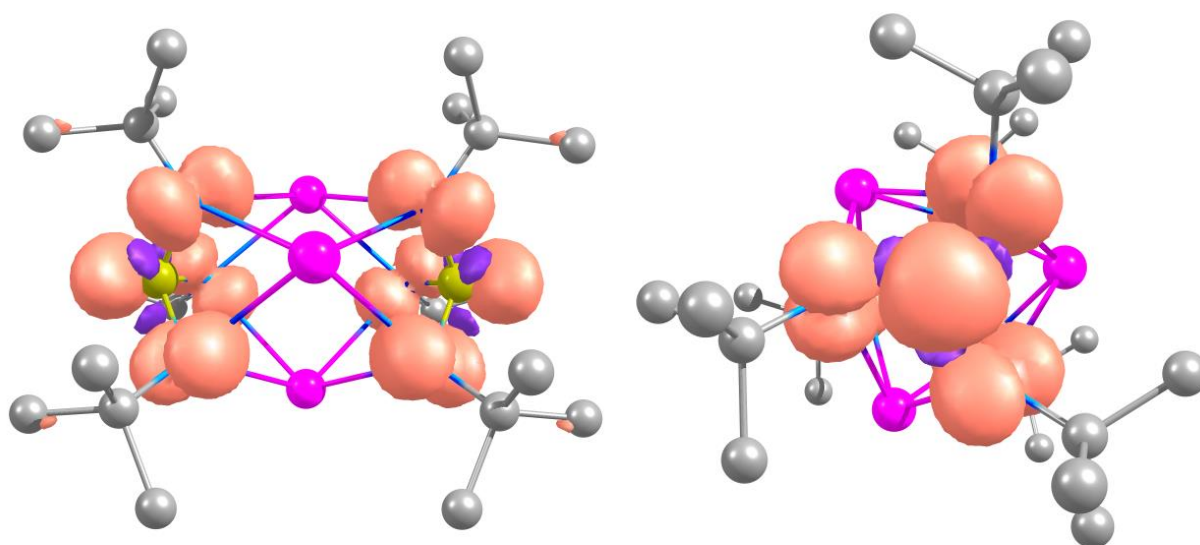


Figure 1.4.9. Calculated spin density plots for $\{\text{L}_2\}_2\text{K}_3$. Positive and negative densities are depicted in light pink and light blue, respectively (isosurfaces at 0.001 level). Both top-down (left) and side views (right) are depicted for better clarity. Hydrogens are omitted for clarity.

Additionally, the calculations reveal that the spin density locates on all six nitrogen atoms with a significant amount on the sulfur atoms as well, which seems to rule out the potassium nuclei for the superhyperfine coupling. Simulations of the EPR spectrum with superhyperfine coupling from the sulfur atoms, however, were unsuccessful.

$\{L_2\}_2K_3$ was then further characterized by UV-vis spectroscopy. Since diluted solutions of $\{L_2\}_2K_3$ lose color intensity over time, the data collection for UV-vis spectroscopy (as well as for EPR) must be done as quickly as possible and only on freshly prepared solutions. The UV-vis spectrum of $[S(N^tBu)_3]_2K_3$ reveals a broad, unstructured absorption band from approx. 550 to 750 nm, with a maximum at 636 nm (**Figure 1.4.10**). An additional small shoulder is visible around 400 nm. These features are confirmed by theoretical calculations (**Figure 1.4.10**, black rectangles). Noteworthy, the present vis spectrum is also very similar to those of the reference ultramarine pigment (which comes from the lapis lazuli semi-precious stone) or of other materials containing the trisulfur radical anion $S_3^{\cdot-}$.⁶³⁻⁶⁵ It also reveals that both compounds $[S(N^tBu)_3]_2M_3$, ($M = Li, K$), share the broad absorption band, irrespective of the alkali metal variations. The small difference of 1 nm between the maxima of the absorption band in the two compounds is in the range of the instrument's error margin. The further differences around 400 nm, however, are probably attributable to the alkali metals, since the absorption bands at 443, 436 and 427 nm in $\{L_2\}_2Li_3$ involve the lithium ion (**Figure 1.4.6**).

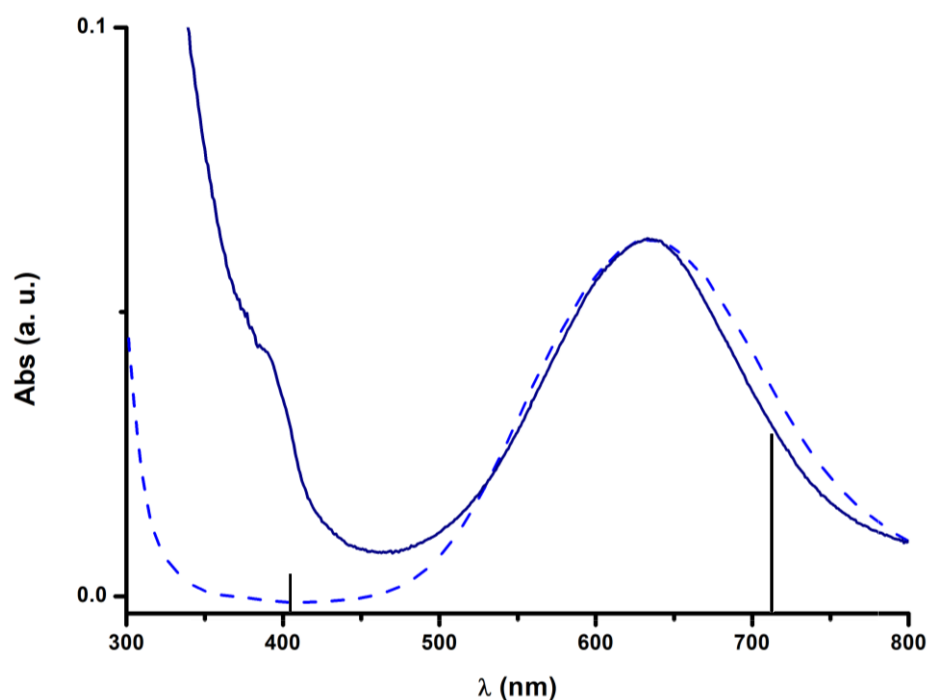


Figure 1.4.10. Experimental vis spectrum of $\{L_2\}_2M_3$ ($M = Li$, dashed blue line, $M = K$, solid dark blue line) in toluene at RT. Calculated absorption peaks for the potassium compound are represented as black rectangles.

The calculations further reveal that the electronic density localized on the nitrogen atoms is responsible for the strong absorptions at 404 and 736 nm. The TD-DFT difference density plots for the corresponding transitions show that, similar to $\{L_2\}_2Li_3$, these both absorption peaks arise from the transfer of electron density from one or two nitrogen atoms to the other ones on the same cap via the central sulfur atom (**Figure 1.4.11**). This is in good agreement with the EPR spectrum (**Figure 1.4.8**). It is however not possible to say if some electron density is being exchanged between the nitrogen atoms of one capping ligand to the other. The other absorption bands obtained from the theoretical calculations are at least 10 times less intense than the main

absorption bands and are due to similar electron density transfers between the nitrogen atoms via the central sulfur atoms (at 655 nm). Remarkably and different to $\{\text{L}_2\}_2\text{Li}_3$, the potassium atoms are not involved in any of the electron transfers.

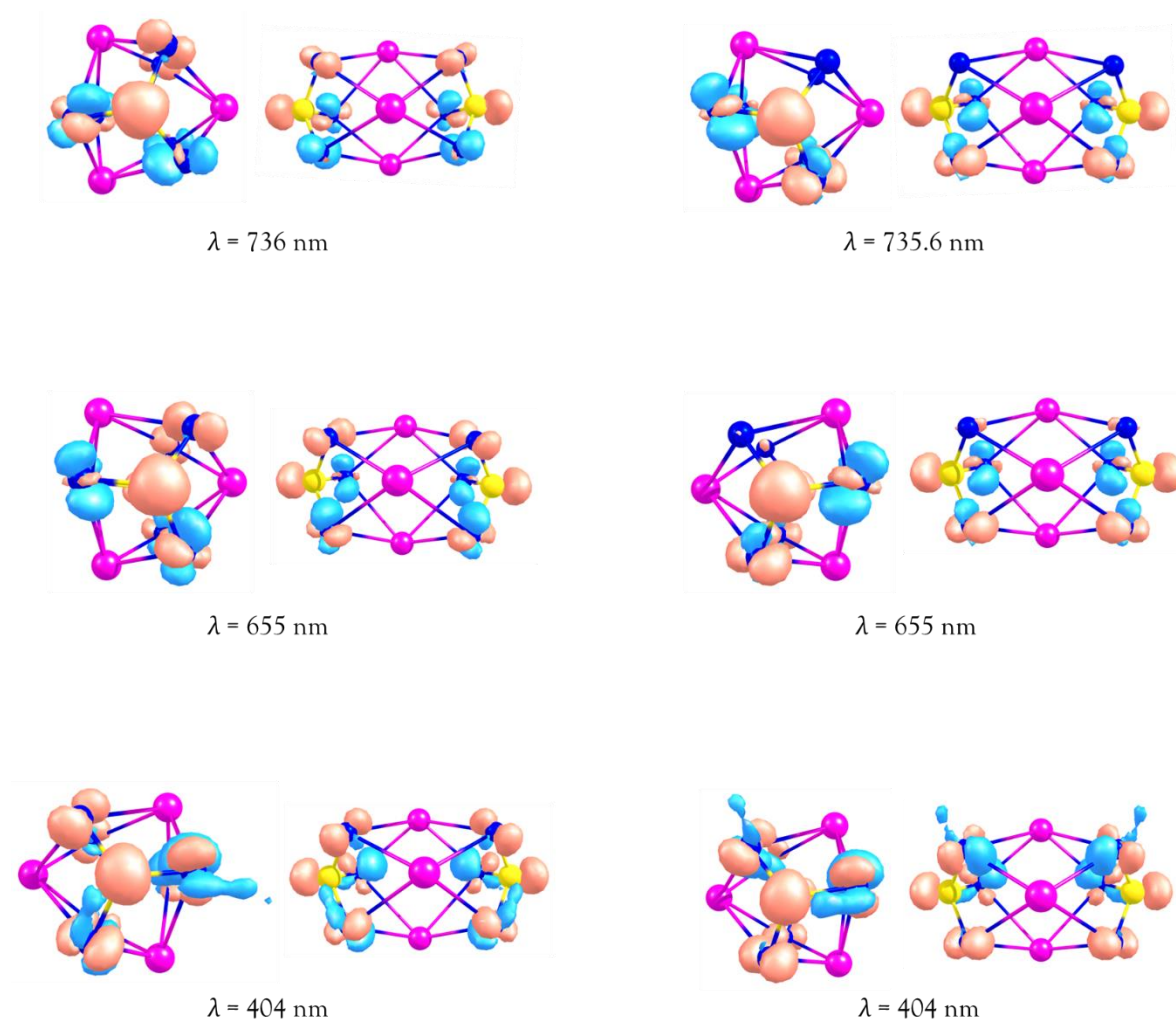


Figure 1.4.11. TD-DFT difference density plots for the eight states responsible for the absorption bands in the vis range for $\{\text{L}_2\}_2\text{K}_3$. Top and side views are shown for better clarity. Carbon and hydrogen atoms are omitted for clarity. Positive and negative densities are depicted in orange and blue, respectively (isosurfaces at 0.001 level).

1.4.3. Solid-state structure of $\{L_2\}_2K_3$

Crystallization attempts of $\{L_2\}_2K_3$ were successful and crystals suitable for X-ray diffraction of $\{L_2\}_2K_3$ were obtained from a concentrated toluene solution at -35°C over a week. The X-ray structure is shown in **Figure 1.4.12**.

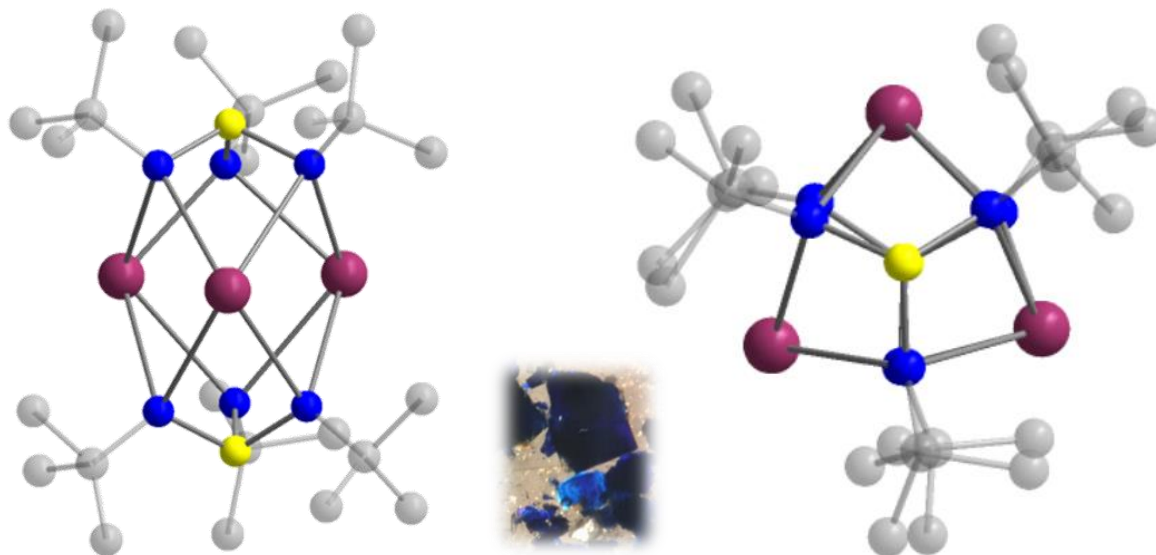


Figure 1.4.12. Crystal structure of $\{L_2\}_2K_3$ at 120K (side view on the left and top view on the right). Hydrogens are omitted for clarity. Potassium, sulfur, nitrogen and carbon atoms are represented in Bordeaux, yellow, blue and light grey, respectively. Picture of the blue crystals under the microscope prior to the SCXRD experiment.

X-ray diffraction confirmed that three potassium atoms are capped by two $\{S(N'Bu)_3\}^-$ ligands. Interestingly, the cooling process before crystal mounting on the diffractometer influences the crystal arrangement and packing (**Figures 1.4.13** and **1.4.14**). Through shock-freeze (structure at 100K), the compound crystallizes in the monoclinic space group $P2_1/c$ and the asymmetric unit contains a two complex molecules. The molecules are forming weakly interacting chains in two preferred orientations resulting in a superposition of zig-zag sheets separated by a distance of about 4 Å. While slowly cooled down to 120 K, the crystal rearranges in the $P2_1/n$ space group and the asymmetric unit, smaller in this case, contains only one $[S(N'Bu)_3]_2K_3$ unit. The packing is similar if the axes *a* and *c* are interchanged. The average distance between two $[S(N'Bu)_3]_2K_3$ units of less than 3 Å. In both cases, the three potassium atoms are found in between two $\{S(N'Bu)_3\}^-$ capping ligands (further denominated caps A and B) in an eclipsed conformation. The two unit cells, at 100K and 120K, are probably parent and, upon cooling further to 100 K, the crystal does not undergo a phase transition. Additionally, a systematic analysis in the software XPREP for cell transformations of the unit cell at 100K gives the smaller unit cell found at 120K if a B-centering is considered. The analysis of the bond lengths and angles supports that both structures are very close (**Table 1.4.1**). Further conclusions may be hazardous, since the structures are highly disordered, and therefore, the error range on the angles and bond lengths analysis relatively high.

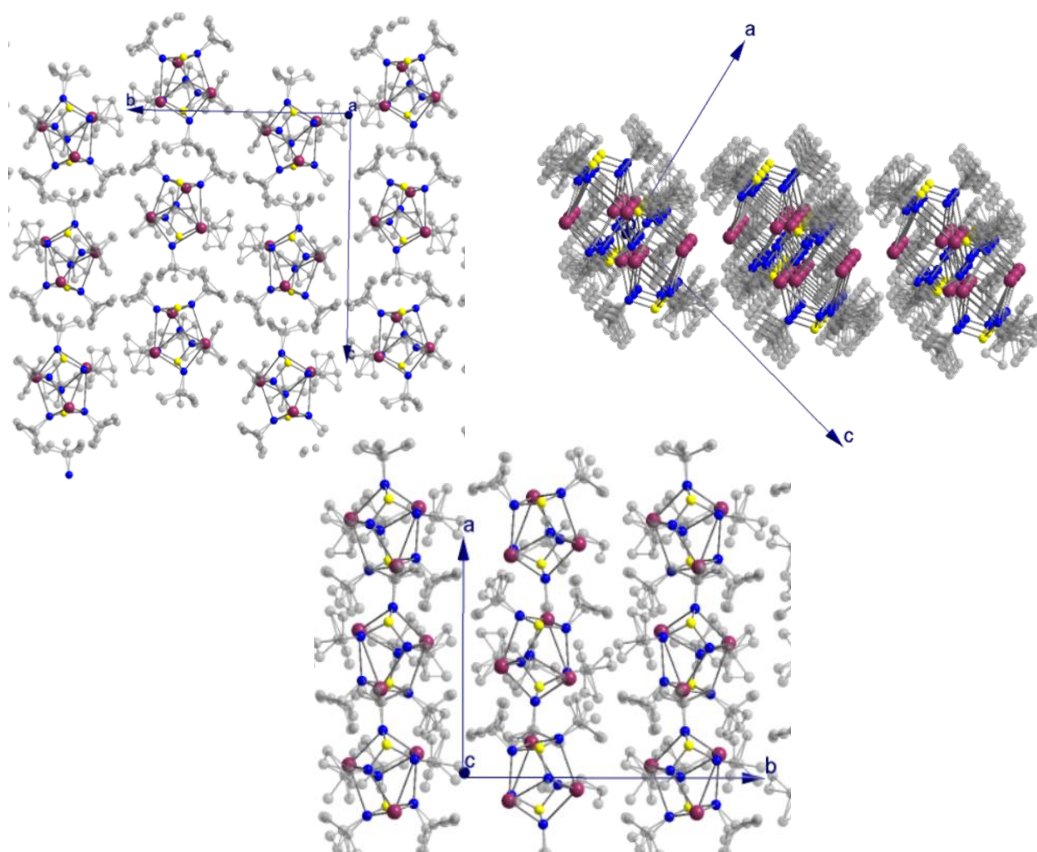


Figure 1.4.13. Structure packing along the cell axes for $\{L_2\}_2K_3$ at 120K

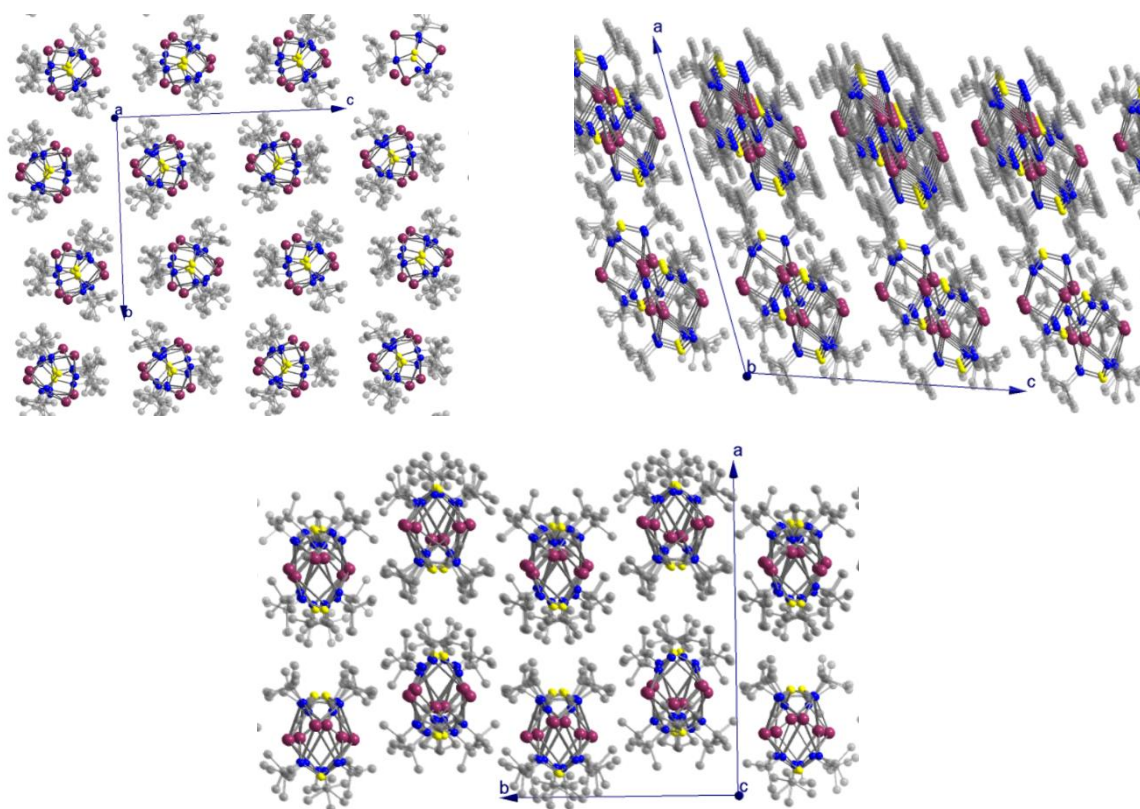


Figure 1.4.14. Structure packing along the cell axes for $\{L_2\}_2K_3$ at 100K

Table 1.4.1. Comparison of the ranges of bond lengths and angles in $\{L_2\}_2K_3$ at 100K and 120K.

Bond length (Å)/ Angle (°)	$\{L_2\}_2K_3@100K$	$\{L_2\}_2K_3@120K$
NSN angle	99.2 – 104.2	99.0 – 104.5
SN distance	1.61 – 1.66	1.60 – 1.68
CNS angle	115.5 – 119.7	116.0 – 118.5
K-K distance	3.75	3.75
N-K distance	2.6 – 2.8	2.6 – 3.0
CNK angle	112 / 128	111 / 132
Shortest intermolecular distance	2.99	2.94

Focusing on the analysis of the crystal structure at 120K gives very interesting insights (the same trends are observable at 100K as well). One capping ligand, further called cap A, shows three almost equivalent S-N bonds (1.639(4), 1.644(4) and 1.645(5) Å). The other capping ligand, further called cap B, possesses one larger S-N bond while the two other S-N distances in the same cap are shorter and of comparable length (1.680(4) vs 1.601(5) and 1.606(4) Å). This is reminiscent of $[(Li_2(tBuN)_2S)_2](THF)$, where one capping ligand also possesses a S-N bond with some double-bond character.¹⁴ Here, it seems that two S-N bonds share the double bond character, while the third S-N bond is undoubtedly a single bond (**Figure 1.4.15**).

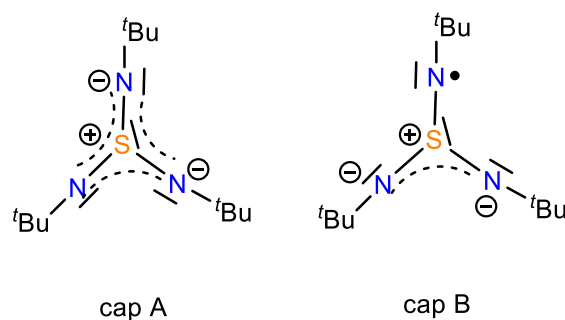


Figure 1.4.15. Related mesomeric forms for cap A and cap B in $\{L_2\}_2K_3$. On cap A, the electronic density is fully delocalized on all S-N bonds (similar to L_3). On cap B, the free electron is localized on one of the S-N bonds.

This could hint at cap B as the electron-bearing capping ligand. The spin density analysis is calculated based on the solid-state coordinates and is presented in the previous section (**Figure 1.4.9**). It seems that, at low temperatures (X-ray experiment at 100K), the free electron is more localized on one of the two capping ligands. At room temperature and in solution, however, the electron is delocalized on all nitrogen atoms, which explains the coupling with the six ^{14}N nuclei in the EPR spectrum (**Figure 1.4.8**). The calculations were performed with the low-temperature coordinates, however upon optimization, the system becomes more symmetric, with a C_3 axis through the sulfur atoms and a mirror plane between the two capping ligands. This results in a

more balanced repartition of the spin density over the entire molecule and better reflects the solution state of the molecule. Direct calculations prior to optimization give a different result, with the spin density gathered on one of the two capping ligands only. Unfortunately, no resolved EPR spectra at low temperatures nor in the solid-state were obtained to verify this hypothesis.

The S-N distances are all significantly larger than those found in similar S^{VI} compounds (av. S-N distance of 1.56 Å) but comparable to those of similar S^{IV} compounds. This suggests that the sulfur atoms in $\{L_2\}_2K_3$ are in the +IV oxidation state.

1.4.4. Perspectives for $\{S(N^tBu)_3\}^-$ -based radical species.

The determination of the experimental X-ray structure of $\{L_2\}_2K_3$ allowed a much more detailed analysis of the physical properties presented before, as well as theoretical calculations. All theoretical calculations presented in the previous sections were performed based on the coordinates obtained from the crystallographical dataset. Additionally, the calculations for $\{L_2\}_2Li_3$ were performed on the same coordinates while replacing the potassium atoms by lithium atoms. Given the difference in ionic radii between Li and K, the structure of $\{L_2\}_2Li_3$ may be different in reality. Nevertheless, the existence of the crystal structure for $\{L_2\}_2K_3$ allowed the comparison between the two parent radical species and added precious understanding to their physical properties. Both at 100K and 120K, the molecules are highly disordered in the crystal structure, mainly due to the free rotations of the *tert*butyl groups. This structural disorder in the molecular crystal structure prevents the further acquisition of a dataset suitable for charge density analysis. In sum, a clear synthesis route has been successfully designed to isolate the transient radical species $\{L_2\}_2K_3$ (Figure 1.4.16).

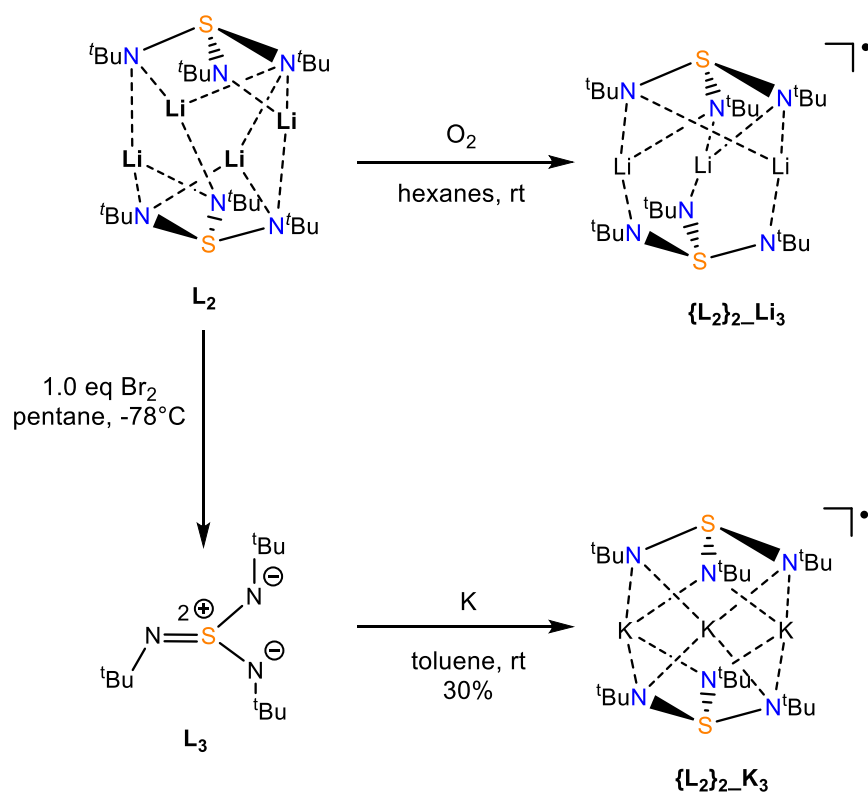
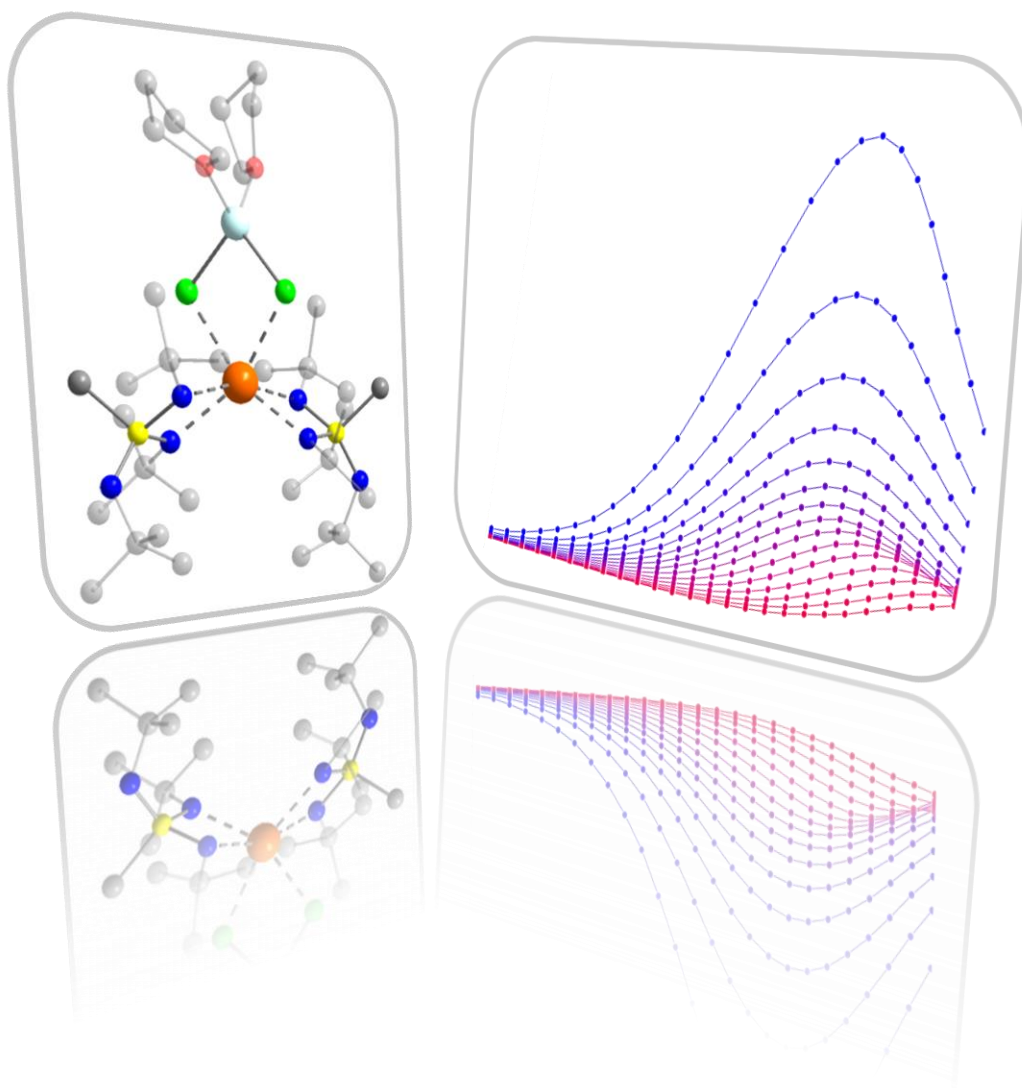


Figure 1.4.16. Synthesis route to $\{L_2\}_2K_3$. For $\{L_2\}_2Li_3$, the crystal structure is still unknown.

Furthermore, a crystallization method was found, giving dark blue crystals of $\{\mathbf{L}_2\}_2\mathbf{K}_3$ suitable for SC-XRD. The subsequent determination of the long sought-after crystal structure of $\{\mathbf{L}_2\}_2\mathbf{K}_3$ enables to better understand its fascinating spectroscopic properties. Additionally, it shows that these features constitute a clear blueprint for this family of radicals obtained from alkali metal derivatives of the polyimido anions $[\text{S}(\text{N}^i\text{Bu})_3]^-$. Delicate variations are observable while changing the nature of the alkali metal from Li to K. Similar Se-, Te- centered polyimido anions from previous works were shown to possess comparable spectroscopic properties.⁶⁶⁻⁷⁰ The present series could be further investigated with the synthesis of the sodium analog.

Chapter Two

Magneto-structural correlations in dysprosium-containing SMMs: from field induced relaxation to hysteresis



2.1. Single-molecule magnets (SMM): Historical timeline

A single-molecule magnet can be defined as a molecular compound that exhibits slow relaxation of its magnetization. The first SMM, $[\text{Mn}_{12}\text{O}_{12}(\text{OAc})_{16}(\text{H}_2\text{O})_4]$,⁷¹ was discovered in 1993. Today, it refers to a broad family of diverse molecular materials. Some examples are provided in the present work. Contrary to molecule-based magnets⁷² and permanent bulk magnets,^{73,74} the magnetic properties of a SMM are of purely molecular origin. This means that they are not associated with ordering or magnetic propagation due to bulk effects, but solely arise from the total molecular non-null spin preserved by the anisotropic environment around the paramagnetic center. Along with magnetic quantum dots,⁷⁵ SMMs are nanometric materials with two or more different magnetic states, which are stable even upon the removal of an external field. They are considered highly promising alternatives to current data storage devices, as they embody the vision of the smallest support for a computer storage unit (usually the bit, with two coding possibilities, 0 and 1).⁷⁶ Beside high-density data storage, SMMs are envisioned for other industrial applications, such as magnetic refrigeration, quantum computing or spintronics.^{47,51,77-79} Towards these goals, many studies involving 3d transition metals^{53,80-82} – especially manganese – followed the discovery of the first single-molecule magnet.⁸³ The race for the molecule with the highest possible spin,⁸⁴ which was thought to be the most important criteria for designing SMMs, lasted for at least one decade and had its finest hour when Powell *et al.* synthesized a huge manganese cluster with a record spin of $83/2\ldots$ that did not show any SMM behavior!⁸⁵ The origins of the slow magnetic relaxation of the magnetization were then carefully re-assessed.^{86,87} Both a high spin state *and* a high magnetic anisotropy at the paramagnetic center were found mandatory for the generation SMM behavior.⁸⁷⁻⁹⁵ The two parameters, however, are inversely proportional to each other in the case of 3d metals. Powell's manganese cluster⁸⁵ possessed a high spin due to the ferromagnetic coupling between the manganese centers but presented an overall poor anisotropy. Nevertheless, this achievement was an important breakthrough and led to probe 4f elements towards SMM design.^{96,97}

4f elements represent a subunit of the f-block, from La to Lu, and include the lanthanide elements (Ln, Ce-Lu). Some trivalent lanthanide ions possess a large magnetic anisotropy arising from a strong spin-orbit coupling. This is due to their intrinsic orbital angular momentum, which is unquenched and remarkably large.⁸⁸ They also have some of the highest magnetic moments in the entire periodic table.⁹⁸ These features already predisposed lanthanides for magnetic applications, for example in permanent magnetism (SmCo_5 ,⁹⁹ $\text{Nd}_{12}\text{BFe}_{14}$ ^{74,100}) magnetic resonance imaging¹⁰¹ and, later, in single-molecule magnetism.^{96,102-105} The first SMM containing a f-element was reported in 2003 by Ishikawa *et al.*⁹⁶ It displayed a huge anisotropy, about five times higher than in the first SMM (Mn_{12} cluster) discovered by Sessoli *et al.* (**Figure 2.2.2**).¹⁰⁶ The careful description of the electronic structure of 4f ions^{88,107} and the development of strategic ligand design promoted them to highly promising candidates for SMMs,^{108,109} and even more so for SIMs.^{97,102-104,110} (SIMs are monometallic SMMs). The current best performing SMMs contain a lanthanide ion, more precisely a dysprosium sandwiched between two substituted cyclopentadienyl ligands.^{103,104,110,111} However, despite their numerous advantages, lanthanides are quite expensive and difficult to separate from their ores, as their chemical and physical properties

are close to each other.¹¹² The development of novel lanthanide based SMMs seems to currently suffers from a lack of innovation. After the major breakthroughs with dysprosocenium complexes in 2017, it seems that the performances of SMMs reached a plateau that scientists struggle to overpass – or at least reorient research away from the cyclopentadienyl chemistry, which cannot be indefinitely exploited.⁴⁹ Three merging research areas are currently developed, as proposed as follows:

- (1) a regain of interest towards transition metals, with the design of highly anisotropic single-ion magnets;¹¹³⁻¹²¹
- (2) the introduction of heavy main group elements into the paramagnetic metal's environment (whether the metal is a f-element or a transition metal);¹²²⁻¹²⁴
- (3) a regain of interest towards multinuclear complexes,^{84,108,125-132} and sometimes multifunctional multidimensional structures,^{52,133-135} to create synergies between the metals or to exploit the advantages of higher-dimensionality.^{48,51,136}

These strategies do not have to be mutually exclusive, although their separate study may result in simpler models that provide further knowledge to the broader goal. The present work mainly addresses directions (1) and (2). Some results based on strategy (3) will be briefly mentioned in the experimental section at the end of this work.

2.2. SMM: design basics, theory of magnetic anisotropy and characterization methods

2.2.1. The double well potential model: how does a single-molecule magnet work?

The functioning of a single-molecule magnet can be well described with the help of the double well potential model,¹³⁷ which only takes the magnetic spin into account. This simplified approach, however, has its limits, which will be discussed later to explain why a non-zero spin cannot be the only criteria for the presence of slow relaxation of the magnetization. In the first instance, special cases will not be considered in order to facilitate the understanding of this complex topic.

A SMM need to possess a source of paramagnetism, *i. e.* unpaired electrons. Each electron carries a non-zero spin, which may be cancelled through electron pairing up- and downwards (closed-shell system). In SMMs, a least one electron must be unpaired, which means that the total molecular ground state spin is non null (open-shell system). For multinuclear SMMs, it is also necessary to make sure that the magnetic coupling (if antiferromagnetic) does not cancel out the contributions of all the paramagnetic centers. (**Figure 2.2.1**). Considering the first SMM Mn₁₂-cluster (**Figure 2.2.2. left**),¹⁰⁶ the total molecular ground state spin is $S = 10$. As a SMM *per se*, the cluster possesses a bistable ground state, one with the magnetic spin number $M_S = -10$ and the other with $M_S = +10$.¹³⁸ The spin reversal from -10 to $+10$ and vice versa costs a certain amount of energy U , which ensures the ground state bistability. The higher-lying energy levels have $M_S = \pm 9, \pm 8, \dots, \pm 1, 0$, completing each well in the model. Each pair of magnetic state with the same absolute $|M_S|$ is called a Kramers doublet (KD).¹³⁹ In an ideal system, thanks to the energy barrier U , the system can relax from one well to the other only if it overcomes the energy barrier U , as shown in **Figure 2.2.2**.

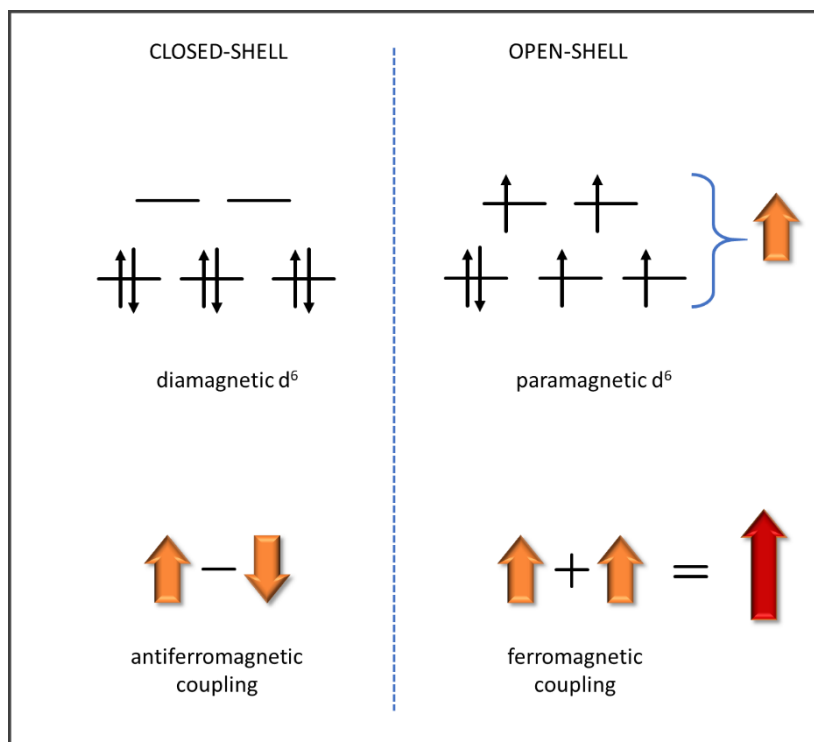


Figure 2.2.1: Example of closed-shell and open-shell systems. (Top) example for mononuclear 3d systems (octahedral geometry). (Bottom) example for dinuclear systems.

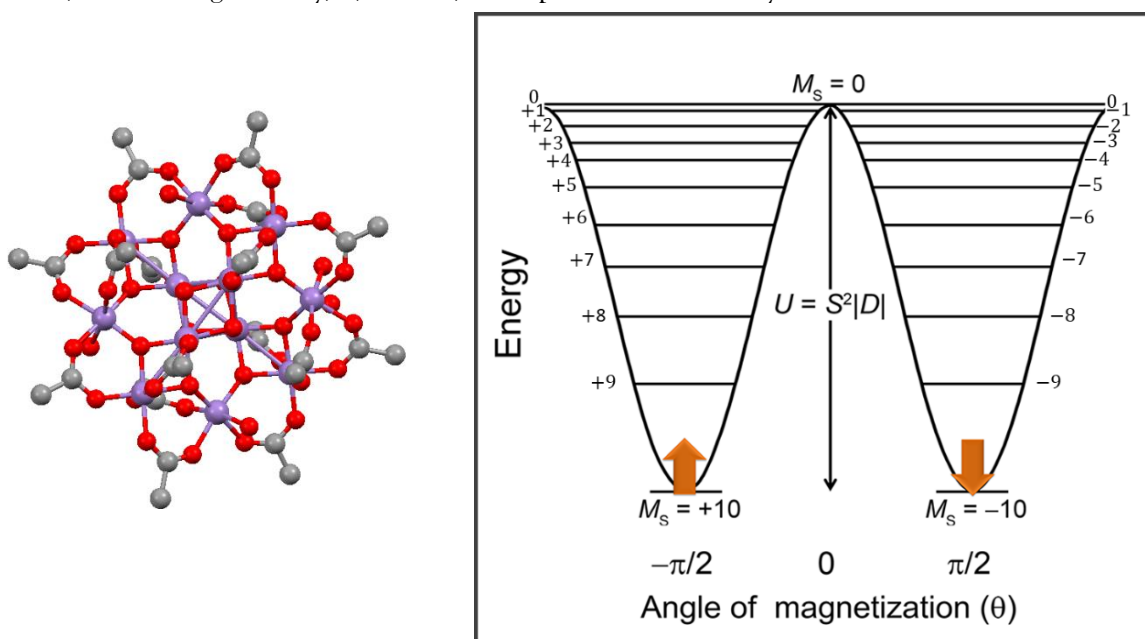


Figure 2.2.2: (Left) Crystal structure of the Mn₁₂-cluster.¹⁰⁶ (Right) Model of the double well potential for a system of a total ground state spin of $S = 10$. Light purple, red and grey spheres represent manganese, oxygen and carbon atoms, respectively. Hydrogens are omitted for clarity.

Ideally, this relaxation can only be triggered by an external source of energy, such as a magnetic field or temperature. Without this input of energy, the system stays indefinitely in its current, stable magnetic ground state. From this perspective, the SMM could be used as a nano-bit.⁴⁷ The $M_S = (-10, +10)$ ground states correspond to (0, 1), respectively. They would be stable and

therefore safely store the information without loss of magnetization. To erase or change the information, an external source would need to address the SMM – for example with a magnetic tip of a magnetic force microscope (MFM) on SMMs previously deposited on a surface– to give enough energy to the system to overcome the energy barrier U .^{54,140–147} Each SMM of the surface would then again be ready to receive a new information to store on it. If a magnetic field is considered for the external stimulus, the magnetization of the SMM is dependent on its strength, resulting in a magnetic hysteresis (**Figure 2.2.3**).¹⁴⁸

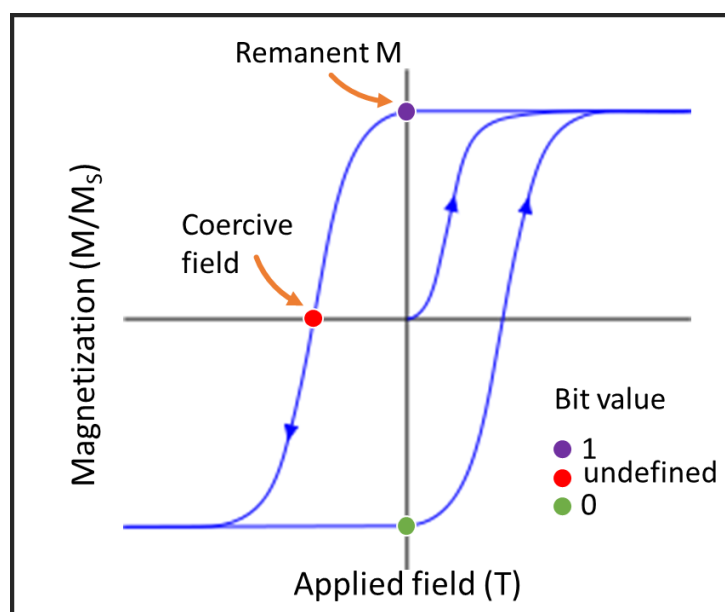


Figure 2.2.3: Example of magnetic hysteresis. Upon removal of the external field, the system conserves the remnant magnetization. To completely reset the magnetization of the SMM back to zero, a certain amount of magnetic field is necessary, which is the coercive field. The corresponding ‘bit values’ are indicated as colored dots.

In reality, however, the system relaxes over time through the exchange of the phonon (spin) energy with the surrounding thermal bath (lattice).^{149–151} This energy exchange is not particularly favored and can therefore be extremely slow. The slower the better, since it determines how long the information can be stored on the SMM. This ideal type of relaxation corresponds to the slow Orbach process,^{151,152} which is a characteristic of all SMMs. The relaxation rate of this process, however, depends on each system. Additionally, there are unfortunately several other relaxation processes, which shortcut the energy barrier and result in a decrease performance.^{104,150,153} All relaxation processes are presented in the next section.

2.2.2. Relaxation processes of the magnetization in SMMs

A single-molecule magnet can be magnetized with an external applied field to reach a specific magnetic state, aligned with the magnetic field. Upon the removal of this magnetic field, there are several possible processes of relaxation from this magnetic state back to the thermodynamic equilibrium, as pictured in **Figure 2.2.4**. They describe the energy exchanges between a certain

number of phonons (originating from the spin system) with the lattice. The spin-lattice relaxation rates are usually explained in terms of the temperature dependencies.¹⁵⁰

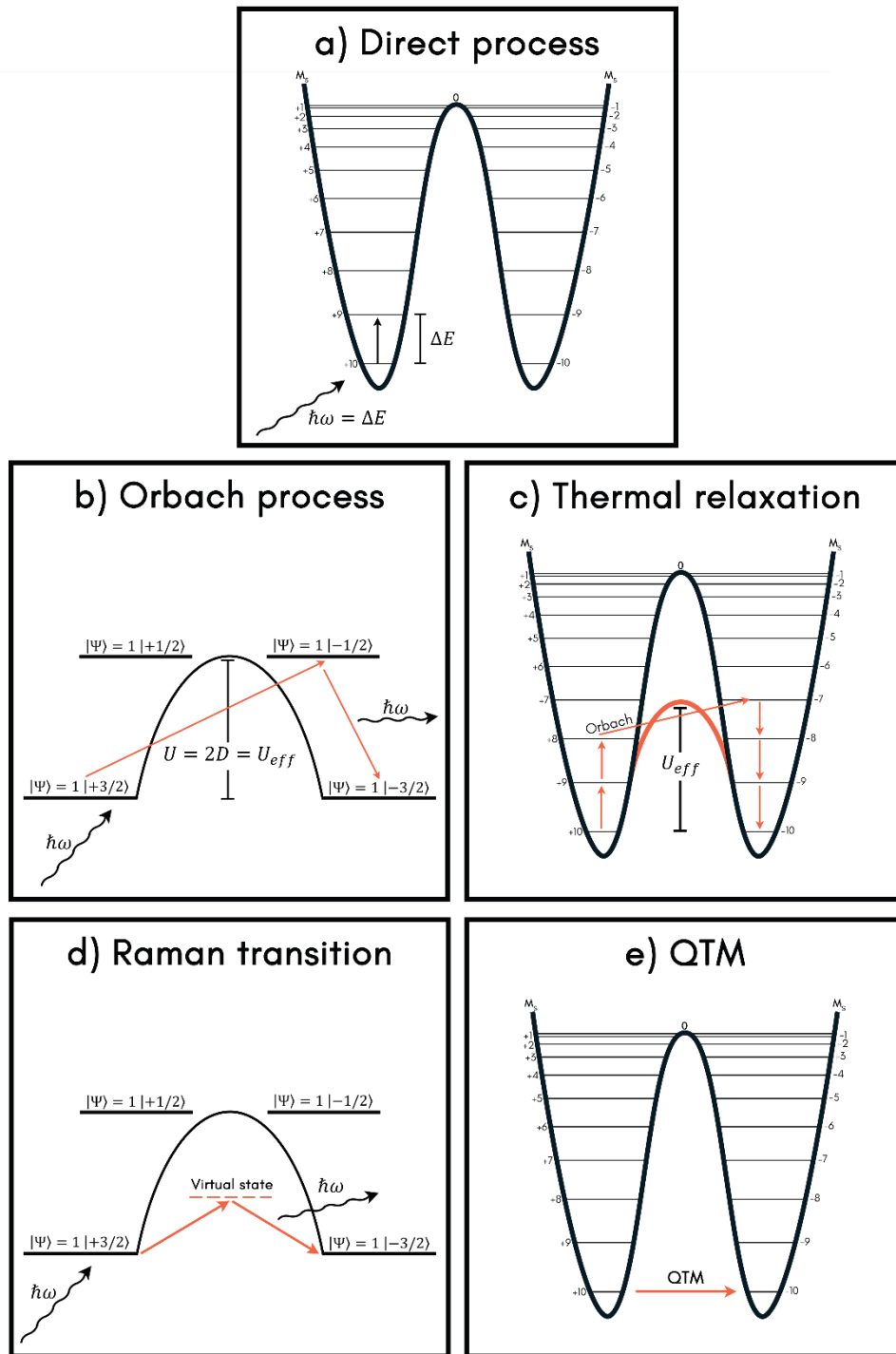


Figure 2.2.4.: Transitions and relaxation processes occurring in a SMM. (a) direct process, (b) Orbach process for a $S = 3/2$ system, (c) example of a relaxation pathway for a $S = 10$ system, when the Orbach process occurs at a point where there is a significant mixing of the MS states, resulting in an effective barrier lower than U , (d) example of a Raman transition for a $S = 3/2$ system, (e) Quantum Tunneling of the Magnetization (QTM) at the ground state KD for a $S = 10$ system. (picture reproduced with permission by Dr. E. Damgaard-Møller)¹⁵⁴

(a) The direct process¹⁵⁵ is a one-phonon process which requires a phonon whose energy exactly matches the energy difference of the transition. This process is proportional to the temperature.

(b) The Orbach process¹⁵¹ requires two phonons: a phonon is absorbed and causes an excitation to a higher-lying energy state followed by a subsequent deexcitation to another state via a phonon emission. This describes the process of relaxation at spin reversal, which necessitates to overcome the energy barrier U . The relaxation rate of the Orbach process is also temperature dependent and follows the Arrhenius law as $\exp(U_{eff}/k_B T)$. The effective energy barrier U_{eff} can be equal or different than U , depending on the number of magnetic states and on the mixing rate. For a system with $S = 3/2$, the magnetic states may be $M_S = \pm 1/2$ and $M_S = \pm 3/2$. In this case, $U_{eff} = U$ since U_{eff} involves at least one thermal transition per definition (c). For lanthanides, U_{eff} and U may take different values, as there are more than two magnetic states.¹⁵²

(d) The Raman process may involve two or more phonons and consists of the absorption of a phonon whose energy is not sufficient to reach the next higher-lying magnetic state. It is followed by the emission of another phonon and the system reaches a new magnetic state. The Raman process¹⁵⁶ is often described as a relaxation through a virtual state whose energy corresponds to the energy of the absorbed phonon. The difference between the two phonon frequencies is equal to the spin level difference. The rate of Raman relaxation is in the order of T^n (with $n = 1, 2, 3, 4, 5, 6, 7, 9$ or 12)¹⁵⁰ depending on the temperature ranges, the number and nature (acoustic or optical) of phonons involved and the structure of the energy levels.¹⁵⁵ This is the one of the most complex but also most common relaxation process.

(e) If the compound relaxes *solely* through quantum tunneling of the magnetization (QTM),¹⁵⁷ the system completely shortcuts the energy barrier U and can switch from one magnetic state to another one of the same energy. In this case, the process is not a spin-lattice relaxation and is temperature-independent. The compound is then not considered to be a SMM. QTM can occur due to the M_S (or M_J) mixing, which is generally inevitable in practice.

Additional processes such as temperature-assisted direct processes, temperature assisted QTM or bottlenecked Orbach processes, are also possible but will not be discussed in detail here. The relaxation rate τ of the magnetization of one specific system can therefore be described with the following equation eq 2.1., considering all possible relaxation processes:

$$\tau^{-1} = \underbrace{AH^4 T}_{\text{Direct}} + \underbrace{\tau_0^{-1} e^{(U_{eff}/k_B T)}}_{\text{Orbach}} + \underbrace{\tau_{QTM}^{-1}}_{\text{QTM}} + \underbrace{CT^n}_{\text{Raman}} \quad (\text{eq 2.1})$$

where A , C and n are constants, H the applied magnetic field, τ_0 the initial characteristic relaxation rate for the Orbach process, U_{eff} the effective energy barrier to spin reversal, k_B the Boltzmann constant, and τ_{QTM} the relaxation rate for QTM.

2.2.3. Magnetic anisotropy

The magnetic anisotropy, a prerequisite for SMM behavior, indicates a non-uniform magnetization of a molecule, with a maximization of this magnetization along one or two preferred orientations.^{86,87} The magnetic anisotropy arises from the presence of an unquenched OAM. Lanthanide intrinsically possess huge unquenched OAM⁸⁸ while 3d transition metals

require particular ligand fields to prevent full quenching.¹²¹ The OAM is the angular momentum generated by the circulating electrons in an orbital (L). Their circular motion then generates a current, resulting in a small magnetic field internal to the molecule. If present, the unpaired electrons, carrying a spin angular momentum (S), will interact with this magnetic field, creating a spin-orbit coupling (SOC). The relative orientations of the OAM and of the spin angular momentum will determine the strength of the SOC.

It is possible to qualitatively predict whether the OAM is quenched or not by determining the matrix elements $\langle \Psi_i | \hat{L}_u | \Psi_j \rangle$, where $u = x, y \text{ or } z$, Ψ_i is one of the wavefunctions associated with the irreducible representation $^{2S+1}\Gamma$ and \hat{L}_u the orbital angular momentum operators. If it exists at least one $i = j$ for which $\langle \Psi_i | \hat{L}_u | \Psi_j \rangle \neq 0$, then the ‘first-order’ OAM is unquenched. Otherwise, the OAM is quenched. In this case, if it exists at least one $i \neq j$ for which $\langle \Psi_i | \hat{L}_u | \Psi_j \rangle \neq 0$, then the ‘second-order’ OAM is unquenched. Both first- and second-order OAM can lead to the observation of SMM behavior, but the first-order OAM usually ensures a higher magnetic anisotropy. In 3d metals, more intuitively, the presence of OAM can be associated with the degeneracy of two 3d orbitals sharing the same m_L quantum number and occupied with an odd number of electrons.¹²¹ The 3d orbital pairs ($d_{x^2-y^2}, d_{xy}$) and (d_{xz}, d_{yz}) are linear combinations of the $m_L = (\pm 2)$ or (± 1) and contribute with an orbital angular momentum $L = 2$ or $L = 1$, respectively. There are only a few examples in literature where this configuration is observed for 3d transition metals. An even number of electrons in the orbital pair will lead to a quenched first-order OAM with $L = 0$ due to the Pauli Exclusion Principle. Second-order OAM occurs when the two relevant d-orbitals are not fully degenerate but still close enough in energy to couple. This configuration is less rare than the former one and examples will be given in **Chapter 3**.

Due to the presence of repulsive interactions between the unpaired electrons, the degeneracy of the magnetic states M_S (or M_J for lanthanides) is lifted even at zero external magnetic field, giving the zero-field splitting (ZFS). The ZFS can be described by two parameters, the axial parameter D keeping the M_S states pure and the rhombic parameter E , which mixes the M_S states with $\Delta M_S = (\pm 2)$. These parameters describe how well separated the energy levels are, and highly depend on the system’s symmetry. They can be accessed through various experiments or calculated theoretically. In cases of unquenched OAM with a strong SOC, the ZFS may become very large, and the quantum number S and ZFS axial parameter D do not give a proper description of the Kramers’ doublets anymore. S should be replaced by the quantum number J , usually reserved to lanthanides ($J = |S \pm L|$). The ZFS parameter D does not have a counterpart and will be used here further for comparison purposes with existing SMMs.

Tuning the magnetic anisotropy is possible since the magnetic properties are highly influenced by the structural properties of the complexes.^{158,159} These indeed determine the SOC and the ZFS parameter responsible for the magnetic anisotropy. The energy splitting of the orbitals and of the magnetic states (KDs) can then determine much of the relaxation process of the magnetic

moment. Depending on the difference in the energy levels, the ratio of mixing between states and the external energy sources (applied magnetic field, temperature variations, and light irradiation), the magnetic moment will relax according to the processes presented before, often through a combination of them. It is therefore important to evidence which complex geometries give interesting magnetic properties and understand which structural parameters influence or at least are somewhat related to the magnetic anisotropy. This will bring fundamental information for ligand and complex engineering in order to design better performing SMMs. A succinct overview of the current existing classes of SMMs will be given.

2.2.4. Design of mononuclear SMMs: actual trends and challenges

In the design of mononuclear SMMs, a paramagnetic metal center is required to offer a source of unpaired electrons. Some transition ions (Cr^{II} , Mn^{III} , Mn^{IV} , Fe^{I} , Fe^{II} , Fe^{III} , Co^{II} , Ni^{I} , Ni^{II} , Re^{IV}), almost all lanthanides ($\text{Ln} = \text{Ce}^{\text{III}}$, Nd^{III} , Tb^{II} , Tb^{III} , Dy^{II} , Dy^{III} , Ho^{III} , Er^{III} , Tm^{III} , Yb^{III}) and some actinides ($\text{An} = \text{U}^{\text{III}}$, U^{V} , Np^{IV} , Pu^{III}) – are relevant to this aim.^{81,105,160} Among these, ions with half-integer spins (possessing an odd number of unpaired electrons), so called Kramers' ions, are usually preferred for the design of SMMs. According to Kramers' degeneracy theorem,¹³⁹ the eigenstates of a half-integer spin system obey to time-inversion symmetry, which guarantees that the time reversal operator applied to one M_s (M_J) eigenstate generates another eigenstate of the same energy. This will ensure that the eigenstates come in pairs and are degenerate (Kramers' doublets (KD)). For non-Kramers' ions, which possess integer spins, they do not have time-symmetry inversion and therefore the eigenstates do not necessarily come in pairs. This explains why SMMs containing the Kramers' ions Fe^{III} , Fe^{I} , Co^{II} and Dy^{III} are more common in the literature.^{93,105,161} In this thesis, mainly Co^{II} and Dy^{III} SMMs will be presented.

The design of a mononuclear SMM goes as follows. Once the paramagnetic center is chosen amongst the aforementioned metals, the design of the ligand environment to surround the metal ion is as equally important. Numerous comparative reviews and theories have been developed to this aim,^{87,162} often distinguishing the ligand design strategies for transition metals¹²¹ and for f-elements⁸⁸ (Ln and An). For Ln and An , it depends on the free ion anisotropy (oblate or prolate shape of the electronic cloud).⁸⁸ Common to all f elements, it seems that rigid ligands interacting as less as possible with the 4f electrons cloud, such as alkyl-substituted cyclopentadienyl or cyclooctatetraenyl ligands, can generate low coordination complexes, which usually display interesting magnetic properties. Such compounds are possible yet challenging to achieve as lanthanides tend to form high-coordination complexes.

For 3d transition metals, the complexation with certain ligand types gives forecastable geometries.^{163,164} This facilitates the design of SMMs with 3d transition metals over lanthanides. For 3d transition metals, the design of SMMs based on transition metals seem to require ligands that yield linear or distorted complex geometries.¹²¹ The Werner-type ligands, together with the well-established N- and O-donor ligands, constitute the current popular ligands that are used for the design of SMMs. They, for example, include Schiff-bases, polyamines, pyrazolylborates, poly(pyridyls), cyano-ligands, halides, β -diketonates, carboxylates, phenolates, alkoxides, silanolates, phosphonates, phosphinoxides, and polyphosphines.^{105,160,165–167}

Since the regain of interest in 3d metals (strategy (1)), scientists also designed some systems containing heavy p-block elements, as hinted in strategy (2). Whereas the previously mentioned coordination chemistry is well-established, the influence of main group elements on the magnetic properties is still under-investigated. Sparse contributions are reported starting 2011 for transition metals¹¹⁸ and 2015 for lanthanides.¹⁶⁸ They show the immense potential of introducing more systematically heavy p-block elements for the design of SMMs. Besides participating in the diversification of the types of SMMs, heavy p-block elements can highly influence the magnetic anisotropy. The presence of unquenched spin-orbit coupling generated by the heavy p-block elements can drastically influence the zero-field splitting responsible for the magnetic anisotropy.^{122,169} In a sense, they offer an opportunity to explore if there are existent synergies with the 4f or 3d metal that could lead to new types of paramagnetic centers, which are yet to be investigated. The characterization methods for the investigation of a SMM are described in the next section and a user guide for the SQUID magnetometer is available in the experimental section.

2.2.5. Current characterization methods of SMMs

The characterization of SMMs results from the combination of data obtained from different analytical methods. The most common and relatively accessible methods necessitate the use of a superconducting quantum interference device (SQUID) magnetometer. Various magnetic measurement techniques on the SQUID include direct current (dc) susceptibility and magnetization measurements, as well as alternating current (ac) susceptibility data acquisition. These methods allow to assess the magnetic nature of a compound and to describe the relaxation processes of the magnetization that are occurring in a specific sample. They give access to the blocking temperature and the effective energy barrier, which are the two most important characteristics of a SMM, and which allows its comparison with previously reported SMMs. However, some parameters such as the ZFS parameter are challenging to obtain through this method, and several independent experiments are usually necessary to do so precisely (for example Variable Temperature Variable Field experiments (VTVH), Variable Temperature dc measurements, or dc magnetization curves). Less common methods, such as high-field high-frequency EPR, far-IR spectroscopy, torque magnetometry, or inelastic neutron scattering, can predict more accurately the anisotropy parameters of a SMM (the sign and amplitude of the g and D tensors).¹²¹ More recent methods also include electron charge density with multipole refinement or polarized neutron diffraction. These former and latter methods, however, are very specific and require access to some few specialized facilities. Post-HF multiconfigurational theoretical calculations taking the spin-orbit coupling into account (CASSCF-NEVPT2/SA_CASSCF/CASPT2/MCRI/DMRG) and *ab initio* ligand field theory (AILFT) are then of a great help to verify experimental values, get access to the valence orbital energy splitting and to draw magneto-structural correlations.^{163,170,171} For dysprosium containing compounds, an additional tool (Magellan software) may also give the orientation of the main magnetic axis *i.e.*, the direction of the magnetic anisotropy¹⁷²

2.3. Dy³⁺: the magical ion for the design of lanthanide single-ion magnets

2.3.1. Dy³⁺: the most investigated paramagnetic lanthanide ion in molecular magnetism

Since their discovery in 2003,⁹⁶ f-element based SMMs – and more specifically lanthanide SIMs – are in the focus of the research field. As previously mentioned, lanthanides and actinides (Ln and An) are indeed highly suitable candidates towards the design of such compounds, thanks to their large magnetic moments and huge intrinsic magnetic anisotropy stemming from strong spin-orbit coupling.⁸⁸ Amongst An/Ln, Dy³⁺ is an ion that requires special attention. Even in its own family, it can be very much distinguished from other An/Ln. The spin-orbit coupled ground state 4f⁹ is described by the term symbol ⁶H_{15/2}, which reflects a huge orbital contribution to the magnetic moment. As underlined in **section 2.2.4**, this is crucial for a large magnetic anisotropy. Additionally, Dy³⁺ is a Kramers' ion, which ensures the presence of a bistable ground state.¹³⁹ Remarkable complexes featuring Dy³⁺ were obtained in the last decade, which presently hold the record for both hysteresis temperature and magnetic anisotropy,^{104,173} as shown in **Table 2.3.1**.

2.3.2. Strategies towards the design of dysprosium SMMs

Dy³⁺ possesses a strongly oblate spheroidal shape of its electron density.⁸⁸ Thus, its anisotropy is particularly well enhanced in ligand environments that generate a strongly axial crystal field (perpendicular to the long spheroidal axis) and a weak transverse crystal field (parallel to the long spheroidal axis).¹⁷⁴ Other lanthanides with an oblate shaped electron density (Ce, Pr, Nd, Tb, Ho) behave similarly, whereas lanthanides with prolate shaped electron density (Pm, Sm, Er, Tm, Yb) would require the opposite design.^{88,175–177} Based on this simplified view of the electron density, a plethora of sandwiched complexes, including the first lanthanide containing SMM,⁹⁶ was successfully synthesized.

Table 2.3.1: Comparison of selected magnetic and structural parameters in 0D mononuclear {Cp^R₂Dy}⁺–based SIMs. The compounds are listed by decreasing *T*_{hyst}. *T*_B is defined as the arbitrary chosen 100s magnetic blocking temperature.

{Cp ^R ₂ Dy} ⁺ -based SIM	Cp ^R -Dy-Cp ^R (°)	<i>T</i> _B (K)	<i>U</i> _{eff} (cm ⁻¹)	<i>T</i> _{hyst} (K)
[Cp [*] DyCp ^{iPr5}][B(C ₆ F ₅) ₄] ¹⁰⁴	162.5	65	1541	80
[Cp ^{iPr4Me} ₂ Dy][B(C ₆ F ₅) ₄] ^{173,178}	156.6	62	1468	72
[Cp ^{iPr4Et} ₂ Dy][B(C ₆ F ₅) ₄] ^{173,178}	161.1	59	1380	66
[Cp ^{iPr5} ₂ Dy][B(C ₆ F ₅) ₄] ^{173,178}	162.1	56	1334	66
[Cp tm ₂ Dy][B(C ₆ F ₅) ₄] ¹⁷⁹	152.7	53	1223/1277	60
[Cp ^{iPr4H} ₂ Dy][B(C ₆ F ₅) ₄] ^{173,178}	147.2	17	1285	32
[Cp [*] ₂ Dy][BPh ₄] ¹⁸⁰	133.4	3.2	312	5.3
[Cp [*] ₂ Dy(NH ₃) ₂][BPh ₄] ¹⁸¹	140.2	4	546	5.2
[Cp [*] ₂ DyI(THF)] ¹⁸²	136.0	?	419	4
[Cp [*] ₂ DyBr(THF)] ¹⁸²	136.1	0	163	3
[Cp [*] ₂ DyCl(THF)] ¹⁸²	136.8	0	112	2

Their magnetic properties were shown to be strongly correlated to the $\text{Cp}^{\text{R}}\text{-Dy-Cp}^{\text{R}}$ angle and its deviation from perfect linearity. The best magnetic performances were observed for the most linear molecules featuring a Kramers' ion. Perfect linearity can be achieved in Dy^{2+} or Tb^{2+} compounds, where the former holds the record in terms of magnetic performances for terbium-based SMMs.¹⁷⁸ Overall, the $\{\text{Cp}^{\text{R}}_2\text{Dy}\}^+$ unit (where Cp = cyclopentadienyl ligand, R = alkyl group) represents a powerful building block for multidimensional, multinuclear magnetic materials.^{174,183} Several strategies can be developed in this direction, as presented below (**Figure 2.3.1**).^{162,184} These strategies notably include the strong magnetic coupling of two units through a radical.^{108,127,185}

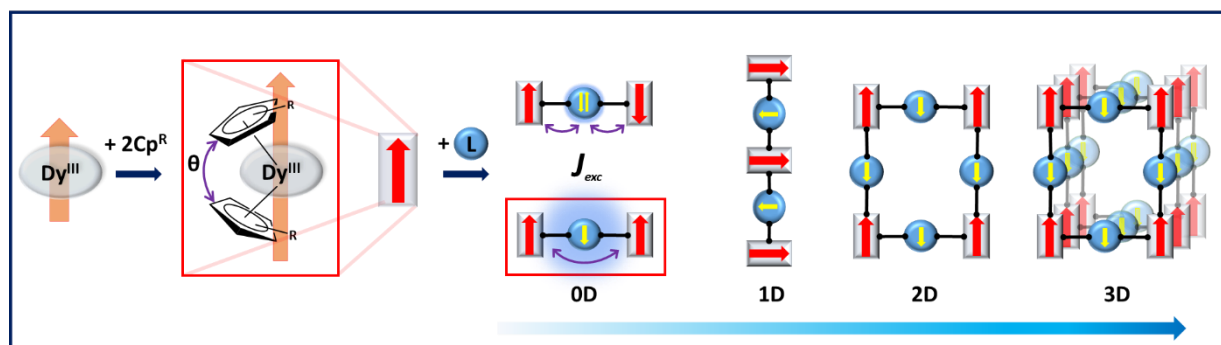


Figure 2.3.1: Design of magnetic materials with the $\{\text{Cp}^{\text{R}}_2\text{Dy}\}^+$ unit as starting building block. On the left, θ can be experimentally maximized up to 180° if Dy^{3+} is reduced to Dy^{2+} . Upon addition of a ligand, two units can be coupled (J_{exc}), either antiferromagnetically (upper center, through a diamagnetic ligand) or ferromagnetically (bottom center, through a radical). Through subsequent adequate reactions, this former magnetic coupling results in multinuclear, and even multidimensional magnetic materials.

2.3.3. Current challenges in dysprosium SMMs

Even though the pursuit of multinuclear multidimensional magnetic materials and SMMs with the $\{\text{Cp}^{\text{R}}_2\text{Dy}\}^+$ unit seems promising, there are still several drawbacks and alternative routes to consider.¹⁷⁴ Although the breakthrough achievements presented in **section 2.3.2** clearly demonstrate the superiority of cyclopentadienyl ligands in lanthanide based mononuclear SMMs, one would probably wonder how to surpass the current best SMMs. Since the angle θ has been maximized up to its limit,¹⁷⁸ are there any more improvements possible through the infinite substitution of cyclopentadienyl ligands? Probably not, which is the reason why scientists are currently investigating new classes of ligands.^{46,102,122,186–190} As such, this chapter will further focus on the design and synthesis of SN based mononuclear dysprosium complexes. It should give some insights regarding the potential of the SN ligand class towards single-molecule magnetism. Alternatively, the paucity of multinuclear compounds containing lanthanide moieties suggests that the coupling of highly anisotropic lanthanide units has yet a role to play in the development of new classes of magnetic materials (see **Chapter 4**, structures 4.2.16 and 17).

2.4. Novel mononuclear dysprosium complexes based on the S-N motive.

The extreme flexibility of sulfur coupled with the hardness of the nitrogen donor atoms within the SN ligands offers a promising compromise for the obtention of an appropriate environment around a paramagnetic center, as previously highlighted and observed with 3d metals.^{46,186} The same type of ligands was probed also with dysprosium yielding the novel complexes {Dy(PPh₂S(N^tBu)₂)₂(μ²-Cl₂)Li(THF)₂} (**1_Dy**), {Dy(PhSN(N^tBu)₂)₂(μ²-Cl₂)Li(THF)₂} (**2_Dy**), and {Dy(MeS(N^tBu)₃)₂(μ²-Cl₂)Li(THF)₂} (**3_Dy**), which are presented in the following sections.

2.4.1. Synthesis of the mononuclear dysprosium complexes 1-3_Dy

The one-step synthesis of complexes **1_Dy**, **2_Dy** and **3_Dy** consists of mixing both ligand and metal THF solutions together to give creamy mixtures, which are left to stir overnight. Upon filtration of lithium chloride through celite, the clear yellowish solutions are reduced to viscous materials and triturated with pentane or hexane until becoming solid. The subsequent layering of a THF solution with pentane (ratio 1:5) at room temperature yields the desired complexes as colorless crystals in fairly good yields, as depicted in **Figure 2.4.1**. Albeit the use of different ligands, no variations in reactivity were noticed during the reaction.

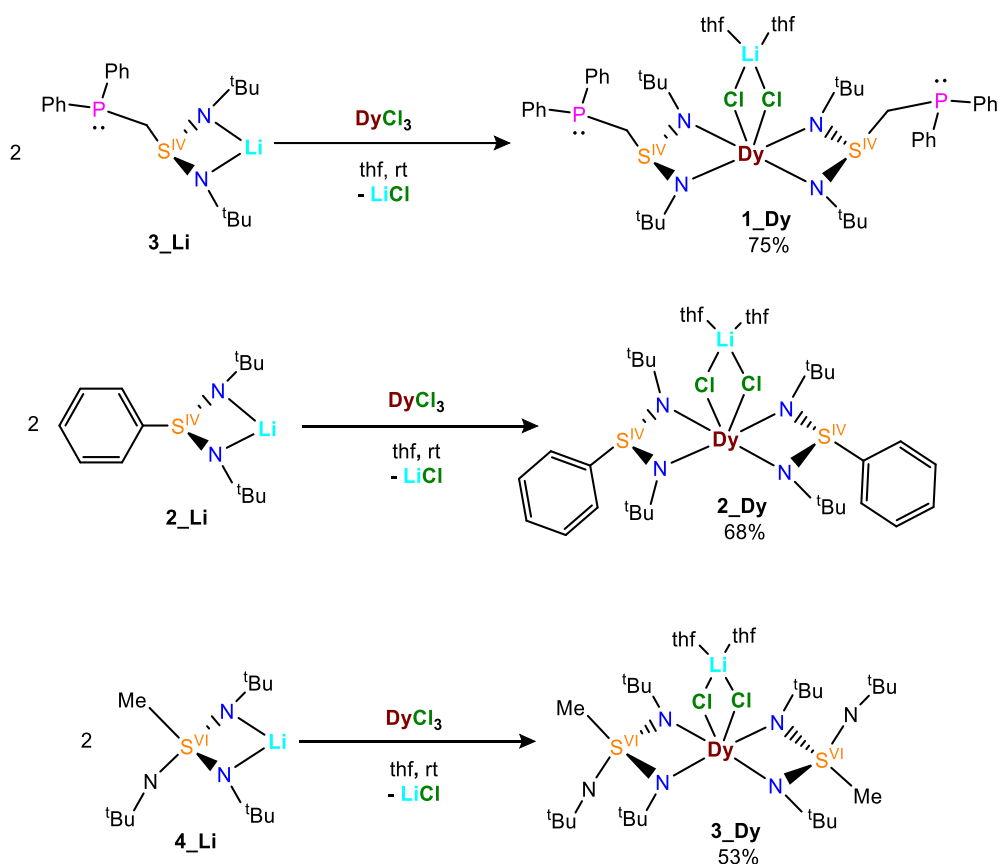


Figure 2.4.1: Synthesis route to complexes 1-3_Dy

Noteworthy, the complexes only form in THF, while reaction attempts in toluene result in undissolved starting materials. As a consequence, a lithium chloride bound to two THF coordinates through μ^2 chlorine bridges to the dysprosium center.

2.4.2. Crystallographic analysis of 1-3_Dy

X-ray diffraction of the respective complexes reveals that all three complexes crystallize in the triclinic space group $P\bar{1}$. Their structural arrangements, however, are different. 1_Dy crystallizes as one complex molecule and one THF molecule in the asymmetric unit. 2_Dy crystallizes with two complex molecules in the asymmetric unit, without the presence of any solvent molecule. 3_Dy crystallizes with two complex molecules and two additional non-coordinating THF molecules in the asymmetric unit. For all three complexes, the molecular structures show that the trivalent dysprosium center is hexa-coordinated. Two SN ligands chelate the lanthanide ion through the two nitrogen donors, while two remaining chlorine atoms constitute a μ -bridge to a lithium ion carrying two THF molecules (**Figure 2.4.1**). Selected bond lengths and angles are given in **Table 2.4.1**.

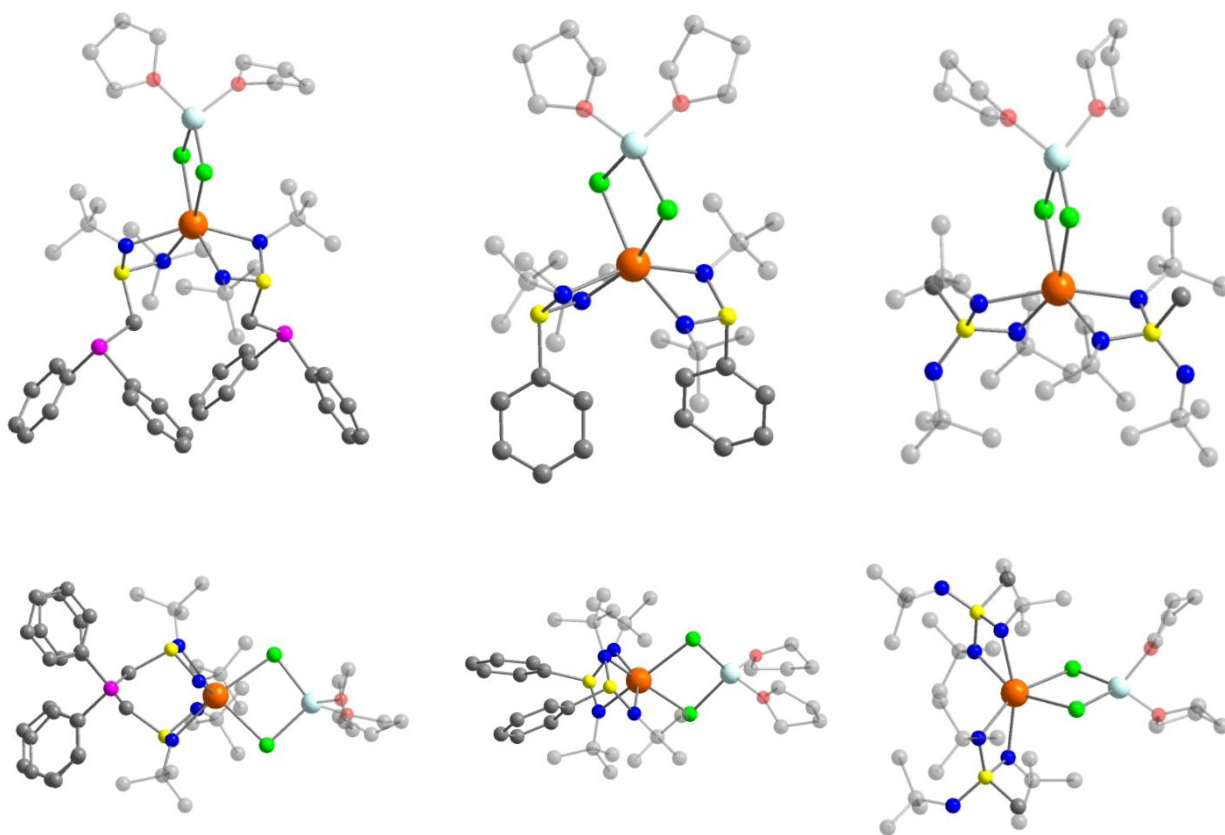


Figure 2.4.1. Crystal structures of 1_Dy (left), 2_Dy (center) and 3_Dy (right) in two orientations. Orange, green, yellow, pink, red, dark blue, grey and light blue represent dysprosium, chlorine, sulfur, phosphorus, oxygen, nitrogen, carbon and lithium atoms, respectively. Hydrogens are omitted for clarity.

In 1_Dy, the phosphorus atom, which could possibly participate in bonding,^{56,57} does not orient towards the dysprosium. On the contrary, both phosphine groups point in the opposite direction, resulting in a large Dy-P distance of av. 5.2 Å. This is probably due to the fact that the coordination sphere of the Dy ion is already almost saturated (although it is difficult to predict how many ligands should coordinated the ion). The lithium ion presents a slightly elongated tetrahedral geometry, which has been observed in comparable 3d metal complexes.⁴⁶ Attempts to avoid the formation of such lithium chlorine adducts with the use of the bulkier ligand 3_Li or

with the corresponding crown ether during the metalation were unsuccessful.⁴⁶ Similarly, the use of Dy(HMDS)₃ instead of the metal halide salt prevented the formation of any of the three presented complexes. This issue could be addressed by using the protonated species such as the dimer {1_H}₂ instead of 2_Li for complex 1_Dy. In complexes 1_Dy and 2_Dy, the sulfur atom is in the oxidation state +IV, but it seems that the reduced electro-positivity of the sulfur atom, in comparison to complex 3_Dy, has no significant impact on the Dy-N bond lengths (shortest 2.34 in 1_Dy to longest 2.38 Å in 3_Dy), similar to 3d metal complexes.^{42,46,56,57,191} The influence of the sulfur oxidation state is only mirrored in the S-N distances. The dysprosium-coordinated S(IV)-N distances in 1_Dy and 2_Dy are 1.63 Å long and hence about 0.03 Å longer than the S(VI)-N distances in 3_Dy. This is the expected decrease while rising the sulfur oxidation state. The pendent S(VI)-N distance is the shortest of all S-N distances in this set of compounds (0.08 Å shorter). Additionally, the chemical tuning of the sterics around the metal center greatly influences the bite angle and the folding angle variations, as well as the overall spatial arrangement, as shown in **Table 2.4.1**. Noteworthy, 3_Dy displays the most acute N-Dy-N angles, meaning that the compound is the most ‘pseudo-linear’ one amongst the present series.

Table 2.4.1. Analysis of various structural parameters in complexes 1-3_Dy. Bond lengths are given in Å and angles in degrees (°).

^aangle between the two NSN planes; ^bdeviation from the magnetic easy axis determined by Magellan (**Figure 2.4.8**), ^cnearest neighbors; ^cper complex molecule; ^ddistance of two closest parallel aromatic rings

Compound	1_Dy	2_Dy	3_Dy
Dy-N	2.34–2.40	2.35–2.37	2.37–2.39
Dy-Cl	2.70–2.73	2.70–2.72	2.71–2.72
S-N	1.63–1.64	1.63–1.64	1.59–1.61
N-Dy-N	63.9–64.0	62.9–63.0	60.1–60.6
S-Dy-S	108	118–121	133–135
Folding angle ^a	97.4	104.8–108.1	117.9–118.2
Easy axis deviation ^b	117–118	125–126	114–116
av Dy-Dy ^c	10.50	10.91	10.94
# of THF molecules ^c	1	0	1
Packing density	1.366	1.387	1.350
π interactions ^d	Weak (6.5 Å)	unlikely (≈ 8 Å)	No π system

The analysis of the structure packing reveals very different arrangements from 1_Dy to 3_Dy. (**Figure 2.4.2**) The significant steric hindrance of the phosphine and the *tert*-butyl groups in 1_Dy results in a relatively sparse space arrangement of the complex molecules, allowing two THF molecules to fill the empty spaces. For 2_Dy, the phenyl groups are oriented almost perpendicular

to the S-Dy-S axis, which prevents steric hindrance but may allow π stacking. This arrangement allows up to twelve molecules to fit into the unit cell, resulting in a denser packing (density 1.387 vs 1.366 and 1.350), which hampers the inclusion of THF molecules in the unit cell. The packing in **3_Dy** reveals that the complex molecules alternate head to tail while the non-binding solvent molecule fills the space left by the coordinating THF molecules on two nearest neighbors. In all **1-3_Dy**, the distance between two nearest dysprosium neighbors should be large enough to avoid any magnetic coupling. Weak π interactions may still be present in **1_Dy** and **2_Dy**, due to the relative proximity of the phenyl groups of two neighboring complex molecules (**Table 2.4.1**), but there is no clear orientation of the aromatic rings for an overlap that would suggest the presence of significant quadrupole-quadrupole interactions.

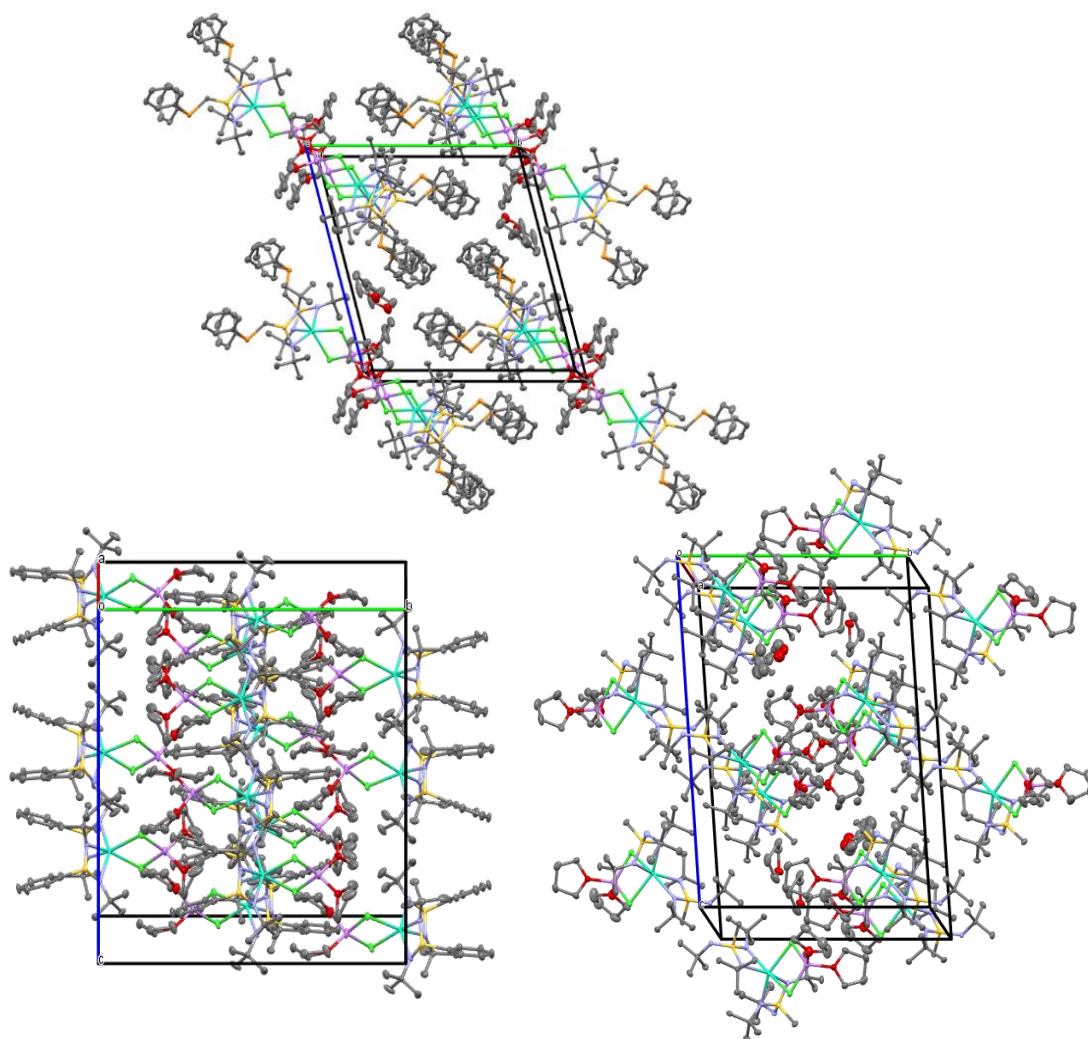


Figure 2.4.2. Views of structural packing of **1_Dy** (top), **2_Dy** (bottom left) and **3_Dy** (bottom, right) along the a^* axis (Mercury software). Hydrogen atoms are omitted for better clarity. Light blue, green, yellow, orange, red, blue, grey and purple represent dysprosium, chlorine, sulfur, phosphorus, oxygen, nitrogen, carbon and lithium atoms, respectively.

2.4.3. Magnetic characterization of **1-3_Dy**

The initial temperature-dependency of the product of the magnetic susceptibility and the temperature $\chi_M T$ were measured on the SQUID magnetometer for all three complexes. The

resulting curves show high-temperature values of $14.21 \text{ cm}^3\text{mol}^{-1}\text{K}$ for **1_Dy**, $14.15 \text{ cm}^3\text{mol}^{-1}\text{K}$ for **2_Dy** and $14.41 \text{ cm}^3\text{mol}^{-1}\text{K}$ for **3_Dy**, as displayed in **Figure 2.4.3**. These $\chi_M T$ values are slightly different than the expected value for the free Dy^{3+} ion ($14.17 \text{ cm}^3\text{mol}^{-1}\text{K}$) but still are in the range of previously reported dysprosium single-ion magnets.^{103–105,192} Notably, the highest value is found for **3_Dy**, which is also the only complex to have no potential intermolecular interactions. Therefore, the slightly lower 210 K $\chi_M T$ value for **1_Dy** may be attributed to the presence of magnetic impurities (despite many recrystallizations). For **2_Dy**, the almost ideal high temperature $\chi_M T$ value suggests that intermolecular interactions are negligible, if non-existent. For all complexes, the $\chi_M T$ value then decreases with the temperature, due to magnetic saturation and similar to previously reported complexes.^{105,193,194}

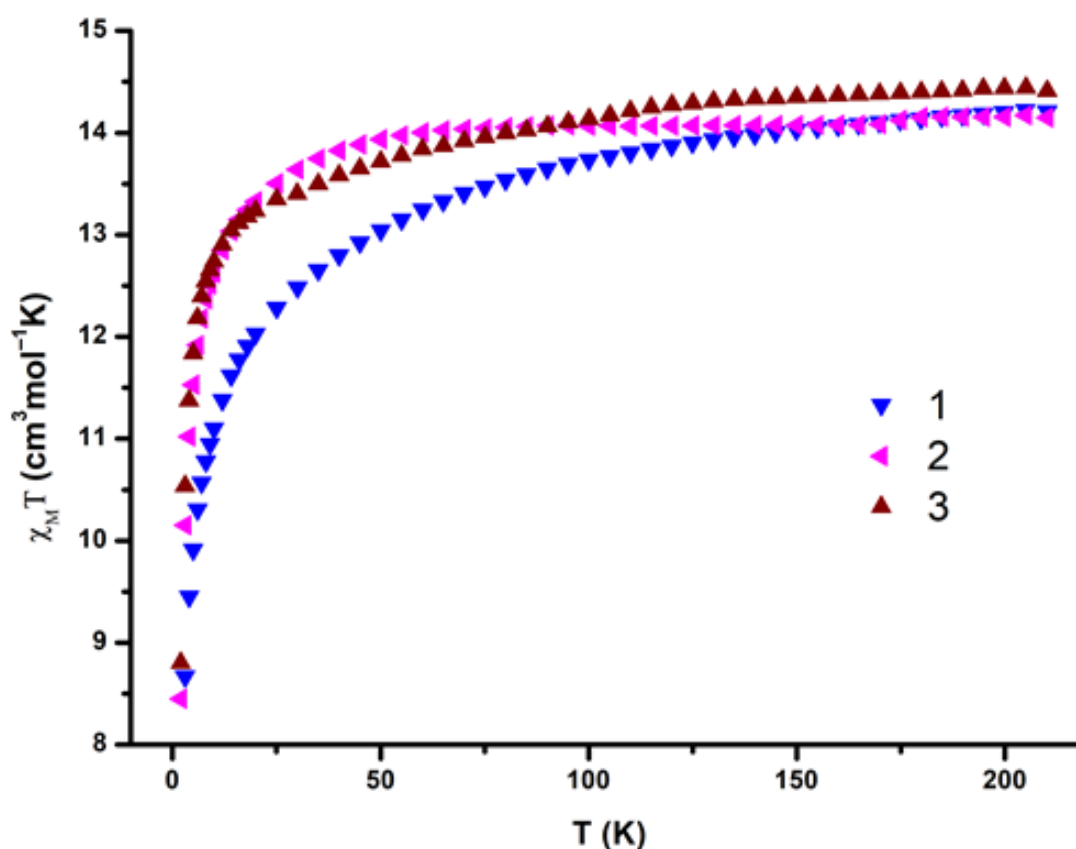


Figure 2.4.3. Temperature dependency of $\chi_M T$ for complexes **1-3_Dy**.

This analysis suggests that **3_Dy** may have the best magnetic performances amongst the present series. Further investigations of the magnetic relaxation dynamics of **1-3_Dy** via variable-temperature variable-frequency ac susceptibility measurements corroborated this hypothesis. **1_Dy** did not show in and out of phase signals characteristic for SMM behavior at zero-field (**Figure 2.4.4**). With an optimal external field of $H_{dc} = 1000 \text{ Oe}$, however, it exhibits a broad peak maximum for the imaginary part of the dynamic susceptibility (**Figure 2.4.4b**) at 100 Hz at 2 K, which then shifts towards higher frequencies with the temperature increase, indicative of slow relaxation of the magnetization. The relaxation times τ are extracted from the Cole-Cole plot generated from the in and out of phase dynamic susceptibility via the CC-fit program¹⁹⁵ and used to draw the Arrhenius plot, as shown in **Figure 2.4.4d**. A full fit (blue line) taking into account

the Orbach, QTM, Raman and direct relaxation processes^{150,152} (Eq 2.1) gives an energy barrier $U = 20.8 \text{ cm}^{-1}$.

$$\tau^{-1} = \underset{\text{Direct}}{AH^4T} + \underset{\text{Orbach}}{\tau_0^{-1}e^{(U_{eff}/k_BT)}} + \underset{\text{QTM}}{\tau_{QTM}^{-1}} + \underset{\text{Raman}}{CT^n} \text{ (Eq 2.1)}$$

where A, C and n are constants, H the applied magnetic field, τ_0 the initial characteristic relaxation rate for the Orbach process, U_{eff} the effective energy barrier to spin reversal, k_B the Boltzmann constant, and τ_{QTM} the relaxation rate for QTM.

Overall, the application of an external field suppresses some QTM effects but does not suffice to increase the magnitude of the effective energy barrier to spin inversion.

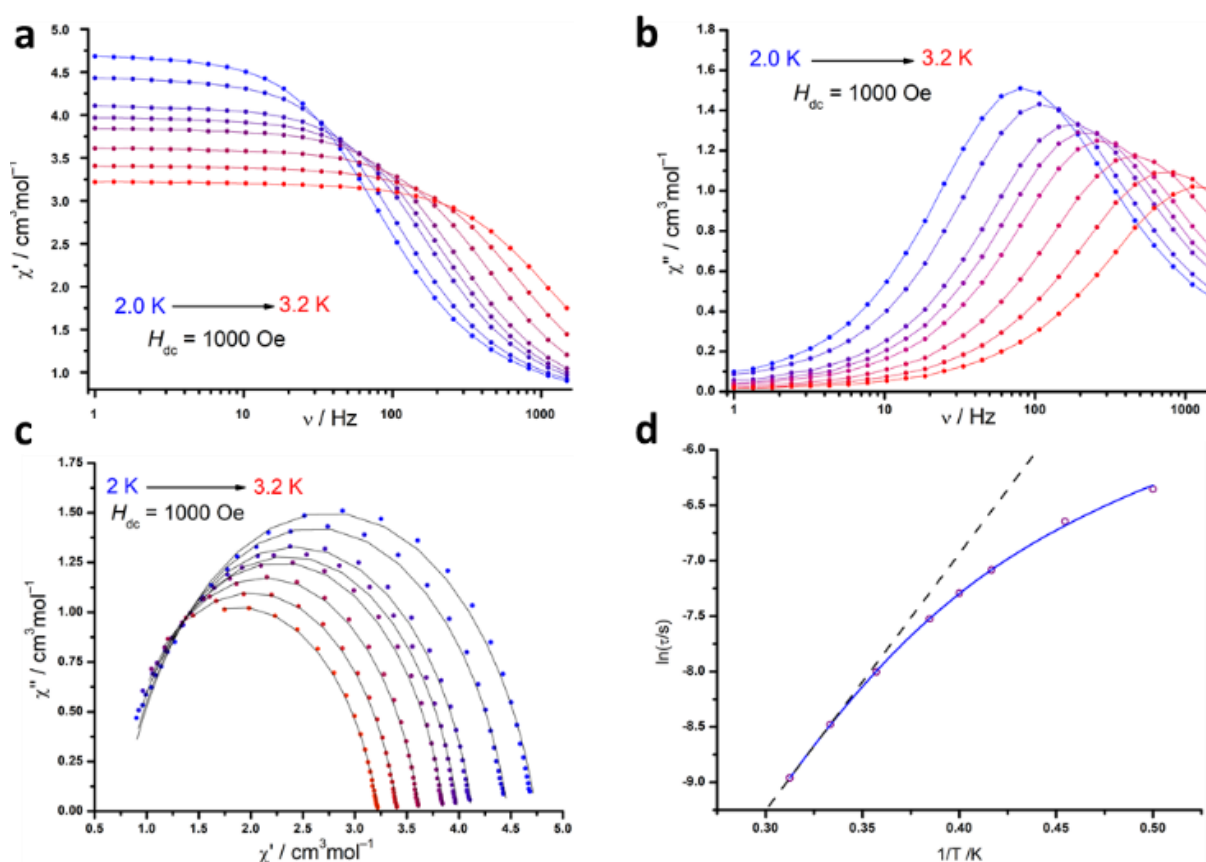


Figure 2.4.4: Relaxation data for **1_Dy** under 1000 Oe. Variable frequency variable temperature in and out of phase signals of the ac dynamic susceptibility (a, b), Cole-Cole plot (c) and Arrhenius plot (d).

A similar analysis for compound **2_Dy** reveals field induced SMM behavior, however with only one relaxation process. Under an applied dc field of 1000 Oe, the maxima of the out-of phase signal of the dynamic susceptibility are observable up to 7K (**Figure 2.4.5b**). The shift to higher frequency with the increase of the temperature is clearly temperature-dependent and suggests the absence of QTM. The corresponding Cole-Cole plot (**Figure 2.4.5c**) confirms this hypothesis, and the Arrhenius plot can be fitted without QTM (**Figure 2.4.5d**). Different than **1_Dy**, the effective energy barrier of **2_Dy** is similar (21.1 cm^{-1}) than the obtained U (19.7 cm^{-1}) when all

relaxation processes are considered. Nevertheless, the arced shape of the curve in the Arrhenius plot strongly suggests that the relaxation mainly occurs through a Raman process.

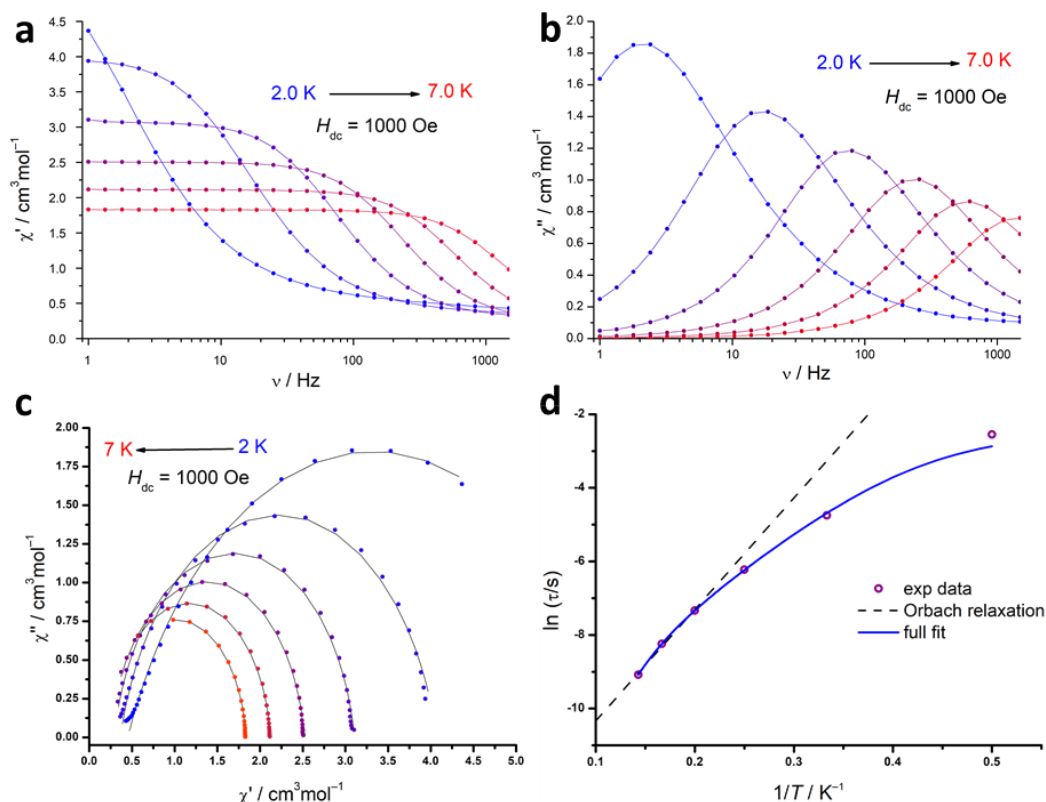


Figure 2.4.5: Relaxation data for 2_Dy under 1000 Oe. Variable frequency variable temperature in and out of phase signals of the ac dynamic susceptibility (a, b), Cole-Cole plot (c) and Arrhenius plot (d).

The last compound of the series, 3_Dy , shows the main promising results. It displays slow relaxation of its magnetization at zero field, as depicted in Figure 2.4.6a and b. However, the out-of-phase signal of the dynamic susceptibility (b) reveals that the process occurring at low temperature is temperature-independent, which suggests strong QTM from 2K to 8K. Thereafter, the maxima are shifting to higher frequencies with the increase of temperature, indicative of slow relaxation of the magnetization. The Cole-Cole plot (**Figure 2.4.6c**) shows almost perfect circular curves, in good agreement with one main slow relaxation process. The Arrhenius plot (**Figure 2.4.6d**) further supports the existence of a linear regime (Orbach-type relaxation) with a $U_{eff} = 42 \text{ cm}^{-1}$. It also clearly indicates the presence of other relaxation processes, as the curve does not stay linear with the temperature decrease. The zone where $\ln(\tau)$ is independent of the temperature corresponds to the QTM phase. The zone at the curvature indicates a T^n dependency of $\ln(\tau)$, which typically corresponds to Raman relaxation processes. A full fit including the Raman relaxation and the QTM gives a much higher energy barrier of $U = 59.3 \text{ cm}^{-1}$. The subsequent application of an external field of $H_{dc} = 1000$ Oe suppresses most of the QTM (**Figure 2.4.7**) and raises the effective energy barrier to spin reversal to 72.4 cm^{-1} .

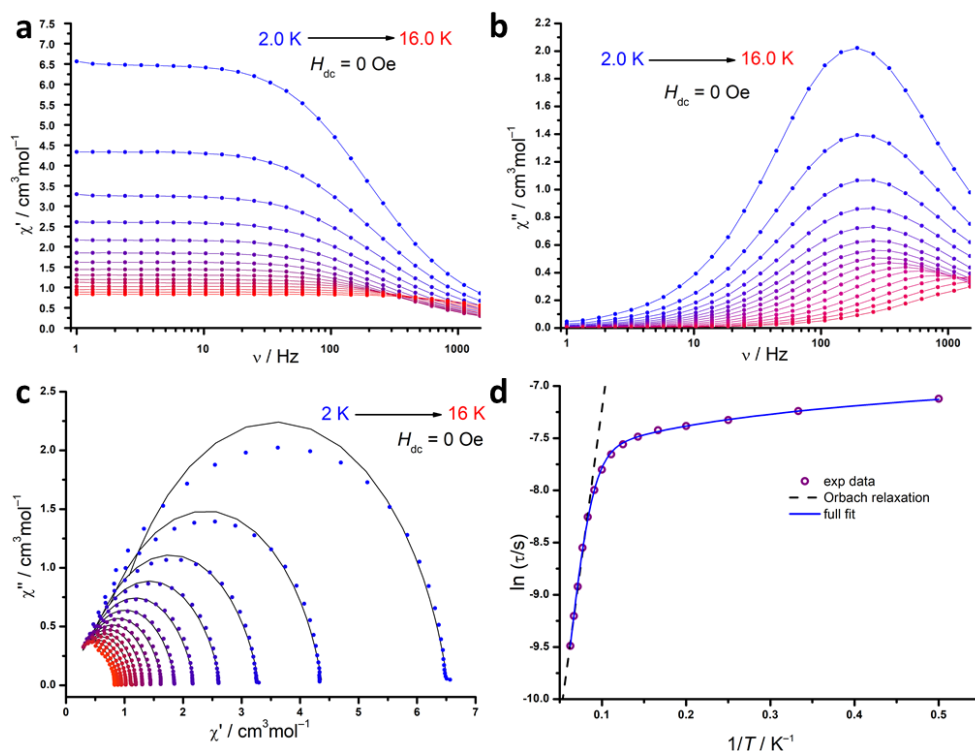


Figure 2.4.6: Relaxation data for 3_Dy under zero field. Variable frequency variable temperature in and out-of-phase signals of the ac dynamic susceptibility (a, b), Cole-Cole plot (c) and Arrhenius plot (d).

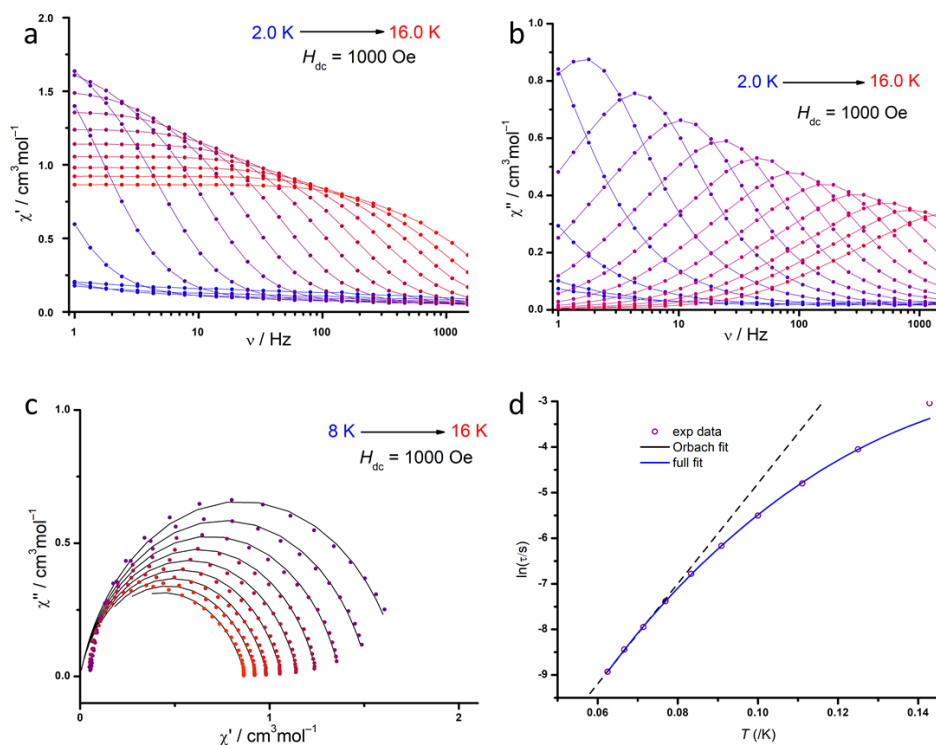


Figure 2.4.7: Relaxation data for 3_Dy under 1000 Oe. Variable frequency variable temperature in and out-of-phase signals of the ac dynamic susceptibility (a, b), Cole-Cole plot (c) and Arrhenius plot (d).

The following magnetic parameters obtained for complexes **1-3_Dy** are summarized in **Table 2.4.2**.

Table 2.4.2. Selected magnetic parameters obtained for **1-3_Dy**.

Compound	1_Dy	2_Dy	3_Dy
$\chi_M T$ at 210 K ($\text{cm}^3 \text{mol}^{-1} \text{K}$)	14.21	14.15	14.41
U_{eff} (cm^{-1}) at 0 Oe	0	0	42
U (cm^{-1}) at 0 Oe	0	0	59.3
U_{eff} (cm^{-1}) at 1000 Oe	13.2	21.1	64.8
U (cm^{-1}) at 1000 Oe	20.8	19.7	72.4
τ_0 (s)	$1.58 \cdot 10^{-8}$	$1.6 \cdot 10^{-6}$	$4.4 \cdot 10^{-6}$

There is a clear trend of enhancement of the magnetic properties from **1_Dy** to **3_Dy**, which suggests that the variations in ligand design are drastically influencing the magnetic anisotropy at the dysprosium center and the overall physical properties of the compounds. The subsequent analysis of the main magnetic axis (or easy axis)¹⁷² suggests that the lithium chlorine co-ordination on the dysprosium center worsens the pseudo-linearity of the molecule. As a result, the two NSN chelating units are not aligned on the main magnetic axis (**Figure 2.4.8**).

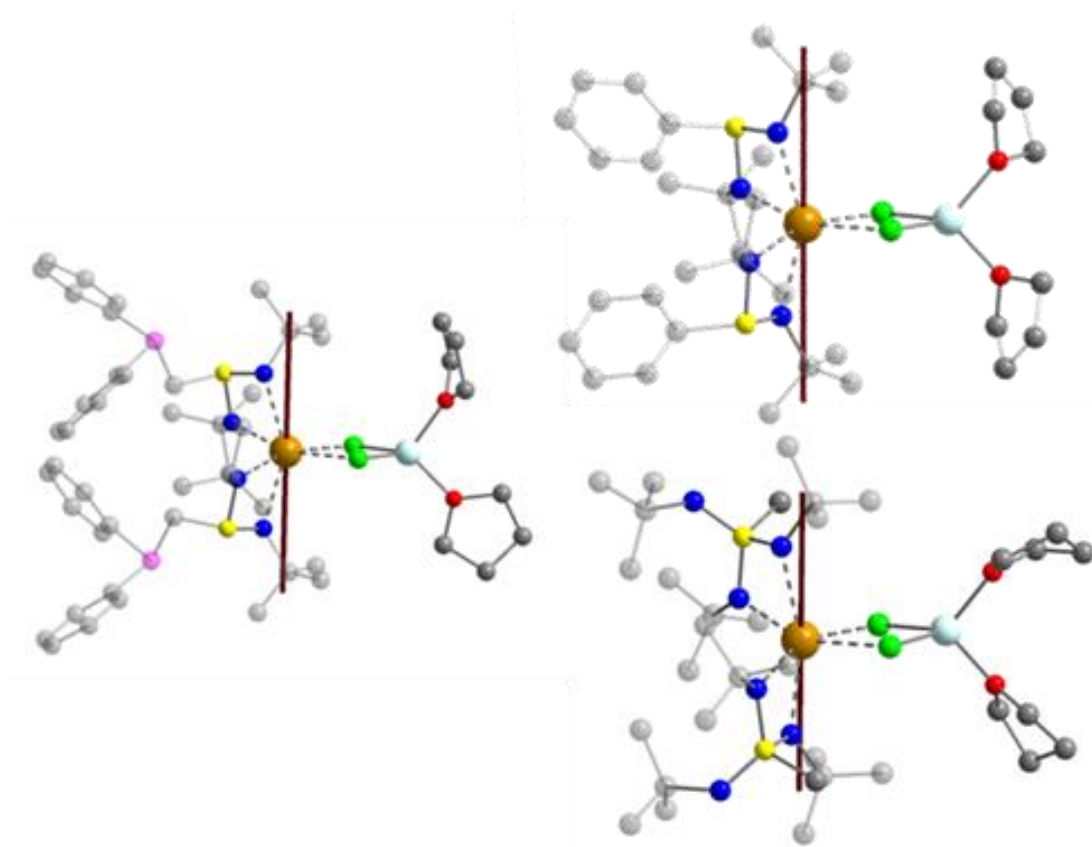


Figure 2.4.8. Orientations of the main magnetic axis of the ground state calculated for the entire molecule for **1-3_Dy** (brown line). Hydrogens are omitted for better clarity. Brown, green, yellow, pink, red, blue, grey and light blue represent Dy, Cl, S, P, O, N, C and Li, respectively.

Thus, both the chlorine bridges and the ligands probably induce a significant transverse anisotropy reducing the magnetic performance. Nevertheless, the additional substitution on the sulfur atom in **3_Dy** clearly provides the best environment around the lanthanide ion in the present series, resulting in better SMM properties than **1_Dy** and **2_Dy**. Overall, there is a trend from **1_Dy** to **3_Dy** with a significant improvement of the magnetic properties while the S-Dy-S folding angle becomes closer to 180° and the spatial arrangement prevents intermolecular interactions.

2.5. Strategies towards pseudo-linear dysprosium complexes

The previous short study of three novel dysprosium complexes **1-3_Dy** clearly demonstrated the potential of the SN moiety as an alternative chelate to cyclopentadienyl ligands in the design of lanthanide containing single-molecule magnets. It further hints that improved ligand tuning towards linear or pseudo-linear structures may lead to better magnetic performances. Next efforts focus on the removal of co-coordinated LiCl to further improve the magnetic properties through the decrease of coordination on the dysprosium center and the gain of linearity. Potential improvement routes also include the screening of SN ligands to discriminate the most suitable ones towards lanthanide SMMs. Parts of this section were done in a collaboration with J. Jung and Dr. S. Demeshko and will be more thoroughly reported in the PhD thesis of J. Jung.¹⁹⁶ The focus on this joint work was to generate a ligand with a potassium atom instead of a lithium atom, in order to avoid LiCl co-coordination on the final dysprosium complex.

2.5.1. Synthesis of $[\{\text{Ph}_2\text{PCH}_2\text{S}(\text{N}^t\text{Bu})_3\}_2\text{DyCl}]$ (**4_Dy**)

To further study the influence of p-block elements on the magnetism, the ligand **6_Li** was chosen. The protonation of **6_Li** with $\text{H}_3\text{N}^t\text{BuCl}$ followed by the addition of KH yields the potassium analog ligand **6_K**, as described elsewhere. It further reacts with DyCl_3 to give the complex **4_Dy** (Figures 2.5.1 and 2.5.2).

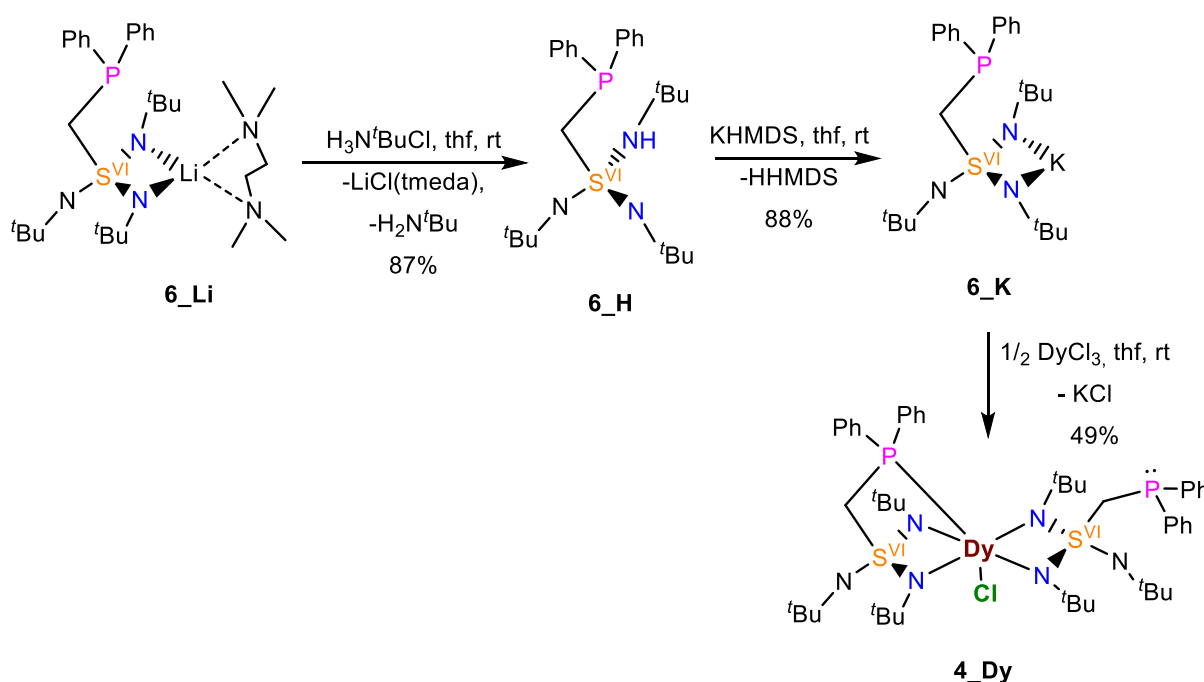


Figure 2.5.1. Scheme of the synthesis route to **4_Dy**

6_Li was dissolved in THF and $\text{H}_3\text{N}^t\text{BuCl}$ was added dropwise as a THF solution. The clear solution became troubled, indicating the precipitation of LiCl. Upon stirring for several hours, the precipitation was removed by filtration through celite, and the clear solution dried to obtain the crude protonated product **6_H**. The product was subsequently reacted with KHMDS in THF for 24 hours, the reaction solution was dried, dissolved in a minimal amount of THF and then layered with pentane (1:5). Colorless crystals of **6_K** were afforded by storing this mixture at -34°C within days. Crystalline **6_K** was then further suspended in a THF/toluene mixture, to which DyCl_3 was added in one portion. A slight change from colorless to light yellow color occurred while everything dissolved. Over time, a cloudy precipitate appeared. After stirring overnight, the solution was filtered to remove KCl and unreacted materials. The volatils were removed and the crude product was dissolved in a minimal amount of THF and layered with pentane. Block shaped crystals grew within an hour at room temperature, giving crystalline **4_Dy** in 50% yield. Subsequent SCXRD analysis showed that **4_Dy** crystallizes in the monoclinic space group C2/c with one complex molecule and one disordered pentane/THF molecule in the asymmetric unit (**Figure 2.5.2**)

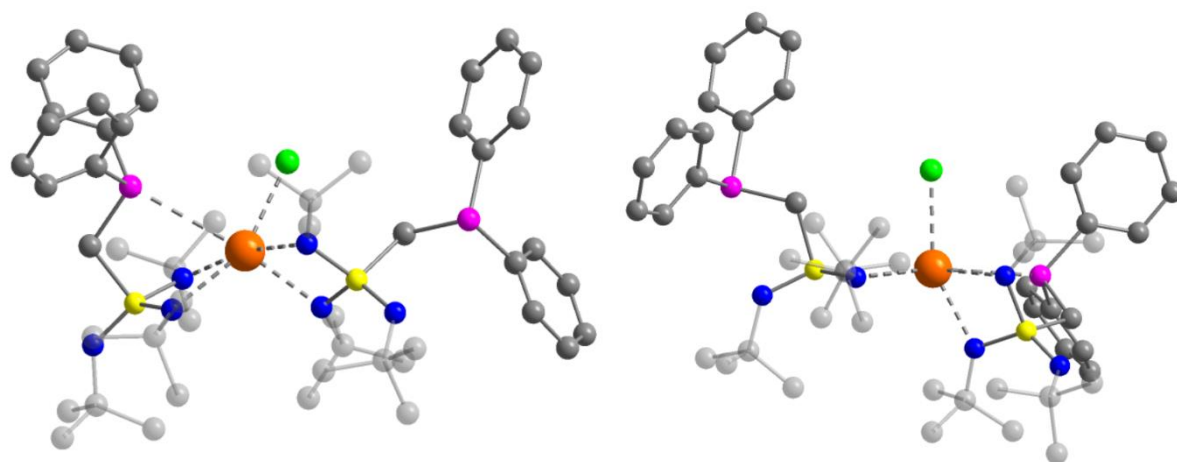


Figure 2.5.2. Crystal structure of **4_Dy** in two orientations. Orange, green, yellow, pink, dark blue, and grey represent dysprosium, chlorine, sulfur, nitrogen, and carbon atoms, respectively. Hydrogens are omitted for clarity.

The dysprosium atom is now hexacoordinated by two *N, N'* chelating sulfur centered ligands, one phosphorus atom and one chlorine atom. Two chlorine atoms were successfully removed and replaced by two SN ligands. No LiCl (or KCl) coordination is observed. Interestingly, one of the phosphorus atoms weakly coordinates the dysprosium atom, with the Dy-P distance of 3.2169(5) Å. The other scorpionate ligand is chelating through the two nitrogen atoms only, with its phosphorus atom pointing away from the dysprosium atom. Complete structure description can be found in the PhD thesis of J. Jung¹⁹⁶ while selected bond lengths and angles are presented in **Table 2.5.1**. Noteworthy, the S-Dy-S angle is larger while the N-Dy-N angles are more acute in **4_Dy** if compared to **1-3_Dy**, indicating a gain in axiality at the paramagnetic center.

Table 2.5.1. Selected bond lengths (Å) and angles (°) for **4_Dy**.

Compound	4_Dy
Dy-P	3.2169(5)
Dy-Cl	2.5996(5)
Dy-S	3.0730(5); 3.0789(5)
Dy-N	2.3147(13); 2.3467(13); 2.3471(13); 2.3837(13)
Dy-Dy	–
N-Dy-N	60.37(5); 60.07(4)
S-Dy-S	141.847(12)
Easy axis deviation	120-125.6

2.5.2. Magnetic properties of $[(\text{Ph}_2\text{PCH}_2\text{S}(\text{N}^i\text{Bu})_3)_2\text{DyCl}]$ (**4_Dy**)

The magnetic properties are found to be drastically improved in **4_Dy** in comparison with **1-3_Dy**. Slow magnetic relaxation is observed up to 12K under zero field and with an optimal applied field of $H_{\text{dc}} = 1000$ Oe, as depicted in **Figure 2.5.3**.

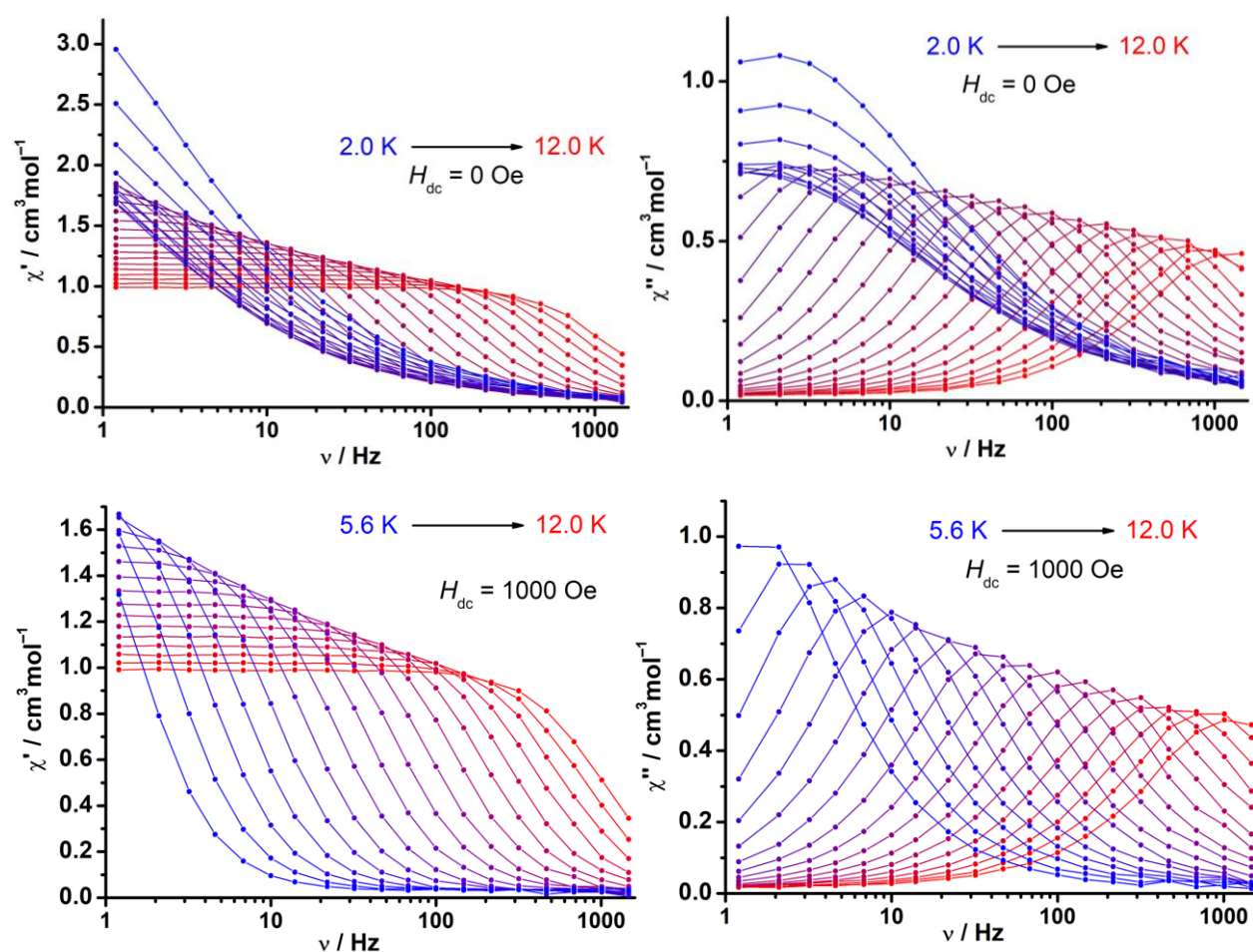


Figure 2.5.3. ac susceptibility data for **4_Dy** under zero field (top) and under a 1000 Oe applied dc field (bottom)

The subsequent fittings of the Arrhenius plot curves yield an energy barrier of 36.9 cm⁻¹ (attempt time of 1.1 10⁻⁶ s) under zero field, and an energy barrier of 66.5 cm⁻¹ (attempt time of 5.6 10⁻⁸ s) under 1000 Oe. The QTM is partially suppressed upon the application of an external field but not entirely. Magnetic parameters are summarized in **Table 2.5.2**.

Table 2.5.2. Selected magnetic data for **4_Dy**

Magnetic parameter	4_Dy
$\chi_M T$ at 210 K (cm ³ mol ⁻¹ K)	12.9
U_{eff} (cm ⁻¹) at 0 Oe	36.9
τ_0 (s)	1.1 10 ⁻⁶
U_{eff} (cm ⁻¹) at 1000 Oe	66.5
τ_0 (s)	5.6 10 ⁻⁸

Impressively, **4_Dy** features a butterfly hysteresis from 2K to 3.5K, as shown in **Figure 2.5.4**. The hysteresis is not open at 2K due to the presence of QTM. Nevertheless, these achievements represent the first SN-based dysprosium compounds that show a magnetic hysteresis. Further details about compound **4_Dy** can be found in J. Jung's PhD thesis.¹⁹⁶

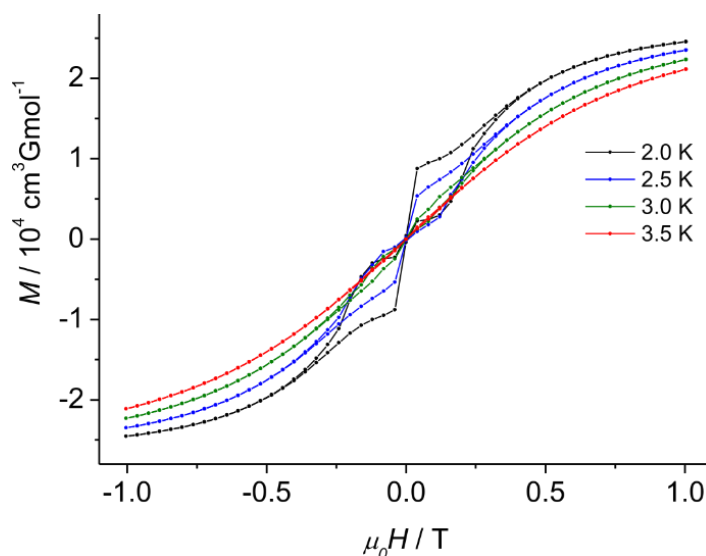


Figure 2.5.4. Magnetic hysteresis for **4_Dy** from 2K to 3.5K in 0.5K steps. Sweep rate of 1.3mT/s.

The improved magnetic properties demonstrated by **4_Dy** in comparison with **1-3_Dy** are probably due to the enhancement of the pseudo-linearity (the S-Dy-S angle is now approx. 142° compared to 135°) and to the removal of the co-coordinating (THF)₂LiCl. The determination of the orientation of the main magnetic axis in **4_Dy** indeed shows a slightly different orientation than in **1-3_Dy** (**Figure 2.5.5**). Because of the asymmetry introduced by the antagonist behavior of the two phosphorus atoms, the main magnetic axis is now shifted from the N-S-N plane towards the binding phosphorus atom. The chlorine atom is in the equatorial plane while all nitrogen atoms are relatively close to the main magnetic axis. Therefore, it is probable that the complex **4_Dy** could show even better magnetic properties without the chlorine coordination.

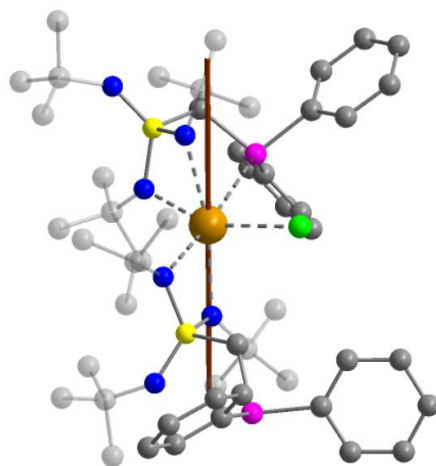


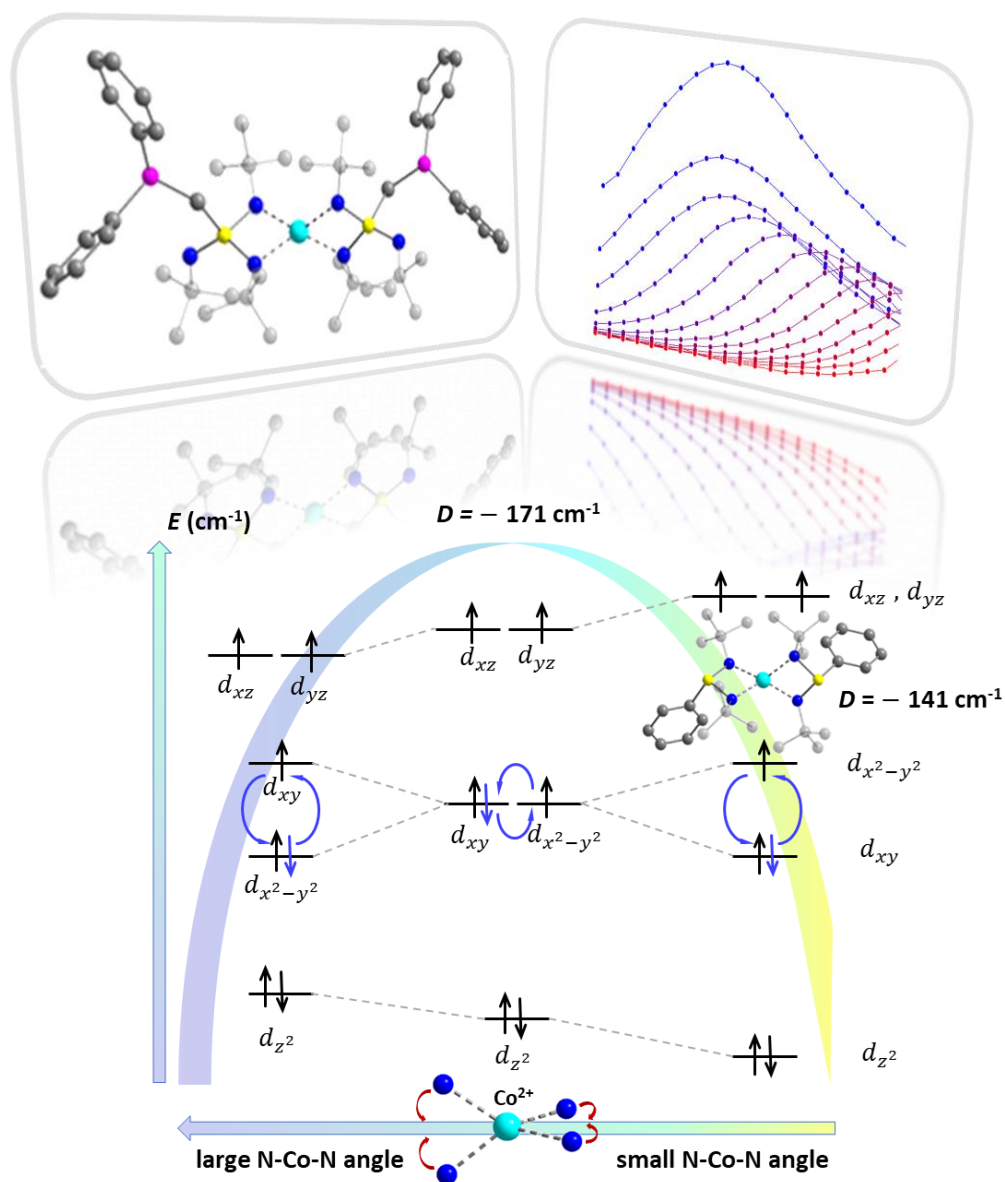
Figure 2.5.5. Orientation of the main magnetic axis of the ground state calculated for the entire molecule for **4_Dy** (brown line). Hydrogens are omitted for better clarity. Orange, green, yellow, pink, dark blue, and grey represent dysprosium, chlorine, sulfur, phosphorus, nitrogen, and carbon atoms, respectively

2.5.3. Conclusion and perspectives

The removal of co-coordinated LiCl was synthetically successful and proved useful for the enhancement of the magnetic properties, as **4_Dy** displays a magnetic hysteresis. Additional complex engineering towards the removal of the remaining chlorine atom in **4_Dy** will potentially further improve the magnetic properties. Some preliminary results under mild conditions are given in section 4.2.8. Alternatively, the successful strategy achieved for the present ligand **6_Li** could be reproduced with other SN ligands to determine the most suitable chelate for the synthesis of dysprosium based SMMs.

Chapter Three

Influence of main group elements in trigonal planar and magneto-structural correlations in highly distorted tetrahedral mononuclear cobalt single-ion magnets



3.1. Cobalt based SMMs: challenging 3d transition metals

As previously mentioned, there is a current regain of interest in transition metal based SMMs (strategy (1)) since 2011.¹¹⁸ 3d transition metals appear to be more rewarding – and cheaper – to work with, in comparison to lanthanides. This is to some extent due to the abundant literature already available for transition metals, which allows comprehensive reading and design of new complexes. The tuning possibilities and influences of their ligand environments are of course infinite, however better understood than these of lanthanides, which gives more control for complex engineering. Predictions with 3d transition metals are therefore easier and the corresponding results are somewhat less due to ‘luck’ than to systematic analysis and careful synthesis.

At first glance however, transition metals seem to have less to offer than lanthanides. In 3d transition metal SMMs, the orbital angular momentum (OAM) is often deteriorated by the ligand field, which substantially prevents zero-field splitting (ZFS). Additionally, due to QTM, most 3d metal based SMMs are therefore field-induced SMMs,¹⁹⁷ which means that they require an external non-zero magnetic field to show slow relaxation of their magnetization. The lack of first-order OAM in 3d metal SMMs is due to the more diffuse valence 3d orbitals, whose energies are greatly affected by ligands fields,⁸⁹ while 4f orbitals barely participate in bonding and are shielded by the outer core electrons. Thanks to the partial screening of the 4f orbitals from the ligands by the outer core orbitals, the first-order OAM in 4f-element based SMMs is intrinsically preserved, and the magnetic anisotropy further benefits from larger spin-orbit coupling (SOC) constants.⁸⁸ On the contrary, the magnetic properties of 3d metal-based complexes often suffer from the lack of OAM and may only rely on the spin magnitude (instead of relying on both L and S). Nevertheless, 3d based systems are still arousing interest, mainly because of their highly tunable properties, contrary to lanthanide-containing compounds.^{81,121}

In the past decade, remarkable 3d SMMs were synthesized,^{119,120} including two-coordinate iron¹¹⁵ and cobalt¹¹³ systems, as well as highly distorted tetrahedral cobalt complexes.^{42,117,118,198–202} Amongst 3d mononuclear SMMs, SMMs containing cobalt as a paramagnetic center are the most numerous for the following reasons. Cobalt, a readily available metal, displays highly interesting magnetic properties: in solid state chemistry, it can be combined with samarium to form the alloy SmCo_5 , a hard permanent magnet.⁹⁹ In molecular chemistry, in the oxidation state $\text{Co}^{2+}(\text{d}^7)$, it can possess the high spin configuration of $S=3/2$. As a Kramers’ ion (with an odd number of unpaired electrons), it is consequently a promising candidate for the design of SMMs.

Although often showing field-induced slow magnetic relaxation, cobalt based complexes can also display SMM behavior under zero dc field. They do so when surrounded by the appropriate coordination environment preserving some OAM, giving a large spin-orbit coupling (SOC) and therefore large zero-field splitting (ZFS).¹¹³ The presence of OAM can be associated with the degeneracy of two 3d orbitals sharing the same $|m_L|$ (magnetic angular momentum quantum number) and together occupied with an odd number of electrons. The 3d orbital pairs are $(d_{x^2-y^2}, d_{xy})$ and (d_{xz}, d_{yz}) are linear combinations of the $m_L = (\pm 2)$ or (± 1) and contribute

with an orbital angular momentum $L=2$ or $L=1$, respectively.¹⁶⁴ An ideal ligand will prevent full OAM quenching and therefore allow optimal spin-orbit coupling. Hence, the choice of ligands – and their associated geometry – is decisive for the design of cobalt containing SMMs. Therefore, recent studies on cobalt based SMMs revealed one major factor.^{93,113,121,167} They showed that some geometries can generate huge spin-orbit coupling and magnetic anisotropy, where cobalt is somewhat comparable to a lanthanide. In this chapter, two different geometries on Co^{2+} centers will be probed: the trigonal planar geometry in asymmetric complexes (**section 3.2**) and highly distorted tetrahedral geometry in symmetric $[\text{CoN}_4]$ SMMs (**section 3.3**). Both series of cobalt complexes are investigated experimentally with theoretical support.

3.2. Trigonal planar field induced cobalt SMMs

Trigonal planar heteroleptic complexes are relatively rare in literature. Challenging and controlled synthesis routes are usually required to obtain such asymmetric compounds.^{93,121} Trigonal planar compounds represent, however, a class of promising complexes towards the design of SMMs, since they display a low coordination number (three) on the paramagnetic metal center. Few magnetically active compounds were reported with 3d transition metals, mostly with cobalt^{94,203,204} and iron.²⁰⁴

This section focuses on two cobalt complexes, each synthesized from a different SN ligand, namely $\text{S}(\text{N}^t\text{Bu})_4^{2-}$ (**L₄**) and $\text{PPh}_2\text{CH}_2\text{S}(\text{N}^t\text{Bu})_3^-$ (**6_Li/6_H**). The obtained cobalt complexes **1_Co** and **2_Co**, respectively, were designed in the hope of observing SMM behavior. Additionally, **2_Co** was designed to probe the influence of the soft weakly donating phosphorus atom on the magnetic performances. A ligand directly coordinating through a negatively charged phosphorus atom would probably result in a loss of rigidity and lower the anisotropy. The use of the ligand **6_Li** enables to chelate the cobalt ion with two hard nitrogen donors while the third donating atom, the phosphorus, can be involved in the coordination sphere through its lone pair of electrons.

The syntheses and structural characterization of **1_Co** and **2_Co** were performed by J. Jung (see **Publication VI**).¹⁸⁶

3.2.1. Synthesis of **1-2_Co**

1_Co and **2_Co** were obtained by a metal exchange reaction. As depicted in Figure 3.2.1, the $\text{Co}(\text{HMDS})_2$ salt was reacted in *n*-pentane with two equivalents of the corresponding ligand **L₄** or **6_H** in order to obtain **1_Co** or **2_Co**, respectively. The ligands were synthesized as described in **Chapter 1**: **L₄** is obtained by sequential additions of tert-butylamine on sulfur diimine **L₁**, while **6_H** is obtained from the addition of previously distilled $\text{PPh}_2\text{CH}_2\text{Li}$ on **L₃** and subsequent protonation with $t\text{BuNH}_3\text{Cl}$. Upon reaction with the metal salt, the solutions turned purple and green, respectively, and became troubled. The reaction mixtures were left to stir for one day. The subsequent filtration of LiHMDS (**1_Co**) or removal of HHMDS under reduced pressure (**2_Co**), followed by cooling the reaction solution at -35°C , afforded the products **1_Co** and **2_Co** in 78% and 92% crystalline yield, respectively.

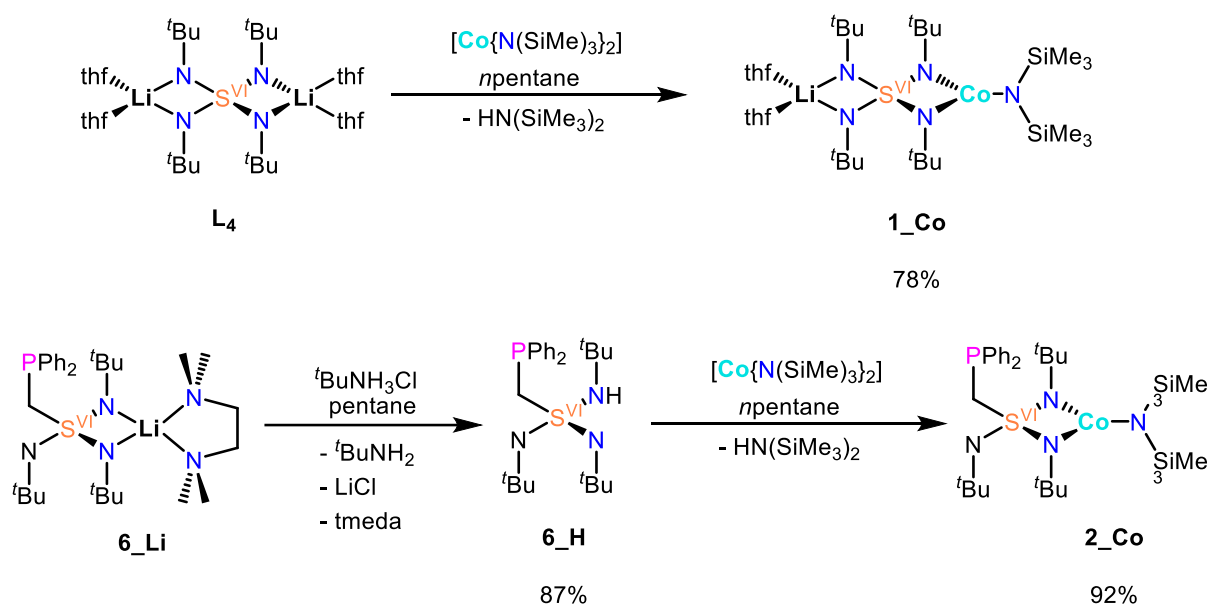


Figure 3.2.1.: Synthesis route to complexes **1_Co** and **2_Co**

3.2.2. Solid-state structures of **1_Co** and **2_Co**

The crystals of **1_Co** and **2_Co** obtained at -35°C from concentrated pentane solutions are purple and green, respectively, and suitable for SC-XRD analysis. Both compounds crystallize in a monoclinic space group, C2/c for **1_Co** and $\text{P2}_1/\text{c}$ for **2_Co**. The solid-state structures, depicted in **Figure 3.2.2**, revealed the absence of solvent molecules for both compounds and long distances between the two nearest cobalt centers (9.1 \AA for **1_Co** and 9.6 \AA for **2_Co**).

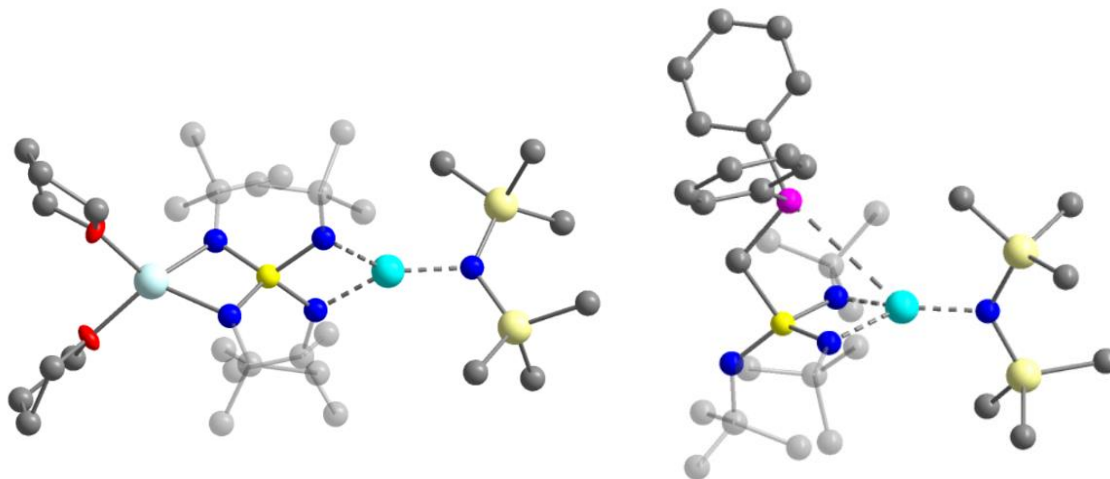


Figure 3.2.2. Crystal structures of **1_Co** (left) and **2_Co** (right). Turquoise, yellow, pink, beige, red, dark blue, grey and light blue spheres represent cobalt, sulfur, phosphorus, silicon, oxygen, nitrogen, carbon and lithium atoms, respectively. Hydrogens are omitted for clarity.

In both structures, the cobalt centers are in a similar trigonal planar environment, where one HMDS ligand coordinates through the nitrogen atom on one side, and the SN-based ligand coordinates to the cobalt atom in a N, N' chelating mode on the other side. In **1_Co**, the ligand $\text{S}(\text{N}^t\text{Bu})_4^{2-}$ remains coordinated to a lithium atom attached to two THF molecules. A special attention should be dedicated to the acute bite angles N-Co-N , which are as small as $73.42(9)^\circ$

in **1_Co** and 72.88(5) Å in **2_Co** (Table 3.2.1). These particular structural characteristics betoken interesting magnetic properties, which are presented in the following section.

Table 3.2.1. Selected bond lengths and angles for **1_Co** and **2_Co**.

Compound	1_Co	2_Co
Co-N(ligand) (Å)	1.9275(16)	1.9581(13); 1.9551(14)
Co-N(HMDS) (Å)	1.901(2)	1.8912(14)
S-N (Å)	1.6356(16); 1.5632(16) (S-N _{Li})	1.6051(13); 1.6099(13); 1.5085(14) (pendent arm)
Li-N (Å)	1.990(4)	
N-Co-N angle (°)	73.42	72.88
P...Co (Å)	–	3.532
Co ... (N, N, N) plane (°)	0	0.224

Both compounds contain a S(VI) centered ligand, which differently adapt to the metal centers. In the compound **1_Co**, the ligand S(N^tBu)₄²⁻ is twice negatively charged. Additionally, the higher positive charge on the cobalt ion than on the lithium ion pulls the imido substituents away from the sulfur, while the S-N_{Li} bond lengths shrink in order to maintain the sum of all S-N distances (6.3976 Å in **1_Co** vs 6.351 Å for the ligand **L₄**). This variation in S-N bond lengths is probably also due to the involvement of the 3d orbitals in the metal-ligand bond. This trend was also observed in the analogous zinc structure [(THF)₂Li{(N^tBu)₄S}Zn{N(SiMe₃)₂}] (sum of all S-N bond lengths is 6.395 Å).¹⁹¹ In **2_Co**, while the S-N distances involving the nitrogens coordinating the metal are about 1.6 Å on average, the pendent nitrogen atom takes advantage on the electropositive sulfur atom, resulting in a much shorter bond distance of 1.51 Å.

In **2_Co**, it seems that the phosphorus atom is oriented towards the cobalt atom. The P...Co distance is too large for a coordination bond (ranging from 2.0 to 2.5 Å), however not large enough to neglect the potential interaction between the two atoms, given the available lone pair on the phosphorus and the unsaturated coordination sphere of the cobalt. It is therefore likely that the phosphine group tends to interact at the apical position of the cobalt complex. This weak interaction could be the reason of the lifting up the cobalt atom from the (N, N, N) plane of about 0.224 Å. In comparison, in **1_Co**, which does not feature a phosphorus arm, the cobalt atom is ideally positioned in the (N, N, N) plane (Table 3.2.1). This hypothesis would corroborate the influence of the phosphorus atom in the coordination sphere of the cobalt. Furthermore, it could explain the drastic differences in the magnetic properties of the two complexes **1_Co** and **2_Co**.

3.2.3. Magnetic characterization of 1-2_Co

The temperature dependency of $\chi_M T$ is shown in Figure 3.2.3. The $\chi_M T$ values at high temperature reveal some appreciable SOC contribution to the magnetic susceptibility, since the $\chi_M T$ values for **1_Co** and **2_Co** are far higher than the spin-only value of 1.875 cm³mol⁻¹K for S=3/2 (section 4.2), especially in **2_Co**.

VTVH and DC measurements were fitted simultaneously according to the following spin Hamiltonian with ZFS and Zeeman splitting.

$$\hat{H} = \mu_B (S_x g_x B_x + S_y g_y B_y + S_z g_z B_z) + D [\hat{S}_z^2 - \frac{1}{3} S(S+1) + \frac{E}{D} (\hat{S}_x^2 - \hat{S}_y^2)] \quad (\text{Eq 1})$$

Attempts to fit the data with an isotropic g value failed. The best fits are obtained with $g_x \approx g_y$. While 1_Co possesses maximal transverse anisotropy ($D = +44 \text{ cm}^{-1}$, $E/D = 0.33$), the fitting for 2_Co reveals a large negative ZFS parameter and some rhombicity ($D = -80 \text{ cm}^{-1}$ and $E/D = 0.10$).

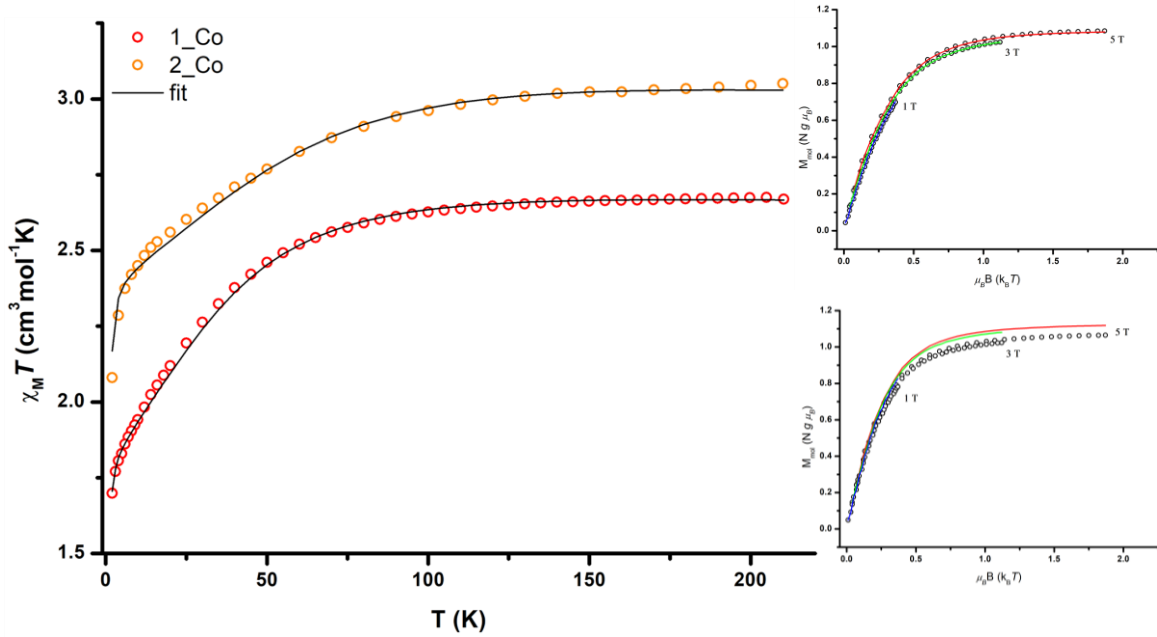


Figure 3.2.3: Temperature dependency of $\chi_M T$ for 1_Co and 2_Co from 210K to 2K (left). The black lines are fit to the experimental data points. It was simultaneously fitted with the variable temperature variable field experiments (VTVH) for 1_Co (top right) and for 2_Co (bottom right). Colored lines are fit to the curves.

Therefore, only 2_Co is expected to be promising for SMM properties. Intriguingly, both 1_Co and 2_Co showed slow relaxation of their magnetization under applied dc field. Maximal χ'' is achieved at 1000 Oe and 2000 Oe, respectively, and the ac dynamic data is shown in **Figures 3.2.4 and 3.2.5**. Some differences, however, are notable. The Cole-Cole and Arrhenius plots show that 1_Co undergoes several relaxation processes, including Raman (non-linear regime) and QTM (temperature independent regime) processes. This is mainly visible in the Arrhenius plot, as a sole Orbach process is insufficient to fit the curve. The behavior at low temperatures hints for QTM, although a dc field is applied. Additionally, the arced shape of the curve strongly suggests additional relaxation through Raman processes. On the contrary, the high temperature data points of the Arrhenius plot for 2_Co can be nicely fitted through a linear curve, while a Raman process may occur at lower temperatures (curvature appearing at 4K).

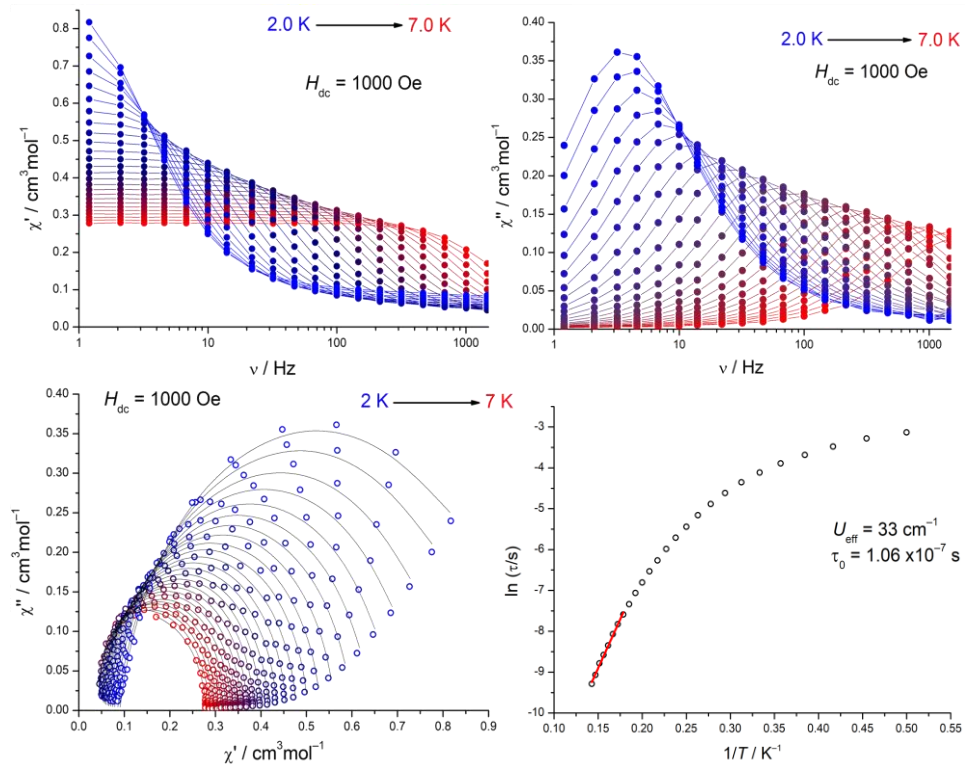


Figure 3.2.4. In and out of phase signals of the dynamic susceptibility for 1_Co (top). Corresponding Cole-Cole plot and Arrhenius plot (bottom).

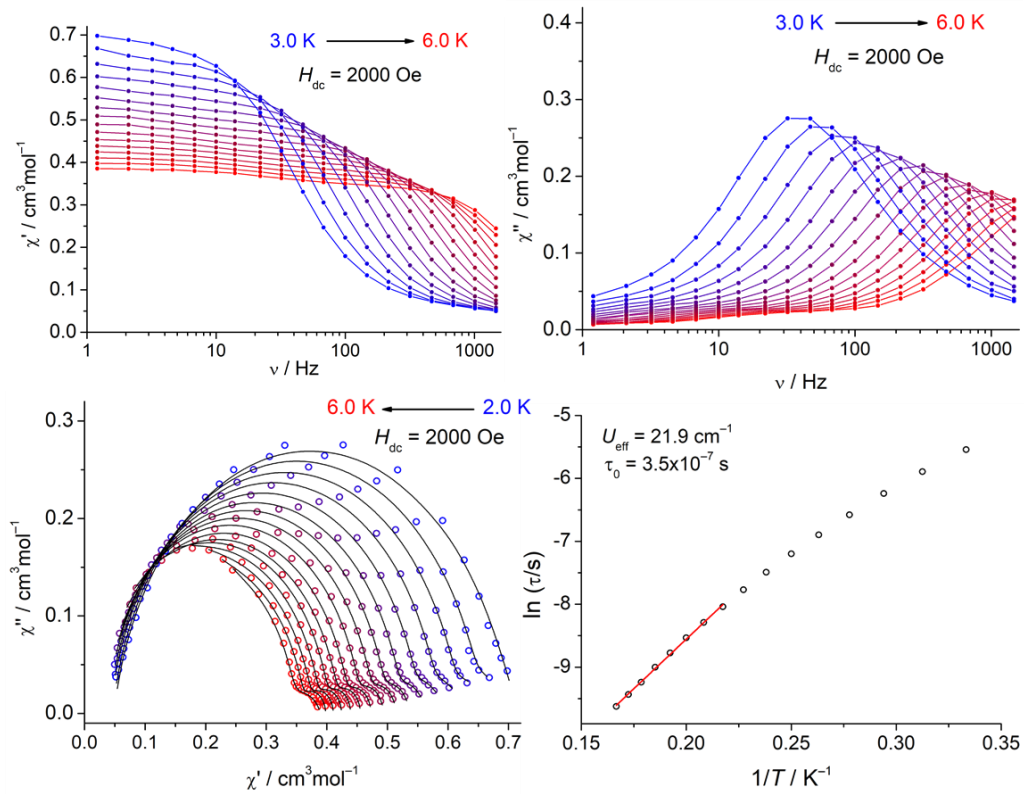


Figure 3.2.5. In and out of phase signals of the dynamic susceptibility for 2_Co (top). Corresponding Cole-Cole plot and Arrhenius plot (bottom).

For both complexes, however, the effective energy barrier is drastically lower than the expected value ($\approx 2|D|$). It is likely that the $M_S = \pm 1/2$ doublet are not reached during the relaxation process. In the case of **1_Co**, this is probably due to a bottlenecked Orbach process (shortage of phonons that transfer the spin energy to the thermal bath, resulting in a slower relaxation of the magnetization),^{155,205} which explains the presence of slow relaxation albeit the positive D value. In **2_Co**, this is due to the two-phonon Raman relaxation process.¹⁵⁰

3.2.4. Multiconfigurational calculations: probing the influence of the soft P-donor on the magnetic properties

Subsequent CASSCF/NEVPT2-AILFT calculations on **1_Co** (calculation 1) and **2_Co** (calculation 2) confirmed experimental results. Both complexes possess large E/D transverse anisotropies, for **1_Co** of $E/D = 0.31$ and for **2_Co** of $E/D = 0.13$. The D values are found +59 and -105 cm^{-1} , respectively, in very good agreement with the experimental results (Table 3.2.2).

Table 3.2.2. Selected structural and magnetic parameters for **1_Co** and **2_Co**

Compound	1_Co	2_Co
<i>Experimental data</i>		
N-Co-N angle ($^\circ$)	73.42	72.88
P...Co (\AA)	-	3.532
Co ... (N, N, N) plane (\AA)	0	0.224
χ_{MT} ($\text{cm}^3\text{mol}^{-1}\text{K}$)	2.66	3.05
D (cm^{-1})	+43	-80
E/D	0.33	0.10
g ($g_x = g_y, g_z$)	2.55, 1.92	2.44, 2.91
U_{eff} (cm^{-1})	33.0	21.9
τ_0 (s)	$1.1 \cdot 10^{-7}$	$3.5 \cdot 10^{-7}$
<i>Theoretical data</i>		
D (cm^{-1})	+59	-105
E/D (cm^{-1})	0.31	0.13
g_x, g_y, g_z	1.98, 2.55, 2.93	1.86, 2.39, 3.33
ΔE (<i>d-orbs</i>) (cm^{-1})	1 882	1 130
ΔE (<i>KD</i>) (cm^{-1})	133.4	215.7

These values are comparable to the known trigonal planar cobalt SIMs, with the negative D value for **2_Co** higher than most of the other three-coordinate cobalt SIMs previously reported. The theoretical energy difference ΔE (*KD*) between the two first Kramers' doublets (*KD*) is relatively large, but high mixing rates of the M_S states prevent a clear splitting and therefore hamper slow magnetic relaxation without applied field. The d orbital splitting predicts that the two relevant d orbitals are d_{xz} and d_{yz} , whose energy levels are separated of $\Delta E = 1\,882$ and $1\,130 \text{ cm}^{-1}$, for **1_Co** and **2_Co** respectively (Figure 3.2.6). Ideally, these orbitals should be completely degenerate to

preserve the first-order orbital angular momentum (OAM) responsible for spin-orbit coupling and enhanced magnetic anisotropy. Nevertheless, the present configuration should still prevent a complete quenching of the OAM (second-order OAM) and should give negative D values, as predicted by the d-orbital splitting (d_{z^2} lower in energy than the two d_{xz} and d_{yz} orbitals). For **1_Co**, however, the CASSCF-NEVPT2 calculation predicts a positive D value, but since the E/D parameter is close to 0.33, the sign of D cannot be determined reliably.

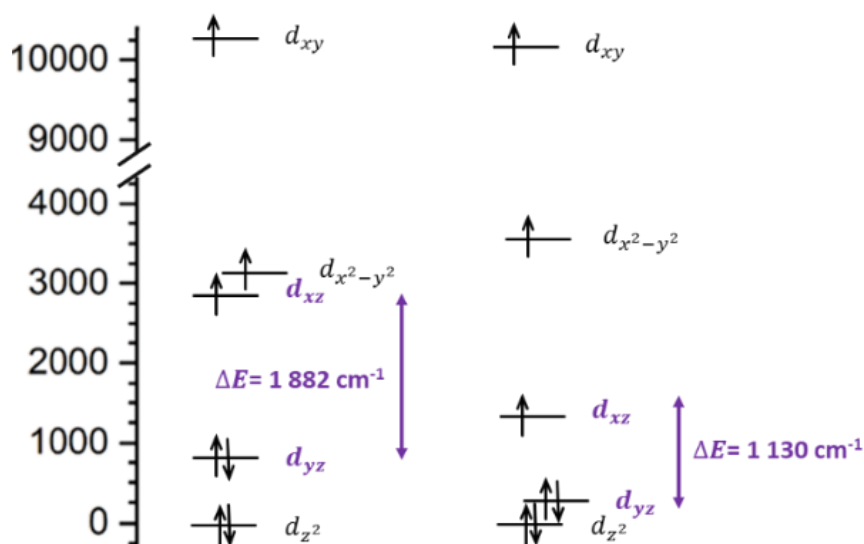


Figure 3.2.6. Energy splitting diagram for **1_Co** and **2_Co** from AILFT calculations. The difference of energy ΔE between the two important orbitals is indicated with a purple arrow.

To better assess the origin of the drastically different magnetic anisotropies in **1_Co** and **2_Co**, additional calculations were performed (modified structures presented in **Figure 3.2.7**). First, the influence of the phosphorus side arm in **2_Co** by replacing the phosphino group by a hydrogen atom (calculation 3) or by displacing it away from the metal ion (calculation 4). The calculated axial anisotropy decreases from -105 cm^{-1} to -80 cm^{-1} and the rhombic parameter slightly increases. Additionally, modifying **2_Co** to have all Co and coordinating nitrogen atoms coplanar (similar to **1_Co**, calculation 5) results in a drastic change: the ZFS parameter becomes positive, reaching a value of $+63 \text{ cm}^{-1}$ and the E/D value is about 0.10. Finally, the importance of the electronic effects in **1_Co** was assessed by considering a heavier alkali metal instead of lithium (calculation 6). The potassium analog shows exactly the same ZFS and rhombic parameters as **1_Co**. The energy gaps between the relevant orbitals and the KD1 are also in the same range. The relevant magnetic parameters summarized in **Table 3.2.3**.

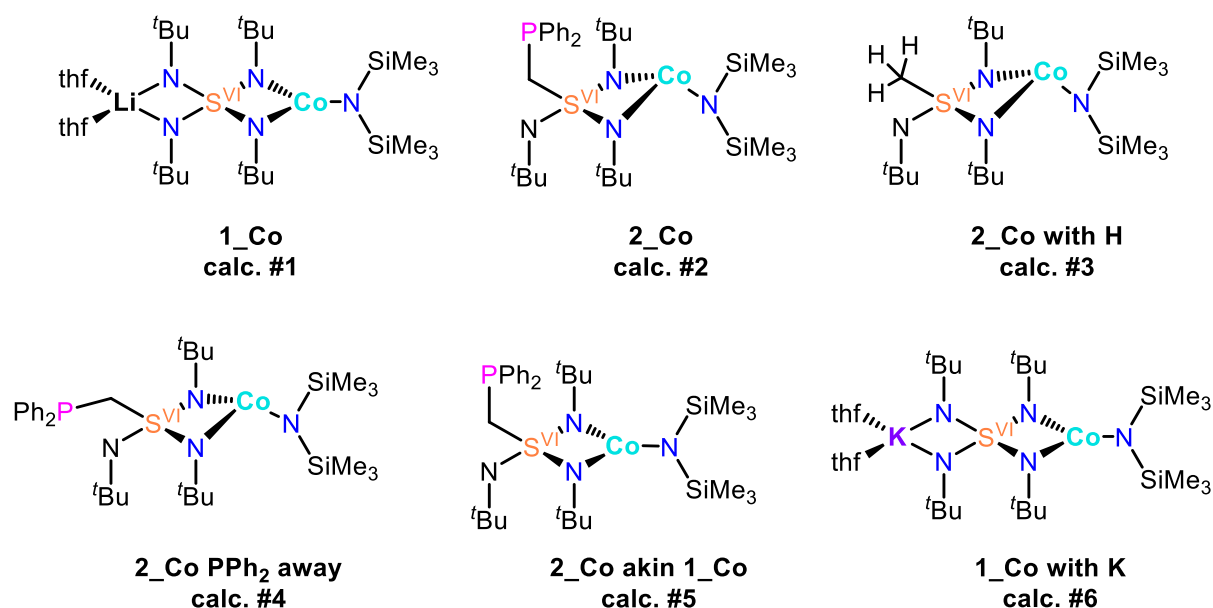


Figure 3.2.7. Modified structures for the calculations with their respective abbreviations and calculation number. The Co position in 2_Co modified structures is exaggerated for better clarity.

Table 3.2.3. Comparison of selected theoretical parameters from calculations 1-6

Calc. #	Compound	D (cm ⁻¹)	E/D	g_x, g_y, g_z values	ΔE (cm ⁻¹) (d-orbitals)	ΔE (KD) (cm ⁻¹)
1	1_Co	+59	0.31	1.98, 2.55, 2.93	1 882	133.4
2	2_Co	-105	0.13	1.86, 2.39, 3.33	1 130	215.7
3	2_Co with H	-90	0.16	1.94, 2.37, 3.18	1 095	186.0
4	2_Co PPh ₂ away	-87	0.16	1.94, 2.39, 3.16	1 083	181.1
5	2_Co akin 1_Co	+63	0.10	1.96, 2.74, 2.87	1 585	154.2
6	1_Co with K	+59	0.31	1.98, 2.55, 2.93	1 929	134.4

The main difference is visible from calculation 2 to calculation 5, when the structure is modified in such a way that the respective first coordination spheres of 1_Co and 2_Co are almost identical (the cobalt atom in 2_Co is then in the N, N, N plane). In calculation 5, the ZFS parameter becomes positive, and its value is comparable to the D value found for the unmodified 1_Co complex (calculation 1). The additional two calculations 3 and 4 assessing the influence of the phosphine group on the magnetic anisotropy parameters D and E/D hint at the importance of the presence of the soft donor atom. Calculation 5 further suggests that the weak interaction between the cobalt and the phosphorus atoms may be responsible for the geometrical differences

in **1_Co** and **2_Co** at the cobalt center: the cobalt atom is coplanar to the binding nitrogen atoms in **1_Co** and **2_Co** (calculation 5) whereas the interaction between P and Co seems to lead to the slight lift up of the cobalt atom out of the (N, N, N) plane in **2_Co**. This could further explain why the magnetic properties are so different from **1_Co** to **2_Co**.

3.2.5. Conclusion and perspectives

2_Co displays better magnetic performances as **1_Co**, especially in terms of axial magnetic anisotropy. Further calculations on modified structures suggest that the structural deviation arising from the attraction of the cobalt atom by the side arm's phosphorus atom may benefit to the magnetic properties. This could be experimentally probed by synthesizing and magnetically investigating the modified complex **2_Co** from calculation 3. Overall, the theoretical calculations as well as the experimental data strongly suggest that the phosphorus atom, albeit not binding, is precisely positioned at a sensitive spot regarding the magnetic properties.

The introduction of the $P \cdots M$ interactions might be even more advantageous with larger metal ions, such as lanthanides, which are prone to build complexes with higher coordination numbers. With 3d metals, further ligand optimization to prevent under barrier relaxation is necessary. Using a more flexible ligand than HMDS may enhance the interaction between the cobalt and the phosphorus atom. Alternatively, other soft donor atoms could be probed.

3.3. Distorted tetrahedral mononuclear cobalt single-ion magnets

It is well established that strongly distorted tetrahedral cobalt systems $[\text{CoE}_4]$ (E = donor atom) can serve as zero-field SMMs. Along with linear cobalt complexes, these systems benefit from their unusual geometries, leading to a preserved orbital angular momentum (OAM), which then results in remarkable magnetic properties. Complexes featuring acute E-Co-E angles were even found to withstand small magnetic fields before demagnetization. Several studies, including a reference study of a highly distorted tetrahedral mononuclear cobalt SMM, (**CoMSA**, $\text{MSA} = \text{N}_2(\text{CH}_3\text{SO}_2)_2\text{C}_6\text{H}_4$),¹⁹⁹ further suggest that the smaller the E-Co-E bite angle the larger the ZFS. This follows the philosophy that a stronger distortion narrowing two donor atoms to each other ultimately approaches a linear coordination environment, where the $d_{x^2-y^2}$ and d_{xy} orbitals are degenerate. Neither the limits of distortion for the bite angle nor the possible existence of an optimal angle have been mentioned. Instead, theoretical^{92,93,123,200} or experimental magneto-structural investigations focused on other structural variations,^{92,158} such as changing the donor strength and the counter ion^{132,200,206,207} or applying high-pressure.^{82,124,159,208,209} None of these studies formulate the hypothesis of an ideal bite angle. All of them are based on the common perception of compression from distorted tetrahedral D_{2d} to linear C_{∞} geometry as the best strategy towards superior SMMs. This section aims to show the existence of such an optimal E-Co-E bite angle for the specific case where E are nitrogen donor atoms. (**Figure 3.3.1**).

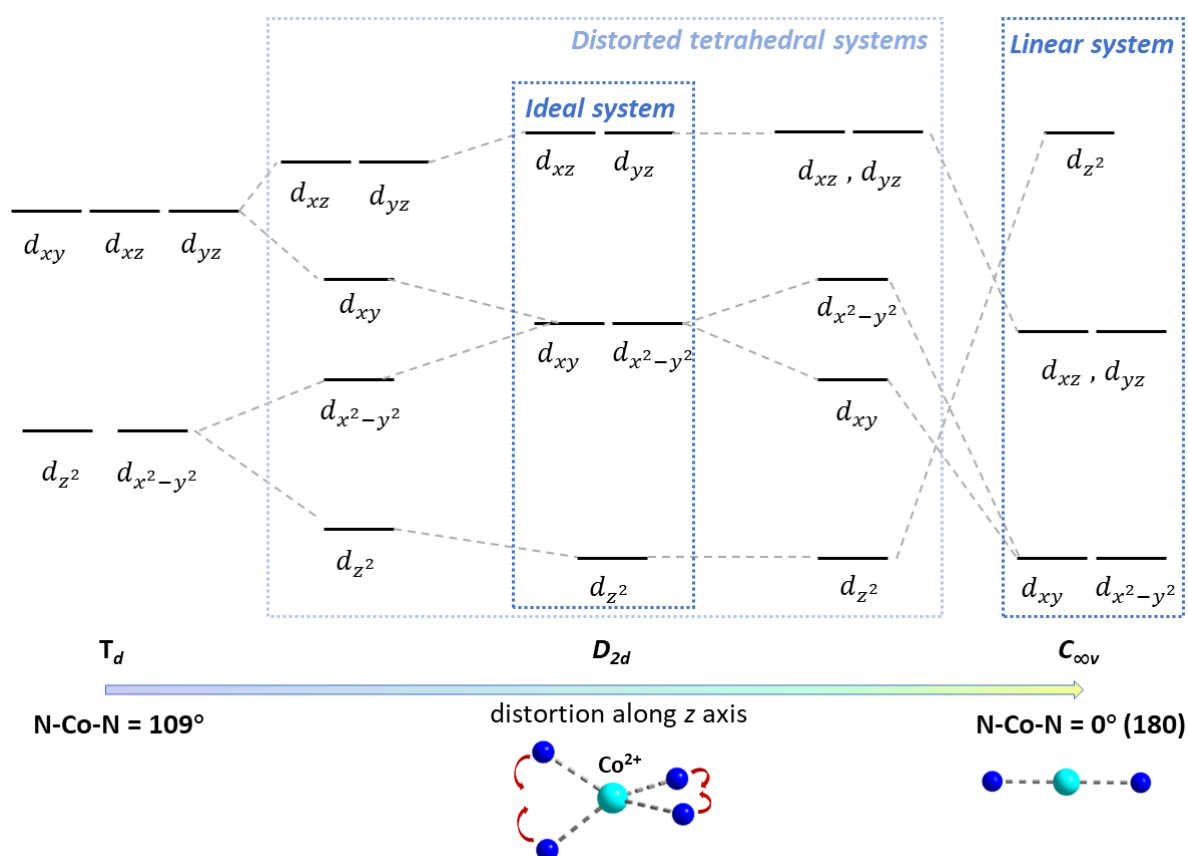


Figure 3.3.1. Evolution of the 3d orbital splitting from tetrahedral to linear geometry through distortion along the z axis. Both linear and ideally distorted tetrahedral systems give optimized magnetic properties.

This is done by combining experiments with computations on five highly distorted tetrahedral mononuclear cobalt SMMs with small variations of 2-3° of the N-Co-N bite angle. Starting from the previously reported compound $[\text{Co}\{(\text{N}^t\text{Bu})_3\text{SMe}\}_2]$, (**5_Co**),⁴² four novel complexes $[\text{Co}\{(\text{N}^t\text{Bu})_2\text{SMe}\}_2]$, (**3_Co**), $[\text{Co}\{(\text{N}^t\text{Bu})_2\text{SPh}\}_2]$, (**4_Co**), $[\text{Co}\{(\text{N}^t\text{Bu})_3\text{SPh}\}_2]$, (**6_Co**), and $[\text{Co}\{(\text{N}^t\text{Bu})_3\text{SCH}_2\text{PPh}_2\}_2]$, (**7_Co**) are herein presented (**Figures 3.3.2 and 3.3.3**). They all feature a Co^{2+} Kramers' ion (d^7 , $S = 3/2$) coordinated to two identical RSN_2 bidentate ligands. Furthermore, the complexes are rare examples of cobalt compounds possessing extremely acute N-Co-N bite angles. Hence, magnetic properties may be expected. These results were partially published in **Publication IV**.

3.3.1. Synthesis of 3-7_Co

This section focuses on the synthesis of the aforementioned cobalt complexes, while the synthesis of the various used ligands can be found in the first chapter of this work. Similar to previously reported synthesis of similar cobalt complexes, mixing CoCl_2 with two equivalents of the appropriate ligand (**1_Li**, **2_Li**, **4_Li**) in pentane in an argon glovebox afforded the desired products **3_Co**, **4_Co** and **5_Co** in acceptable yields (**Figures 3.3.2 and 3.3.3**). The addition of the ligand solution to the blue cobalt salt suspension resulted in immediate color change to dark purple or pink and complete dissolution of all materials. The reactions were left to stir overnight. After filtration through celite and removal of the volatiles, the colorful (purple, pink or red) obtained solids were recrystallized from concentrated pentane in the freezer at -35°C . The same procedure was applied to synthesize compounds **6_Co** and **7_Co** from the ligands **5_Li** and **6_Li**. They however appeared to be less soluble in pentane in comparison with the other cobalt complexes, which resulted in very poor yields. Therefore, for compound **6_Co** and **7_Co**, the reaction took place in toluene. The volatiles were subsequently removed, the obtained solids were washed with cold pentane and were then redissolved in a minimal amount of toluene. Upon filtration, the colorful pink toluene solutions were set to recrystallize by slow evaporation at room temperature and crystals suitable for X-ray analysis were obtained in good yields after a week. Strongly paramagnetic, the compounds could not be characterized by NMR spectroscopy.

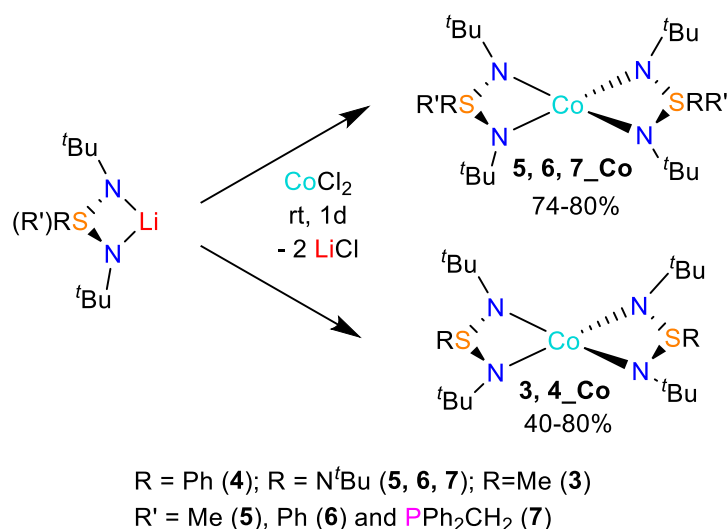


Figure 3.3.2. Synthesis route to complexes 3-7_Co

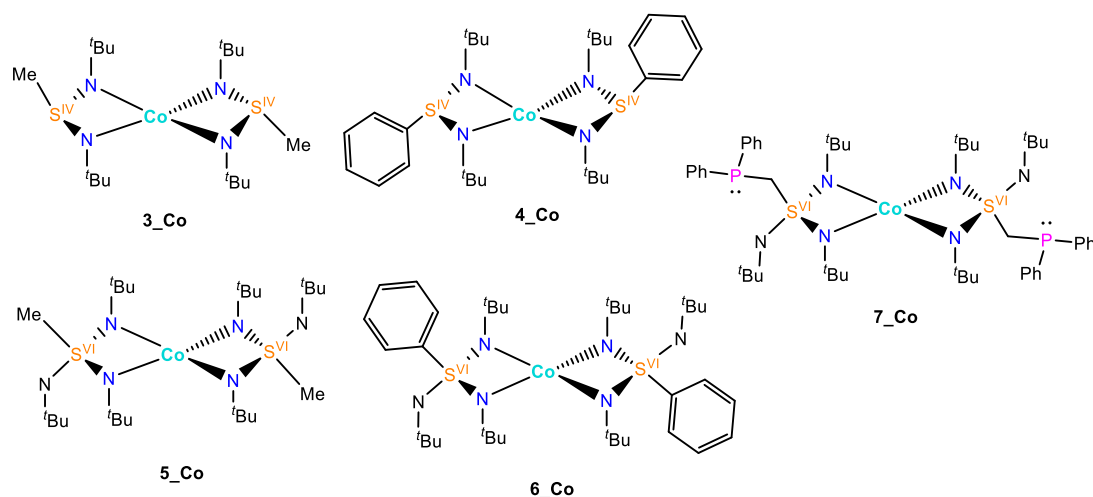


Figure 3.3.3. Scheme of the cobalt complexes 3-7_Co

The respective crystallization conditions, color, and yield of compounds 3-7_Co are summarized in **Table 3.3.1**. All complexes are colorful (see UV-vis spectra in **Figure 4.2.15.2**). Unfortunately, the last Co complex of the series with the ligand 3_Li ($[\text{Co}(\text{N}^t\text{Bu})_2\text{SCH}_2\text{PPh}_2]_2$, S(IV) analog to 7_Co) could not be isolated, although the reaction mixture turned dark purple upon mixing the two starting materials. While the complexation probably takes place, it is likely that the S(IV) species are less stable and more difficult to recrystallize, which would explain the poorer yield for 3_Co. On the contrary, the high yield observed for 4_Co may be due to better packing arrangements arising from π interactions between the phenyl groups. The S(VI) based species may be more stable due to the strong electrostatic interactions between the sulfur and the nitrogen atoms.

Table 3.3.1. Crystallization conditions, color and yield for 3-7_Co

Product	Recrystallization solvent and temperature (°C)	Color	Crystalline yield (%)
$\text{Co}(\text{MeS}(\text{N}^t\text{Bu})_2)_2$ (3_Co)	Pentane, -35°C	Purple	40
$\text{Co}(\text{PhS}(\text{N}^t\text{Bu})_2)_2$ (4_Co)	Pentane, -35°C	Pink red	78
$\text{Co}(\text{MeS}(\text{N}^t\text{Bu})_3)_2$ (5_Co)	Pentane, -35°C	Pink	80
$\text{Co}(\text{PhS}(\text{N}^t\text{Bu})_3)_2$ (6_Co)	Toluene, +25°C	Pink purple	78
$\text{Co}(\text{PPh}_2\text{CH}_2\text{S}(\text{N}^t\text{Bu})_3)_2$ (7_Co)	Toluene, +25°C	Pink	74

3.3.2. Solid-state structures of 3-7_Co

All complexes were further characterized with single crystal X-ray diffraction to determine their molecular structure. In each structure, the cobalt atom is coordinated in an *N,N'*-chelated fashion by two ligand molecules. It forms a distorted tetrahedral coordination polyhedron. The steric

hindrance created by the *tert*-butyl peripheral substituents ensure that the intermolecular Co^{2+} ions are magnetically well isolated, which corroborates the relatively long intermolecular distances in crystal packing.

Herein, **3_Co** and **4_Co** both feature a sulfur atom in the oxidation state +IV (with one free electron pair) and will therefore be first structurally analyzed together. **3_Co** crystallizes in the monoclinic space group $C2/c$ while **4_Co** crystallizes in the monoclinic space group $P2_1/c$ with one molecule in the asymmetric unit. The crystal structures are presented below.

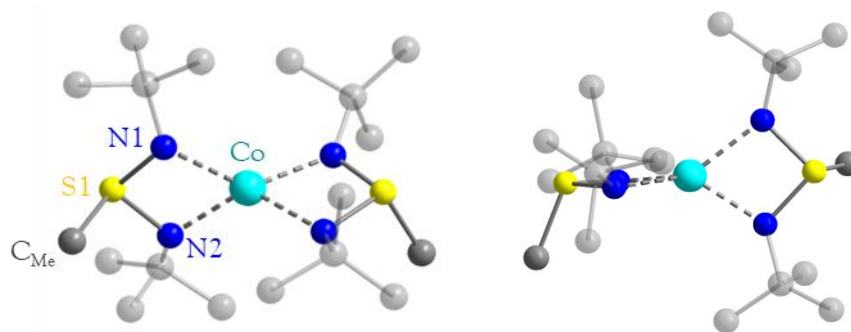


Figure 3.3.4 Crystal structure of **3_Co** in two different orientations. Turquoise, grey, dark blue and yellow represent cobalt, carbon, nitrogen and sulfur atoms, respectively. Hydrogen atoms are omitted for clarity.

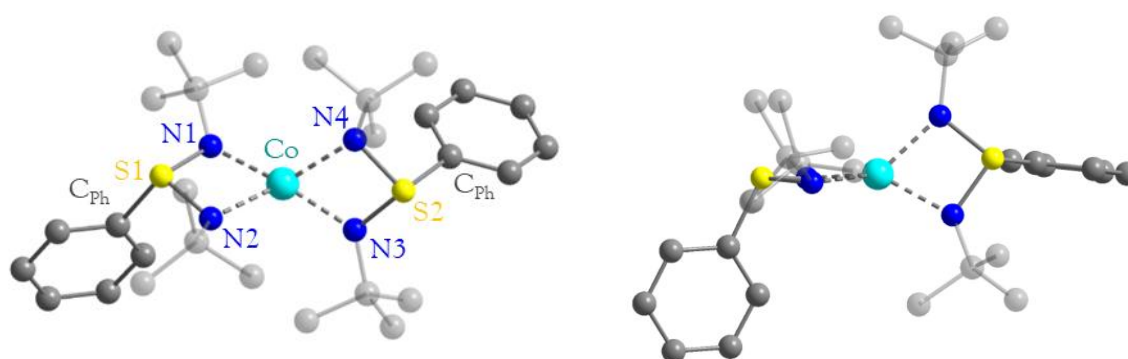


Figure 3.3.5. Crystal structure of **4_Co** in two different orientations. Turquoise, grey, dark blue and yellow represent cobalt, carbon, nitrogen and sulfur atoms, respectively. Hydrogen atoms are omitted for clarity

Selected bond lengths and angles for **3_Co** and **4_Co** are presented in the following **tables 3.3.2** and **3.3.3**. The Co-N distances are standard for high spin tetracoordinated Co^{2+} complexes, between 1.75 and 2.05 Å.²¹⁰ They are shorter of 0.01-0.02 Å in **3_Co** than in **4_Co**, similar to the variations in S-N bond lengths (max. 0.014 Å). The S- $\text{C}_{\text{Me/Ph}}$ distance also varies of 0.01 Å. This shows how the change of substituents in the second coordination sphere reflects into the first coordination sphere. Sharp $\text{C}_{\text{Ph/Me}}$ -S-N angle of about 102-105° are observable, as the free electron pair on the sulfur atom pushes the methyl group in **3_Co** and the phenyl group in **4_Co** away from the N-S-N plane. This results in a trigonal pyramidal geometry on the sulfur atoms, with the sulfur atom at 0.874 and 0.754 Å away from the (N, $\text{C}_{\text{Ph/Me}}$, N) plane, respectively. The N-Co-N bite angles are small: only 72.2° and 72.6°, respectively (vs. 109.58° in tetrahedron). Such

acute bite angles are rare in the literature, a search for tetrahedral Co[N₄] complexes with N-Co-N angles between 60° and 80° gives only 7 hits (excluding the present complexes), with only 2 other complexes with 70 < N-Co-N < 75°. The packing analysis of **3_Co** and **4_Co** shows that two nearest Co atoms are well separated from each other by a distance of 9.16 Å and 8.66 Å, respectively. These large distances should prevent intermolecular magnetic coupling, otherwise resulting in diminished SMM properties.

Table 3.3.2. Selected bond lengths and angles for **3_Co**

Bond lengths (Å)		Angles (°)	
Co-N1	1.982(9)	N1-Co-N2	72.15(10)
Co-N2	1.998(10)	N1-S1-N2	93.84(13)
Co-S1	2.7302(7)	C _{Me} -S1-Co	114.32(17)
S1-N1/2	1.623(2) - 1.625(3)	N1-Co-N2'	131.80(11)
S1-C _{Me}	1.814(4) - 1.806(13)	N2-Co-N2'	135.51(18)

Table 3.3.3. Selected bond lengths and angles for **4_Co**

Bond lengths (Å)		Angles (°)	
Co-N1/2	2.004(2) - 2.010(7)	N1-Co-N2	72.7(2)
Co-N3/4	2.006(8) - 2.004(3)	N3-Co-N4	72.6(3)
Co-S1/2	2.729(2) - 2.724(2)	N1-S1-N2	93.5(3)
S1-N1/2	1.629(6) - 1.637(3)	N3-S2-N4	93.3(3)
S1-C _{Ph}	1.805(8)	C _{Ph} -S1-Co	117.77(8)
S2-N3/4	1.635(4) - 1.630(6)	C _{Ph} -S2-Co	119.00(9)
S2-C _{Ph}	1.804(7)	N1/2-Co-N4/3	133.42(19) 138.36(8)

5_Co, **6_Co** and **7_Co** differ from the two previous compounds mainly because of the sulfur oxidation state +VI, which allows a further *tert*-butyl amine substitution. The sulfur atom is therefore now tetra-substituted while, in the case of S(IV) species, it is only tri-substituted and possesses a lone pair of electrons.

The structure of **5_Co** was previously reported by Stalke *et al.* and can be described as follows. The X-ray structure determination revealed that **5_Co** crystallizes in the monoclinic space group C2/c with half a molecule in the asymmetric unit. The twofold rotation axis running through the central Co²⁺ generates the full picture.

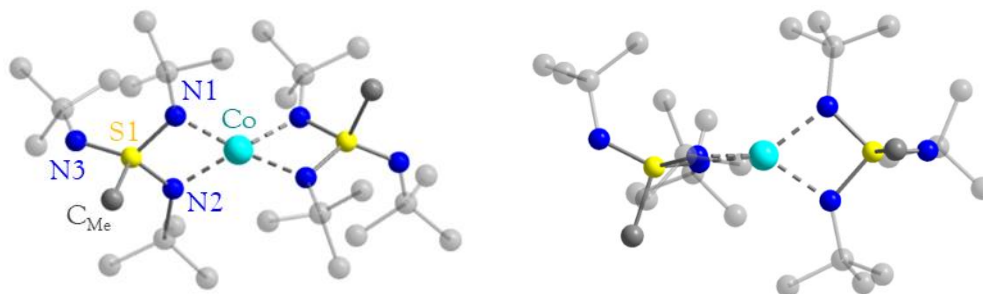


Figure 3.3.6. Crystal structure of **5_Co** in two different orientations. Turquoise, grey, dark blue and yellow represent cobalt, carbon, nitrogen and sulfur atoms, respectively. Hydrogen atoms are omitted for clarity.

In **5_Co**, the Co1-N1/2 bond lengths are again in the standard range for tetra-coordinated high-spin Co²⁺ complexes (between 1.75 and 2.05 Å, **Table 3.3.4**). The S1-N1/2 bond lengths are elongated by 0.06 Å, in comparison to the pending S1-N3 bond. This is probably due to reinforced electrostatic interactions between the sulfur atom in the sixth oxidation state S^{VI} and the negatively charged N3 atom. The N-Co-N bite angle is acute here as well, of 71.46° (vs. 109.58° in tetrahedron). The electrostatic and steric influences of the methyl group substituent on the sulfur seem therefore similar to those of the alkyl groups in the structures **3-7_Co**. The C_{Me}-S1-Co angle is slightly smaller, which may be due to the higher steric hindrance between the 'Bu groups and the Me *vs* Ph group. The S1-C_{Me} distance is nevertheless somewhat larger than S1-C_{Ph} in **6_Co** in agreement with the electron-donating nature of the methyl group and the electron-attracting properties of the phenyl group.

Table 3.3.4. Selected bond lengths and angles for **5_Co**

Bond lengths (Å)		Angles (°)	
Co-N1	1.9873(11)	N1-Co-N2	71.46(4)
Co-N2	1.9939(10)	N1-S1-N2	92.92(5)
Co-S1	2.7159(7)	C _{Me} -S1-Co	113.67(4)
S1-N1/2	1.5989(10) - 1.6084(11)	N1-Co-N2'	130.02(4)
S1-N3	1.5267(10)	N2-Co-N2'	130.25(6)
S1-C _{Me}	1.7867(13)		

Akin to **5_Co**, **6_Co** crystallizes in the monoclinic space group C2/c with half a molecule in the asymmetric unit. The full structure representation is generated by symmetry thanks to the twofold rotation axis running through the central Co²⁺.

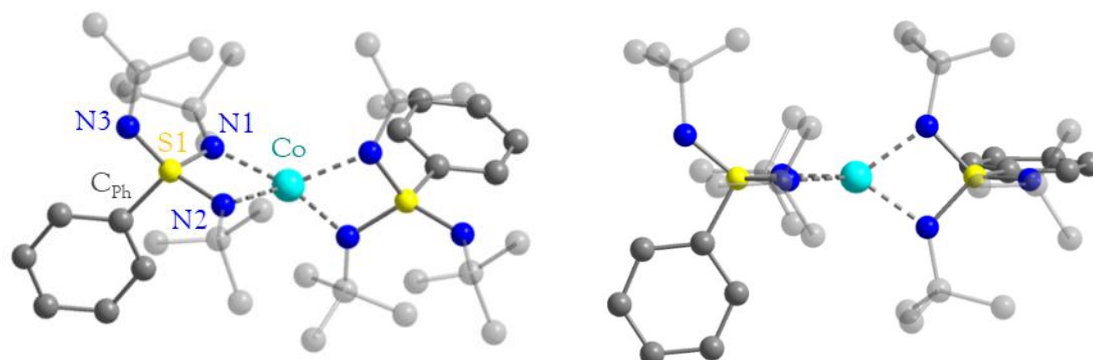


Figure 3.3.7. Crystal structure of **6_Co** in two different orientations. Turquoise, grey, dark blue and yellow represent cobalt, carbon, nitrogen and sulfur atoms, respectively. Hydrogen atoms are omitted for clarity.

The Co-N bond distances are in the same acceptable range of 1.75-2.05 Å for Co²⁺ complexes. A remarkably acute bite angle of 70.8° is observed for N1-Co-N2 (vs. 109.58° in an ideal tetrahedron). Since the phenyl and the free *tert*-butyl amine positions are highly disordered (55% for the main position), precise evaluation of the bond distances and angles involved is difficult. Nevertheless, it seems that the third *tert*-butyl amine group on the sulfur atom, now in the oxidation state +VI, almost perfectly substitutes the free electron pair of the sulfur atom in **4_Co**, in terms of structural geometry. This is observable in the similar angles C_{Ph}-S1-Co : 117.7°-119.0° for **4_Co** and 118.9°-119.3° for **5_Co**.

Table 3.3.5. Selected bond lengths and angles for **6_Co**

Bond lengths (Å)		Angles (°)	
Co-N1	2.001(3)	N1-Co-N2	70.84(11)
Co-N2	2.007(3)	N1-S1-N2	93.27(14)
Co-S1	2.7297(8)	C _{Ph} -S1-Co	118.9(3) - 119.3(2)
S1-N1/2	1.597(3) - 1.598(3)	N1-Co-N2'	130.95(11)
S1-N3	1.571(6) - 1.563(8)	N2-Co-N2'	132.45(17)
S1-C _{Ph}	1.688(10) - 1.735(8)		

7_Co possesses an additional pending phosphine arm, which classifies it as a so-called scorpionate SN ligand, a sub-type of Trofimenko's ligands. These ligands can demonstrate higher chelation thanks to the additional soft donor phosphorus atom. The X-ray analysis of **7_Co**, however, revealed that it does not act in this manner in this particular configuration (**Figure 3.3.8**). **7_Co** crystallizes in the monoclinic space group C2 with half a molecule in the asymmetric unit. The entire structure can be generated by symmetry due to the two-fold rotation axis running through the central cobalt atom. The bite angle for N1-Co-N2 is comparable to these of the **3-6_Co** parent structures, with 71.43° (vs. 109.58° in tetrahedron). The phosphorus atom, instead of showing an orientation towards the cobalt center, is about 6.4 Å away from the metal and points in the opposite direction. The C_{PPh₂}-S1-Co angle of 115° is in the middle range of the C_{alkyl}-S1-Co angles (113-119°), indicative of the adaptability of the ligand to the steric hindrance of the phosphine group. Since the phosphorus atom becomes a worse electron-donor due to the two phenyl groups, the S1-C_{PPh₂} bond is slightly elongated to 1.804(5) Å, whereas the distances S1-C_{Me} and S1-C_{Ph} are shorter in the complexes **5_Co** and **6_Co**, due to the electron-donating nature of the substituents. The S1-C_{PPh₂} distance is slightly shorter to those of the asymmetric lithium complex **6_Li** (1.8182(16) Å) and the asymmetric cobalt complex **2_Co** (1.8101(15) Å).

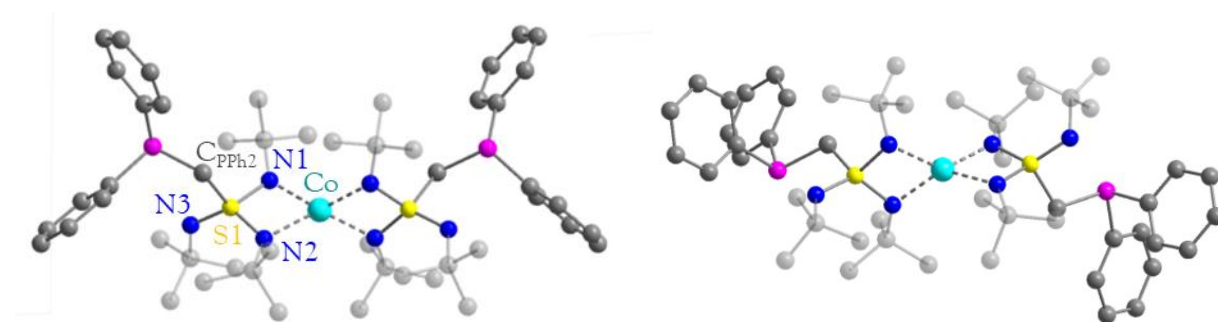


Figure 3.3.8. Crystal structure of **7_Co** in two different orientations. Turquoise, grey, dark blue pink and yellow represent cobalt, carbon, nitrogen, phosphorus, and sulfur atoms, respectively. Hydrogen atoms are omitted for clarity.

Table 3.3.6. Selected bond lengths and angles for **7_Co**

Bond lengths (Å)		Angles (°)	
Co-N1	1.986(4)	N1-Co-N2	71.43(16)
Co-N2	2.002(4)	N1-S1-N2	92.92(5)
Co-S1	2.7176(11)	C _{PPh₂} -S1-Co	115.33(17)
S1-N1/2	1.610(4) - 1.596(4)	N1-Co-N2'	133.35(16)
S1-N3	1.523(4)	N2-Co-N2'	130.0(3)
S1-C _{PPh₂}	1.804(5)		

The metrical variations found in complexes **3-7_Co** could fully be explained in agreement with the sterical and electronical influences of the different substituents. In all five structures, the cobalt atom was found tetra-coordinated in a highly distorted tetrahedral manner. The N1-Co-N2 angles are remarkably acute, regardless of the substitution variations (**Table 3.3.7**). Because the bond distances can be rationalized in this way, it is surprising to notice that the further oxidation of sulfur produces slightly more acute chelating angles, since **3_Co** and **4_Co** display larger N1-Co-N2 angles than **5_Co**, **6_Co**, and **7_Co**.

Table 3.3.7. Comparison of selected characteristics in **3-7_Co**. The complexes are ranged in order of decreasing bite angle N-Co-N.

Compound	Bite Angle N1-Co-N2 (°)	S1-C _R ' (Å)	S(oxidation state), alkyl substituent
4_Co	72.7(2)	1.805(8)	S(IV), Ph
3_Co	72.15(10)	1.814(4) - 1.806(13)	S(IV), Me
3_Co	71.46(4)	1.7867(13)	S(VI), Me
7_Co	71.43(16)	1.804(5)	S(VI), CH ₂ PPh ₂
6_Co	70.84(11)	1.688(10) - 1.735(8)	S(VI), Ph

3.3.3. Magnetic characterization of **3-7_Co**

Through the use of Co²⁺ (*d*⁷) as paramagnetic center, we expect the obtained complexes to show interesting magnetic properties. Additionally, the complex **5_Co** was already magnetically characterized before,⁴² and showed SMM behavior. Thus, comparable magnetic properties are expected for all cobalt complexes of the present series. Therefore, the complexes were magnetically characterized on a SQUID magnetometer, while additional measurements were performed on **5_Co** for full comparison with the other complexes of this series. The temperature-dependence of the product $\chi_M T$ gives information regarding the paramagnetic character of the compound, the number of spins present in the molecule as well as the importance of the contribution of the orbital angular momentum into the magnetic behavior. **Figure 3.3.9** shows the static magnetic susceptibility temperature product $\chi_M T$ as a function of temperature. At high temperature, the values are constant, according to Curie's law for paramagnetic compounds. Notably, the 200 K-values are much larger than the spin-only value of 1.875 cm³mol⁻¹K. If the spin-orbit coupling (SOC) is taken into account for an ideal, strongly coupled *L*=2 and *S*=3/2 system, the product $\chi_M T$ can be as high as 4.02 cm³mol⁻¹K (*J* = 7/2). The complexes **3-7_Co** clearly display $\chi_M T$ values closer to those of ideal, strongly coupled systems. This indicates a significantly large contribution of the orbital angular momentum *L* to the magnetic susceptibility. More generally, it shows that *S* only is not a good quantum number to describe the magnetic properties in these compounds and that the quantum number *J* would be more suitable, especially for **3_Co**, where the $\chi_M T$ value almost reaches the ideal 4.02 cm³mol⁻¹K value for a fully *L-S* coupled system.

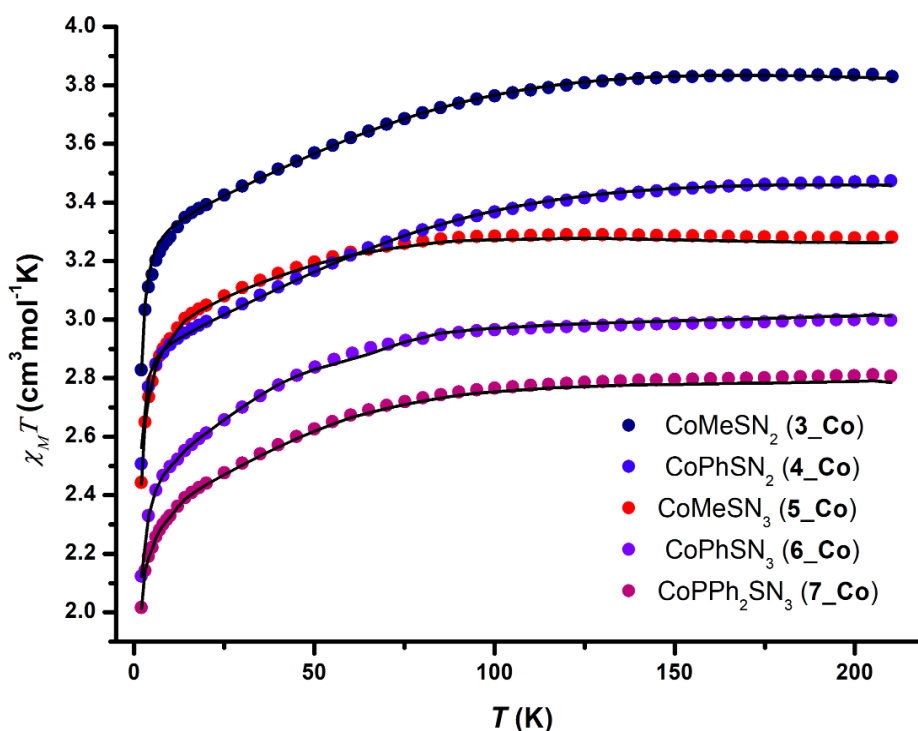


Figure 3.3.9. Temperature dependency of $\chi_M T$ for 3-7_Co. Black lines indicate fit to the experimental data (colorful dots)

The $\chi_M T$ values are constant from 200 K to about 100 K, at the point where they start decreasing. The observed decrease of $\chi_M T$ cannot be attributed to intermolecular interactions because the distance between two nearest Co is far too large in all complexes: at least 8.65 Å. This decrease at low temperature starts around 60 K, which is still a high temperature for the typical sign of magnetic saturation and limitation of Curie's law.

Noteworthy, the complexes 3_Co and 4_Co of the S(IV) series possess higher $\chi_M T$ values at high temperature. This hints that they may perform better in terms of overall magnetic properties than the complexes 5_Co, 6_Co and 7_Co of the S(VI) series. The fit of the curves was performed with the program *Jul2s*. The first attempts to simulate the data with an isotropic g tensor failed. Therefore, anisotropic g values were considered, when possible, with $g_x = g_y$, according to the spin Hamiltonian with ZFS and Zeeman Splitting:

$$\hat{H} = \mu_B (S_x g_x B_x + S_y g_y B_y + S_z g_z B_z) + D \left[\hat{S}_z^2 - \frac{1}{3} S(S+1) + \frac{E}{D} (\hat{S}_x^2 - \hat{S}_y^2) \right] \quad (\text{Eq. 3.1})$$

(See **Annex 1**, Eq. 4.7 for details). The best fitting parameters are given in the **Table 3.3.8**.

Fitting with $g_x = g_y$ was possible for all complexes and explains why no rhombicity is observed ($E/D = 0$). All other parameters were set free, resulting in the rise of intermolecular coupling in all complexes except 4_Co. While 6_Co and 7_Co may possess some weak intermolecular interactions induced by the phenyl substituents (possible π stacking), the origin of intermolecular coupling is still unclear in 3_Co and 5_Co (substituents are methyl groups). Nevertheless, all compounds have negative ZFS parameter values ($-D$), indicating that the $M_S = \pm 3/2$ are the lowest in energy and that SMM behavior may be observable.

Table 3.3.8. Fitting parameters for the modelling of the DC susceptibility of complexes **3-7_Co**

Fitting parameters	3_Co	4_Co	5_Co	6_Co	7_Co
$D(\text{cm}^{-1})$	-120	-114	-81	-76	-80
E/D	0	0	0	0	0
g_x	2.30	2.27	2.14	2.16	2.06
g_y	2.30	2.27	2.14	2.16	2.06
g_z	3.42	3.20	2.70	3.15	2.85
TIP (emu)	0	0	0	0	0
PI (%)	0	0	0.5	0	0
$2zj$ (inter. coupling)	-0.20	-0.02	-0.44	-0.48	-0.51

As expected from their high temperature χMT values, the compounds **3_Co** and **4_Co** clearly possess the largest ZFS parameter values, which is highly promising for their magnetic performances. The best performing distorted tetrahedral cobalt SMMs to date have ZFS values of -115 cm^{-1} (CoN₄ core, complex **CoMSA** (MSA = N₂(CH₃SO₂)₂C₆H₄)) and -165 cm^{-1} (CoS₄ core).^{117,199}

Dynamic susceptibility measurements were further conducted in the search of indication of slow relaxation of the magnetization in complexes **3-7_Co**. Under a small 3Oe ac field and in the absence of dc external field, all complexes exhibit pure SMM behavior. The out-of-phase signals of the ac susceptibility vs the ac frequency show the characteristic maxima at low temperatures and the concomitant decrease and shift at higher temperatures. ac susceptibility measurements for **3_Co** are shown in **Figure 3.3.10**. The in- and out-of-phase signals of the ac dynamic susceptibility reveal that the complex **3_Co** slowly relaxes its magnetization under zero field. Even at low temperatures, the maxima of the curves start shifting towards higher frequencies. This is an indication for very little (or non-existent), temperature independent QTM effects. Peaks are detectable up to 17K, upon which they shift outside of the range of the magnetometer. The Cole-Cole plot was fitted with one relaxation process. The Arrhenius plot, however, shows that at least two relaxation processes, the Orbach (linear area) and the Raman (curved area) processes. From the Orbach process fit, the energy barrier is found to be 25.9 cm^{-1} with an attempt time of $1.03 \cdot 10^{-5} \text{ s}$. The full fit yields a higher energy barrier of 270 cm^{-1} , as expected from the dc data. The application of an external field of 1500 Oe (optimal field maximizing the ac susceptibility) suppresses most of the QTM and slow magnetic relaxation of the magnetization is measurable up to 20K. The Cole-Cole plot can be fitted almost perfectly with one process. The Arrhenius plot is fitted with direct, Orbach and Raman processes, without QTM since none is detectable whether in the ac plots nor in the Cole-Cole plot. Additionally, the Arrhenius plot does not show a temperature independent area. An Orbach-only fit gives a U_{eff} slightly superior to the zero-field value, reaching 35.2 cm^{-1} with an attempt time of $7.29 \cdot 10^{-6} \text{ s}$.

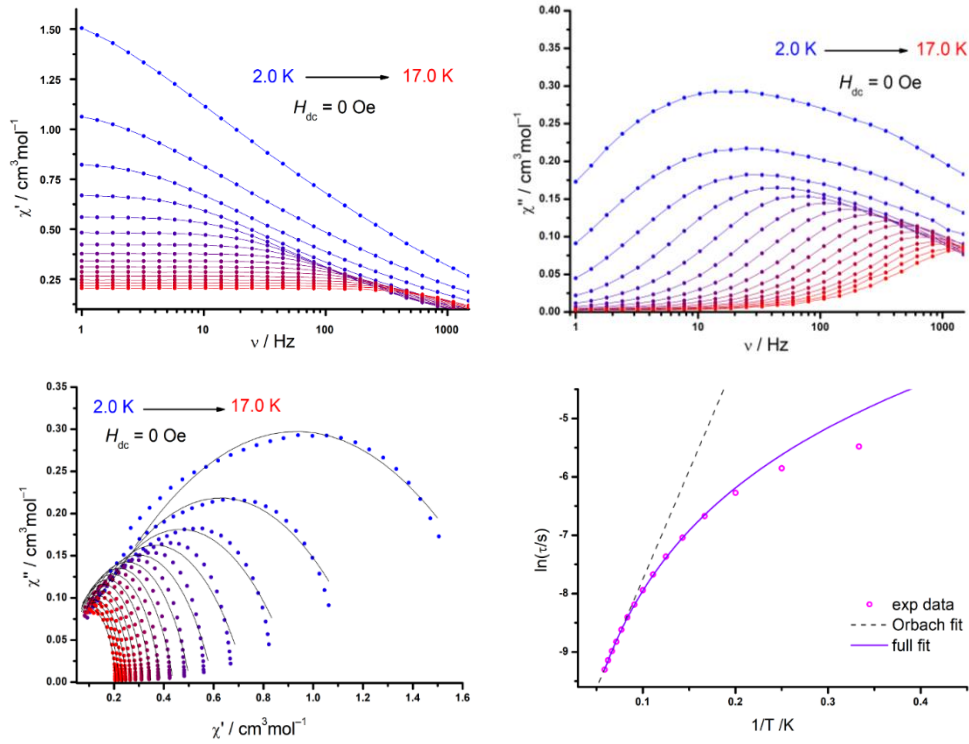


Figure 3.3.10. ac relaxation data for 3_Co under zero field. Real and imaginary parts of the ac susceptibility (top, lines are guide for the eyes), Cole-Cole plot and Arrhenius plot (bottom, lines are fit to the curves). The full fit is done according to Eq 2.1.

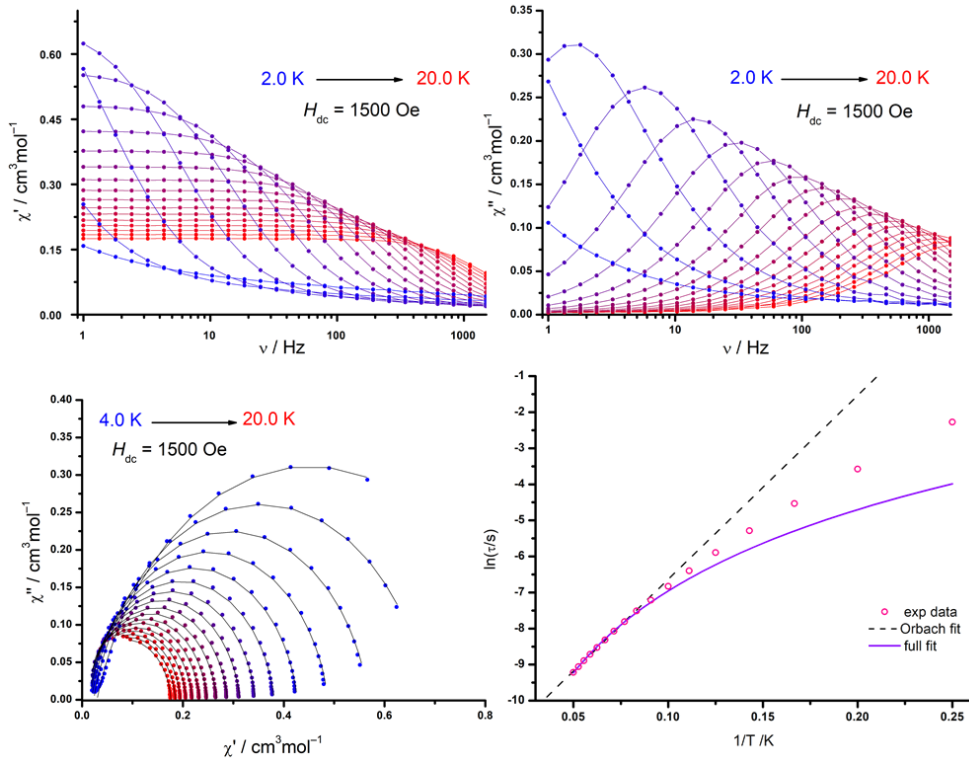


Figure 3.3.11. ac relaxation data for 3_Co under an applied field of $H_{dc} = 1500$ Oe. Real and imaginary parts of the ac susceptibility (top, lines are guide for the eyes), Cole-Cole plot and Arrhenius plot (bottom, lines are fit to the curves). The full fit is done according to Eq 2.1.

The full fit was performed according to Eq 2.1, with a fixed U value of 270 cm^{-1} , and the best parameters for the Raman process of $n \approx 3$ and $C = 0.07$, close to literature values reported for such systems. 3_Co shows a butterfly-shaped hysteresis at low temperatures, from 1.8K to 2.3K, even at very slow sweep rates (200Oe/s), as depicted at the top in **Figure 3.3.12**. A quicker sweep rate at 1.8K shows a greater opening of the wings of the hysteresis but it still remains closed at 0 Oe (**Figure 3.3.12**, bottom).

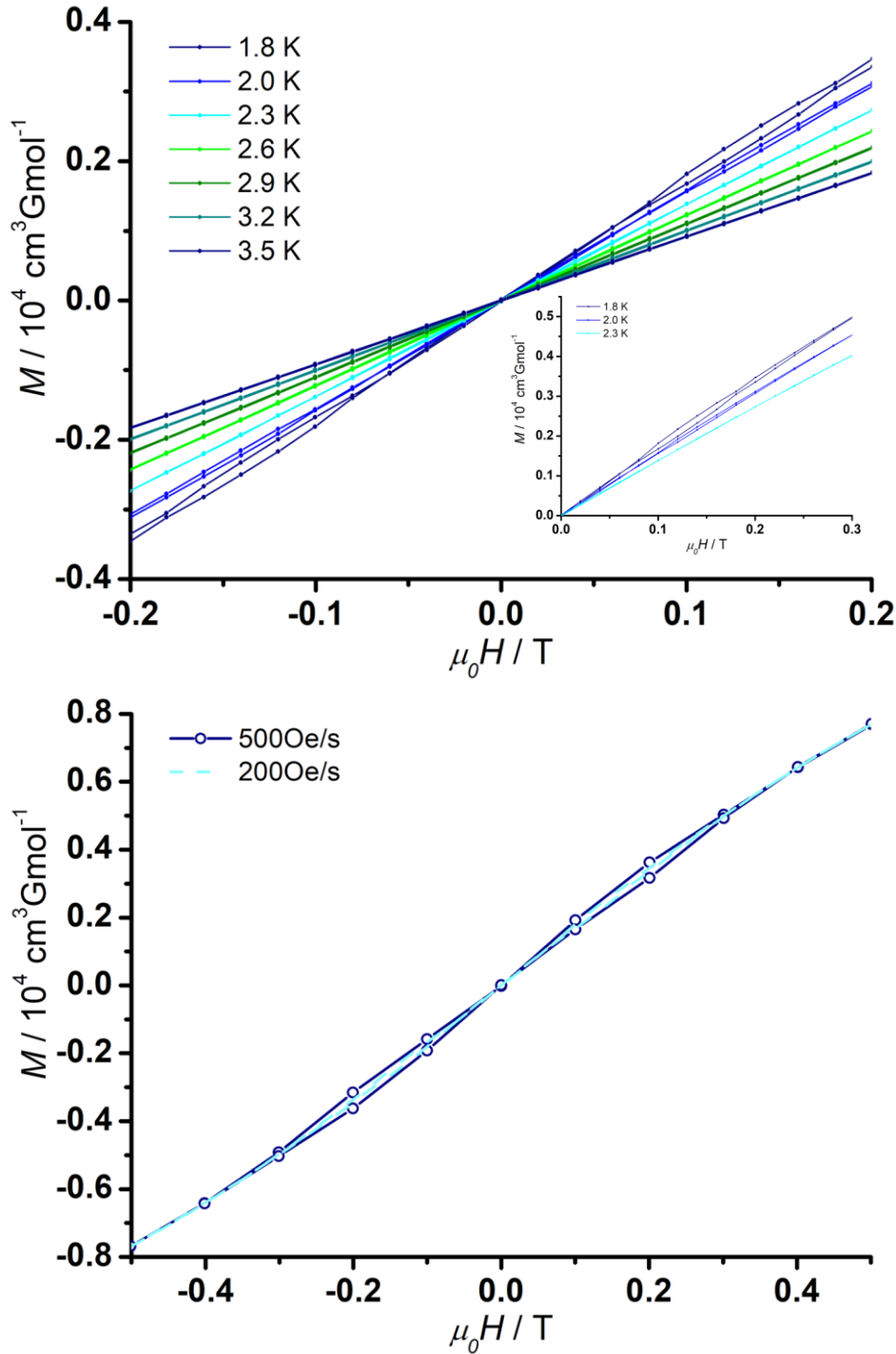


Figure 3.3.12 (Top) Hysteresis at 200Oe/s from 1.8K to 3.5K for 3_Co . The butterfly hysteresis closes at 2.3K. Inset: zoom-in of the (+, +) quadrant of the hysteresis curve. (Bottom) Hysteresis at 1.8K for 200Oe/s and 500Oe/s sweep rates for 3_Co .

4_Co exhibit even better magnetic properties, as well in dynamic susceptibility data as in the dc data. The ac susceptibility data is shown in **Figure 3.3.13**, under zero field and under the optimal field of 1500 Oe.

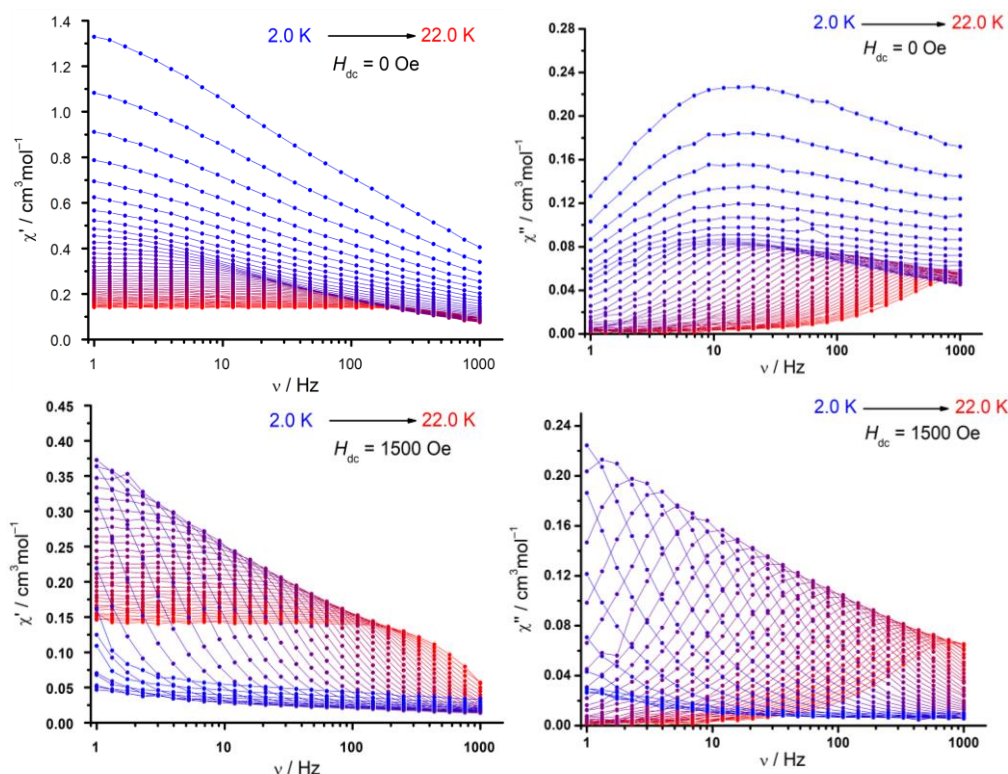


Figure 3.3.13. ac susceptibility data for 4_Co from 2K to 22K under zero field (top) and at 1500 Oe (bottom). Lines are guide for the eyes.

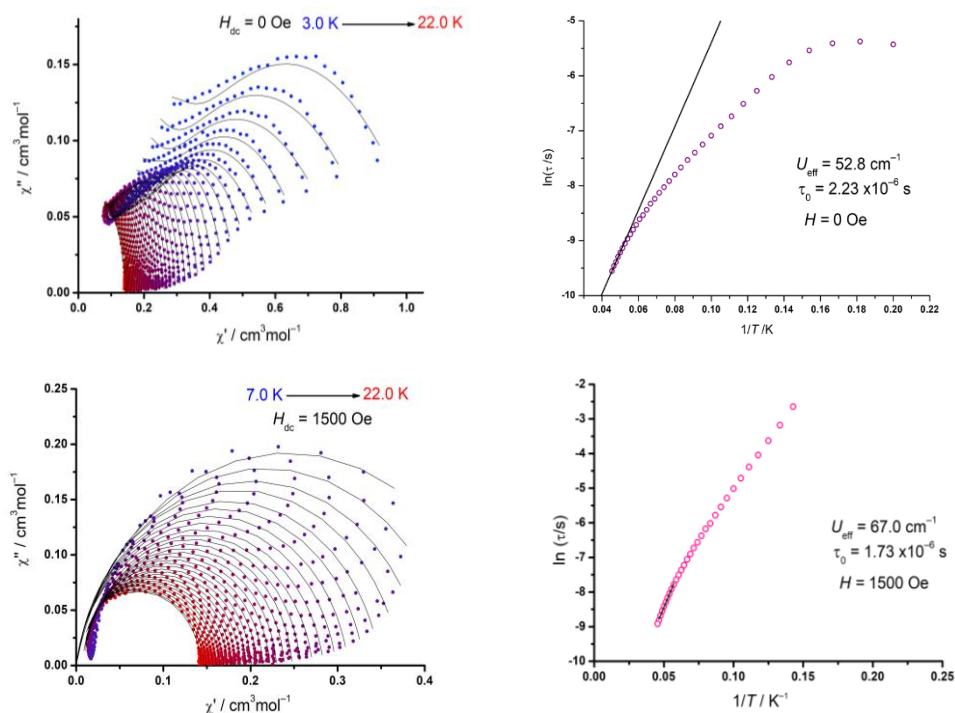


Figure 3.3.14. Cole-Cole and Arrhenius plots for 4_Co under zero field (top) and under 1500 Oe (bottom). The Orbach-only fit is shown in black.

Maxima of the peaks indicative of slow magnetic relaxation are observable up to 22K and the application of an external field enables to completely suppress QTM, as the observable relaxation process is clearly temperature-dependent (**Figure 3.3.13**). The analysis of the Cole-Cole plot under zero field confirms this hypothesis. It shows that several relaxation processes are taking place. Upon application of the external dc field, however, a single slow relaxation process is visible and gives a good fit. The shape of the Arrhenius curve further corroborates the existence of multiple processes, including QTM for data at zero field, and the suppression of QTM with the application of the dc field. The pure Orbach fit gave the following parameters: $U_{\text{eff}} = 52.8 \text{ cm}^{-1}$; $\tau_0 = 2.23 \cdot 10^{-6} \text{ s}$ under zero applied field and $U_{\text{eff}} = 67.0 \text{ cm}^{-1}$; $\tau_0 = 1.73 \cdot 10^{-6} \text{ s}$ with an applied dc field of 1500 Oe. A full fit of the zero field ac data according to Eq 2.1 improves the energy barrier up to 283 cm^{-1} , in good agreement with the dc data.

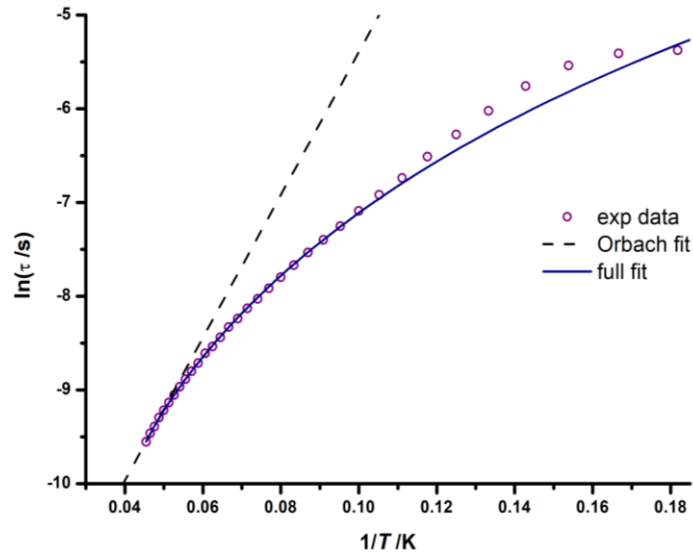


Figure 3.3.15. Arrhenius plot for 4_{Co} . Orbach-only and full fit are represented as dashed black line and solid purple line, respectively. Full fit best parameters: $\tau_0 = 2.67 \cdot 10^{-9} \text{ s}$; $C = 1.22$; $n = 3.0$; no QTM (fixed).

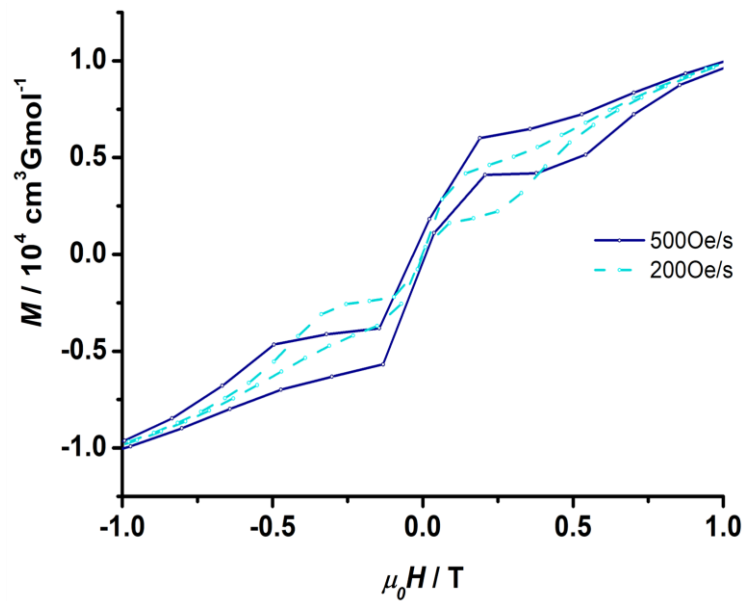


Figure 3.3.16. Magnetic hysteresis for 4_{Co} at the sweep rates of 500 Oe and 200 Oe/s at 1.8K.

Additionally, **4_Co** shows a magnetic hysteresis whose shape is strongly dependent on the field sweep rate. At 1.8K, a rapid sweep rate of 500 Oe/s even results in hysteresis opening at 0 Oe, with a coercivity of 0.02T (200 Oe). (**Figure 3.3.16**). The wings of the hysteresis close at 3.5K.

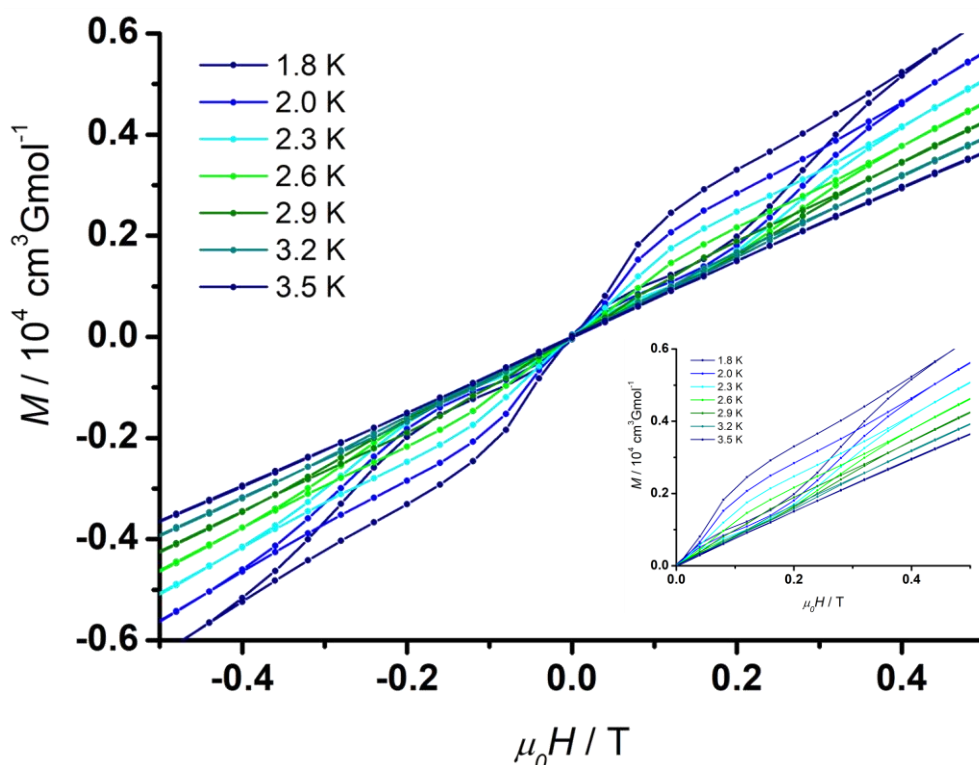


Figure 3.3.17. Magnetic hysteresis for **4_Co** from 1.8K to 3.5K at 200Oe/s. Inset: zoom-in of the (+, +) quadrant of the hysteresis curve.

The shape and field-dependency of the hysteresis curve are very similar to these of the complex **CoMSA** ($\text{MSA} = \text{N}_2(\text{CH}_3\text{SO}_2)_2\text{C}_6\text{H}_4$), which is one of the distorted tetrahedral cobalt SMM with the best magnetic properties to date.¹⁹⁹ Further comparison will be performed with multi-configurational calculations in the following section.

Analysis of the magnetic data for **5_Co** has already been reported elsewhere.⁴² Additional results are briefly described below. Zero-field ac data was analyzed and shows slow relaxation of the magnetization up to 15K. The shapes of the out-of-phase signal of the dynamic susceptibility, as well as the curve of the Arrhenius plot suggest the presence of multiple relaxation processes (**Figure 3.3.18**). The Cole-Cole plot was fitted with one slow relaxation process, but QTM and Raman processes are also identifiable. The Arrhenius plot clearly shows a linear regime (Orbach), a temperature-independent regime (QTM) and a T^n dependent regime (Raman). The pure Orbach fit gives $U_{\text{eff}} = 90.4 \text{ cm}^{-1}$; $\tau_0 = 2.13 \cdot 10^{-9} \text{ s}$, while the following best parameters are found for the full fit according to Eq 2.1: $\tau_0 = 6.10 \cdot 10^{-10} \text{ s}$; $C = 1.65 \cdot 10^{-5}$; $n = 7.94$; $\tau_{\text{QTM}} = 8.13 \cdot 10^{-4} \text{ s}$. In comparison with **3_Co** and **4_Co**, the Raman constant is very small, and n is much higher, which indicates the presence of an additional pure Raman process (expected value of 7, or Kramers Raman process, expected value of 9). Application of an external field of 1500 Oe gives an n value of 9.6, closer to the expected value of 9 for a Kramers Raman process. Additionally, the energy barrier is lower than without external field, 75 cm^{-1} , with a characteristic time of $\tau_0 = 2.64 \cdot 10^{-8} \text{ s}$.

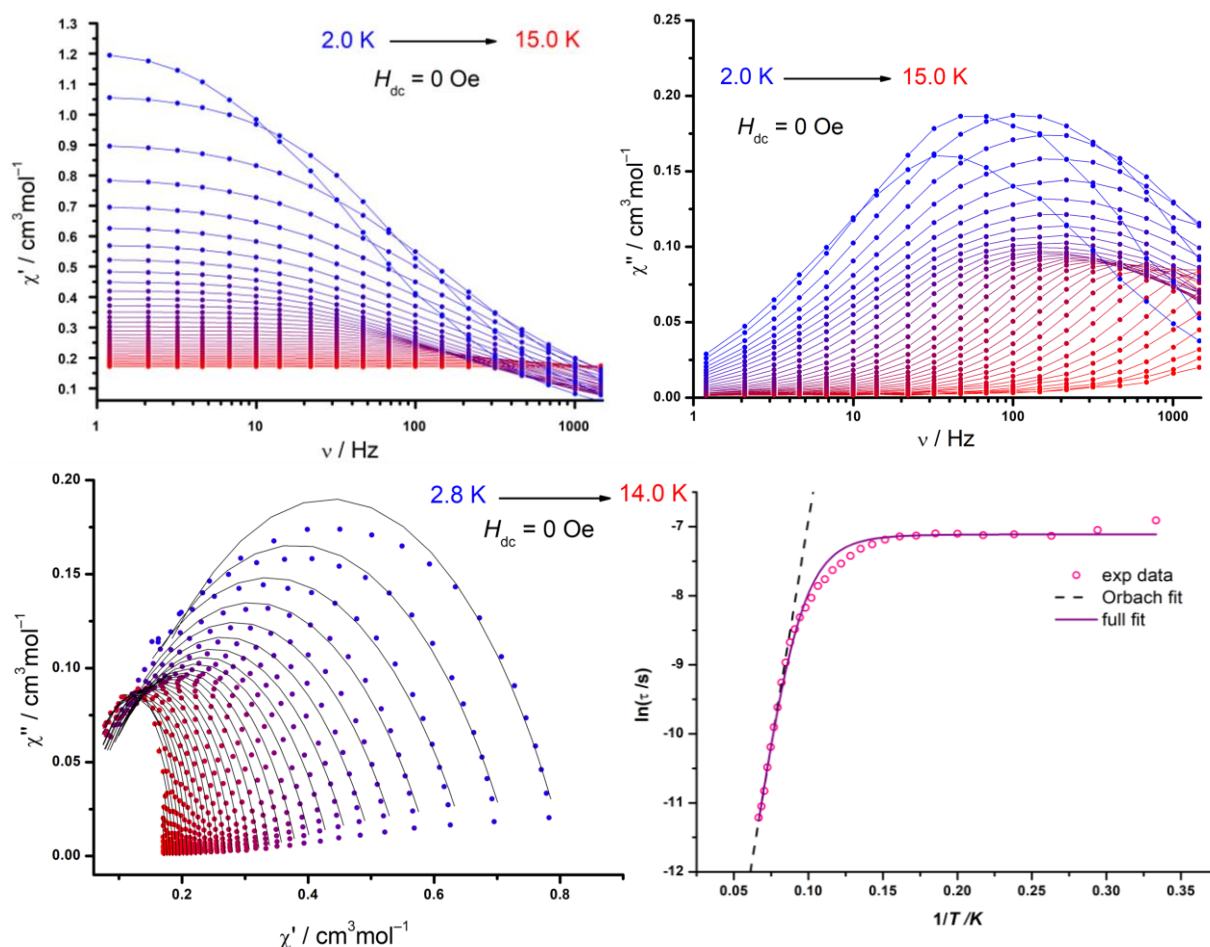


Figure 3.3.18. ac susceptibility data for 5_Co from 2K to 14K under 0 Oe (top, reproduced from elsewhere with permission). Lines are guide for the eyes. Cole-Cole fit (bottom left) and Arrhenius plot (bottom right). Lines are fits to the curves.

A butterfly-shaped hysteresis is also observable for 5_Co , as previously reported,⁴² and is comparable to the hysteresis found in 4_Co . The wings of the hysteresis, however, close at 2.9K and no hysteresis opening was observed while varying the sweep rate. The closing of the hysteresis at 0 Oe and the jump at the origin of the axes is typical of the presence of QTM effects.

The magnetic behavior of 6_Co is comparable to 3_Co (**Figure 3.3.19**). Slow relaxation of the magnetization is observable up to 15K and a temperature-independent regime is identified from 2K to 5K, where the maxima of the out-of-phase signals are not shifted towards higher frequencies. Upon the application of an external magnetic field of 1500 Oe, the QTM effects are suppressed. The Cole-Cole plots further confirm this hypothesis. Additionally, the Orbach-only fit of the linear area of the Arrhenius curve shows the increase of the energy barrier from 35.5. cm^{-1} (0 Oe) to 57.6 cm^{-1} (1500 Oe) with comparable characteristic times (**Figure 3.3.20**). At low temperatures (higher $1/T$), no plateau is observable in the presence of the dc field. A full fit for ac data at 0 Oe gives a much higher energy barrier value of 213 cm^{-1} , in better agreement with the dc data (**Figure 3.3.21**). The Raman parameters are found $C = 2.30$ and $n = 3.19$, similar to those found for 4_Co .

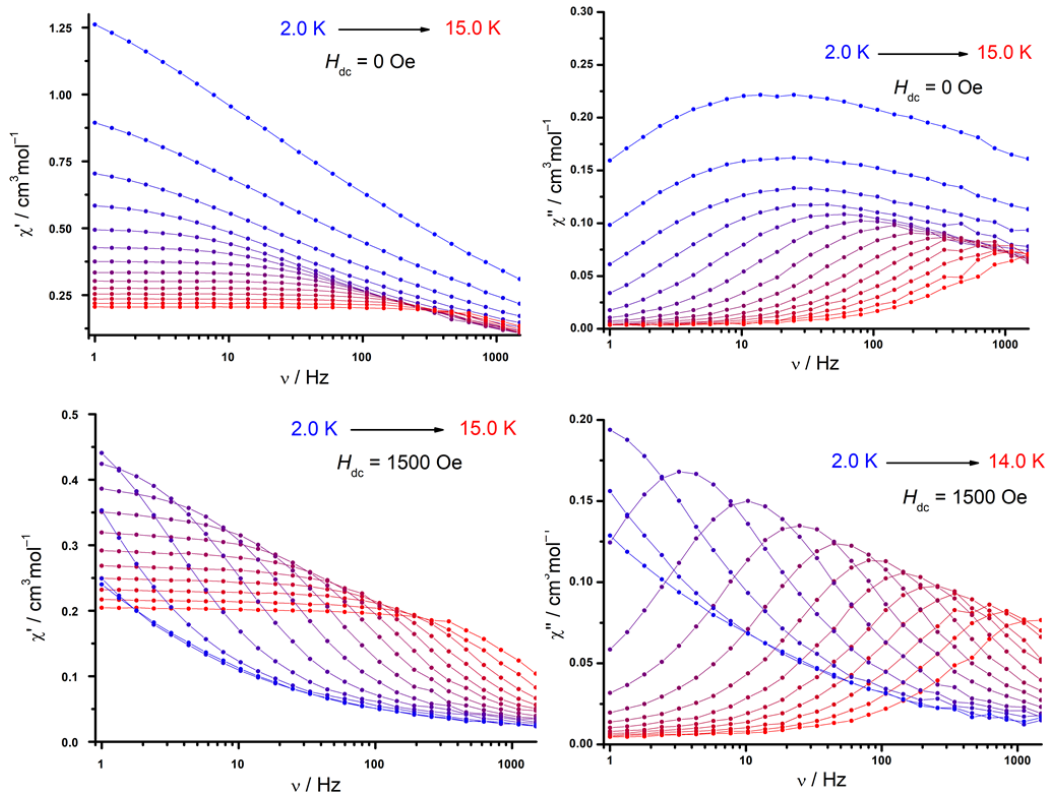


Figure 3.3.19. ac susceptibility data for **6_Co** from 2 K to 15 K under 0 Oe (top) and 1500 Oe (bottom). Lines are guides for the eyes.

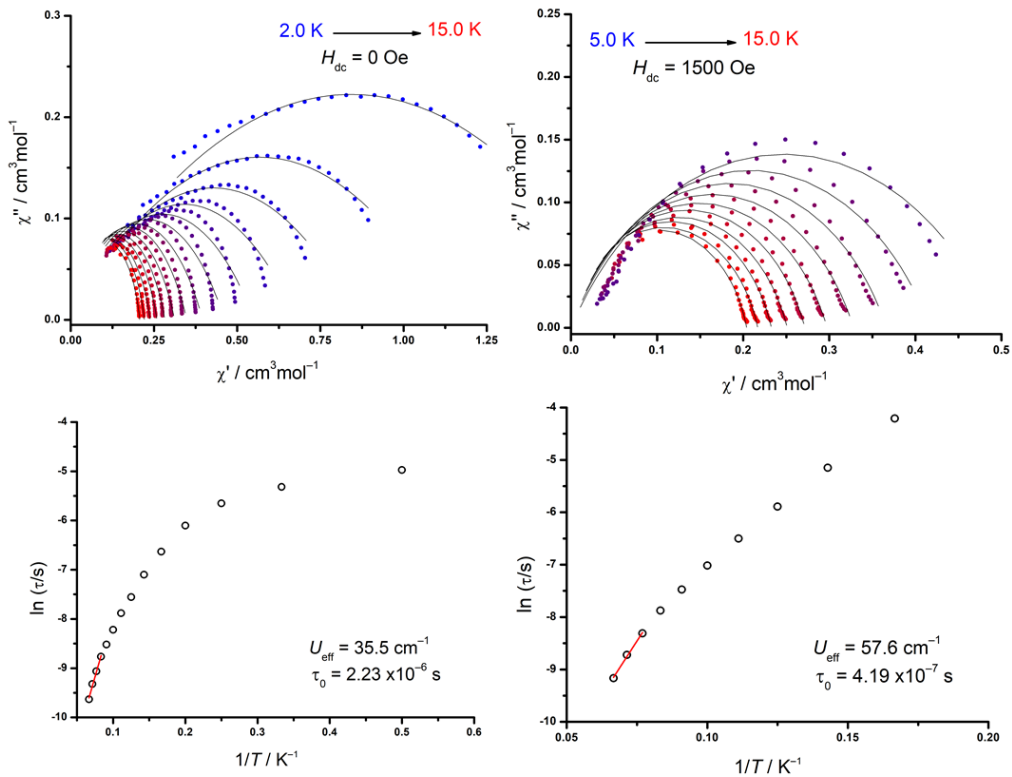


Figure 3.3.20. Cole-Cole plots (top) and Arrhenius plots (bottom) for **6_Co** under 0 Oe and 1500 Oe. Black lines in the Cole-Cole plots and red lines in the Arrhenius plots represent the fit to the curves.

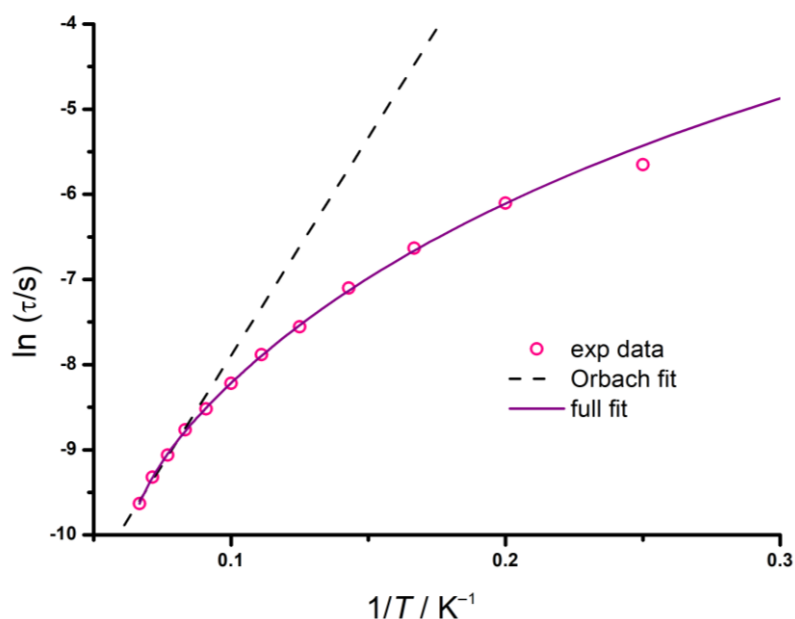


Figure 3.3.21. Arrhenius plot for 6_Co with fits of the ac relaxation under zero applied field.

Akin to parent complexes 3-5_Co, the present 6_Co compound also displays a magnetic hysteresis (Figure 3.3.22). In this case, the wings of the butterfly-shaped hysteresis close only at 3.5K, while sweep rates variations do not result in hysteresis opening. The hysteresis is closed at 0Oe probably due to QTM effects.

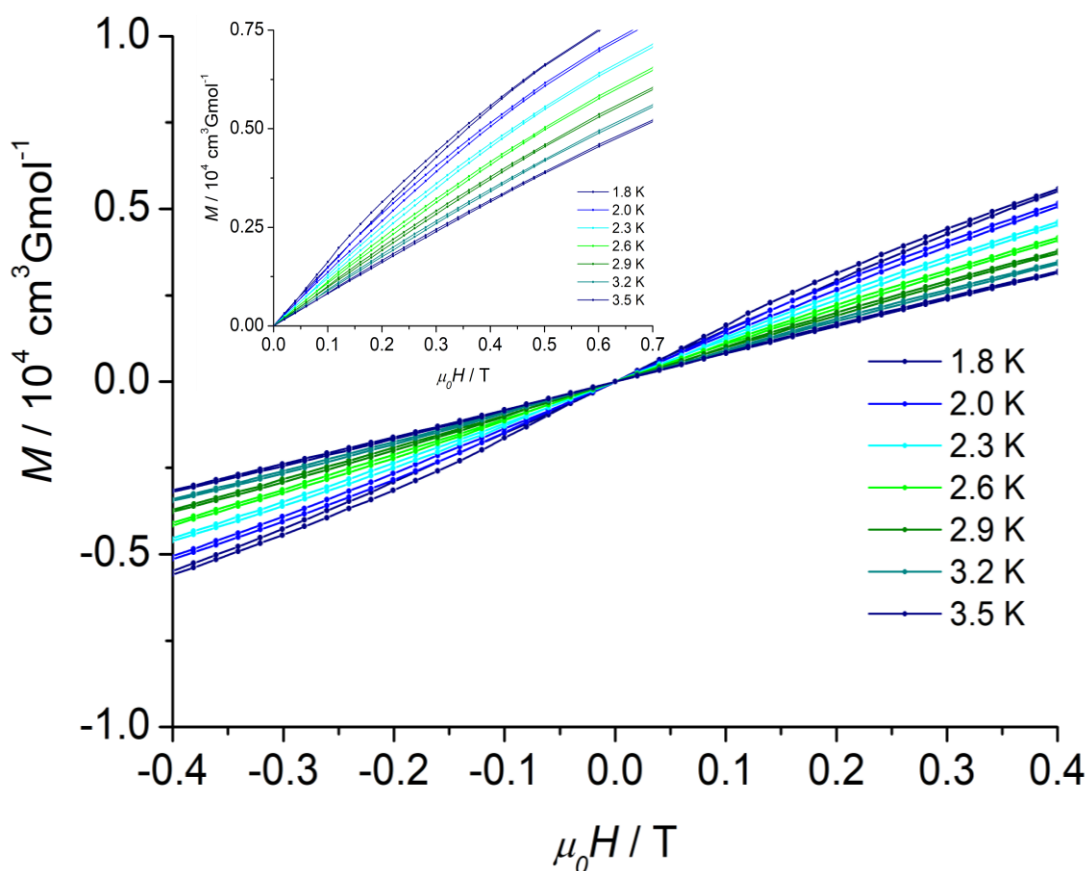


Figure 3.3.22. Magnetic hysteresis for 6_Co from 1.8K to 3.5K at 200 Oe/s. Inset: zoom-in of the (+, +) quadrant of the hysteresis curve

Finally, the last complex of the series, **7_Co**, displays similar magnetic properties to **6_Co**. It features slow relaxation of its magnetization up to 14K, both without and with external field. The QTM effects observable at low temperatures (2K to 4K) are completely suppressed by the application of the optimal dc field of 1500 Oe, as depicted in **Figure 3.3.23**.

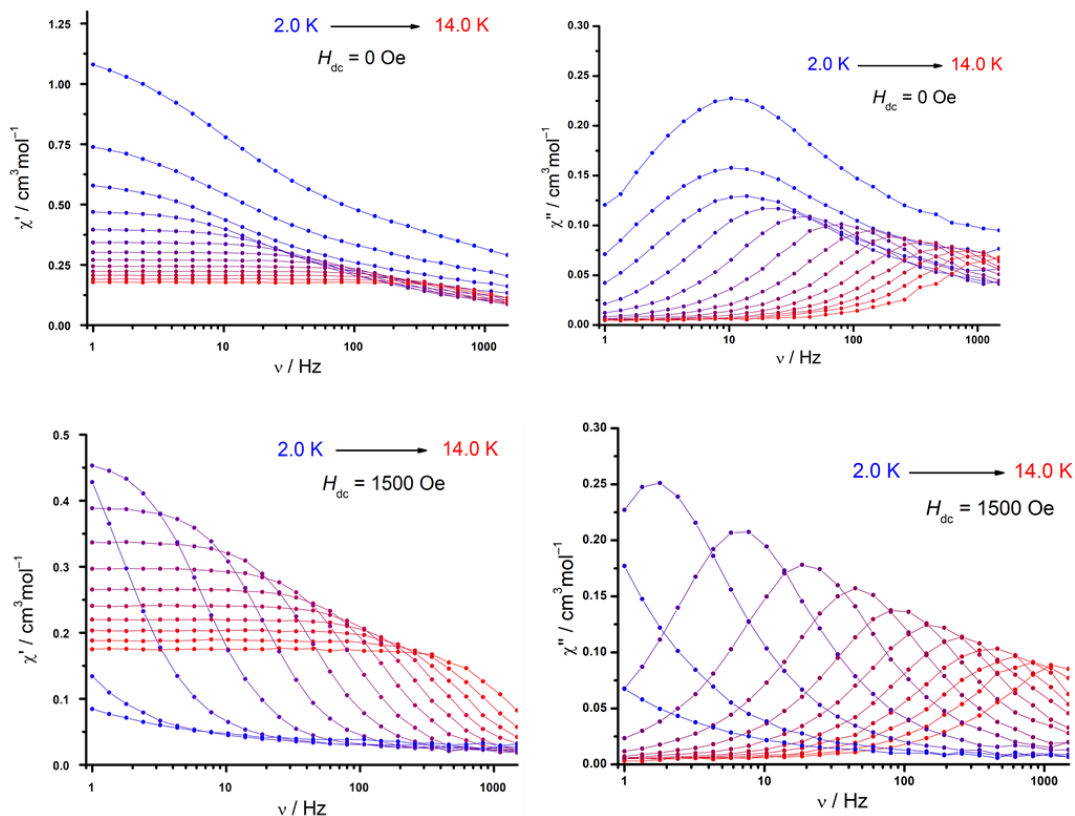


Figure 3.3.23. AC susceptibility data for **7_Co** from 2K to 14K under 0 Oe (top) and 1500 Oe (bottom). Lines are guides for the eyes

The corresponding Cole-Cole plots are in good agreement with this hypothesis, as well as the shapes of the Arrhenius curves (**Figure 3.3.24**). The plateau visible at low temperatures (high $1/T$) is not present anymore upon the application of the external field. Additionally, the pure Orbach fits give an energy barrier of $U_{\text{eff}} = 37.1 \text{ cm}^{-1}$ at 0 Oe and a slightly increased value of $U_{\text{eff}} = 41.2 \text{ cm}^{-1}$ at 1500 Oe, with similar characteristic times. For all complexes **3-7_Co**, this demonstrates how the application of an external field both suppresses the QTM and, more generally, improves the magnetic properties. The full fit taking all relaxation processes into account again yields a higher energy barrier value of 199 cm^{-1} , as expected from the dc data. The concomitantly fitted Raman parameter values are $C = 0.31$ and $n = 4.18$. For complexes **3_Co**, **4_Co**, **6_Co** and **7_Co**, these values are close to each other, indicative that the same type of Raman process may take place during the slow relaxation of the magnetization in these complexes. These values are further comparable to those found for **CoMSA** ($C = 0.087$ and $n = 3.65$).¹⁹⁹ Surprisingly, for complex **5_Co**, the n value is quite offset to 7.9 at 0Oe (or 9.6 at 1500 Oe), suggesting the presence of another type of Raman process, possibly the Kramers Raman process. It is however unclear which structural variations in these compounds may be responsible

for the changes in the nature of the relaxation processes – and difficult to suggest a hypothesis without further theoretical insights.

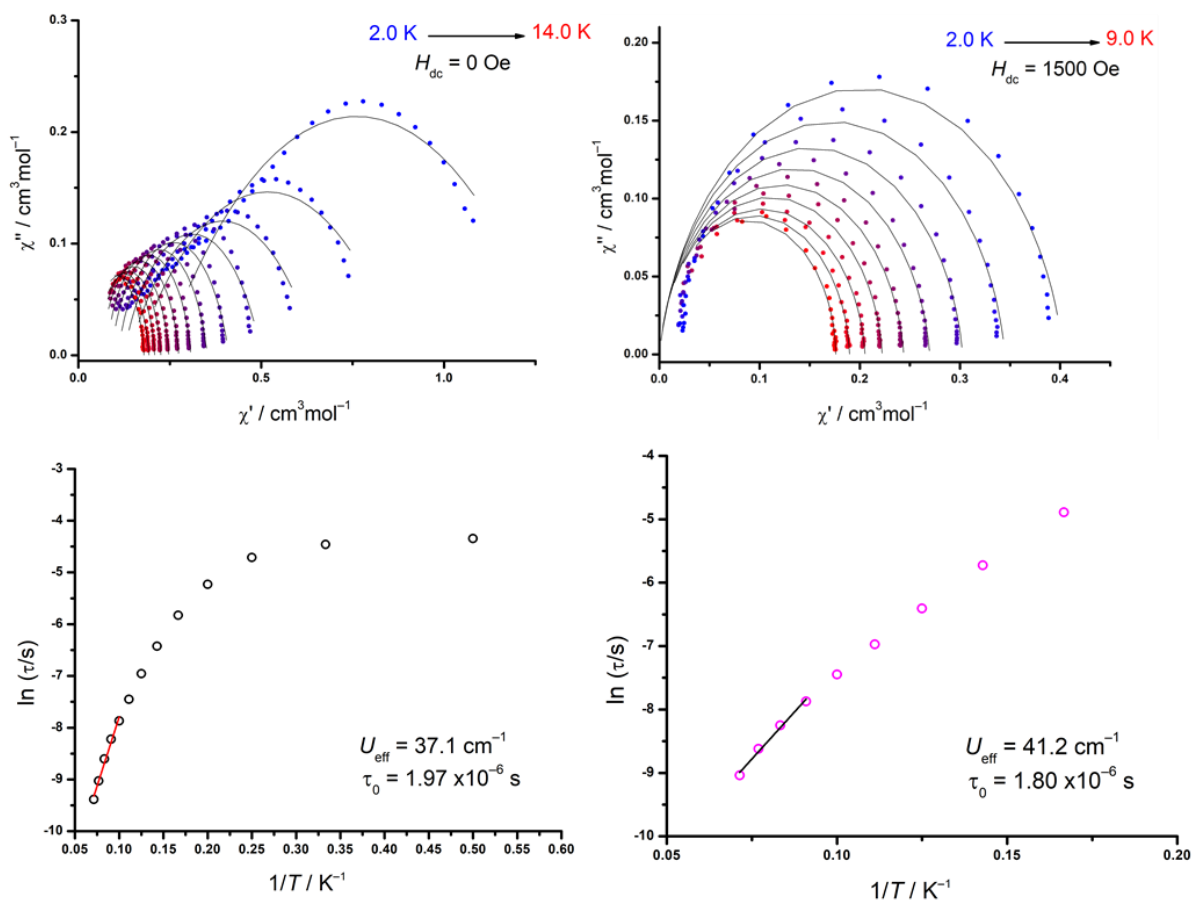


Figure 3.3.24. Cole-Cole plots (top) and Arrhenius plots (bottom) for 7_{Co} under 0 Oe and 1500 Oe. Black and red lines represent the fit to the curves

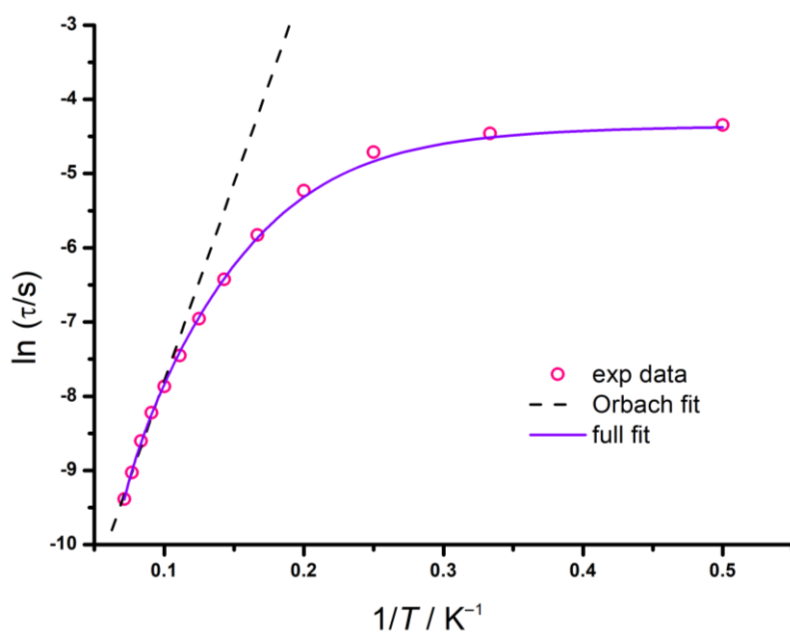


Figure 3.3.25. Arrhenius plot for 7_{Co} with fits of the ac relaxation under zero applied field

7_Co also displays a magnetic hysteresis with a butterfly shape. The wings, however, are less opened than in the previous complexes and already completely closed at 2.6K (**Figure 3.3.26**).

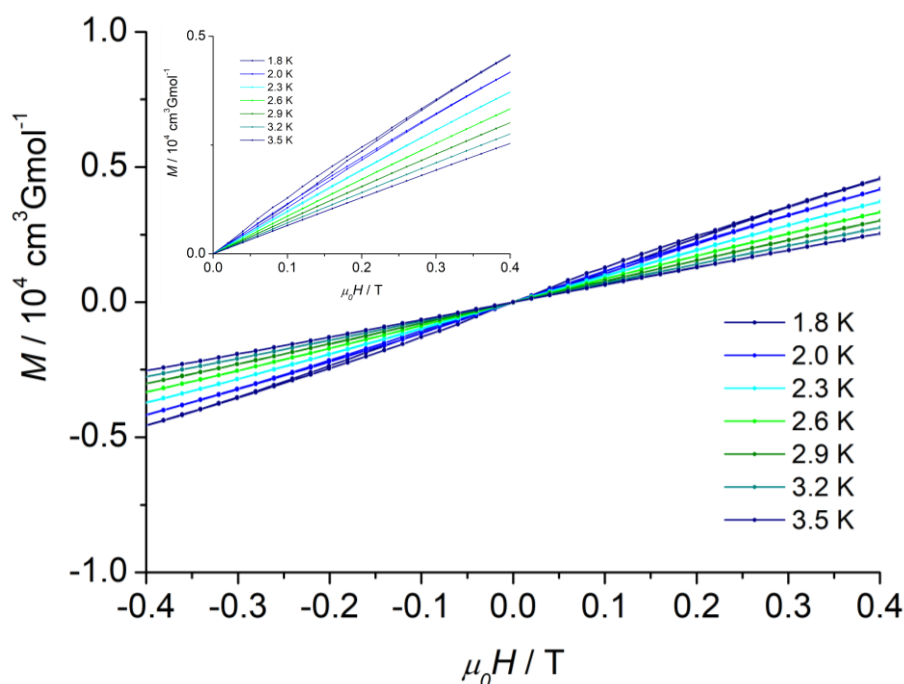


Figure 3.3.26. Magnetic hysteresis for 7_Co from 1.8K to 3.5K at 200 Oe/s. Inset: zoom-in of the (+, +) quadrant of the hysteresis curve

Overall, in terms of increased magnetic performances, the present cobalt complexes series have experimental ZFS parameters than range from -76 to -120 cm^{-1} , and energy barriers that range from 160 to 283 cm^{-1} , as summarized in **Table 3.3.9**. Compared to the literature, they further represent a family of very well performing cobalt SMMs.

Table 3.3.9. Selected experimental structural and magnetic parameters for 3-7_Co

Compound	N-Co-N angle ($^{\circ}$)	D (dc data) (cm^{-1})	U (full fit, ac data) (cm^{-1})
3_Co	72.15	-120	270 (f)
4_Co	72.70	-114	283
5_Co	71.46	-81.3	159
6_Co	70.84	-75.5	213
7_Co	71.43	-79.3	199

It seems that the N-Co-N angle variations from 70.84 to 72.7° are responsible for the drastic variations of the magnetic properties. Since these variations are apparently tiny, it is necessary to further investigate the possible influence of the N-Co-N bite angle in order to assess if there is a clear direct magneto-structural correlation. In order to do so, multi-configurational calculations were performed on 3-7_Co, as well as on a larger population of strongly distorted tetrahedral Co based single-molecule magnets. Results are presented in the next section.

3.3.4. Multiconfigurational calculations: correlating magnetic anisotropy with the N-Co-N angle

Complexes **3-7_Co** were found to display remarkable magnetic properties, especially in terms of axial magnetic anisotropy. Variations of more than 100 cm⁻¹ in terms of energy barrier were determined, while the N-Co-N bite angle only varied less than 2°. Therefore, multiconfigurational CASSCF(7,5) and NEVPT2 calculations for **3-7_Co** were performed to give access to the theoretical *D* and *g* tensors values, which were then compared to the experimental values obtained in the previous section. Such calculations were done using the ORCA software,^{170,211} on the molecular geometries obtained from experimental SCXRD. Subsequently, the *ab initio* ligand field theory (AILFT)¹⁶³ provides the d-orbital splitting energy diagram, in order to assess the energy gap between the two *d_{x²-y²}* and *d_{xy}* orbitals. The comparison between the magnetic results obtained in **section 3.3.3 (dc and ac magnetometry)** and the present calculations (*theory*) are summarized in **Table 3.3.10**, along with the N-Co-N angle variations (*X-ray*). Additionally, to quantify the degeneracy of the (*d_{x²-y²}*, *d_{xy}*) orbitals, the electronic occupancies obtained from the spin orbit coupling (SOC) wavefunctions and the energy gap ΔE between the two orbitals are also reported in **Table 3.3.10**. Theoretically, the closer to degeneracy with an electron population of 1.50 in each orbital and an energy gap of $\Delta E = 0$ cm⁻¹, the larger the ZFS parameter (ideal *L* = 2 system). The structural and magnetic parameters are further compared to those of the complex **CoMSA**, (MSA = N₂(CH₃SO₂)₂C₆H₄),¹⁹⁹ which shows experimental dc and ac magnetic properties that are comparable to those of complexes **3-7_Co**. This complex, albeit possessing a larger N-Co-N angle of 80.5°, is the only literature-known magnetically characterized compound with such an acute angle. The same calculations were performed on **CoMSA** to allow its comparison with **3-7_Co** and to draw magneto-structural correlations for this series of complexes.

Table 3.3.10. Selected experimental and computational structural and magnetic parameters for **3-7_Co**, sorted from the smallest to the largest bite angle. CoMSA is shown for comparison. The ideal *L*=2 system and the idealized **4'_Co** complex are indicated below.

Complex	N-Co-N (°)	$\chi_M T^a$ (cm ³ mol ⁻¹ K)	D_{exp}^b (cm ⁻¹)	<i>g</i> values (<i>g_x</i> = <i>g_y</i> , <i>g_z</i>)	U_{eff}^c (cm ⁻¹)	$U = 2 D $ (cm ⁻¹)	Number of electrons in (<i>d_{x²-y²}</i> , <i>d_{xy}</i>)	Energy gap ΔE between <i>d_{x²-y²}</i> and <i>d_{xy}</i> (cm ⁻¹)
	<i>X-ray</i>		<i>dc-mag</i>		<i>ac-mag</i>		<i>theory</i>	
6_Co	70.84	3.21	-75.5	2.16, 3.15	213	206	(1.20, 1.79)	736.4
7_Co	71.43	2.75	-79.3	2.17, 2.84	199	196	(1.21, 1.78)	701.8
5_Co	71.46	3.00	-81.3	2.14, 2.97	159	183	(1.18, 1.82)	826.3
3_Co	72.2- 72.8 ^d	3.79	-120	2.30, 3.45	270	290	(1.40, 1.61)	280.0
4_Co	72.7	3.48	-114	2.27, 3.20	283	282	(1.37, 1.62)	263.7
CoMSA	80.5	3.14	-115	2.20, 3.03	230	238	(1.73, 1.26)	548.2
4'_Co	77.4	-	-	-	-	309	(1.51, 1.48)	20.8
Ideal <i>L</i> =2 system	-	4.02	-171	2.00, 4.00	-	343	(1.50, 1.50)	0

^a at 210K, ^b fitted with Jul-2s, ^c full fit from Eq 2.1 ^ddisordered structure

In **3-7_Co**, it seems that the highly distorted tetrahedral geometries preserved some orbital angular momentum (OAM) thanks to the relatively close ($d_{x^2-y^2}$, d_{xy}) orbital pair, giving rise to large magnetic anisotropies.¹⁶⁴ There is a trend from **CoMSA** to **3_Co** with an overall increase of the magnetic parameters' values and an overall decrease of the energy gap. Then, surprisingly, the magnetic performance seems to degrade despite the more acute bite angles. Calculations revealed that the distortion induced by the extremely acute bite angle is so large in all five complexes **3-7_Co** that the $d_{x^2-y^2}$ and d_{xy} energy order has become inverted (**Figures 3.3.1 and 3.3.27**) compared to typical tetrahedral coordination.^{114,117,118,124,199} Therefore, the two orbitals are again going away from each other instead of staying degenerated. CoMSA shows the typical 3d orbital energy splitting diagram with $d_{x^2-y^2}$ laying lower in energy than d_{xy} . This is well illustrated in the fact that, in contrast to the general perception that the largest distortion, i.e. the smallest bite angle, would provide the largest ZFS parameter, the complexes **3_Co** and **4_Co** are found to exhibit the largest anisotropy despite owing the largest bite angle in the present series (72.2 and 72.7°, respectively). Thus, for distorted tetrahedral [CoN₄]-SMMs, it is clear that there must exist a compound with an ideal bite angle leading to maximum anisotropy, corresponding to that of a pure system (ideal $L=2$, **Table 3.3.10, Figure 3.3.27**).^{114,164} Of all complexes **3-7_Co** and **CoMSA**, compound **3_Co** is the closest to perfect degeneracy holding 1.61 and 1.40 electrons in the ($d_{x^2-y^2}$, d_{xy}) orbitals with an energy gap between the ground and first excited spin-orbit free state of $\Delta E = 280.0 \text{ cm}^{-1}$. **4_Co** is the second-best compound of the series with an even smaller energy gap of $\Delta E = 263.7 \text{ cm}^{-1}$ but slightly higher orbital occupancies of 1.62 and 1.37. The other complexes **5-7_Co** and **CoMSA** all possess an energy gap $\Delta E \geq 500 \text{ cm}^{-1}$ and their ($d_{x^2-y^2}$, d_{xy}) electronic population are further away from the degeneracy population (**Table 3.3.10**).

Altogether, the variations in D -values originate from the energy difference between the more or less populated $d_{x^2-y^2}$ and d_{xy} orbitals. This means that ΔE strongly depends on the magnitude of the bite angle N-Co-N. This latter dependency, however, is not linear: by plotting D or the d_{xy} population against the bite angle, a parabolic fit can be obtained, giving a rough estimate of the ideal bite angle in the range between 76-78° (**Figure 3.3.27**).

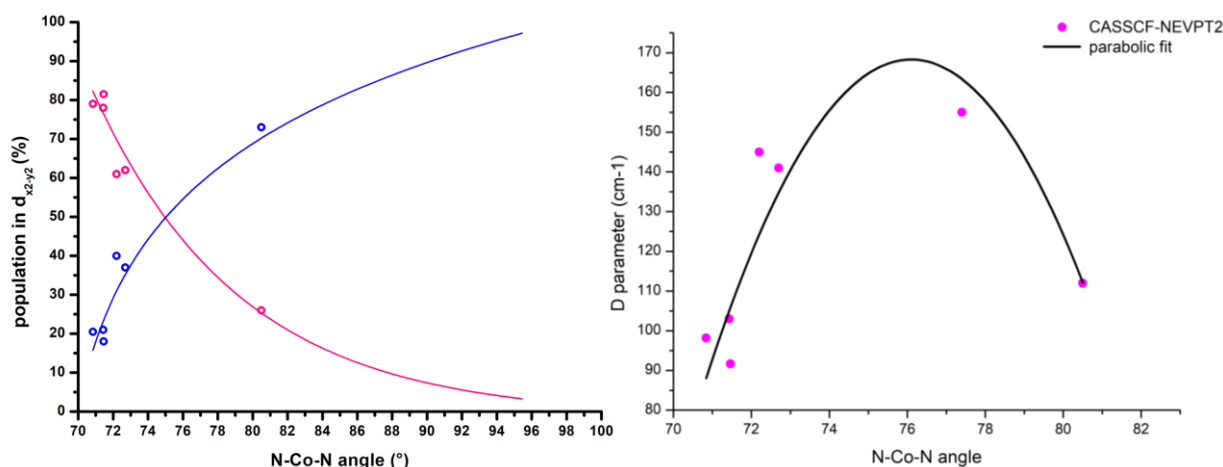


Figure 3.3.27. Plots of the calculated population in the important d orbitals (left) and the ZFS parameter against the N-Co-N angle for complexes **3-7_Co** and **CoMSA**.

Subsequent calculations on the theoretically modified complex **4_Co** indeed give the best result with a bite N-Co-N angle of 77.4°. A nearly degenerate ($d_{x^2-y^2}, d_{xy}$) orbital pair was obtained for **4'_Co**, with a tiny energy gap $\Delta E = 20.8 \text{ cm}^{-1}$ and a ZFS parameter $D = -155 \text{ cm}^{-1}$ (Table 3.3.10). Noteworthy, the ZFS parameter for the idealized **4'_Co** is lower than -171 cm^{-1} (in theory, the largest value can be $2 |D| = 343 \text{ cm}^{-1}$, for a $(S=3/2, L=2)$ system with optimal SOC). Additional fine-tuning of the ligand in order to optimize the spatial arrangement of the backbone may still be required to observe a fully degenerate situation with maximum magnetic anisotropy.

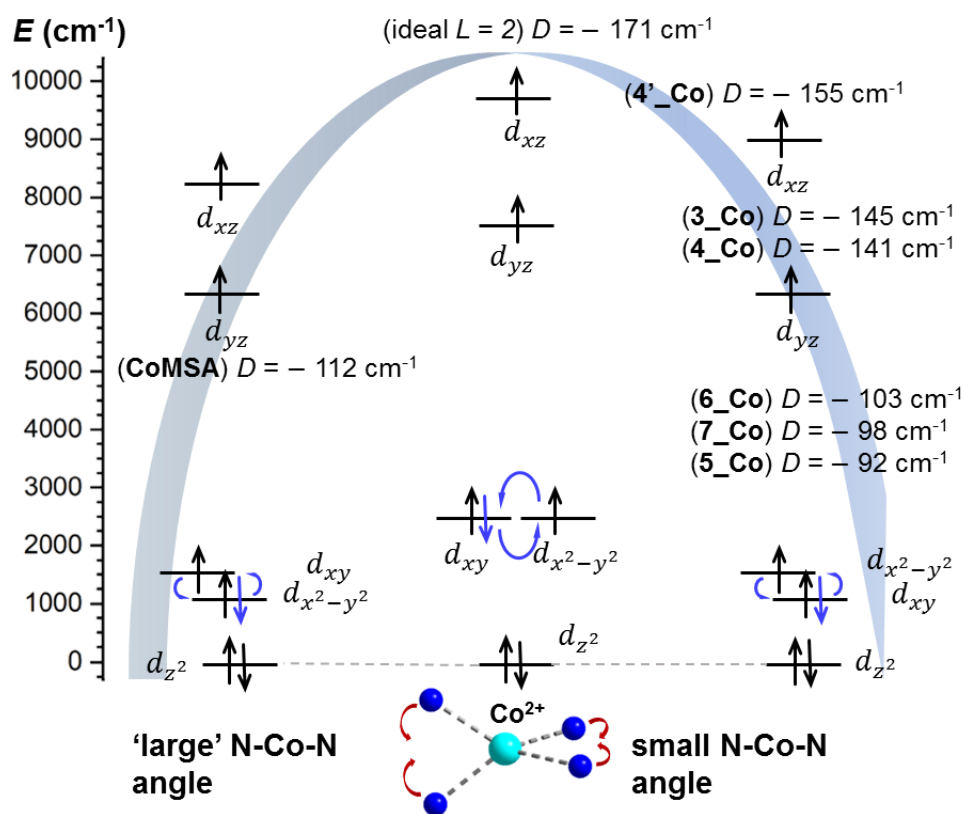


Figure 3.3.28. 3d orbital energy diagram for **4_Co**, **4'_Co** and **CoMSA**.¹⁹⁹ The relative magnitude of the ZFS parameter D is indicated for complexes **3-7_Co**, **4'_Co** and **CoMSA**. The present results suggest that the $d_{x^2-y^2}$ and d_{xy} orbitals energy gap is responsible for the variations of ZFS parameter, with an optimum reached when this energy gap is zero.

The hypothesis of the existence of an ideal E-Co-E angle was further probed on a wider population of distorted tetrahedral cobalt SMMs. In order to further validate our hypothesis on a larger population of compounds, we performed similar calculations for additional twenty $[\text{CoE}_4]$ structures (with $E = \text{O, N, S, Se}$) available from the CSD database (Table 3.3.11).^{117,123,198-200,210,212-223} They were selected according to their ligand types and to the value of their E-Co-E angle. These additional calculations allow to cover a broader range of E-Co-E angles from 66 to 107° and to verify the hypotheses on ligand types other than sulfimidates and imido-sulfates in **3-7_Co**. Subsequently, for all these complexes, $-D$ was plotted against the bite angle E-Co-E, as depicted in Figure 3.3.29.

Table 3.3.11 List of compounds used for magneto-structural correlations. N-, N&O-, O-, S-, Se-based compounds are shown in blue and purple, pink, red, orange and black respectively. The same color code is used for **Figure 3.3.29**.

Compound	E-Co-E angle (°)	<i>D</i> (cm ⁻¹)	CCDC#	Ligand class
Co[(Me) ₂ N] ₂ CS] ₂ Cl ₂	106.71	-17.5	#1817778	thiourea
Co[(Me) ₂ N] ₂ CS] ₂ Br ₂	106.31	-18.6	#1817777	thiourea
Co[(Me) ₂ N] ₂ CS] ₂ (ClO ₄) ₂	105.96	-15.2	#1447667	thiourea
Co(OPh) ₄ [PPh ₄]	105.89	-11.8	#919744	alcoolate
Co(N(TMS)C(^t Bu)CHC (piperidino)N(TMS))	103	-10.5	#192416	β-diketiminato
Co(^t BuNNCHCHNR) ₂	96.22	-19.2	#939193	triaz-pentadienyl
Co(MeBox) ₂	96.2	-26.6	–	box
Co(MeNC(Me)CHC(Me)NMe) ₂	95.766	-30.1	#1577787	pentadienyl
[Co(SPh) ₄][PPh ₄]	95.6	-51.4	#1100265	thiolate
Co[(ⁿ Bu)N] ₂ CS](ClO ₄) ₂	95.34	-67.9	#1447665	thiourea
Co(SePh) ₄ [PPh ₄]	94.24	-71.0	#919746	selenolate
Co[C ₃ S ₅] ₂ [^t Bu ₄ N] ₂	94.06	-104.3	#1005501	thionate
Co[(Ph)PhNCH ₂ C ₁₀ H ₆ O]	93.5	-33.7	#1424466	Schiff base
Co[(2,9-dimethyl-1,10- phenanthroline) ₂] [OTf] ₂	84.34	-66.2	#1898231	phenanthroline
Co[(ⁱ Pr)NC ₇ H ₅ N(ⁱ Pr)] ₂	81.803	-86.4	#151189	aminotroponimine
Co[(N(SO ₂ Me) ₂ C ₆ H ₄) ₂][HNEt ₃] ₂ (CoMSA)	80.5	-112	#971167	sulfonamide
Co[(ⁿ Bu) ₂ SPh] ₂ ideal (4'_Co)	77.4	-155	–	sulfimidinate
Co[(^t BuC ₆ H ₄ N(Ph ₂)) ₂ P] ₂	73.6	-147	#233898	aminoimino- phosphorane
Co[(ⁿ Bu) ₂ SPh] ₂ (4_Co)	72.7	-141	#2046685	sulfimidinate
Co[(ⁿ Bu) ₂ SMe] ₂ (3_Co)	72.2	-145	–	sulfimidinate
Co[(ⁿ Bu) ₃ SMe] ₂ (5_Co)	71.46	-91.7	#1426594	imido-sulfate
Co[(ⁿ Bu) ₃ SPh] ₂ (7_Co)	71.43	-103	#2046687	imido-sulfate
Co[(ⁿ Bu) ₃ SPh] ₂ (6_Co)	70.84	-98.2	#2046686	imido-sulfate
Co[(ⁿ Pr) ₂ CN(TMS) ₂]	66.1	-118	#1537874	amidinate
Co{(2,6-(2,4,6- Me ₃ Ph) ₂ Ph)C(N ⁱ Pr) ₂ }	66	-114	#182079	amidinate
Co[(^t BuN) ₂ CMe] ₂	65.85	-117	#674856	amidinate
Co[(ⁱ PrN) ₂ CMe] ₂	65.57	-93.1	#229483	amidinate

The following plot is obtained:

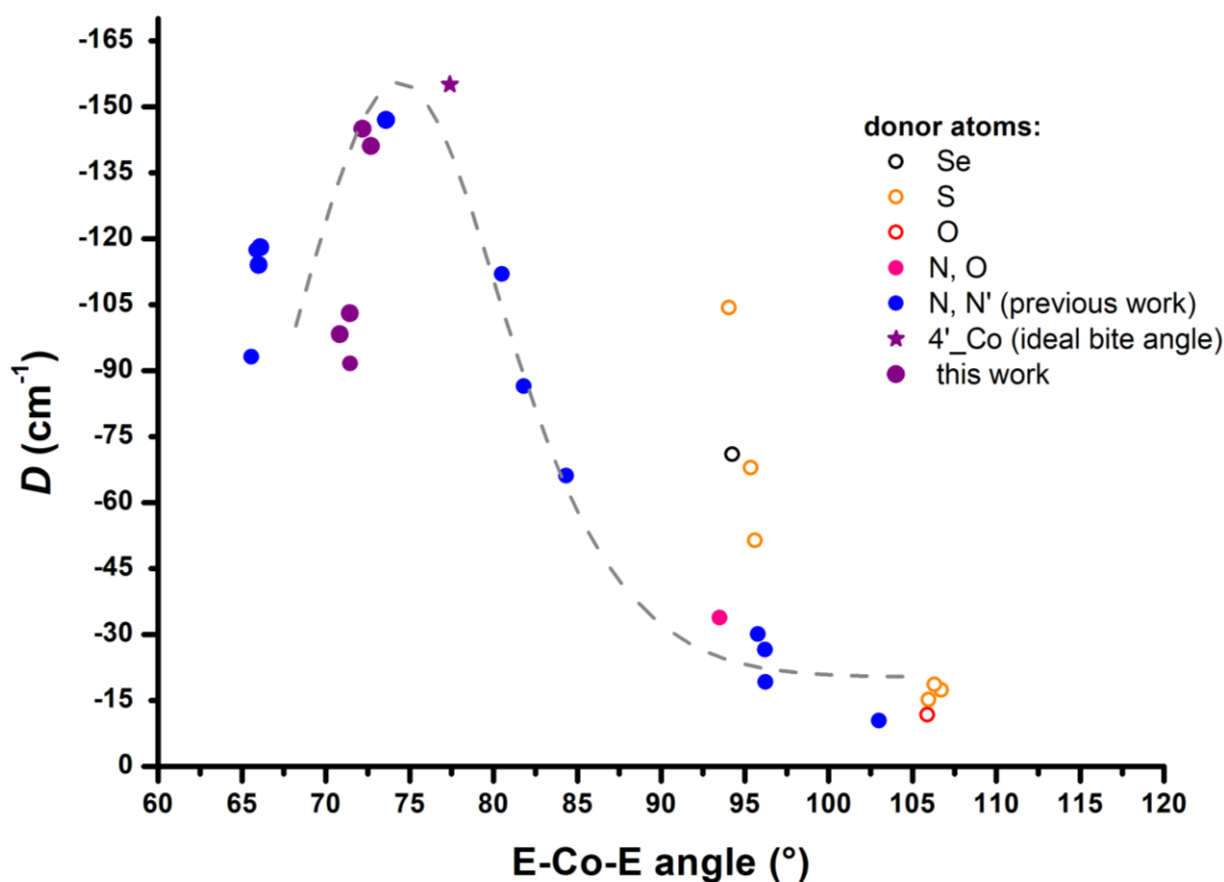


Figure 3.3.29. ZFS parameter against the E-Co-E angle for complexes of **Table 3.3.11**. The grey dashed line is a guide for the eyes.

While [CoN₄]-SMMs show a clear trend supporting the existence of the ideal bite angle, cobalt SMMs based on donor atoms other than nitrogen are less numerous and do not possess acute bite angles. Thus, these classes of complexes may not be relevant to accurately predict an ideal bite angle. Additionally, generating an ideal structure for Co(SPh)₄ with a S-Co-S angle of 77.4° (or larger) for calculation purposes was impossible due to the larger ionic radius of the sulfur atoms.¹¹⁸ It is however possible that another ideal angle may exist for [CoS₄]-SMMs. The small deviations from the overall trend observed in **5-7_Co** compounds compared to the substituted aminidates (for example [Co(RN)₂(CR')₂], where R = ⁱBu, ⁱPr, and R' = Me or N(TMS)₂; [Co{(2,6-(2,4,6-Me₃Ph)₂Ph)C(NⁱPr)₂}]^{216,217} are attributed to the differences in their respective second coordination spheres. Nevertheless, the dependency of the ZFS on the bite angle follows a clear trend for [CoN₄]-SMMs, as shown by the dashed grey line on **Figure 3.3.29**. The $-D$ value increases from -17.4 cm^{-1} (107°) up to -155 cm^{-1} at the optimal bite angle 77.4°. It then decreases with smaller bite angles.

In contrast to the wide-spread assumption that the smaller angle the better the ZFS which has influenced synthetic activities for a long time, the present results strongly support that, in fact, the target compound should possess an ideal N-Co-N angle of around 77° in a highly distorted tetrahedral geometry.

3.3.5. Conclusion and perspectives

The complexes **3-7_Co** are featuring remarkable magnetic properties because of their highly distorted tetrahedral geometries. Notably, the complexes **3_Co** and **4_Co** are currently amongst the best performing distorted tetrahedral cobalt single-ion magnets, with giant magnetic anisotropies of -145 and -141 cm^{-1} , respectively, close to the ideal theoretical value. Additionally, their experimental energy barriers to spin reversal are also higher than the reported value of 230 cm^{-1} for **CoMSA**, ($\text{MSA} = \text{N}_2(\text{CH}_3\text{SO}_2)_2\text{C}_6\text{H}_4$).¹⁹⁹

Furthermore, the present study enabled to extract the following hypotheses:

- The best N-Co-N angle for an ideally distorted tetrahedron with Co^{2+} (d^7 , $S=3/2$, $L=2$, perfect degeneracy) is around $76-78^\circ$. The highest possible ZFS parameter for such systems is -343 cm^{-1} which corresponds to $D = -171\text{ cm}^{-1}$. Complexes with larger or smaller angles will show reduced magnetic performances.
- The two $d_{x^2-y^2}$ and d_{xy} orbitals have to be perfectly degenerated for optimal magnetic properties, which means that each orbital should be populated by 1.5 electron and ΔE should be as close as possible to 0.
- This design rule should be applicable to all distorted tetrahedral $[\text{CoN}_4]$ compounds in order to predict their magnetic performances.

Based on these assumptions, smart ligand design needs to focus on providing a ligand that would generate an N-Co-N angle of $76-78^\circ$. This hypothesis was herein probed and very well verified with the theoretical complex **4'_Co** featuring an ideal angle of 77.4° . Once achieved experimentally, the obtained complex should fulfill all conditions to display the best possible magnetic properties for $[\text{CoN}_4]$ -SMMs. Once such a mononuclear system is available experimentally, a possible route is to explore the assembly of sub-units containing this highly anisotropic $[\text{CoN}_4]$ core in order to give larger ferromagnetic clusters, single chain magnets or multidimensional multifunctional magnetic materials.

General conclusion and perspectives

The present work explored various compounds containing the S-N motive with a strong focus on their magnetic properties and probed the potential of mononuclear dysprosium and cobalt SN-based complexes as competitive SMMs via magneto-structural correlation studies.

In **Chapter 1**, the broad family of SN based compounds and some novel SN-based complexes were presented. Notably, the successful trapping of the long-time elusive $[\text{S}(\text{N}^i\text{Bu})_3]_2\text{K}_3$ species gave evidence of a rare type of radical and unveiled some exotic facets of SN chemistry.

In **Chapter 2**, the SN ligands were further utilized with lanthanides in order to benchmark the resulting complexes **1-3_Dy** and appreciate the potential synergies between main group chemistry and molecular magnetism towards novel SMM design. Further perspectives for improvement and ligand engineering were given with the complex **4_Dy**.

In **Chapter 3**, the potential of SN ligands was further exploited and investigated within cobalt complexes. In the first section of **Chapter 3**, the investigation of the influence of a soft element interacting with the metal center in the complexes **1_Co** and **2_Co** confirmed the positive impact of a weak P-Co interaction on the magnetic performances. In the second section of **Chapter 3**, highly distorted tetrahedral cobalt complexes **3_Co** to **7_Co** revealed fundamental trends towards the design of the best possible $[\text{CoN}_4]$ SIMs. Different from the common perception that the smaller N-Co-N angle the better, this comprehensive study concluded that an ideal angle exists, for which the optimal 3d orbital splitting maximizes the magnetic anisotropy. For both sections. Additional experimental examples will be welcome to further support the present conclusions.

Overall, the class of chelates containing the SN moiety represents a challenging yet highly promising alternative to more traditional ligands towards SMM design. Although under-investigated, interesting magnetic performances may be expected thanks to the advantageous synergy between sulfur and nitrogen, as demonstrated by the results with the cobalt complexes.



Chapter Four: Experimental section

4.1. Methods

4.1.1. General considerations

All reactions (synthesis of both ligands and complexes) were carried out under strict exclusion of air and moisture using modified Schlenk techniques or in an Argon glovebox, if not indicated otherwise. Solvents were dried on various drying agents and freshly distilled from sodium/potassium alloy (Et₂O, *n*-pentane), potassium (THF) or sodium (*n*-hexane, toluene). The solvents were degassed with minimum three freeze-pump-thaw cycles. The absence of oxygen and moisture was then confirmed by a benzophenone/ketyl test before use.

Importantly, the metal halides (LnCl₃, CoCl₂, MnCl₂, FeCl₂, NiCl₂) were purchased from Sigma-Aldrich as 99.9% anhydrous salts and used without further purification. All other employed reactants were either commercially available as well or synthesized according to previously published literature.

4.1.2. Single-crystal X-ray diffraction

Crystal selection and manipulation. Crystal picking was performed either in an argon glovebox or from a Schlenk flask under argon atmosphere. The crystals were deposited in perfluorinated polyether inert oil on a microscope slide. An appropriate single crystal was selected using a microscope equipped with polarization filter, mounted on the tip of a MiTeGen[®]MicroMount or glass fiber, fixed to a goniometer head and shock-cooled by the diffractometer cooling device.

Data collection and processing. The compounds were measured using either an Incoatec molybdenum microfocus source with mirror optics or on a molybdenum rotating anode turbo X-ray source. Both are equipped with an Incoatec mirror optics APEX II CCD detector mounted on a three circle D8 goniometer, which supplies molybdenum MoK α radiation ($\lambda = 0.71073 \text{ \AA}$). All crystals were centered optically using a video camera after being fixed on the goniometer. The data collection strategy was calculated to achieve maximum resolution data suitable for publication (between 0.6 and 0.83 \AA resolution). Therefore, a test run (matrix scan) was recorded prior to each experiment to check the crystal quality, to get a rough estimate of the cell parameters, and to determine the optimum exposure time. All scans of the data collections were performed in an ω -scan mode, usually with a step-width of 0.5° at fixed ϕ -angles. The unit cell was indexed with the tools in the Bruker APEX2 software suite. The intensities on the raw frames were integrated with SAINT.²²⁴ The orientation matrix was refined in several integration runs, and the maximum resolution was adjusted so that only useable data with a maximum R_{int} of 0.20 (except some rare cases) were integrated. The software SADABS²²⁵ was used for absorption correction and scaling. TWINABS²²⁶ was used in the cases of non-merohedral twins or split crystals. Both programs refine an empirical error function by symmetry-equivalent reflections.

XPREP²²⁷ was used for the examination of data statistics and as final setup of the files for structure solution.

Structure solution and refinement. The structures were solved with direct methods using SHELXT.²²⁸ All refinements were performed on F^2 in the SHELXL-GUI.²²⁹ All non-hydrogen-atoms were refined with anisotropic displacement parameters. The C-bonded hydrogen atoms were set on calculated positions and refined isotropically using a riding model with their U_{iso} values constrained equal to 1.5 times the U_{eq} of their pivot atoms for methyl carbon atoms and 1.2 times for all other carbon atoms. The N-bonded hydrogen atom coordinates were refined freely from the residual density map and constrained to 1.5 U_{eq} of their pivot nitrogen atom. If not stated otherwise, the hydrogen bond lengths were restrained to a sensible value and the U_{iso} were constrained as mentioned above. In the absence of restraints, the only data the structural model is refined against are the measured intensities in the form of squared structure factors. Theoretical structure factors are calculated from the atomic model and the so-calculated intensities are then compared with the measured intensities. The best model is the one that minimizes $M(pi, k)$ (Eq. 4.1) using the weights w defined in Eq. 4.2.

$$M(pi, k) = \sum w[k |F_{obs}|^2 - |F_{calc}|^2]^2 = \min \text{ (Eq. 4.1)}$$

with pi the structural parameters, k the scale factor and

$$w^{-1} = \sigma^2(F_{obs}^2) + (g1 \times P)^2 + g^2 \times P \text{ with } P = (\text{Max} ((F_{obs,0}^2 + 2F_{calc}^2)/3)) \text{ (Eq. 4.2)}$$

The results of the refinements were verified by comparison of the calculated and the observed structure factors. Commonly used criteria are the residuals $R1$ (Eq. 4.3) and $wR2$ (Eq. 4.4).

$$R1 = \sum ||F_{obs}| - |F_{calc}|| / \sum |F_{obs}| \text{ (Eq. 4.3)}$$

$$wR2 = \sqrt{\sum w(F_{obs}^2 - F_{calc}^2)^2 / \sum w(F_{obs}^2)^2} \text{ (Eq. 4.4)}$$

Additionally, the goodness of fit (GoF, S), a figure of merit showing the relation between deviation of F_{calc} from F_{obs} and the over-determination of refined parameters is calculated (Eq. 4.5).

$$S = \sqrt{\sum (w(F_{obs}^2 - F_{calc}^2)^2) / n - p} \text{ (Eq. 4.5)}$$

where n is the number of reflections and p the number of parameters

The residual densities from difference Fourier analysis should be low. Due to the model restrictions, the residual densities are normally found in the bonding regions. Higher residuals for heavy scatterers (such as Ln ions) are acceptable as they arise mainly from absorption effects and Fourier truncation errors due to the limited recorded resolution range. The highest peak and deepest hole from difference Fourier analysis are listed in the crystallographic tables. Additionally, the orientation, size and ellipticity of the ADPs show the quality of the model. Ideally, the ADPs should be oriented perpendicular to the bonds, be equal in size and show little ellipticity. All graphics presented in this chapter were generated and plotted with the XP program²²⁹ at the 50 % probability level. In the other chapters, the software Diamond was used.²³⁰

Treatment of disorder. Structures containing disordered fragments were refined using constraints and restraints. Constraints used within this work are, for example, the site occupation factor and the AFIX instruction, which defines and constrains rigid groups. Mathematically, restraints are treated as additional experimental observations, thus increasing the number of data to refine against. In the presence of restraints, the minimization function changes as follows:

$$M = \sum w(F_{obs}^2 - F_{calc}^2)^2 + \sum wr(R_{target} - R_{calc})^2 \text{ (Eq. 4.6)}$$

The geometries of chemically equivalent but crystallographically independent fragments can be fitted to each other by distance restraints. Especially the 1,2 distances (bond lengths) and 1,3 distances (bond angles) are set to be equal within their effective standard deviations. This was helpful for refining disordered positions as the averaging of equivalent fragments implements chemical information and stabilizes the refinement. Within this work, disordered moieties were refined using distance restraints (SADI) and anisotropic displacement parameter restraints (SIMU and RIGU).

4.1.3. Magnetic measurements

Description of the instruments. Magnetic measurements were carried out with a Quantum Design MPMS XL 5 SQUID magnetometer equipped with a 5 Tesla magnet (reaching a maximum of 1 500 Hz) or with a Quantum Design MPMS 3 SQUID magnetometer equipped with a 7 Tesla magnet (reaching a maximum of 1 000 Hz).

Sample preparation. Crystalline, pure material was crushed and dried thoroughly. It was then charged into a gel bucket and covered with Fomblin Y45 oil to avoid torqueing. The assembled sample was fixed in a long, symmetric, non-magnetic sample holder (straw) and closed with two rubber septa. It was then brought to the measuring instrument into a Schlenk tube under argon and introduced into the instrument as quickly as possible to avoid contact with air.

Data collection. Standard data collection was performed in this order:

- dc magnetic susceptibility measurement at 0.5T to validate the molecule's nuclearity and multiplicity, as well as to determine the orbital angular momentum contribution to the magnetic properties,
- MS (magnetization measurement) at 2K from 0 to 5T (or 7T) to look for remnant magnetization, indicative of potential hysteresis behavior,
- ac susceptibility test at 1488Hz under 0Oe and 1000Oe to look for slow relaxation of the magnetization.
- At the optimal temperature, a field-dependent measurement was carried out to determine which amount of field is necessary to observe SMM behavior or to prevent QTM.
- In case of detection of SMM behavior, additional AC and hysteresis measurements were carried out accordingly (see Introduction)

Guide for the characterization of a SMM. Let's imagine that a new sample is to be measured on the SQUID magnetometer, with previous structure determination (SC-XRD) and purity assessment (EA, NMR, or powder XRD). First, at centering the sample in the SQUID, it is already possible

to quickly determine the magnetic nature of it (diamagnetic, paramagnetic). Then, a variable temperature dc measurement from RT to low temperatures will give the following information:

- the purity of the sample (1)
- the value of the product of the temperature and the susceptibility $\chi_M T$ at high temperature, which can be then compared to the tabulated values (specific metal ion, spin value, number of spins, SOC contribution, etc...) (2)
- the estimation of the axial (D) and rhombic (E/D) parameters and of the g values, which further describe the anisotropy of the system (3)
- the presence or absence of magnetic or dipole-dipole coupling (4)

From (1) and (2), the composition of the sample can be verified in terms of magnetic purity, especially when elemental analysis or NMR spectroscopy are challenging. (2) gives some magnetic information specific to the metal ion(s) contained in the sample and hints the SOC contribution to the magnetic susceptibility. Indeed, a specific metal ion in a specific magnetic spin state will give a different signature if it is modelled as a spin-only system (S) or if both the spin and the orbital angular momenta are non-negligible (presence of SOC, description with J or S and L). The values obtained in (3) describes the anisotropy of the sample and should give a first estimate of the energy barrier U ($U \approx |2D|$). The values are extracted through a fit constructed on the relevant Hamiltonian

The full Hamiltonian would be:

$$\hat{H} = \hat{H}_{e-} + \lambda \hat{L}\hat{S} + \hat{H}_{CF} + \hat{H}_{Zeem} \text{ (Eq. 4.7)}$$

where \hat{H}_{e-} is the electron-electron interaction

$\lambda \hat{L}\hat{S}$, the spin-orbit coupling (SOC)

together giving $(\hat{H}_{e-} + \lambda \hat{L}\hat{S})$, the contribution of the free ion

\hat{H}_{CF} , the crystal field splitting (upon addition of ligands to the free ion)

\hat{H}_{Zeem} , the Zeeman splitting (upon application of an external field to the complex)

Herein, the following anisotropic spin Hamiltonian taking the ZFS and Zeeman splitting into account was used:

$$\hat{H} = \mu_B (S_x g_x B_x + S_y g_y B_y + S_z g_z B_z) + D \left[\hat{S}_z^2 - \frac{1}{3} S(S+1) + \frac{E}{D} (\hat{S}_x^2 - \hat{S}_y^2) \right] \text{ (Eq. 4.8)}$$

where S_i is the spin operator, g_i the operators of the g -tensor, and B_i the anisotropic values of the external magnetic field.

Finally, information extracted from step (4) will help assess the need for subsequent experiments, such as magnetic dilution in a diamagnetic matrix (to avoid dipole-dipole coupling or intermolecular magnetic coupling). In multinuclear compounds, it will provide information on the type of magnetic coupling between the paramagnetic centers (antiferromagnetic or ferromagnetic), the strength of this coupling, and the number of magnetic centers involved. If

the sample contains a transition metal, additional variable temperature variable field (VTVH) experiments will be conducted at 7T, 4T and 1T from 2K up to 50 or 100K to populate the higher-lying energy levels and therefore better assess the ZFS parameter. If the sample contains a 4f-element, the ZFS parameter D becomes an obsolete and inaccurate description of the anisotropy, due to the extremely strong SOC. Therefore, the additional VTVH experiment is not necessary in this case. Moving forward, the dc magnetization of the sample can be measured at 2K from 0T to 7T upwards and downwards, allowing to observe the magnetic behavior of the sample in the presence of an applied field. Additionally, if the upwards and downwards curves do not match, it may be a hint for the presence of a magnetic hysteresis. A zero-field cooled/ field-cooled (zfc/fc) experiment can also reveal the divergence of magnetic behavior at a certain temperature, which is indicative of magnetic blocking. In both cases, subsequent hysteresis measurements should be performed (at various temperatures, various sweep rates, etc). A series of test ac measurements can follow in order to determine the presence of slow relaxation processes. The temperature-dependency of the ac susceptibility at maximal frequency (1000 or 1500 Hz) indicates the highest temperature at which slow magnetic relaxation of the magnetization can be measured on the instrument. For example, if the curve shows a maximum at 10 K, it means that slow magnetic relaxation should be detectable up to 10 K. If there is no maximum, then the sample does not show any slow magnetic relaxation and is not a SMM. This test can be done at different dc field values. While doing so, it is possible to access the following information:

- the presence or absence of slow magnetic relaxation at zero applied dc field (pure SMM behavior)
- the highest temperature at which slow magnetic relaxation at zero field is measurable by the instrument
- the presence or absence of slow magnetic relaxation with applied dc field (field induced SMM behavior)
- the highest temperature at which slow magnetic relaxation with applied field is measurable by the instrument
- the optimal dc field which allows to reach the highest ac susceptibility value for the sample

Depending on the results in these test experiments, different variable frequency ac susceptibility measurements must be performed. This gives access to the optimal applied field and to the maximal temperature at which ac susceptibility shall be measured. These dynamic susceptibility measurements, containing both the in- (χ') and out-of-phase (χ'') signals of the ac susceptibility, will subsequently allow us to access the values for the effective energy barrier and the characteristic relaxation time τ_0 of the sample. Additionally, the qualitative shape of the curves and further analysis of the data will highlight the different relaxation processes occurring in the sample. Detailed description of the ac susceptibility curves will be given in the next chapters for each sample when relevant. The final step of the characterization of this sample (if it is indeed a SMM!) consists in reading the relaxation times τ for each temperature of the ac data acquisition. It is possible to do so manually, as described by Tang *et al.*¹⁹³ In this work, the software CC-Fit developed by Chilton *et al.*^{193,195} was used to this purpose. Upon the construction of a Cole-Cole

plot (χ'' vs χ'), it extracts each relaxation time τ per temperature. The temperature dependency of the relaxation time is then assessed following Eq 4.9, usually thanks to two plots: an Arrhenius plot of $\ln(\tau)$ vs T and a plot of τ^{-1} vs T . Together, they provide information about the type of relaxation processes and the characteristic parameters of the sample, including the effective energy barrier to spin reversal U_{eff} . More details will be given in the following chapters for each of the herein presented compounds.

$$\tau^{-1} = AH^4T + \tau_0^{-1}e^{(U_{eff}/k_B T)} + \tau_{QTM}^{-1} + CT^n \text{ (Eq 4.9)}$$

Direct Orbach QTM Raman

where A, C and n are constants, H the applied magnetic field, τ_0 the initial characteristic relaxation rate for the Orbach process, U_{eff} the effective energy barrier to spin reversal, k_B the Boltzmann constant, and τ_{QTM} the relaxation rate for QTM.

If irrelevant, a term of Eq 4.9 can be removed or equaled to zero (for example in the absence of external magnetic field).

Data work-up and fitting. Each raw data file was worked-up on OriginPro 8.5 or 9.0.²³¹ Each data file for the measured magnetic moment was corrected for the diamagnetic contribution of the gelatin bucket and of the inert oil according to $M_{dia} = \chi_g \cdot m \cdot H$, with experimentally obtained gram susceptibility of gelatin bucket ($\chi_g = -5.70 \cdot 10^{-7}$ emu/(g·Oe)) and of the oil ($\chi_g = -3.51 \cdot 10^{-7}$ emu/(g·Oe)). The molar susceptibility χ_M data were corrected for the diamagnetic contribution according to $\chi_{M,dia}(\text{sample}) = -0.5 \cdot M \cdot 10^{-6} \text{ cm}^3 \cdot \text{mol}^{-1}$. Temperature-independent paramagnetism (TIP) was included according to $\chi_{calc} = \chi + \text{TIP}$.⁷² Fitting of the $\chi_M T$ and VTVH data was performed with the *Julx-v16/Jul-2s* program²³² developed by E. Bill at the MPI of Mulheim an der Ruhr or with the PHI program developed by N. F. Chilton at the University of Manchester.²³³, and compared to theoretical results based on the following formula:

$$\sqrt{\frac{3k_B}{N_A \cdot \mu_B^2}} \cdot \sqrt{\chi_M \cdot T} = g_e \sqrt{S(S+1)} \text{ (Eq. 4.10)}$$

$$\text{and } \mu_{eff} = 2.828 \sqrt{\chi_M T} = 2 \sqrt{S(S+1)} = \sqrt{n(n+2)} \mu_B \text{ (Eq. 4.11)}$$

where $k_B = 1.38 \cdot 10^{-23} \text{ J} \cdot \text{K}^{-1}$; $N_A = 6.02 \cdot 10^{23} \text{ mol}^{-1}$ (Avogadro's number), $\mu_B = 9.27 \times 10^{-24} \text{ J} \cdot \text{T}^{-1}$ (Bohr's magneton); $g_e = 2$; μ_{eff} = effective magnetic moment ; S = spin; n = number of unpaired electrons.

Fitting of the Cole-Cole plots were obtained *via* the CC-Fit program.^{193,195} The extracted values of the Cole-Cole plots were further used to construct the Arrhenius plot to determine the value of U_{eff} . Magnetic anisotropy axis in dysprosium complexes were obtained from experimental X-ray xyz data files computed in the MAGELLAN program developed by N.F. Chilton at the University of Manchester.¹⁷²

4.1.4. Computational calculations

CASSCF/NEVTP-2. Multi-configurational calculations based on the X-Ray geometry from experimental single crystal X-ray diffraction experiments were used to calculate the electronic

energy levels of the cobalt complexes in **Chapter 3**. Correlated calculations were carried out using Complete Active Space Self Consistent Field (CASSCF) in combination with N-Electron Valence Perturbation Theory to second order (NEVPT2) as implemented in the ORCA package.^{170,171} The d^7 configuration of Co(II) gives rise to ten $S = 3/2$ and forty $S = 1/2$ electronic multiplets. Nonrelativistic CASSCF energy levels and wave functions have been computed averaging over the electron densities of all considered states and taking an active space with 7 electrons distributed over the 5 3d-MOs (CAS(7,5)). Spin-orbit coupling (SOC) was taken into account using a mean field spin-orbit coupling operator. Mixing of non-relativistic CI eigenfunctions and splitting of the corresponding eigenvalues are accounted for by Quasi Degenerate Perturbation Theory (QDPT). The Douglas-Kroll-Hess triple- ζ DKH-def2-TZVP basis-set was used when possible or the def2-TZVP/C basis-set for structures with a high number of atoms (7_Co).

AILFT. *Ab initio* ligand field theory calculations were based on the wave functions obtained from CASSCF-NEVPT2 calculations thanks to the *act orbs dorbs* command in the input file.¹⁶³

Output file analysis. Coordinates were obtained from experimental X-ray data. For the section 3.3, before the calculations, the molecular coordinate system was chosen in agreement with the axes for an ideal D_{2d} symmetry (Avogadro software²³⁴). The origin of the coordinate system thus became the cobalt ion, while the z axis pointed approximatively towards the sulfur atom and the xy plane locates equidistantly from the four coordinating nitrogen atoms. For 4'_Co, the bite angle N-Co-N was modified per hand in the Avogadro software by selecting the two binding N'Bu groups and rotating them symmetrically from the Co-S axis.

For 1_Co and 2_Co, the molecules were rotated so that the origin of the coordinate system becomes the cobalt ion, while the xy plane locates in the (N1, N2, N4) plane and the z axis points perpendicularly out of this plane.

NEVPT-2 calculations gave more realistic results than pure CASSCF calculations. Therefore, the presented results in the work are relying on the results obtained after the application of the NEVPT-2 perturbation.

The values of the D and g -tensors, the populations of the 3d orbitals and the Kramers' doublets (KD) energy levels are reported from the NEVPT-2 calculations and the energy levels are reported from AILFT calculations. The non-integer d population values for the $d_{x^2-y^2}$ and d_{xy} orbitals were obtained from calculation of the wavefunctions. The application of a tetrahedral crystal field to a free Co^{2+} corresponds to the splitting of the term 4F into the $^4A_{2g}$, $^4T_{2g}$, and $^4T_{1g}$ states. Upon distortion along the z axis lowering the symmetry to the point group D_{2d} , the $^4T_{2g}$ term splits and the resulting 4B_2 state shifts closer to the ground state (4B_1). In the D_{2d} point group, these two states are associated to the following electron configurations (and hence d-orbital populations):

$$^4B_1: d_{xy}^1 d_{yz}^1 d_{z^2}^2 d_{xz}^1 d_{x^2-y^2}^2$$

$$^4B_2: d_{xy}^2 d_{yz}^1 d_{z^2}^2 d_{xz}^1 d_{x^2-y^2}^1$$

Each of the two lowest CASSCF states were found to consist essentially of a single Slater determinant (more than 95%):

$$(1^{\text{st}} \text{ state}) d_{xy}^2 d_{yz}^1 d_{z^2}^2 d_{xz}^1 d_{x^2-y^2}^1$$

$$(2^{\text{nd}} \text{ state}) d_{xy}^1 d_{yz}^1 d_{z^2}^2 d_{xz}^1 d_{x^2-y^2}^2$$

Therefore, each CASSCF state can be associated with 4B_1 and 4B_2 . From the application of the SOC in the calculation, the Kramers' doublets (KD) were obtained as linear combinations of the first and second states, therefore of the 4B_1 and 4B_2 states, the coefficients being the weight of the states. For example, for **4_Co**:

$$(\text{KD1}): 0.62 |^4B_2\rangle + 0.37 |^4B_1\rangle$$

$$d_{xy}^{1.62} d_{yz}^1 d_{z^2}^2 d_{xz}^1 d_{x^2-y^2}^{1.37}$$

For additional details, this method was previously published elsewhere.¹¹⁴

Computational assessment of spectroscopic features. Atom coordinates were obtained directly from experimental X-ray datasets. UV-vis spectroscopy features were determined through TD-DFT calculations using RIJCOSX-approximation with the CAM-B3LYP functional and def2-SVP basis sets on all atoms for 10 states. EPR predictions were obtained from orca calculations using RIJCOSX approximation with the PBE0-D3BJ and def2-tzvp basis sets on all atoms. Spin density plots and TD-DFT plots were drawn with the Chemcraft software.²³⁵

4.1.5. Additional characterization methods.

NMR. Inside of an argon glovebox, Young NMR tubes were charged with approx. 10mg of dissolved pure crystalline material (in 1mL of deuterated solvent). Deuterated solvents were obtained from Euriso-Top GmbH, dried over sodium/potassium alloy, distilled by trap-to-trap transfer in *vacuo* and stored on molecular sieves for at least a week prior to use. Spectra were recorded at variable temperatures at a Bruker Advance 300, a Bruker Advance 400, or a Bruker Advance 500 NMR spectrometer. All chemical shifts δ are given in ppm, relative to the residual proton signal of the deuterated solvent and the additional internal TMS reference. If necessary, assignments of the chemical shifts were checked by two-dimensional correlation spectra.

EA. Elemental analysis was performed as a combustion analysis by the Analytic Laboratory of the Institute of Inorganic Chemistry of the University of Göttingen with an Elementar Vario EL III device. The inclusion of argon, from canning in an argon glovebox, unfortunately led to systematic errors. Additionally, the sensitivity and precision of the instrument systematically decreased in the case of samples containing both alkali metals and sulfur atoms.

MS. Mass spectra were recorded at the Mass spectrometry facility of the Faculty of Chemistry of the University of Göttingen applying a Liquid Injection Field Desorption Ionization-technique (LIFDI) on a JEOL accuTOF instrument with an inert-sample application setup under argon atmosphere. The injection capillary was washed several times with dry, distilled and inertly injected toluene before the samples were injected. Samples usually had a concentration of 1 - 2

mmol/L in pentane, toluene or THF and were prepared in an argon glovebox. Unfortunately, in the presence of heavy Ln elements, the recorded spectra inevitably showed a high amount of fragment peaks, which prevented further interpretation of the data. Complexes containing transition metals, however, were detectable and characterized through this method. ESI-MS measurements were not possible neither for any Ln-containing samples, nor for 3d-metal containing samples, so that only the LIFDI-MS measurement method was systematically probed for all samples.

IR. Infrared spectra were recorded neat, in an argon glovebox. The data were recorded with a Bruker ALPHA FT-IR spectrometer with Platinum ATR module, visualized with the Opus program and worked up with the OriginPro 8.5 or 9.0 program.²³¹

UV-vis. Experimental UV/Vis spectra were recorded on an Agilent Cary 60 or an Agilent Cary 50 spectrometer using quartz cuvettes fitted with Young-type Teflon-valves. The obtained data were worked up with the OriginPro 8.5 or 9.0 program.²³¹

EPR. EPR spectra were recorder on a EPR Bruker ELEXSYS E 500 Spectrometer at the microwave frequency of 9388.2 MHz. The 10⁻³M diluted solutions were freshly prepared inside of an argon glovebox and immediately inserted in the instrument for measurement at room temperature. The g factor was determined according to the following formula:

$$h\nu = g\mu_B B_0 \text{ (Eq. 4.12)}$$

with B_0 the magnetic field at which resonance occurs.

The predicted resonance for the free electron ($g = g_e = 2$) should occur at 3350 G.

The data was worked up with the OriginPro 8.5 or 9.0 program.²³¹

Cyclic voltammetry. CV was measured using glassy carbon (1.6 mm diameter) working and Pt wire counter electrodes and an Ag wire pseudo-reference electrode in a fritted sample holder compartment and referenced against the [Fe(Cp)₂]^{+ / 0} couple. A 0.1 M (nBu₄N)PF₆ solution in THF was used as electrolyte. The data was worked up with the OriginPro 8.5 or 9.0 program.²³¹

4.2. Compound synthesis and characterization

4.2.1. $\{\text{Ph}(\text{N}^t\text{Bu})\text{S}(\text{BuNH})\}_2$ ($\{1_H\}_2$)

The ligand **2_Li** (1eq, 200mg, 0.77mmol) was dissolved in pentane and $\text{H}_3\text{N}^t\text{BuCl}$ (1eq, 84.8mg, 0.77mmol) was added to the clear yellowish solution in one portion. The white suspension did not dissolve over time and more white material precipitated after 2-3h. The reaction mixture also turned more yellow. Upon overnight stirring, the mixture was filtered over celite to afford a clear yellowish solution and the solvent was volumetrically reduced to a minimal amount. Crystals suitable for X-ray diffraction were obtained over a week from a pentane solution stored at -35°C . Crystalline yield: 35%. Anal Calc for $\text{C}_{14}\text{H}_{24}\text{N}_2\text{S}$ (252.42 g/mol) C, 66.62; H, 9.58; S, 12.70; N 11.10; Found: C, 66.95; H, 10.21; S 12.68; N 11.20. ^1H -NMR (300 MHz, $\text{THF-}d_8$): δ (ppm) = 7.83 (m, 2H, *o*-H), 7.34 (m, 3H, *p* and *m*-H), 4.35 (s, 1H, N-H), 1.28 (s, 18 H, ^tBu -H). ^{13}C -NMR (300 MHz, $\text{THF-}d_8$): δ (ppm) = 127.62 (*p*-C), 128.67 (*m*-C), 128.30 (*o*-C), 55.03 (^tBu -C), 32.84 (^tBu terminal-C).

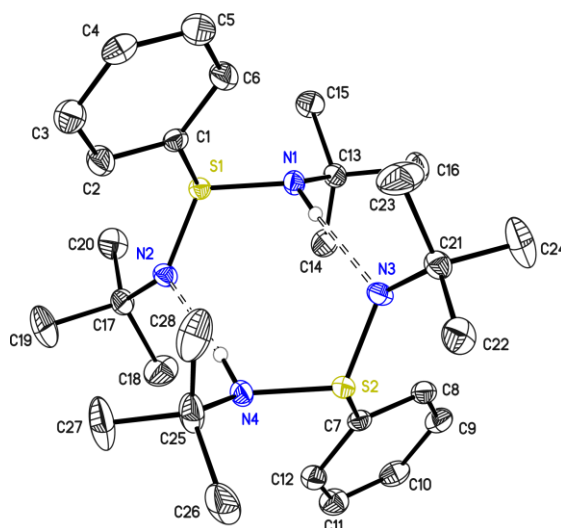


Figure 4.2.1: Crystal structure of $\{1_H\}_2$. The asymmetric unit contains the dimer. Thermal ellipsoids are shown at the 50% probability level.

Structure code	2_protonated	CCDC Number	2076511
Empirical Formula	$\text{C}_{28}\text{H}_{48}\text{N}_4\text{S}_2$	μ [mm^{-1}]	0.199
Formula weight [g mol^{-1}]	504.82	F(000)	1104
Sample temperature [K]	100(2)	θ range [$^\circ$]	1.658 to 30.854
Wavelength [\AA]	0.71073	Reflections collected	92257
Crystal System	Monoclinic	Unique Reflections	9354
Space group	$P2_1/c$	R_{int}	0.1034
Unit cell dimensions [\AA]	$a=9.6385(16)$	Completeness to θ_{max} [%]	100
	$b=20.075(3)$	restraints/parameters	1 / 327
	$c=16.207(3)$	GooF	1.031
Volume [\AA^3]	3004.4(9)	R1 (all data)	0.0585
Z	4	wR2 (all data)	0.1040
Crystal dimensions [mm]	0.176 x 0.116 x 0.099	max. diff. peak / hole [$\text{e}\text{\AA}^{-3}$]	0.446 and -0.312
Crystal shape and color	Colorless blocks		

DOSY-NMR of $\{1_H\}_2$.

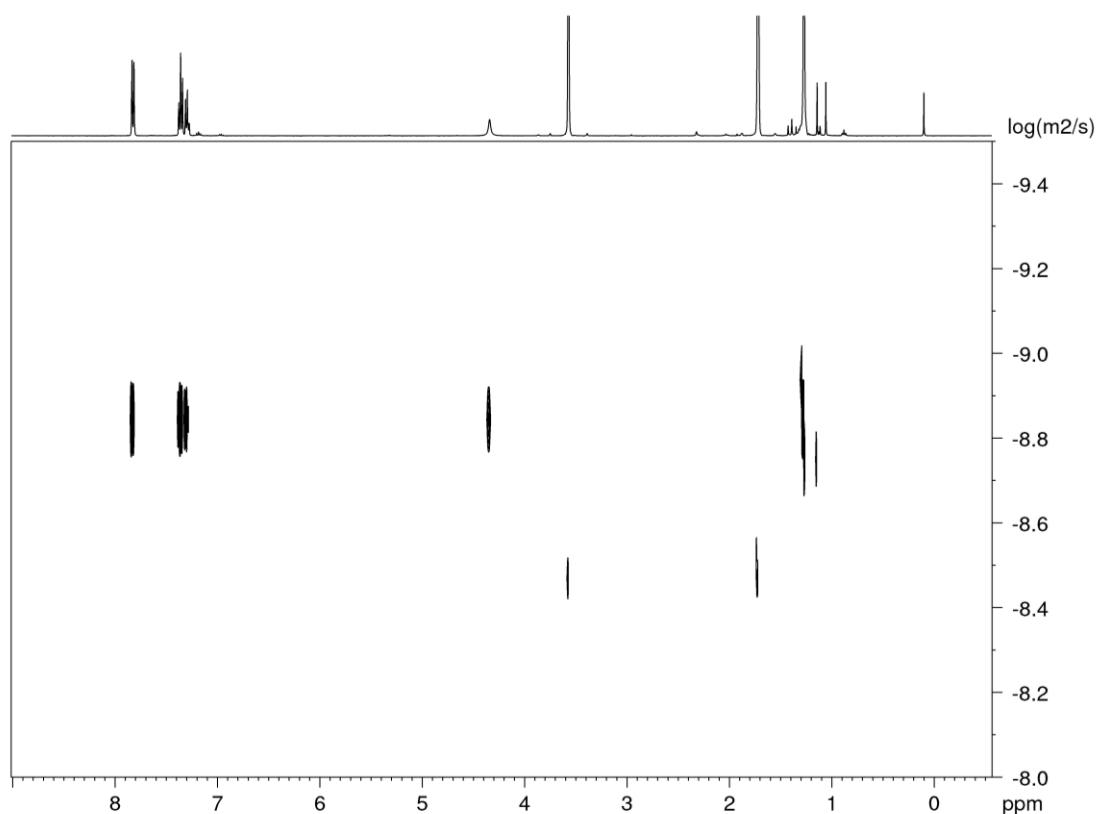


Figure 4.2.1.1. DOSY-NMR of $\{1_H\}_2$ in deuterated THF, measured by A. Kreyenschmidt. The normalized diffusion coefficient is $\log(D_{x, \text{norm}}) = -8.9434$, giving $MW_{\text{det, merge}} = 269 \text{ g/mol}$ ($MW_{\text{dif}} = -6\%$) and $MW_{\text{det, DSE}} = 258 \text{ g/mol}$ ($MW_{\text{dif}} = -2\%$). The MW of the monomer species is 252.42 g/mol . Thus, the compound is a monomer in solution.

$MW_{\text{det, merge}}$: molecular weight without taking the geometry into account;

$MW_{\text{det, DSE}}$: molecular weight with dissipated spheres and ellipsoids;

MW_{dif} : % error to the molecular weight of the monomeric species.

4.2.2. $[(\text{PhS}(\text{NtBuH})_2)_2][[(\text{'BuNH})\text{PhS}(\text{'BuN}(\text{LiCl}_2))_2] \{(\text{8}_\text{H}_4)(\text{8}_\text{H}_2\text{LiCl}_2)\}]$

In an argon glovebox, the ligand **8_Li** (1eq, 50mg, 9.7 μmol) was combined with $\text{H}_3\text{N}^+\text{BuCl}$ (2eq, 21.3mg, 19.4 μmol) in 5 mL THF. The solution turned yellow and clear. After ten minutes, a white cloud was observed and the white solid precipitated. The solution was let to stir for eight hours, upon which the precipitate was removed by filtration through celite and the clear solution subsequently dried. The crude product was dissolved in a minimal amount of THF and layered with pentane. Crystals were obtained over a week. Crystalline yield $\approx 10\%$. No further analysis was performed the yield was very poor.

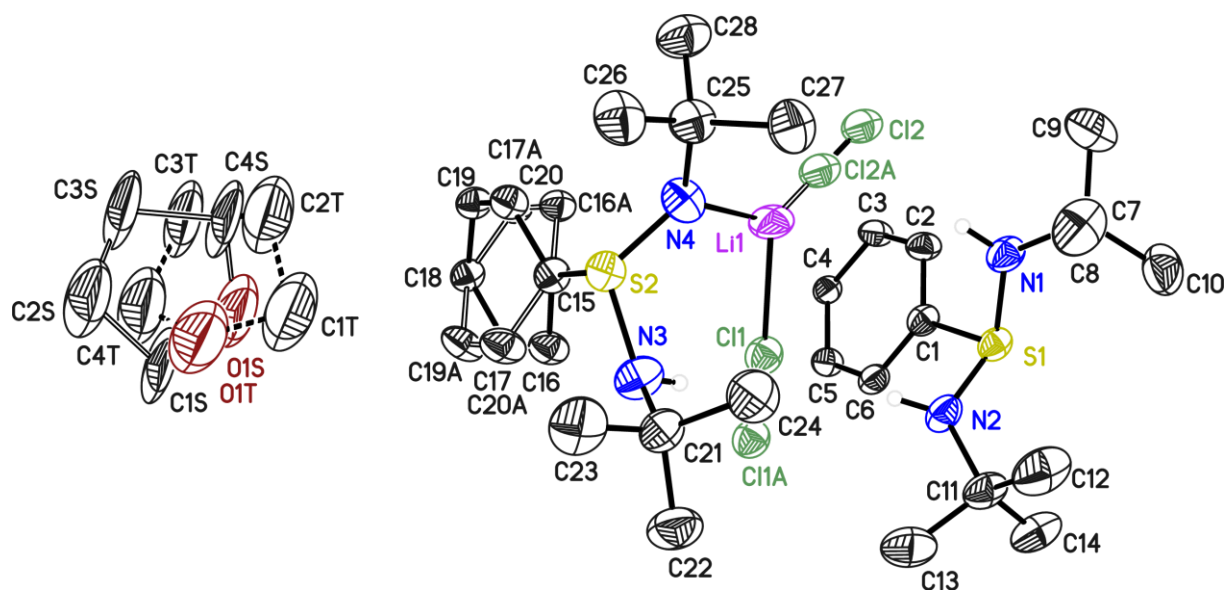


Figure 4.2.2. Asymmetric unit of $\{(\text{8}_\text{H}_4)(\text{8}_\text{H}_2\text{LiCl}_2)\}$. Hydrogens (except N-H hydrogens) are omitted for clarity. Thermal ellipsoids are depicted at the 50% probability level.

Structure code	8_protonated	CCDC Number	/
Empirical Formula	$\text{C}_{60}\text{H}_{102}\text{Cl}_4\text{Li}_{1.8}\text{N}_8\text{OS}_4$	μ [mm^{-1}]	0.323
Formula weight [g mol^{-1}]	1233.99	F(000)	2654
Sample temperature [K]	100(2)	θ range [$^\circ$]	1.452 to 25.349
Wavelength [\AA]	0.71073	Reflections collected	142406
Crystal System	Tetragonal	Unique Reflections	6572
Space group	$P4_2/c$	R_{int}	0.0676
Unit cell dimensions [\AA]	$a = 16.871(2)$	Completeness to θ_{max} [%]	99.9
	$b = 16.871(2)$	restraints/parameters	479 / 490
	$c = 25.216(3)$	GooF	1.097
Volume [\AA^3]	7177.2(19)	R1 (all data)	0.0625
Z	4	wR2 (all data)	0.1257
Crystal dimensions [mm]	0.345 x 0.237 x 0.229	max. diff. peak / hole [$\text{e}\text{\AA}^{-3}$]	0.655 and -0.214
Crystal shape and color	Colorless blocks		

4.2.3. $[\text{S}(\text{N}^t\text{Bu})_3]_2\text{K}_3 (\{\text{L}_2\}_2\text{K}_3)$

In an argon glovebox, L_3 (2eq, 300mg, 1.2mmol) and potassium metal (3eq, 72mg, 1.8mmol) were reacted in 2-3 mL toluene. Upon heavy stirring for one hour while the mixture turns troubled and light blue, the potassium was triturated in order to dissolve the blue product forming on its surface. The solution then turned deep blue, was filtered and the solvent removed *in vacuo*. Crystals were grown from a highly concentrated toluene solution at -35°C . Crystalline yield: 35%. Attempts to improve the yield by stirring longer after trituration resulted in solution color loss after a few minutes. The reaction itself should not last longer than one hour. Anal. Calc. for $\text{C}_{48}\text{H}_{108}\text{K}_3\text{N}_{12}\text{S}_4$ (one radical molecule and two L_3 molecules): $M = 1097.66 \text{ g/mol}$. C, 52.46; H, 9.91; N, 15.29; S, 11.67. Found: C, 53.05; H, 9.65; N, 14.98; S, 11.97.

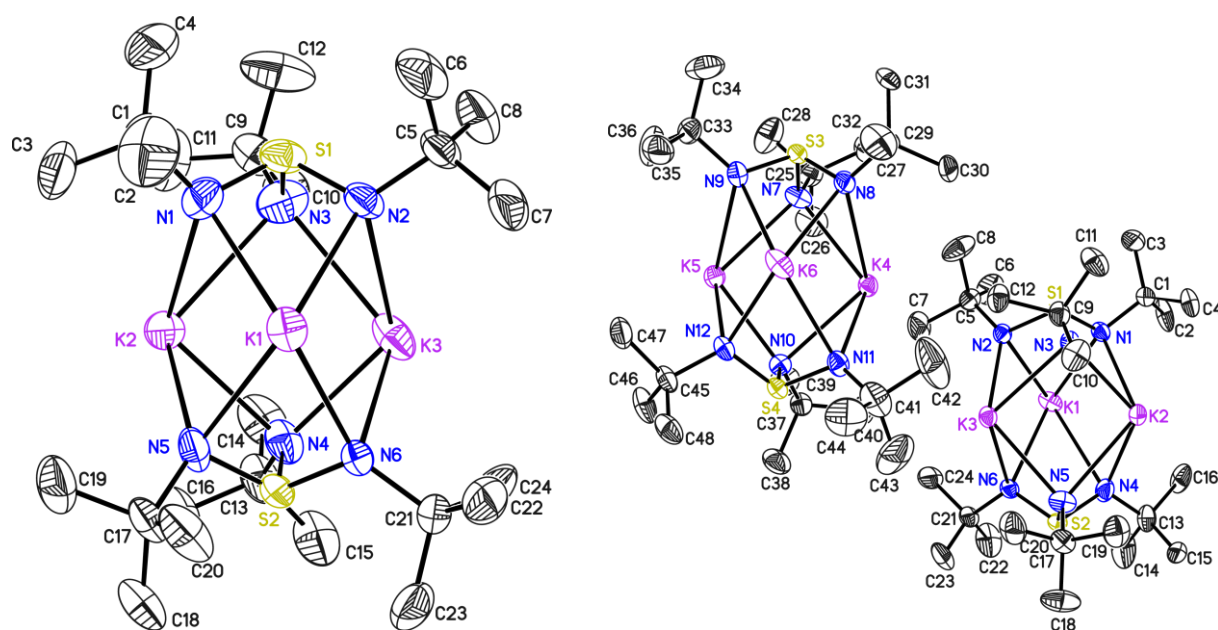


Figure 4.2.3. Crystal structure of $\{\text{L}_2\}_2\text{K}_3$ at 120K (left) and 100K (right). ^tBu disorders and hydrogens are omitted for clarity. Thermal ellipsoids are depicted at the 50% probability level.

Structure code	Radical_120K (twin)	CCDC Number	2117636
Empirical Formula	$\text{C}_{24}\text{H}_{54}\text{K}_3\text{N}_6\text{S}_2$	$\mu [\text{mm}^{-1}]$	0.539
Formula weight $[\text{g mol}^{-1}]$	608.15	$F(000)$	1316
Sample temperature [K]	120(2)	θ range $[\circ]$	1.745 to 26.449
Wavelength $[\text{\AA}]$	0.71073	Reflections collected	
Crystal System	Monoclinic	Unique Reflections	7406
Space group	$P2_1/n$	R_{int}	
	$a=12.6234(4)$	Completeness to θ_{max}	100
Unit cell dimensions $[\text{\AA}]$	$b=15.9110(6)$ $\beta=102.476(2)$	restraints/parameters	1304 / 515
	$c=17.5763(6)$	GooF	1.030
Volume $[\text{\AA}^3]$	3446.9(2)	R1 (all data)	0.1583
Z	4	wR2 (all data)	0.1889
Crystal dimensions [mm]	0.201 x 0.123 x 0.094	max. diff. peak / hole	0.571 and -0.508
Crystal shape and color	Deep blue blocks	$[\text{e}\text{\AA}^{-3}]$	

Structure code	Radical_100K (twin)	CCDC Number	2117635
Empirical Formula	C ₄₈ H ₁₀₈ K ₆ N ₁₂ S ₄	μ [mm ⁻¹]	0.540
Formula weight [g mol ⁻¹]	1216.30	F(000)	2632
Sample temperature [K]	100(2)	θ range [°]	1.565 to 28.310
Wavelength [Å]	0.71073	Reflections collected	104467
Crystal System	Monoclinic	Unique Reflections	17091
Space group	P2 ₁ /c	R _{int}	0.0613
Unit cell dimensions [Å]	$a = 23.665(3)$	Completeness to θ_{\max} [%]	100
	$b = 16.005(2)$ $\beta = 109.23(2)$	restraints/parameters	1596 / 847
	$c = 19.223(3)$	GooF	1.103
Volume [Å ³]	6874.6(18)	R1 (all data)	0.0662
Z	4	wR2 (all data)	0.1724
Crystal dimensions [mm]	0.500 x 0.367 x 0.184	max. diff. peak / hole [eÅ ⁻³]	1.723 and -0.969
Crystal shape and color	Deep blue blocks		

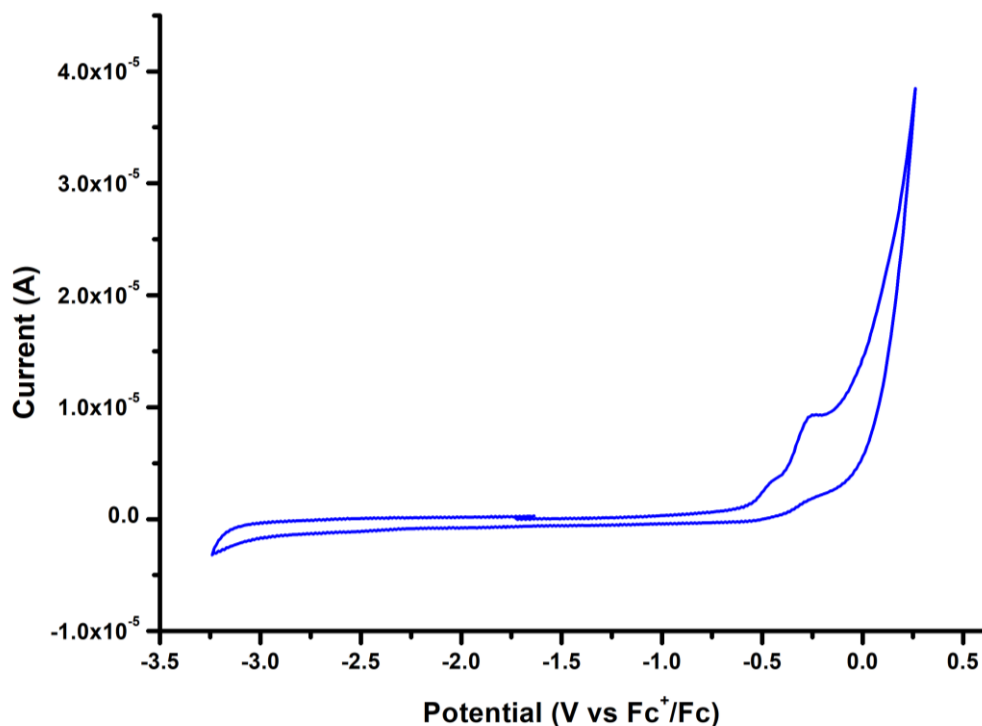


Figure 4.2.3.1. Cyclic voltammogram of **L**₂ in THF at a scan rate of 200 mV/s. An irreversible oxidation wave at about -0.25 V is visible. Unfortunately, direct CV investigation of the radical species was impossible due to electrolyte and solvent incompatibilities.

4.2.4. Dy(PPh₂CH₂S(NⁱBu)₂)₂Cl₂Li(THF)₂ (1_Dy)

DyCl₃ (0.13 mmol, 35.3 mg, 1eq) and Li(PPh₂CH₂S(NⁱBu)₂) (0.26 mmol, 100 mg, 2eq) were dissolved together in THF (4mL) and a yellow solution was obtained. After stirring for 1d, the clear solution was filtered, dried *in vacuo* and the crude off-white product was washed with pentane. Small colorless plate-shaped crystals were obtained from the slow evaporation of pentane into a high-concentrated THF solution. Crystalline yield: 75%, IR (neat): 3056w, 2937w, 2890w, 1418m, 1362m, 1187m, 948m, 828m, 737s, 681s, 498m cm⁻¹. Anal. Calc. for C₅₀H₇₆Cl₂DyLiN₄O₂P₂S₂ (M = 1131.37g/mol): C, 53.07; H, 6.77; N, 4.95; S, 5.67. Found: C, 52.83; H, 6.81; N, 5.36; S, 5.67

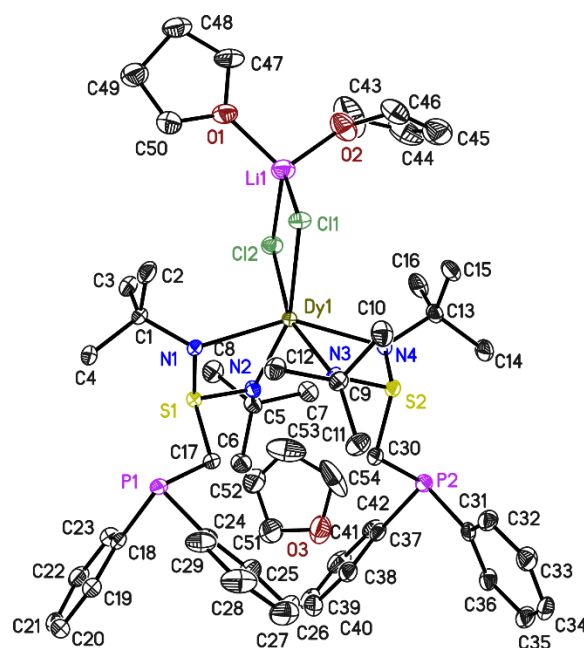


Figure 4.2.4. Molecular structure of 1_Dy. The asymmetric unit contains one complex molecule and one THF molecule. Thermal ellipsoids are shown at 50% probability level. Hydrogens are omitted for clarity.

Structure code	1_Dy	CCDC Number	2072893
Empirical Formula	C ₅₄ H ₈₄ Cl ₂ DyLiN ₄ O ₃ P ₂ S ₂	μ [mm ⁻¹]	1.537
Formula weight [g mol ⁻¹]	1203.65	F(000)	1250
Sample temperature [K]	100(2)	θ range [°]	1.233 to 26.373
Wavelength [Å]	0.71073	Reflections collected	116196
Crystal System	Triclinic	Unique Reflections	11960
Space group	<i>P</i> $\bar{1}$	R _{int}	0.0709
Unit cell dimensions [Å]	<i>a</i> = 10.820(2) α = 74.80(2)	Completeness to θ_{\max} [%]	100
	<i>b</i> = 16.445(3) β = 84.60(4)	restraints/parameters	0 / 634
Volume [Å ³]	<i>c</i> = 17.159(3) γ = 85.10(2)	GooF	1.032
	7828.0(19)	R1 (all data)	0.0362
Z	2	wR2 (all data)	0.0580
Crystal dimensions [mm]	0.308 x 0.183 x 0.086	max. diff. peak / hole [eÅ ⁻³]	0.630 and -0.525
Crystal shape and color	Colorless blocks		

4.2.5. Dy(PhS(N^tBu)₂)₂Cl₂Li(THF)₂ (2_Dy)

DyCl₃ (0.19 mmol, 52 mg, 1eq) and Li(PhS(N^tBu)₂) (0.39 mmol, 100 mg, 2eq) were dissolved together in THF (4mL) and a yellow solution was obtained. After stirring for 1d, the clear solution was filtered, dried *in vacuo* and the crude off-white product was washed with pentane. Small colorless plate-shaped crystals were obtained from the slow evaporation of pentane into a high-concentrated THF solution. Crystalline yield: 68%, IR (neat): 3045w, 2951w, 2895w, 1457m, 1361m, 1184m, 1040m, 951s, 828s, 736s, 672s, 527m, 431m cm⁻¹. Anal. Calc. for C₃₆H₆₂Cl₂DyLiN₄O₂S₂ (M = 887.38g/mol): C, 48.73; H, 7.04; N, 6.31; S, 7.31. Found: C, 48.11; H, 7.13; N, 6.41; S, 6.99.

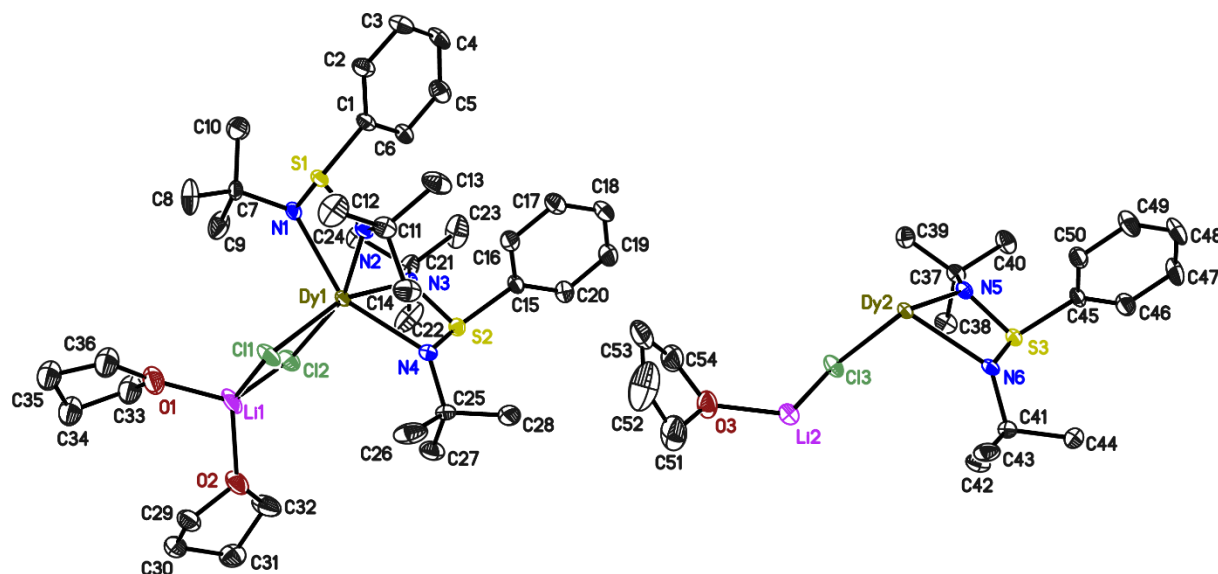


Figure 4.2.5. Asymmetric unit of 2_Dy. The asymmetric unit contains one and a half complex molecule. Thermal ellipsoids are shown at 50% probability level. Hydrogens are omitted for clarity.

Structure code	2_Dy	CCDC Number	2072894
Empirical Formula	C ₅₄ H ₉₃ Cl ₃ Dy _{1.5} Li _{1.5} N ₆ O ₃ S ₃	μ [mm ⁻¹]	2.011
Formula weight [g mol ⁻¹]	1331.03	F(000)	5484
Sample temperature [K]	95(2)	θ range [°]	1.232 to 28.339
Wavelength [Å]	0.71073	Reflections collected	192338
Crystal System	Monoclinic	Unique Reflections	15905
Space group	C2/c	R _{int}	0.0878
	$a = 29.404(4)$	Completeness to θ_{\max} [%]	99.9
Unit cell dimensions [Å]	$b = 20.037(3)$ $\beta = 95.70(2)$	restraints/parameters	0 / 650
	$c = 21.801(4)$	GooF	1.030
Volume [Å ³]	12781(4)	R1 (all data)	0.0584
Z	8	wR2 (all data)	0.0926
Crystal dimensions [mm]	0.378 x 0.313 x 0.273	max. diff. peak / hole [eÅ ⁻³]	1.940 and -1.505
Crystal shape and color	Colorless blocks		

4.2.6. $\text{Dy}(\text{MeS}(\text{N}^t\text{Bu})_3)_2\text{Cl}_2\text{Li}(\text{THF})_2$ (3_Dy)

DyCl_3 (0.074 mmol, 20 mg, 1eq) and $\text{Li}_2(\text{THF})_2(\text{MeS}(\text{N}^t\text{Bu})_3)_2$ (0.074 mmol, 50 mg, 1eq) were dissolved together in THF (4 mL). Upon complete dissolution, the solution turned clear and was let to stir for 1d. It was then filtered, dried *in vacuo* to afford an off-white solid. Large colorless block-shaped crystals were obtained from the slow evaporation of pentane in a high-concentrated THF solution. Crystalline yield: 53%. IR (neat): 3249w, 2944w, 2880w, 1436m, 1344m, 1178m, 1040s, 948s, 820s, 737s, 673s, 535s, 421m cm^{-1} ; Anal. Calc. for $\text{C}_{38}\text{H}_{84}\text{Cl}_2\text{DyLiN}_6\text{O}_3\text{S}_2$ ($M = 977.59\text{g/mol}$): C, 46.69; H, 8.66; N, 8.60; S, 6.56. or for $\text{C}_{34}\text{H}_{76}\text{Cl}_2\text{DyLiN}_6\text{O}_2\text{S}_2 \cdot \text{LiCl}$ ($M = 1019.98\text{g/mol}$): C, 44.75; H, 8.30; N, 8.24; S, 6.26. Found: C, 44.75; H, 7.74; N, 8.15; S, 6.31; 3 contains LiCl impurities.

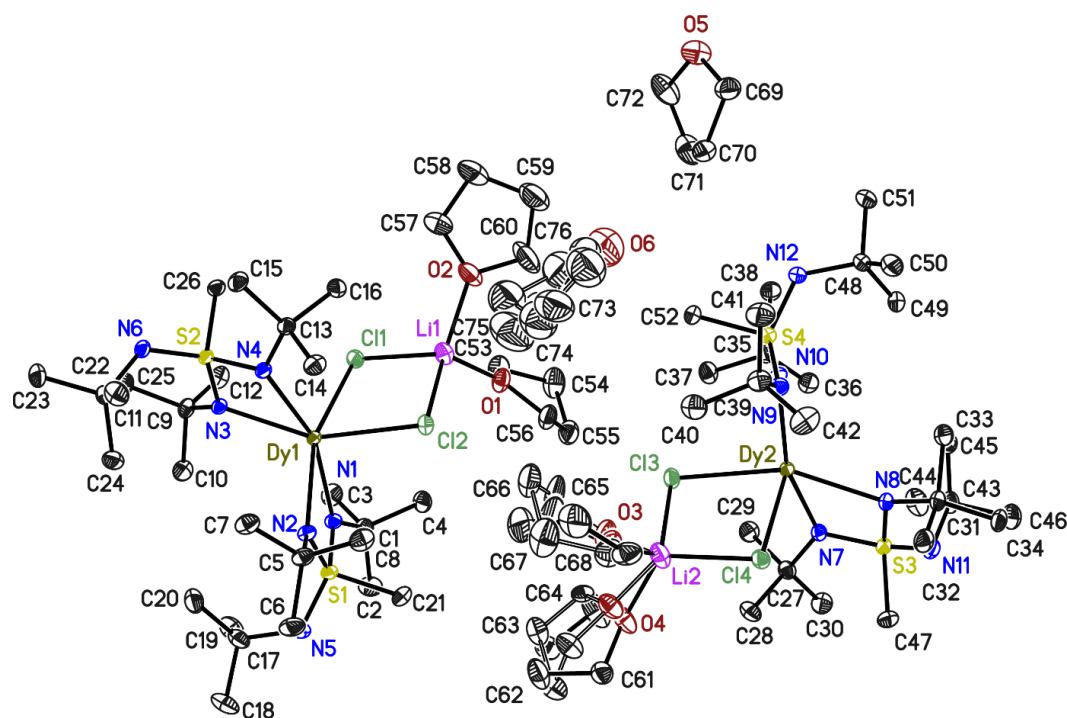


Figure 4.2.6. Molecular structure of 3_Dy. The asymmetric unit contains two complex molecules and one THF molecule. Thermal ellipsoids are shown at 50% probability level. Hydrogens are omitted for clarity.

Structure code	3_Dy	CCDC Number	2072895
Empirical Formula	$\text{C}_{38}\text{H}_{84}\text{Cl}_2\text{DyLiN}_6\text{O}_3\text{S}_2$	μ [mm^{-1}]	1.790
Formula weight [g mol^{-1}]	977.57	F(000)	2052
Sample temperature [K]	100(2)	θ range [$^\circ$]	0.891 to 28.495
Wavelength [\AA]	0.71073	Reflections collected	260661
Crystal System	Triclinic	Unique Reflections	24295
Space group	$P\bar{1}$	R_{int}	0.0308
Unit cell dimensions [\AA]	$a=13.2648(3)$ $\alpha=86.0800(10)$	Completeness to θ_{max} [%]	100
	$b=15.9639(3)$ $\beta=80.3700(10)$	restraints/parameters	794 / 1134
	$c=23.2183(5)$ $\gamma=83.5440(10)$	GooF	1.134
Volume [\AA^3]	4810.47(18)	R1 (all data)	0.0257
Z	4	wR2 (all data)	0.0535
Crystal dimensions [mm]	0.293 x 0.272 x 0.216	max. diff. peak / hole [$\text{e}\text{\AA}^{-3}$]	2.304 and -1.247
Crystal shape and color	Colorless blocks		

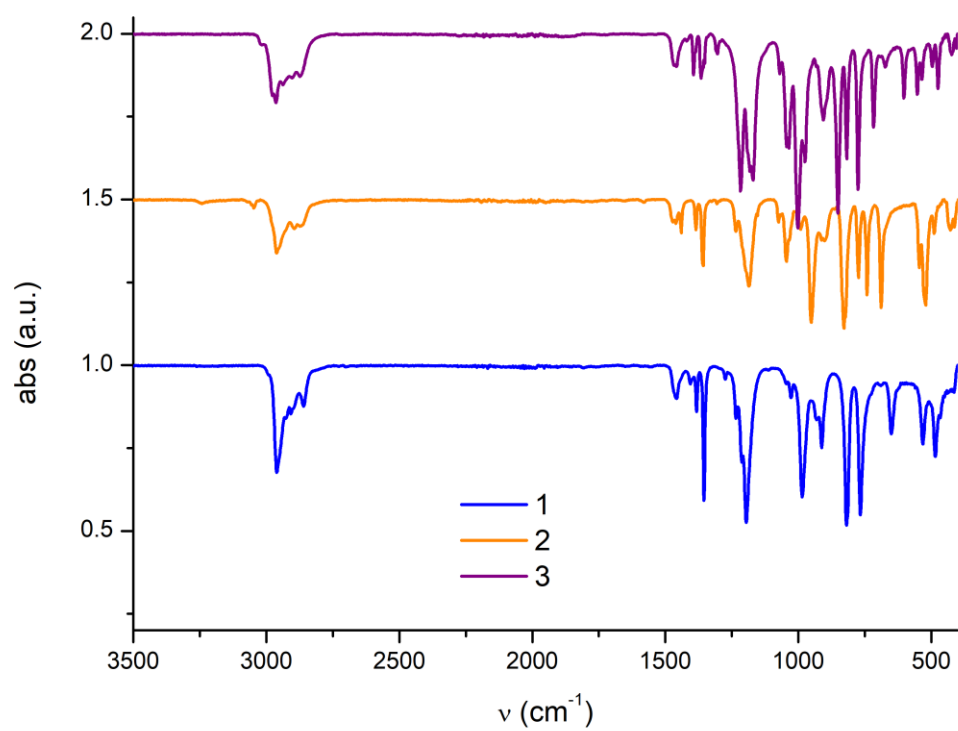


Figure 4.2.6.1. IR spectra for 1_Dy (1), 2_Dy (2) and 3_Dy (3)

4.2.7. $[\{\text{Ph}_2\text{PCH}_2\text{S}(\text{N}^i\text{Bu})_3\}_2\text{DyCl}]$ (4_Dy)

The complex 4_Dy was first characterized by J. Jung¹⁹⁶ and then resynthesized for further reaction and magnetic analysis, as presented in the present work. The ligand $[\text{K}\{\text{Ph}_2\text{PCH}_2\text{S}(\text{N}^i\text{Bu})_3\}]$ (6_K) (500mg, 1.03mmol, 2 eq) and DyCl_3 (153mg, 0.52mmol, 1 eq) were suspended in toluene (40 mL). THF (0.8 mL) was added and the mixture was stirred for 1d at room temperature. Subsequently, KCl was filtered off and the solvent was removed under reduced pressure. The crude sticky product was dissolved in THF and layered with pentane (1:5 THF/pentane ratio). Crystallization started within hours up to several days at ambient temperature yielding pale yellow crystals that were isolated and washed twice with 1 mL pentane. Crystalline yield: 285 mg, 0.25 mmol (49%); LIFDI-MS: m/z : 1052.4 $[\text{M}-\text{Cl}]^+$; Anal. Calc. for $\text{C}_{50}\text{H}_{78}\text{ClN}_6\text{P}_2\text{S}_2\text{Dy}(\text{C}_{2.25}\text{H}_{4.99}\text{O}_{0.25})$: C, 55.87; H, 7.21; N, 7.57; S, 5.71. Found: C 55.80, H 7.21, N 7.57, S 5.92.

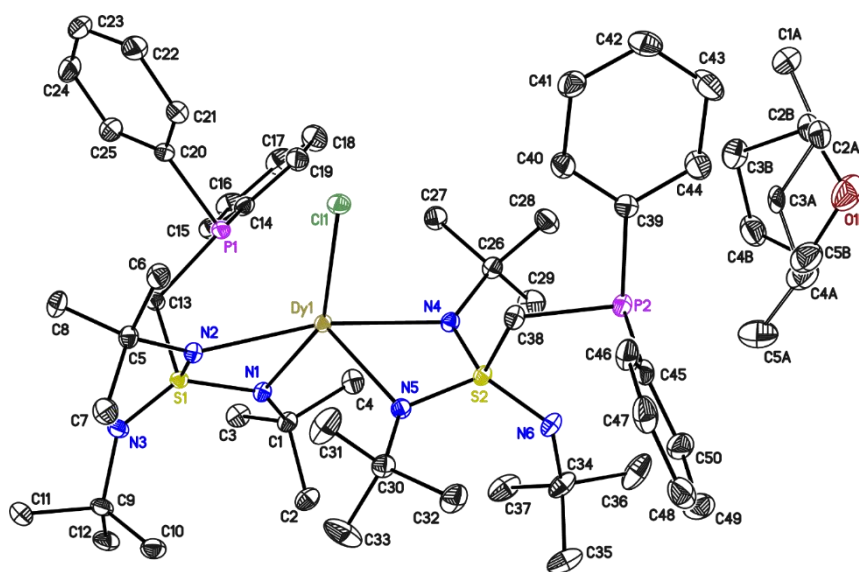


Figure 4.2.7: Molecular structure of 4_Dy. The asymmetric unit contains one complex molecule and one disordered THF/pentane molecule. Thermal ellipsoids are shown at 50% probability level. Hydrogens are omitted for clarity.

Structure code	4_Dy	CCDC Number	2104540
Empirical Formula	$\text{C}_{50}\text{H}_{78}\text{ClN}_6\text{P}_2\text{S}_2\text{Dy}$, $0.252(\text{C}_4\text{H}_8\text{O})$	μ [mm^{-1}]	1.343
Formula weight [g mol^{-1}]	1123.3	F(000)	4684
Sample temperature [K]	100(2)	θ range [$^\circ$]	1.363 to 24.472
Wavelength [\AA]	0.56086	Reflections collected	290042
Crystal System	Monoclinic	Unique Reflections	18647
Space group	$\text{C2}/c$	R_{int}	0.0597
	$a=35.454(4)$	Completeness to θ_{max} [%]	100
Unit cell dimensions [\AA]	$b=15.335(2)$ $\beta=95.29(2)$	restraints/parameters	208 / 658
	$c=20.523(3)$	GooF	1.021
Volume [\AA^3]	11111(3)	R1 (all data)	0.0394
Z	8	wR2 (all data)	0.0526
Crystal dimensions [mm]	0.183 x 0.150 x 0.124	max. diff. peak / hole [$\text{e}\text{\AA}^{-3}$]	0.608 and -0.556
Crystal shape and color	Pale yellow blocks		

4.2.8. $[(\text{Ph}_2\text{PCH}_2\text{S}(\text{N}^t\text{Bu})_3)_2\text{Dy}(\text{C}_3\text{H}_5)(\mu^2\text{-Cl})_2\text{Dy}(\text{C}_3\text{H}_5)(\text{Ph}_2\text{PCH}_2\text{S}(\text{N}^t\text{Bu})_3)_2]$ (5_Dy)

Motivation: Remove the last chlorine atom coordinated to the dysprosium atom in **4_Dy** and replace it with a bulky counter-ion that does not coordinate anymore to the dysprosium atom.

The chlorine atom could be removed in a smooth two step synthesis (1) (**Figure 4.2.8.1, top**). Alternatively, the chlorine extraction could be done with the halide extracting agent $[\text{H}(\text{SiEt}_3)_2][\text{B}(\text{C}_6\text{F}_5)_4]$. (2). However, the use of such reactive materials may result in ligand decomposition due to the potential redox activity of the SN ligands.

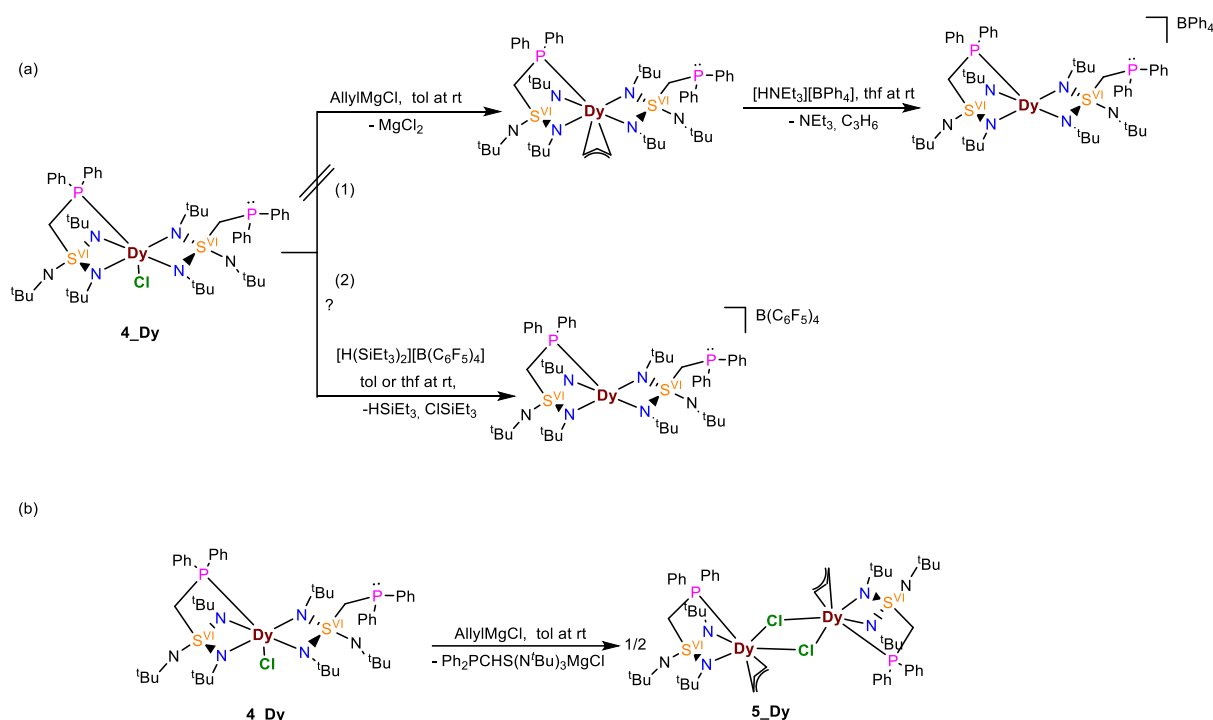


Figure 4.2.8.1. Scheme of the two strategies to synthesize the chlorine-free dysprosium complex $[(\text{Ph}_2\text{PCH}_2\text{S}(\text{N}^t\text{Bu})_3)_2\text{Dy}][\text{BPh}_4]$ or $[(\text{Ph}_2\text{PCH}_2\text{S}(\text{N}^t\text{Bu})_3)_2\text{Dy}][\text{B}(\text{C}_6\text{F}_5)_4]$. (a). Synthesis route for **5_Dy** (b).

The first step of strategy (1) consisted of reacting **4_Dy** with a Grignard reagent and forming an allyl adduct while MgCl_2 precipitated. Subsequently, the allyl group would be protonated with $\text{HNEt}_3\text{BPh}_4$ to give propene gas and the desired product $[(\text{Ph}_2\text{PCH}_2\text{S}(\text{N}^t\text{Bu})_3)_2\text{Dy}][\text{BPh}_4]$. The reaction was carried out in toluene, in which the colorless starting material **4_Dy** was suspended. Upon addition of AllylMgCl , the solution turned clear and bright yellow. The reaction was let to stir for 24h, upon which the solution was filtered, and the solvent reduced. The crude yellow powder was washed with small portions of pentane and set to recrystallize in a minimal amount of toluene layered with pentane. Unfortunately, this first step was already unsuccessful and gave the crystalline compound **5_Dy** in poor yields (**Figure 4.2.8.1, b**) instead of the desired product.

5_Dy crystallizes as bright yellow crystals in the triclinic space group $P\bar{1}$, giving a dimeric structure as two dysprosium atoms are bridged by two chlorine atoms (**Figure 4.2.8.2**). The asymmetric

unit contains half of the complex molecule as the inversion center is located in the middle of the $[\text{Dy}_2\text{Cl}_2]$ core. Each dysprosium atom is octa-coordinated by the three donor atoms of the scorpionate ligand, two chlorine atoms and the three carbon atoms of the allyl group. The distance between the two dysprosium atoms is $4.357(5) \text{ \AA}$, which is short enough to enable them to magnetically couple. Compared to **4_Dy**, the Dy-P distance in **5_Dy** is shortened by 0.05 \AA while the Dy-Cl distance is lengthened by 0.2 \AA . The Dy-S and Dy-N bond lengths are remarkably invariant, and the S-N distances only vary a little (**Table 4.2.8.1**).

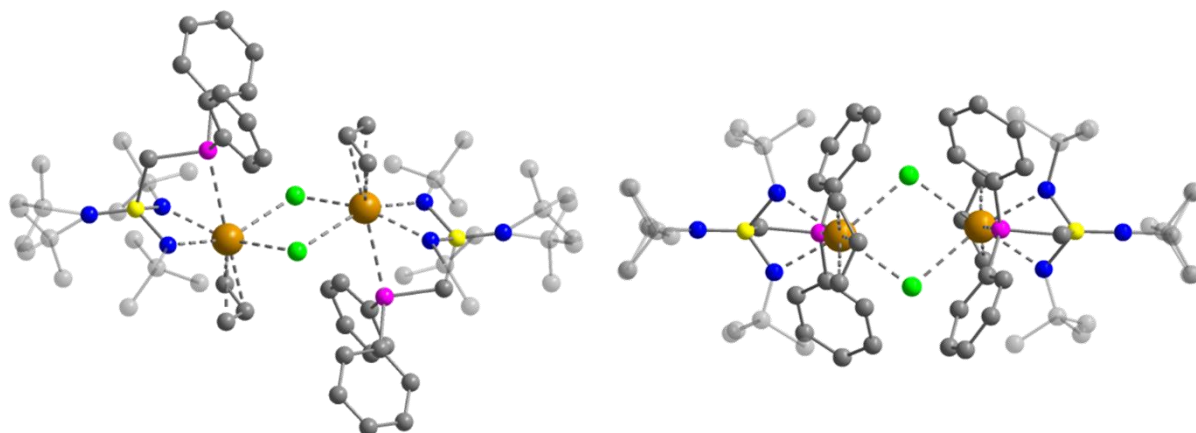


Figure 4.2.8.2. Crystal structure of **5_Dy** in two orientations. Orange, green, yellow, pink, dark blue, and grey represent dysprosium, chlorine, sulfur, nitrogen, and carbon atoms, respectively. Hydrogens are omitted for clarity.

Table 4.2.8.1. Comparison of selected bond lengths (\AA) and angles ($^\circ$) in **4_Dy** and **5_Dy**

Compound	4_Dy	5_Dy
Dy-P	3.2169(5)	3.153(5)
Dy-Cl	2.5996(5)	2.728(5)
Dy-S	3.0730(5); 3.0789(5)	3.070(5)
Dy-N	2.3147(13); 2.3467(13); 2.3471(13); 2.3837(13)	2.325(13); 2.343(14)
Dy-Dy	–	4.357(5)
N-Dy-N	60.37(5); 60.07(4)	61.1(5)
S-Dy-S	141.847(12)	–
Easy axis deviation	120-125.6	122.1

Until now, the low yields prevented further magnetic investigation. Nevertheless, the determination of the main magnetic axes in **5_Dy** was possible on the coordinates of the crystal structure obtained from X-ray diffraction. The two axes are parallel to each other and the bridging chlorine atoms are the coordinating atoms that are the closest to the magnetic axes. The other coordinating atoms, however, are positioned equatorially to the axial magnetic axis and are therefore probably producing a transverse anisotropy. Importantly, the bonds between the dysprosium atom and the strongly binding allyl group are not following the orientation of the magnetic axis, worsening the overall magnetic anisotropy of the complex. Thus, poor magnetic properties are expected. However, magnetic measurements would reveal the nature and strength of the magnetic exchange coupling between the two dysprosium atoms. Additionally, a possible next reaction step would be to react **5_Dy** with $\text{HNEt}_3\text{BPh}_4$ to remove each allyl group on the dysprosium atoms and obtain the bimetallic complex $[(\text{Ph}_2\text{PCH}_2\text{S}(\text{N}^i\text{Bu})_3)_2\text{Dy}(\mu^2\text{-Cl}_2)\text{Dy}(\text{Ph}_2\text{PCH}_2\text{S}(\text{N}^i\text{Bu})_3)_2][(\text{BPh}_4)_2]$. Without the strongly binding allyl groups, better magnetic properties would be expected.

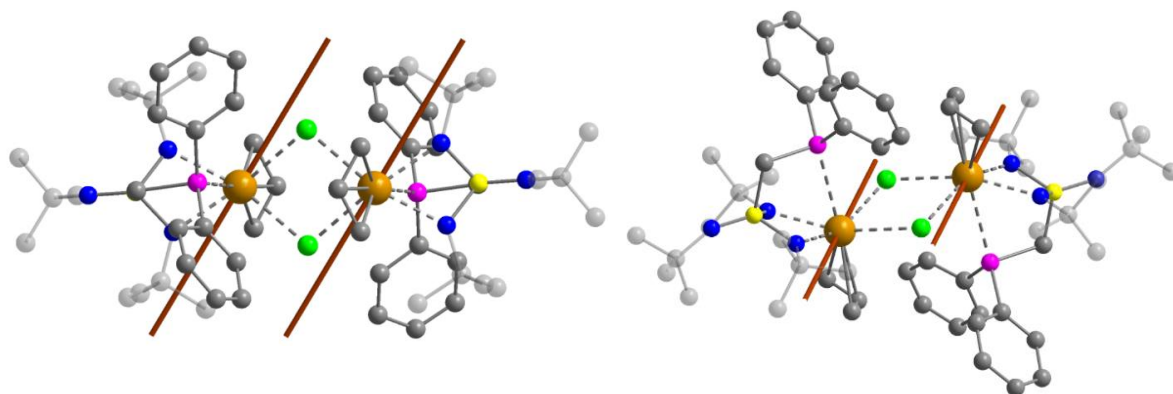


Figure 4.2.8.3. Orientation of the main magnetic axis of the ground state calculated for the entire molecule for **5_Dy** (brown line), in two different views. Hydrogens are omitted for better clarity.

Experimental details: **4_Dy** (200mg, 1eq. 0.2mmol) was completely dissolved in 5 mL THF, giving a colorless solution. AllylMgCl (2M in THF solution, 0.086mL, 1eq, 0.2mmol) was added and the solution immediately turned bright yellow. A white precipitate started to form. After 1 hour, the solution is filtered. The volatils are removed under reduced pressure and the yellow, oily product is extracted with toluene. Crystals are grown over the course of several months from slow evaporation of pentane into concentrated toluene solutions at -35°C . The crystalline yield was only sufficient for a SCXRD experiment.

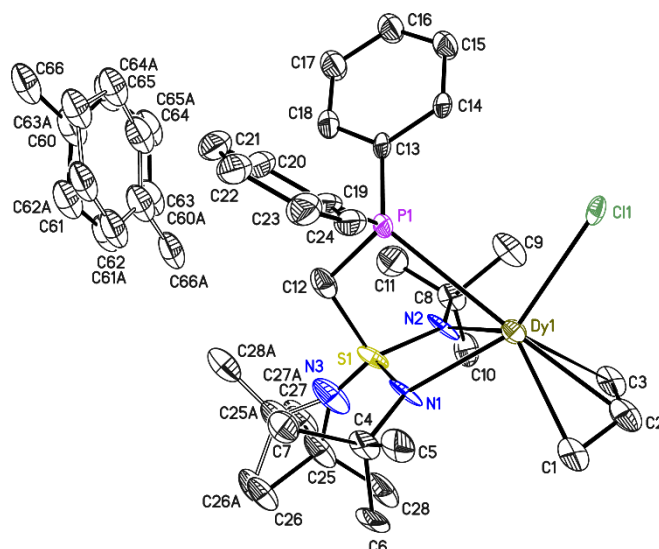


Figure 4.2.8. Asymmetric unit of **5_Dy**. The asymmetric unit contains half of a complex molecule and one disordered toluene molecule. Thermal ellipsoids are shown at 50% probability level. Hydrogens are omitted for clarity.

Structure code	5_Dy (twin)		CCDC Number	/
Empirical Formula	$C_{35}H_{52}ClDyN_3PS$		μ [mm ⁻¹]	2.310
Formula weight [g mol ⁻¹]	775.77		F(000)	794
Sample temperature [K]	100(2)		θ range [°]	1.449 to 27.246
Wavelength [Å]	0.71073		Reflections collected	294804
Crystal System	Triclinic		Unique Reflections	6463
Space group	$P\bar{1}$		R_{int}	0.1337
Unit cell dimensions [Å]	$a=9.911(2)$	$\alpha=80.305(12)$	Completeness to θ_{max} [%]	99.5
	$b=12.811(3)$	$\beta=84.134(10)$	restraints/parameters	961 / 498
	$c=14.314(4)$	$\gamma=84.518(9)$	GooF	1.094
Volume [Å ³]	1776.4(8)		R1 (all data)	0.0468
Z	2		wR2 (all data)	0.0987
Crystal dimensions [mm]	0.1 x 0.1 x 0.1		max. diff. peak / hole [eÅ ⁻³]	3.088 and -1.272
Crystal shape and color	Intense yellow blocks			

4.2.9. [(THF)₂Li{(N^tBu)₄S}Co{N(SiMe₃)₂}] (1_Co)

The synthesis and structural characterization of 1_Co were done by J. Jung.^{186,196} A mixture of [(THF)₄Li₂(N^tBu)₄S] (L₁) (1eq, 250 mg, 0.40 mmol) and Co{N(SiMe₃)₂}₂ (1eq, 0.40 mmol) was dissolved in pentane (15 mL) at rt. After stirring for 1 d, the reaction mixture was filtered, and the filtrate was concentrated (9 mL) under reduced pressure. Crystallization started within minutes after storing at -34°C yielding crystals (267 mg) suitable for X-ray analysis. Crystalline yield: 78%; ¹H-NMR (500.13 MHz, 298 K, C₆D₆): δ [ppm] = -19.98 (s br, 18H, 6 CH₃), -13.36 (s br, 18H, 6 CH₃), -1.80 (s br, 18H, 6 CH₃), 6.84 (s, 8H, THF-H), 13.52 (s, 8H, THF-H). ⁷Li-NMR (194.37 MHz, 298 K, C₆D₆): δ [ppm] = 6.42 (s). ¹³C{¹H}-NMR (125.76 MHz, 298 K, C₆D₆): δ [ppm] = 24.87 (s, CH₃), 32.55 (s, THF-C), 58.54 (s, NC(CH₃)₃), 79.73 (s, THF-C), 318.05 (s, CH₃), 605.26 (s, CH₃), 973.52 (s, NC(CH₃)₃). Anal. for C₃₀H₇₀CoLiN₅O₂SSi₂ (M = 687.03 g/mol) (found (calc.) [%]): C 53.00 (52.45), H 10.47 (10.27), N 10.58 (10.19).

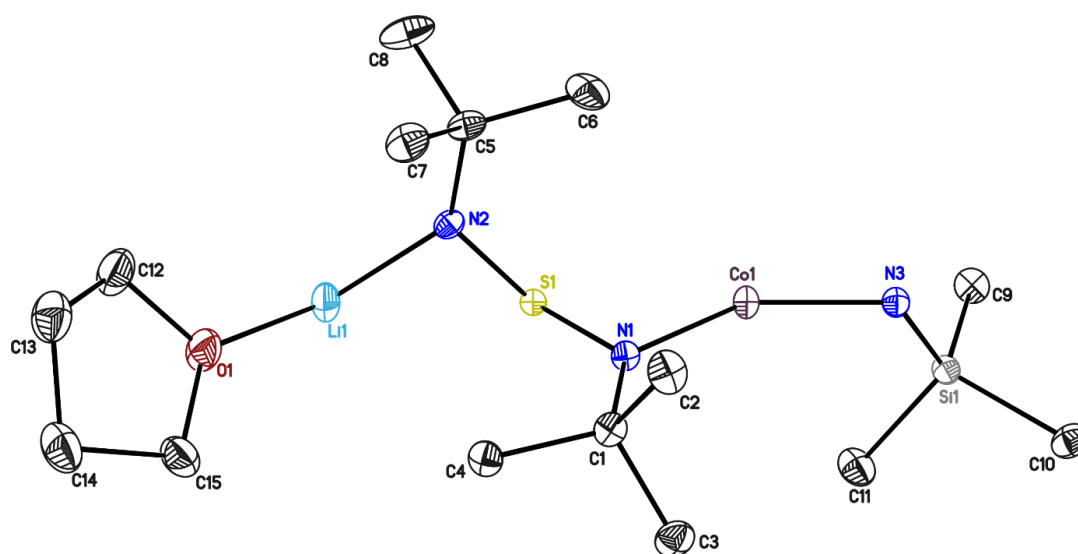


Figure 4.2.9. Asymmetric unit of 1_Co. Hydrogens are omitted for clarity. Thermal ellipsoids are represented at the 50% probability level.

Structure code	1_Co	CCDC Number	2068813
Empirical Formula	C ₃₀ H ₇₀ CoLiN ₅ O ₂ SSi ₂	μ [mm ⁻¹]	0.304
Formula weight [g mol ⁻¹]	687.02	F(000)	1500
Sample temperature [K]	100(2)	θ range [°]	1.538 to 20.066
Wavelength [Å]	0.56086	Reflections collected	35851
Crystal System	Monoclinic	Unique Reflections	3798
Space group	C2/c	R _{int}	0.0696
	<i>a</i> =15.534(2)	Completeness to θ_{\max} [%]	100
Unit cell dimensions [Å]	<i>b</i> =15.343(2) β =113.24(2)	restraints/parameters	0 / 201
	<i>c</i> =18.113(3)	GooF	1.038
Volume [Å ³]	3966.7(11)	R1 (all data)	0.0482
Z	4	wR2 (all data)	0.0744
Crystal dimensions [mm]	0.259 x 0.109 x 0.082	max. diff. peak / hole [eÅ ⁻³]	0.314 and -0.317
Crystal shape and color	Purple blocks		

4.2.10. $[[\text{PPh}_2\text{CH}_2(\text{N}^i\text{Bu})_3\text{S}]\text{Co}[\text{N}(\text{SiMe}_3)_2]]$ (**2_Co**)

The synthesis and structural characterization of **2_Co** were done by J. Jung.^{186,196} The ligand **6_Li** was protonated to give $\text{Ph}_2\text{PCH}_2\text{S}(\text{N}^i\text{Bu})_2\text{NH}^i\text{Bu}$ (**6_H**). This protonated species (1eq, 250.0 mg, 0.5610 mmol) and the metal salt $\text{M}[\text{N}(\text{SiMe}_3)_2]$ (1eq, 0.5610 mmol) were dissolved in pentane (5 mL) at rt. After stirring for 1 d, the reaction mixture was filtered and reduced. Storing at -34°C yielded crystals suitable for X-ray analysis after 2 d. Crystalline Yield: 92%. ^1H -NMR (500.13 MHz, 298 K, C_6D_6): δ [ppm] = -19.12 (s br, 18H, 6 CH_3), -12.50 (s br, 9H, 3 CH_3), -9.90 (s br, 9H, 3 CH_3), 5.59 (s br, 9H, 3 CH_3), 7.72 (s, 2H), 8.24 (s, 4H, Ph-H), 9.76 (s br, 4H, Ph-H), 144.15 (s, 2H). ^1H -NMR (500.13 MHz, 323 K, C_6D_6): δ [ppm] = -15.61 (s br, 18H, 6 CH_3), -10.13 (s br, 18H, 6 CH_3), 5.52 (s br, 9H, 3 CH_3), 8.10 (s, 2H), 8.77 (s, 4H, Ph-H), 11.54 (s br, 4H, Ph-H), 125.96 (s, 2H). $^{13}\text{C}\{^1\text{H}\}$ -NMR (125.76 MHz, 298 K, C_6D_6): δ [ppm] = 46.49 (s), 124.02 (s), 131.79 (s), 133.33 (s), 144.87 (s), 180.69 (s), 475.12 (s), 514.69 (s), 622.50 (s), 830.15 (s). $^{31}\text{P}\{^1\text{H}\}$ -NMR (202.46 MHz, 298 K, C_6D_6): δ [ppm] = 540.01 (s). Anal. for $\text{C}_{31}\text{H}_{57}\text{CoN}_4\text{PSSi}_2$ (found (calc.) [%]): C 56.03 (56.08), H 8.91 (8.65), N 8.40 (8.44).

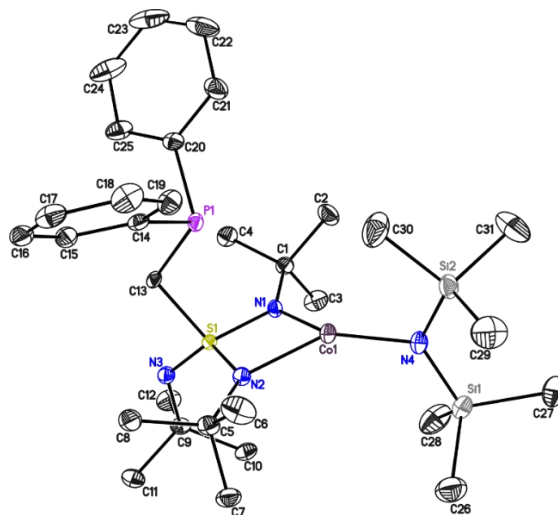


Figure 4.2.10. Asymmetric unit of **2_Co**. Hydrogens are omitted for clarity. Thermal ellipsoids are represented at the 50% probability level.

Structure code	2_Co	CCDC Number	2068815
Empirical Formula	$\text{C}_{31}\text{H}_{57}\text{CoN}_4\text{PSSi}_2$	μ [mm^{-1}]	0.337
Formula weight [g mol^{-1}]	663.94	F(000)	1428
Sample temperature [K]	100(2)	θ range [$^\circ$]	1.514 to 21.387
Wavelength [\AA]	0.56086	Reflections collected	164140
Crystal System	Monoclinic	Unique Reflections	8646
Space group	$P2_1/c$	R_{int}	0.0463
	$a=10.737(2)$	Completeness to θ_{max}	100%
Unit cell dimensions [\AA]	$b=31.049(3)$ $\beta=107.77(2)$	restraints/parameters	0 / 376
	$c=11.858(2)$	GooF	1.101
Volume [\AA^3]	3764.5(11)	R1 (all data)	0.0415
Z	4	wR2 (all data)	0.0754
Crystal dimensions	0.234 x 0.175 x 0.108	max. diff. peak / hole	0.796 and -
[mm]		[$\text{e}\text{\AA}^{-3}$]	0.321
Crystal shape and color	Green blocks		

4.2.11. Co(MeS(NⁱBu)₂)₂ (3_Co)

The ligand **1_Li** (100mg, 0.5mmol, 2eq) was dissolved in 5 mL toluene and added to CoCl₂ (32.9mg, 0.25mmol, 1eq) suspended in toluene (3mL) at room temperature. The color slowly evolved to dark purple and the mixture was left to stir overnight. Upon filtering and solvent removal, the product was extracted with small pentane portions. The obtained clear solution was filtered again and reduced as much as possible for recrystallization at -35°C. Crystals were obtained over a week. Crystalline yield: 40%, Anal. Calc. for C₁₈H₄₂CoN₄S₂ (M=437.22g/mol): C, 49.40; H, 9.67; N, 12.80; S, 14.65. Found: C, 47.98; H, 9.46; N, 12.27; S, 14.06. LIFDI-MS (m/z, pentane): 437.6 g/mol. IR (neat): 2951m, 2849w, 1452w, 1339s, 1185s, 980s, 816s, 764s. vis (pentane): 525, 577, 677nm.

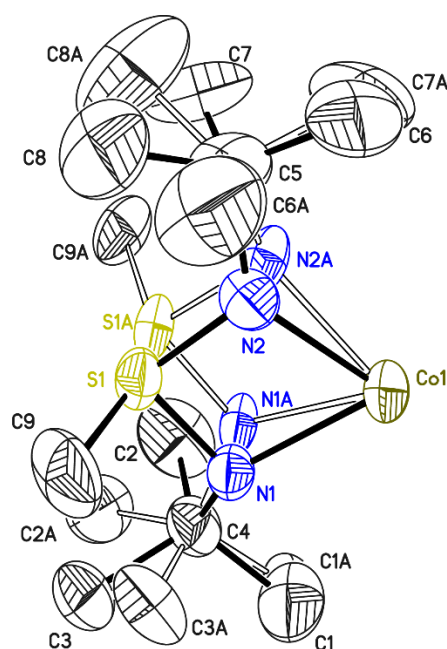


Figure 4.2.11. Asymmetric unit of **3_Co**. The asymmetric unit contains half a disordered complex molecule. Thermal ellipsoids are shown at 50% probability level. Hydrogens are omitted for clarity.

Structure code	3_Co	CCDC Number	/
Empirical Formula	C ₁₈ H ₄₂ CoN ₄ S ₂	μ [mm ⁻¹]	0.844
Formula weight [g mol ⁻¹]	437.60	F(000)	948
Sample temperature [K]	100(2)	θ range [°]	2.498 to 33.344
Wavelength [Å]	0.71073	Reflections collected	56374
Crystal System	Monoclinic	Unique Reflections	4946
Space group	C2/c	R _{int}	0.0591
	$a=18.4426(9)$	Completeness to θ_{\max} [%]	100
Unit cell dimensions [Å]	$b=8.6569(4)$ $\beta=117.8620(10)$	restraints/parameter	418 / 222
	$c=18.0932(13)$	GooF	1.069
Volume [Å ³]	2553.8(3)	R1 (all data)	0.0966
Z	4	wR2 (all data)	0.1691
Crystal dimensions [mm]	0.100 0.100 0.100	max. diff. peak / hole [eÅ ⁻³]	2.295 and -1.163
Crystal shape and color	Pink purple plates		

4.2.12. Co(PhS(N^tBu)₂)₂ (4_Co)

At room temperature, the ligand **2_Li** (100mg, 0.39 mmol, 2eq) was dissolved in Et₂O (3mL) and CoCl₂ (18.5mg, 0.19mmol, 1eq) was added in one portion. The colorless solution immediately turned brown-green but became red after 30min intensive stirring, while a white precipitate was forming. The mixture was left to stir overnight, then filtered and dried to obtain a red solid. Crystals suitable for X-ray analysis were obtained from a concentrated pentane solution stored at -35°C after one day. Crystalline yield: 78%, Anal. Calc. for C₂₈H₄₆CoN₄S₂ (M=561.76g/mol): C, 59.87; H, 8.25; N, 9.97; S, 11.41. Found: C, 60.00; H, 8.69; N, 9.99; S, 11.35. LIFDI-MS (m/z, pentane): 561.5g/mol; Vis (pentane): 525, 575nm; IR(neat): 3072w, 2967m, 1356m, 1220s, 1013s cm⁻¹

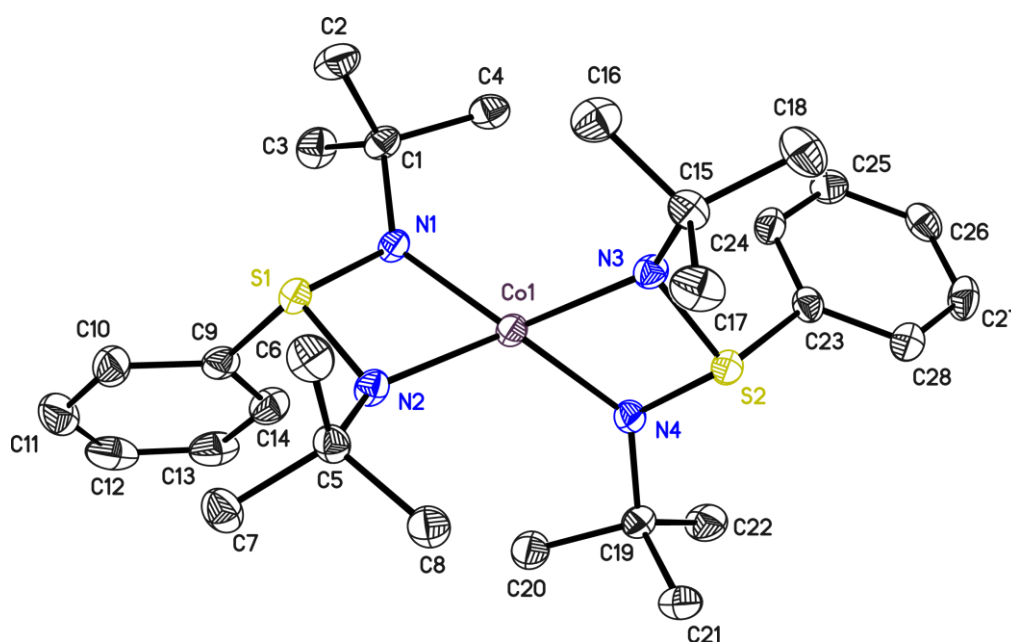


Figure 4.2.12. Molecular structure of **4_Co**. The asymmetric unit contains one complex molecule. Thermal ellipsoids are shown at 50% probability level. Hydrogens are omitted for clarity.

Structure code	4_Co	CCDC Number	2046685
Empirical Formula	C ₂₈ H ₄₆ CoN ₄ S ₂	μ [mm ⁻¹]	0.720
Formula weight [g mol ⁻¹]	561.74	F(000)	1204
Sample temperature [K]	100(2)	θ range [°]	1.323 to 26.533
Wavelength [Å]	0.71073	Reflections collected	67821
Crystal System	Monoclinic	Unique Reflections	6338
Space group	P2 ₁ /c	R _{int}	0.1448
Unit cell dimensions [Å]	$a = 9.04(8)$	Completeness to θ_{\max} [%]	100
	$b = 10.9979(10)$	restraints/parameters	0 / 328
	$c = 30.80(3)$	GooF	0.909
Volume [Å ³]	3056(27)	R1 (all data)	0.0626
Z	4	wR2 (all data)	0.0701
Crystal dimensions [mm]	0.225 x 0.199 x 0.120	max. diff. peak / hole [eÅ ⁻³]	0.335 and -0.345
Crystal shape and color	Pink red needles		

4.2.13. Co(MeS(NⁱBu)₃)₂ (5_Co)

The synthesis and characterization of 5_Co have been previously reported elsewhere by E. Carl *et al.* Herein, 5_Co was synthesized according to the published procedure with CoCl₂ instead of Co(HMDS)₂. Comparable analytical data was obtained. UV-vis was additionally performed to further complete the characterization. Vis (pentane): 536, 576, 677nm.

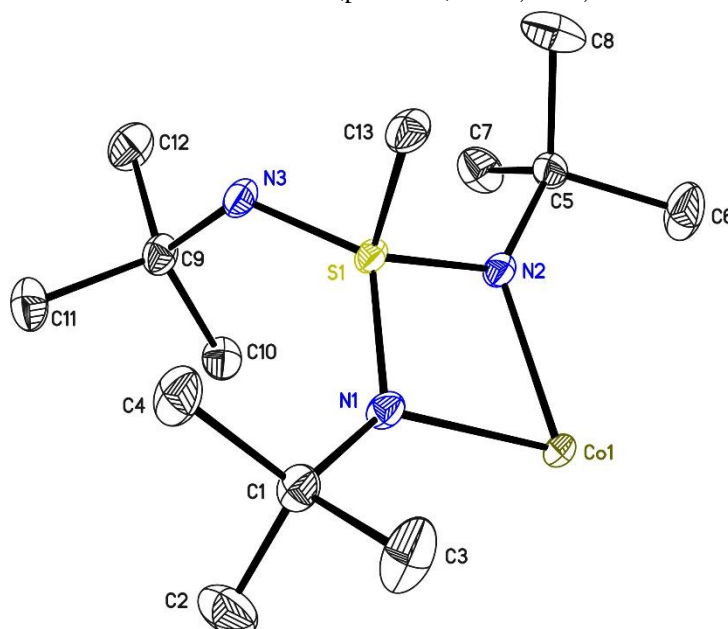


Figure 4.2.13. Asymmetric unit of 5_Co. The asymmetric unit contains half of a complex molecule. Thermal ellipsoids are represented at the 50% probability level.

Structure code	5_Co	CCDC Number	1426594
Empirical Formula	C ₂₆ H ₆₀ CoN ₆ S ₂	μ [mm ⁻¹]	0.681
Formula weight [g mol ⁻¹]	579.85	F(000)	
Sample temperature [K]	100(2)	θ range [°]	1.959 to 27.121
Wavelength [Å]	0.71073	Reflections collected	46244
Crystal System	Monoclinic	Unique Reflections	3585
Space group	C2/c	R _{int}	0.0263
	<i>a</i> =25.274(2)	Completeness to θ_{\max} [%]	100
Unit cell dimensions [Å]	<i>b</i> =8.809(2) β =124.67(2)	restraints/parameters	0 / 169
	<i>c</i> = 17.735(2)	GooF	1.089
Volume [Å ³]	3247.4(11)	R1 (all data)	0.0250
Z	4	wR2 (all data)	0.0635
Crystal dimensions [mm]	0.1 x 0.1 x 0.05	max. diff. peak / hole [eÅ ⁻³]	0.410 and -0.303
Crystal shape and color	Pink plates		

4.2.14. Co(PhS(N^tBu)₃)₂ (6_Co)

The ligand **5_Li** (100mg, 0.30mmol, 2eq) and CoCl₂ (19.5mg, 0.15mmol, 1eq) were combined and suspended in toluene (5mL) at room temperature. The solution directly turned light pink then slowly evolved to darker pink-purple. After 1d of intense stirring, a white precipitate was filtered out and the volatils were completely removed under vacuum. The obtained pink-purple crude product was washed several times with small amounts of cold pentane (3x2mL) and recrystallized from toluene by slow evaporation at room temperature. Crystalline yield: 78% Anal. Calc. for C₃₆H₆₄CoN₆S₂ (703.4g/mol): C, 61.42; H, 9.16; N, 11.94; S, 9.11. Found: C, 61.21; H, 9.09; N, 12.65; S, 9.56; LIFDI-MS (m/z, toluene): 703.3g/mol. Vis (toluene): 540, 555, 750nm; IR(neat): 3553w, 3067w, 2964m, 1231s, 1182s cm⁻¹

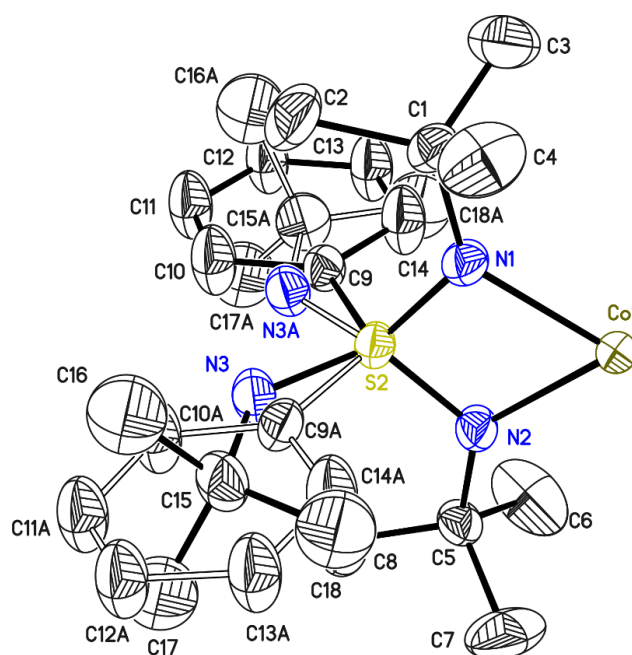


Figure 4.2.14. Asymmetric unit of **5_Co**. The asymmetric unit contains half of a disordered complex molecule. Thermal ellipsoids are shown at 50% probability level. Hydrogens are omitted for clarity.

Structure code	6_Co	CCDC Number	2046686
Empirical Formula	C ₃₆ H ₆₄ CoN ₆ S ₂	μ [mm ⁻¹]	0.574
Formula weight [g mol ⁻¹]	703.98	F(000)	1524
Sample temperature [K]	100(2)	θ range [°]	1.640 to 28.365
Wavelength [Å]	0.71073	Reflections collected	49646
Crystal System	Monoclinic	Unique Reflections	4906
Space group	C2/c	R _{int}	0.1042
	a=26.460(3)	Completeness to θ_{\max} [%]	100
Unit cell dimensions [Å]	b=9.004(2) β =110.200(5)	restraints/parameters	546 / 232
	c =17.587(2)	GooF	1.023
Volume [Å ³]	3932.3(11)	R1 (all data)	0.0978
Z	4	wR2 (all data)	0.1690
Crystal dimensions [mm]	0.381 x 0.316 x 0.137	max. diff. peak / hole [eÅ ⁻³]	0.751 and -0.707
Crystal shape and color	Pink-red needles		

4.2.15. Co(PPh₂CH₂S(NⁱBu)₃)₂ (7_Co)

The ligand **6_Li** (100mg, 0.18mmol, 2eq) and CoCl₂ (11.4mg, 0.09mmol, 1eq) were combined and suspended in pentane (5mL). The color slowly evolved from white-bluish to pink, with a white suspension observable during the entire reaction. After 1d of intense stirring, the mixture was dried, and the product was extracted with toluene (3x2mL) as a pink-purple solution. The solution was filtered, dried under vacuo to yield a pink solid. The crude product was recrystallized from toluene at room temperature by slow evaporation. Crystalline yield: 62mg, 74%. Anal. Calc. for C₁₀₀H₁₅₆Co₂N₁₂P₄S₄: C, 63.33; H, 8.29; N, 8.86; S, 6.76. Found: C, 62.99; H, 8.33; N, 9.06; S, 6.71. LIFDI-MS (m/z, toluene): 947.2g/mol. Vis (toluene): 530, 650nm; IR(neat): 3047w, 2959s, 1441m, 1356s, 1196s cm⁻¹

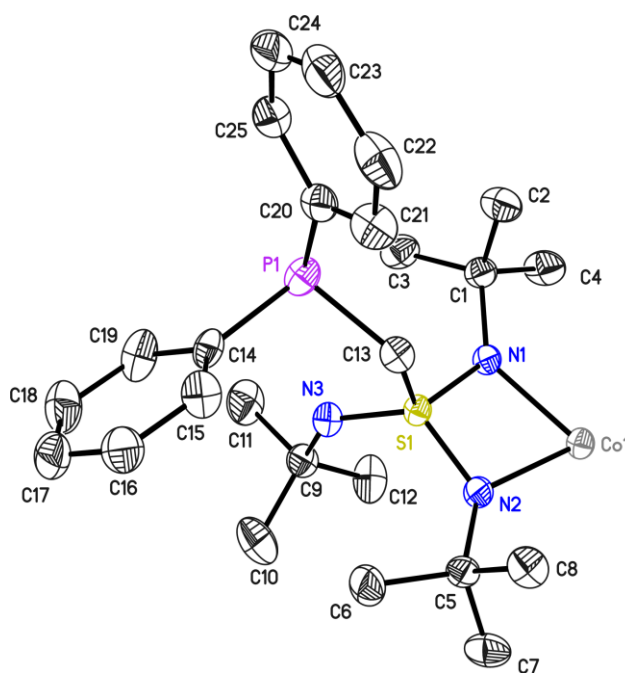


Figure 4.2.15. Asymmetric unit of **7_Co**. The asymmetric unit contains half a complex molecule. Thermal ellipsoids are shown at 50% probability level. Hydrogens are omitted for clarity.

Structure code	7_Co	CCDC Number	2046687
Empirical Formula	C ₅₀ H ₇₈ CoN ₆ P ₂ S ₂	μ [mm ⁻¹]	0.506
Formula weight [g mol ⁻¹]	948.17	F(000)	1018
Sample temperature [K]	100(2)	θ range [°]	1.581 to 26.562
Wavelength [Å]	0.71073	Reflections collected	27272
Crystal System	Monoclinic	Unique Reflections	5439
Space group	C2	R _{int}	0.1008
	<i>a</i> =26.121(3)	Completeness to θ_{\max} [%]	100
Unit cell dimensions [Å]	<i>b</i> =9.373(2) β =99.44(2)	restraints/parameters	1 / 286
	<i>c</i> =10.865(2)	GooF	1.010
Volume [Å ³]	2624.1(8)	R1 (all data)	0.0782
Z	2	wR2 (all data)	0.1003
Crystal dimensions [mm]	0.305 x 0.127 x 0.070	max. diff. peak / hole [eÅ ⁻³]	0.446 and -0.355
Crystal shape and color	Pink needles		

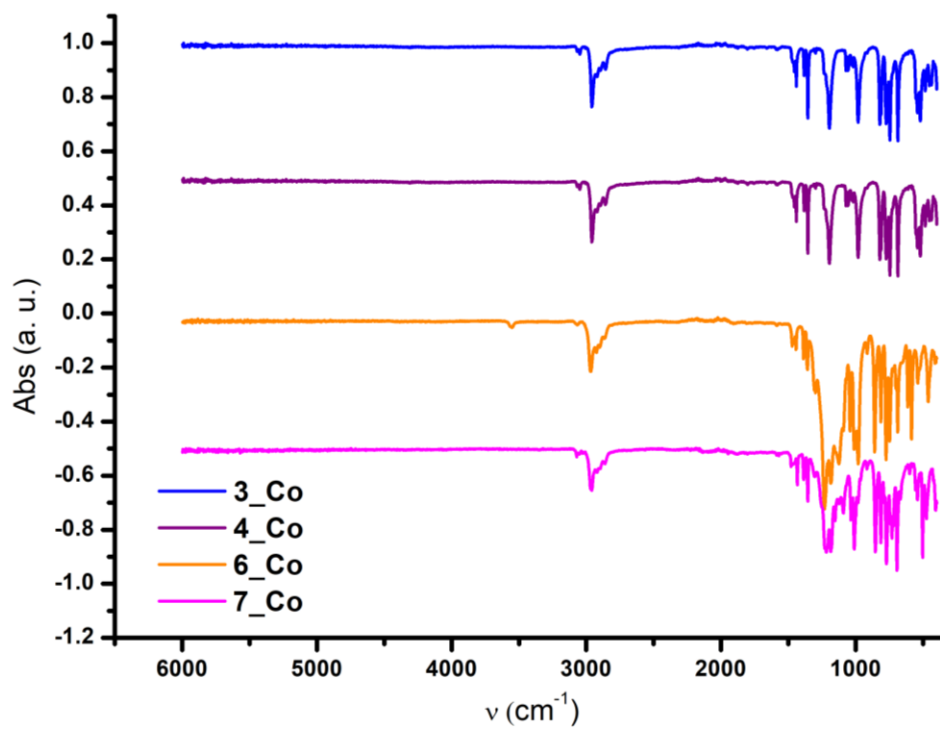


Figure 4.2.15.1. IR data for complexes 3__{Co}, 4__{Co}, 6__{Co} and 7__{Co}.

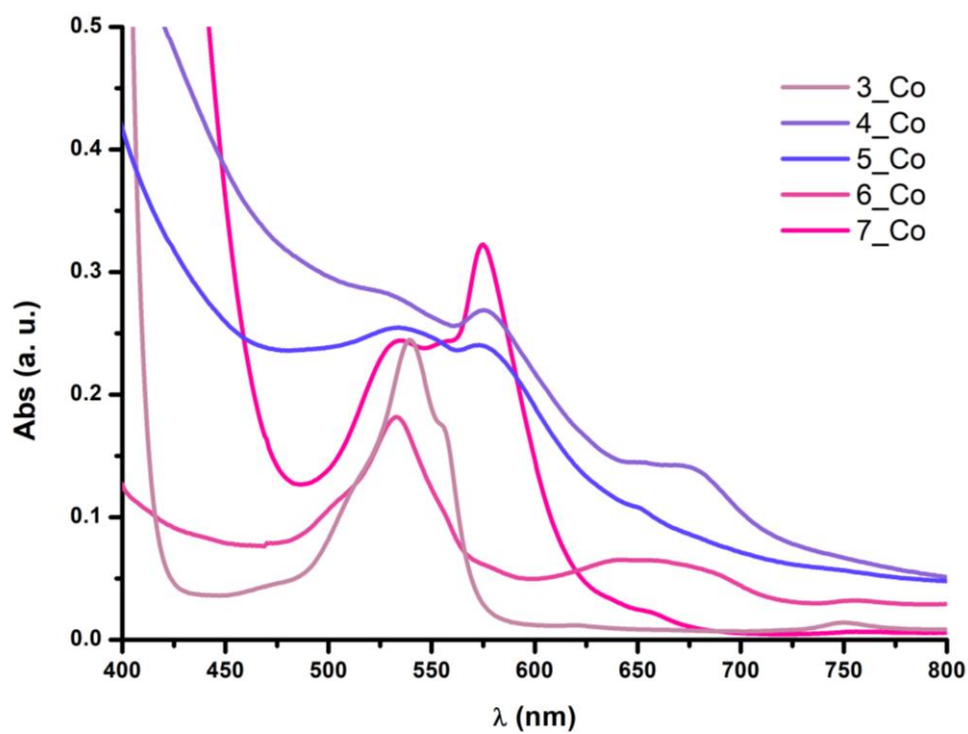


Figure 4.2.15.2. vis data for complexes 3-7__{Co}.

4.2.16. $[(\text{THF})_2\text{Li}(\mu^2\text{-Cl}_2)\text{Dy}\{(\text{THF})\text{Cl}(\text{Ph}(\text{S}(\text{N}'\text{Bu})_2)_2)(\text{THF})\text{Cl}\}\text{DyCl}_2]$

DyCl_3 (1eq, 26mg, 0.1mmol) and **7** -Li_2 (1eq, 42 mg, 0.1 mmol) were mixed together and 5mL THF were added to give a creamy suspension. After 10min heavy stirring, the solution became clear and pale yellow. The mixture was left to stir for 2 hours, upon which it was filtered and reduced. The oily crude product was extracted and triturated with pentane (3x 2mL) until it became a solid powder. The volatils were then removed and 1 mL THF was added. Crystals were grown over a week by slow evaporation of pentane into the concentrated THF solution at -35°C . Crystalline yield: 40%. LIFDI-MS analysis was unsuccessful. Anal. Calc. for $\text{C}_{38}\text{H}_{72}\text{Cl}_5\text{Dy}_2\text{LiN}_4\text{O}_4\text{S}_2$ (1222.33 g/mol): C, 37.34; H, 5.94; S, 5.25; N, 4.58; Found: C, 36.45; H, 6.39; S, 3.28; N, 2.49.

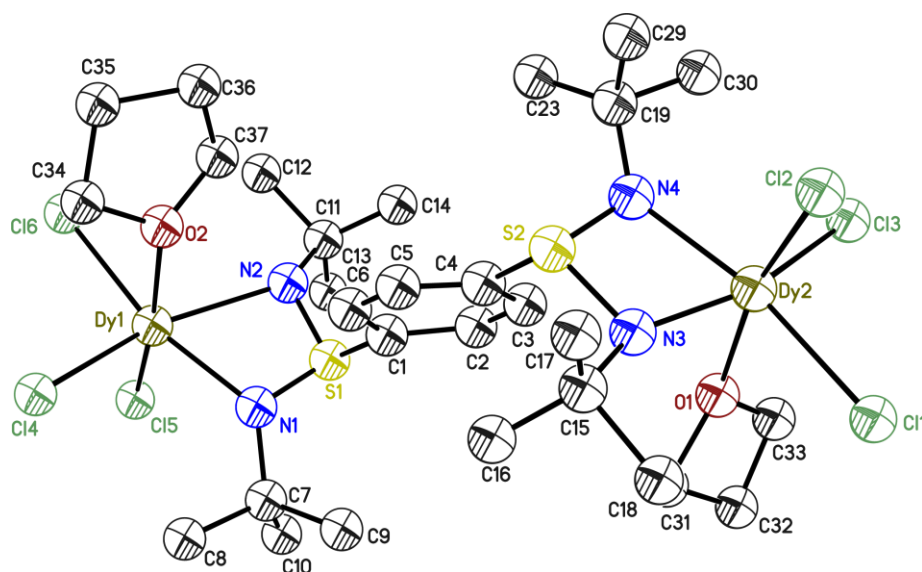


Figure 4.2.16: Structure of $[(\text{THF})_2\text{Li}(\mu^2\text{-Cl}_2)\text{Dy}\{(\text{THF})\text{Cl}(\text{Ph}(\text{S}(\text{N}'\text{Bu})_2)_2)(\text{THF})\text{Cl}\}\text{DyCl}_2]$. Atoms are represented as isotropic spheres because of the low crystal data quality.

The crystal data is not given here since the data quality was poor. The compound was further analysed by SQUID magnetometry.

Magnetic characterization:

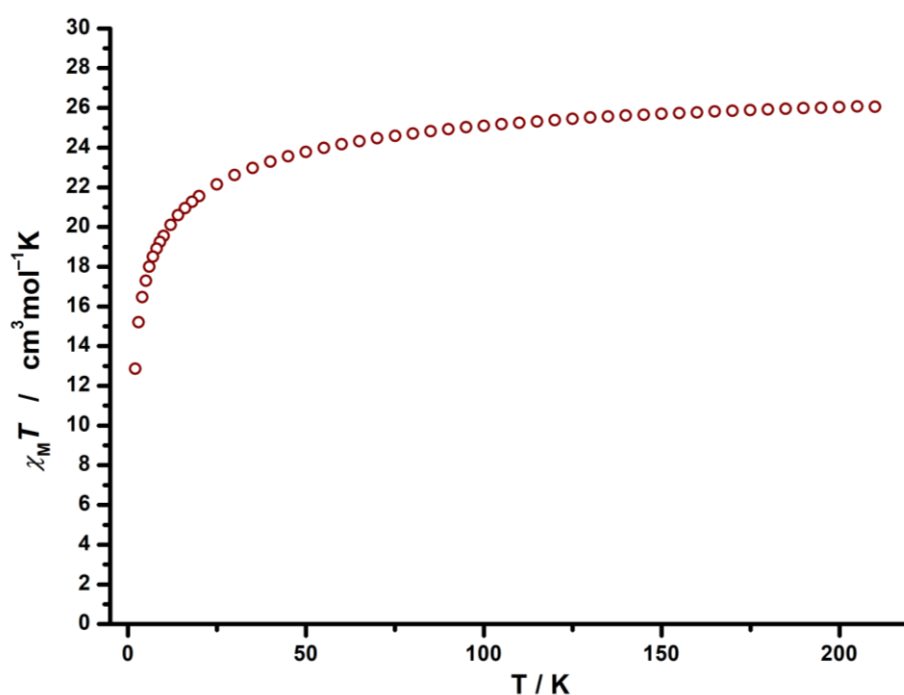


Figure 4.2.16.1. Temperature dependence of the product $\chi_M T$ from 210K to 2K under 5000 Oe dc field. The value at 210K corresponds to two independent dysprosium ions. At low temperatures, no coupling is detected.

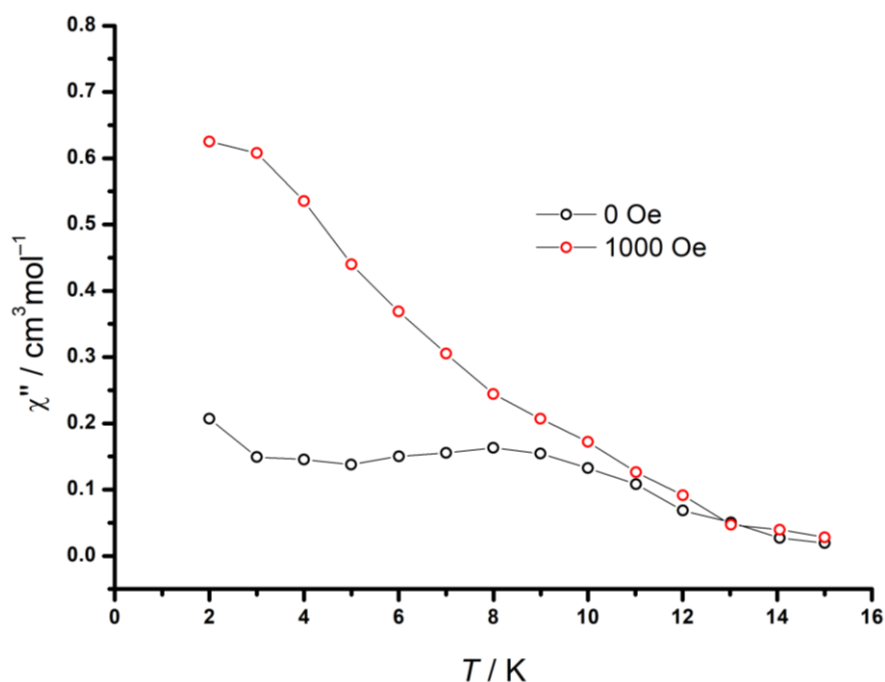


Figure 4.2.16.2. Temperature and field dependency of the imaginary part of the magnetic susceptibility at the highest frequency of 1488 Hz. A peak is detected without external field, at around 9K while no peak is detected when a field of 1000 Oe is applied.

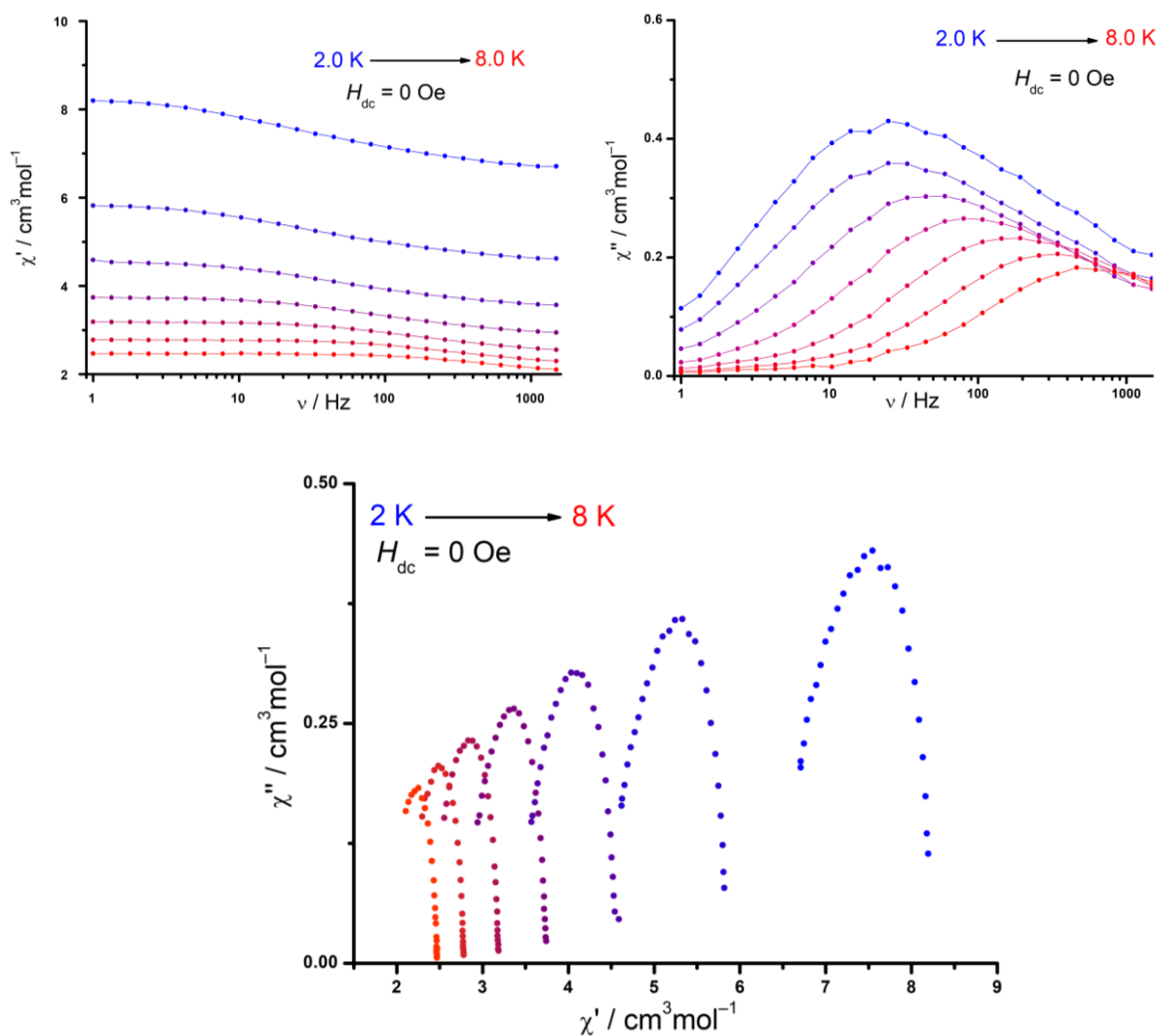


Figure 4.2.16.3. (top) dynamic susceptibility data under 0 Oe. Maxima for the out-of-phase signals are detected up to 8K. (bottom) Cole-Cole plot. Unfortunately, the Cole-Cole plot could not be fitted neither with one nor two relaxation processes, the sample must probably be diluted first. Nevertheless, the Cole-Cole plot indicates the presence of several relaxation processes, probably including a phonon bottleneck process.

4.2.17. [(THF)₂Li(μ^2 -Cl₂)Dy₂{(THF)Cl(Ph(S(N^tBu)₂)₂)(THF)Cl)}DyCl₂]

DyCl₃ (1eq, 26mg, 0.1mmol) and 8_Li₂ (1eq, 50 mg, 0.1 mmol) were mixed together and 5mL THF were added to give a creamy suspension. After 10min heavy stirring, the solution became clear and pale yellow. The mixture was left to stir for 2 hours, upon which it was filtered and reduced. The oily crude product was extracted and triturated with pentane (3x 2mL) until it became a solid powder. The volatils were then removed and 1 mL THF was added. Crystals were grown over a week by slow evaporation of pentane into the concentrated THF solution at -35°C. Crystalline yield: 40%. LIFDI-MS analysis was unsuccessful. Anal. Calc. for C₅₂H₉₂Cl₆Dy₂Li₂N₄O₆S₂ (M=1485.04g/mol): C, 42.06; H, 6.24; N, 3.77; S, 4.32. Found: C, 42.13; H, 6.34; N, 4.43; S, 5.61.

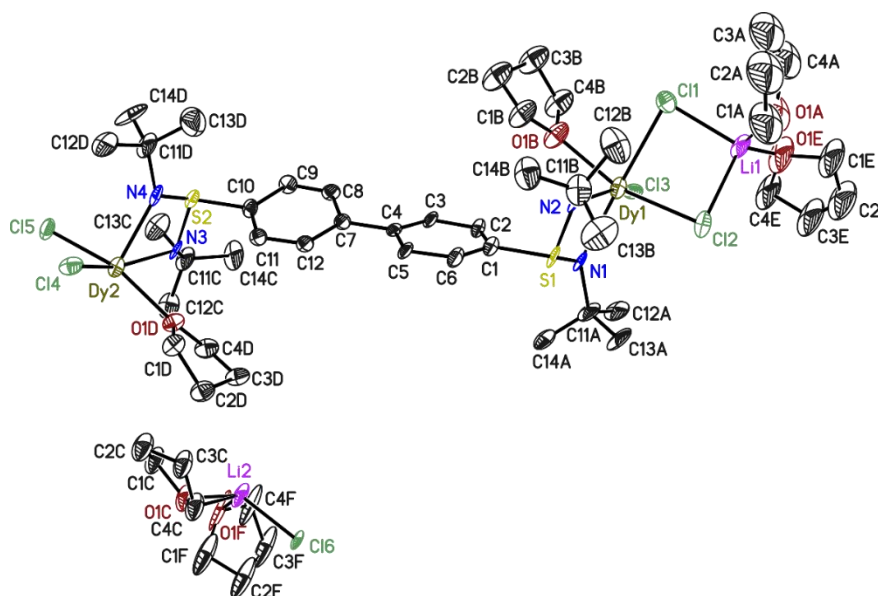


Figure 4.2.17. Crystal structure of [(THF)₂Li(μ^2 -Cl₂)Dy₂{(THF)Cl(Ph(S(N^tBu)₂)₂)(THF)Cl)}DyCl₂]. The asymmetric unit contains a complex molecule and a LiCl(THF)₂ molecule. Thermal ellipsoids are represented at the 50% probability level.

Structure code	DybiPhSN	CCDC Number	/
Empirical Formula	C ₅₂ H ₉₂ Cl ₆ Dy ₂ Li ₂ N ₄ O ₆ S ₂	μ [mm ⁻¹]	2.606
Formula weight [g mol ⁻¹]	1484.99	F(000)	3008
Sample temperature [K]	100(2)	θ range [°]	1.144 to 26.384
Wavelength [Å]	0.71073	Reflections collected	142632
Crystal System	Orthorhombic	Unique Reflections	13455
Space group	Pca2 ₁	R _{int}	0.0978
	$a = 20.027(2)$	Completeness to θ_{\max}	100
Unit cell dimensions [Å]	$b = 9.2298(10)$	restraints/parameters	1367 / 650
	$c = 35.588(4)$	GooF	1.345
Volume [Å ³]	6578.4(12)	R1 (all data)	0.1150
Z	4	wR2 (all data)	0.2404
Crystal dimensions [mm]	0.1 x 0.1 x 0.1	max. diff. peak / hole [eÅ ⁻³]	4.263 and -5.191
Crystal shape and color	Yellow blocks		

Magnetic characterization:

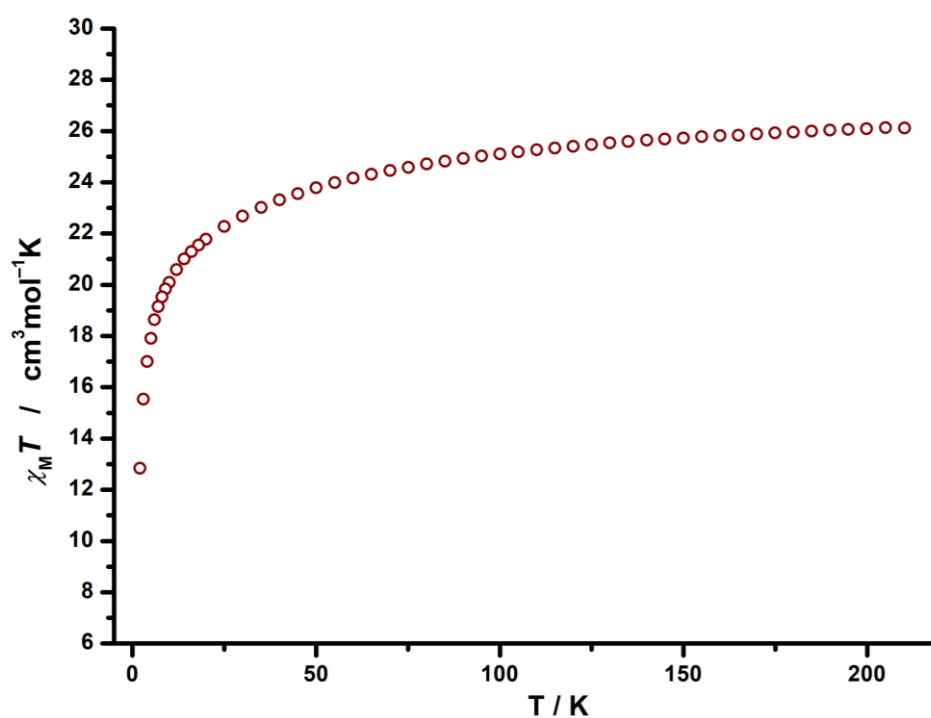


Figure 4.2.17.1. Temperature dependence of the product $\chi_M T$ from 210K to 2K under 5000 Oe dc field. The value at 210K corresponds to two independent dysprosium ions. At low temperatures, no coupling is detected. The data is very similar to the previous Dy_2 compound.

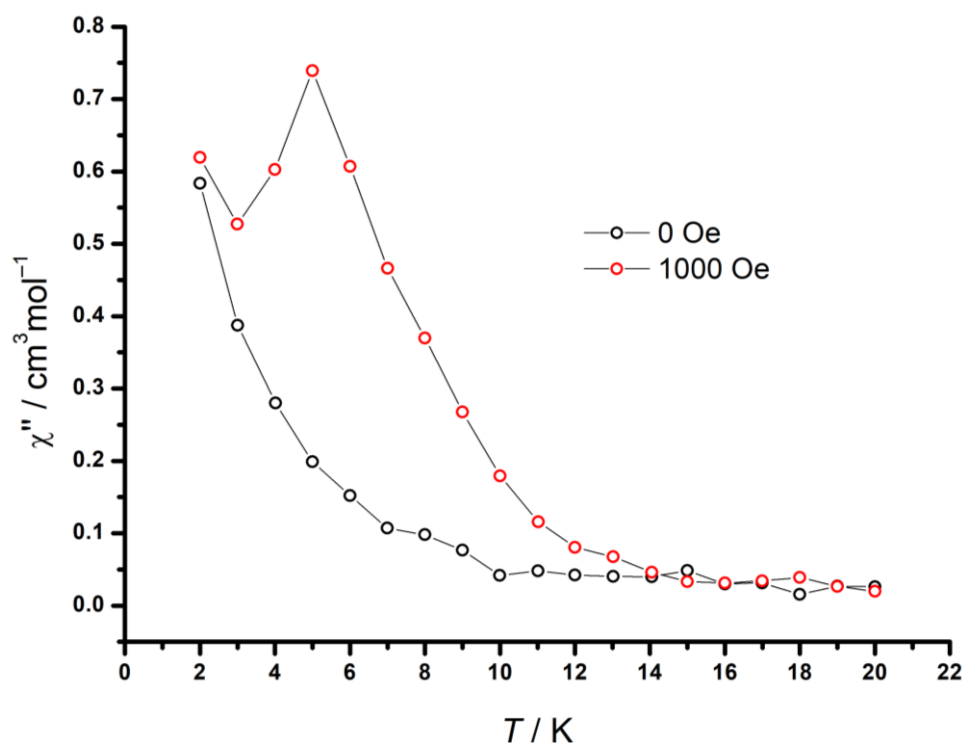


Figure 4.2.17.2. Temperature and field dependency of the imaginary part of the magnetic susceptibility at the highest frequency of 1488 Hz. No peak is detected without external field, a peak around 6K is present when a field of 1000 Oe is applied.

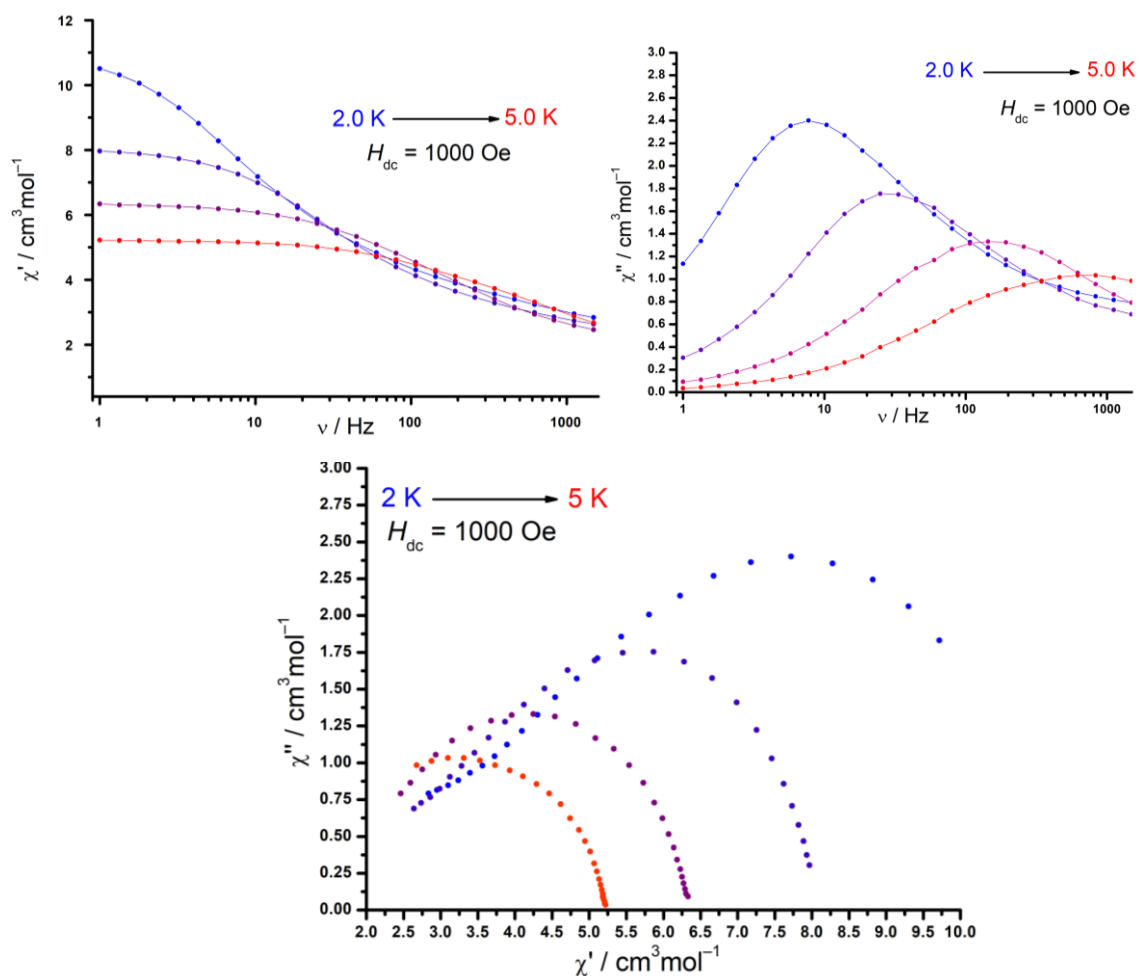


Figure 4.2.17.3. (top) dynamic susceptibility data at 1000 Oe. Maxima for the out-of-phase signals are detected up to 5K. (bottom) Cole-Cole plot. Unfortunately, the Cole-Cole plot could not be fitted neither with one nor two relaxation processes, the sample must probably be diluted first.

4.2.18. $[[(\text{Ph}_2(\text{S}(\text{N}^i\text{Bu})_2)_2)\text{Cl}]\text{Co}(\mu^2\text{-Cl}_2)\text{Co}\{\text{Cl}(\text{Ph}_2(\text{S}(\text{N}^i\text{Bu})_2)_2)\}]_2 (\text{C}_7\text{H}_8)_x$

CoCl_2 (1eq, 12.6mg, 0.1mmol, blue powder) and 8-Li_2 (1eq, 50mg, 0.1mmol) were mixed together and suspended in 5 mL THF. The solution immediately turned darker (yellow to orange to brown) and all solids dissolved. Eventually, after a couple of hours, the solution turned intense dark blue. Upon stirring overnight, the solution was filtered and dried *in vacuo*. The obtained oil was extracted and triturated with 2mL portions of pentane until becoming solid. Some product is slightly soluble in pentane, which turned lightly blue. The volatils were then removed to obtain a dark blue powder. The crude product was then dissolved in a minimal amount of toluene and set to recrystallize at rt. Intense purple crystals were grown over a week while a blue powder precipitated. Attempts to recrystallize the blue by-product were unsuccessful. The purple crystals were further characterized by X-ray diffraction, EA and SQUID magnetometry. LIFDI-MS was unsuccessful. Anal. Calc. for $\text{C}_{70}\text{H}_{104}\text{Cl}_8\text{Co}_4\text{N}_8\text{S}_4$ (1 complex molecule and 2 toluene molecules) ($M=1705.23\text{g/mol}$) C, 49.31; H, 6.15; N, 6.57; S, 7.52. or Anal. Calc. for $\text{C}_{133}\text{H}_{200}\text{Cl}_{16}\text{Co}_8\text{N}_{16}\text{S}_8$ ($M = 3318.32\text{ g/mol}$) (2 complex molecules and 3 toluene molecules) C, 48.14; H, 6.08; N, 6.75; S, 7.73. Found: C, 47.57; H, 5.91; N, 6.22; S, 7.57.

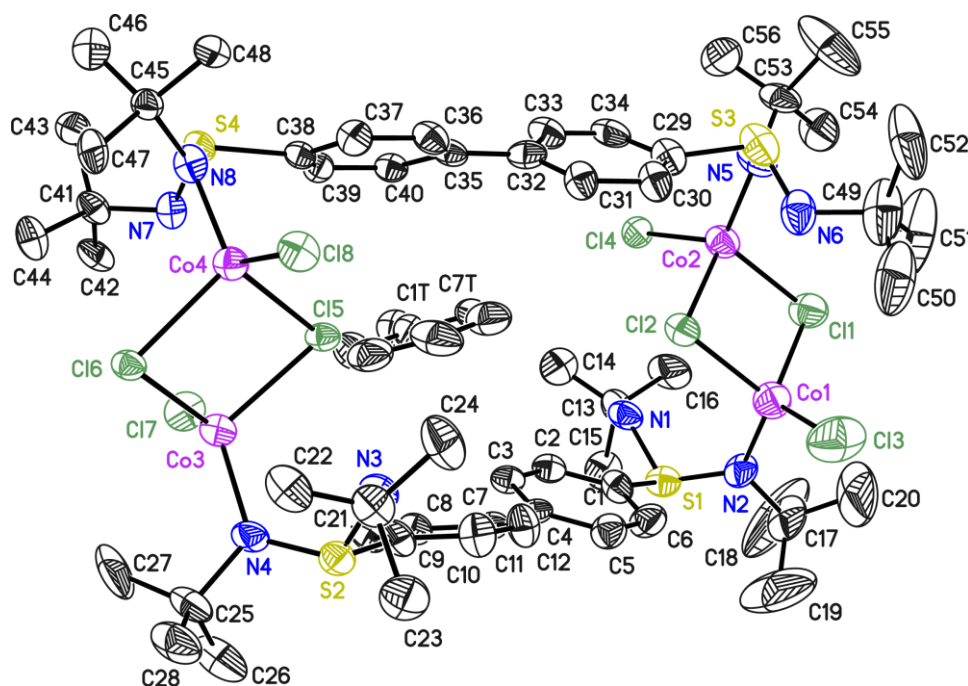


Figure 4.2.18. Crystal structure of $[[(\text{Ph}_2(\text{S}(\text{N}^i\text{Bu})_2)_2)\text{Cl}]\text{Co}(\mu^2\text{-Cl}_2)\text{Co}\{\text{Cl}(\text{Ph}_2(\text{S}(\text{N}^i\text{Bu})_2)_2)\}]_2 (\text{C}_7\text{H}_8)$. Thermal ellipsoids are shown at the 50% probability level. A toluene molecule cocrystallizes between the two biphenyl ligands.

The crystal data is not given here since the data quality is poor. The compound was further analyzed by UV-vis and SQUID magnetometry.

Magnetic characterization:

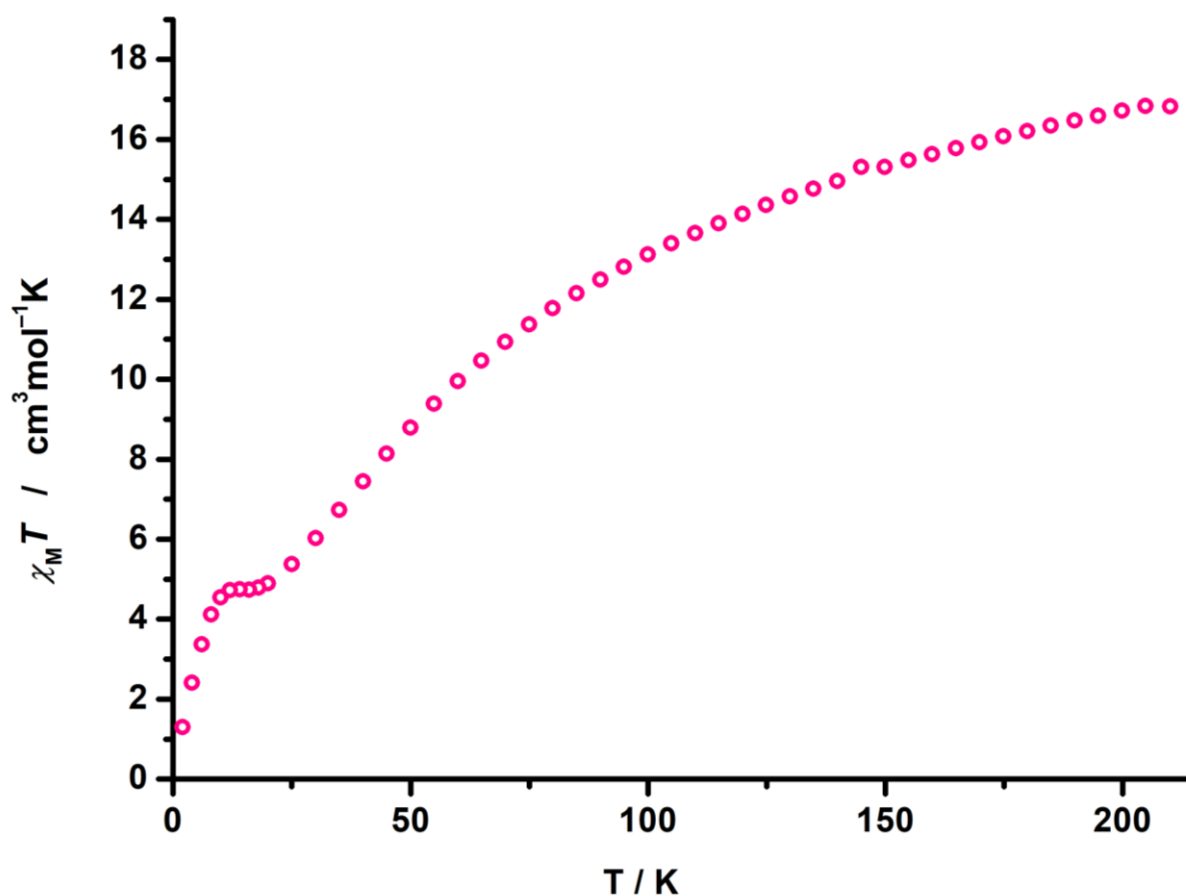


Figure 4.2.18.1. Temperature dependence of the product $\chi_M T$ from 210K to 2K under 5000 Oe dc field. The value at 210K corresponds to four independent cobalt ions with a significant angular contribution. At lower temperature, the value decreases because of antiferromagnetic coupling between the cobalt ions. The small increase around 10-20K is due to paramagnetic impurities.

Fits of the coupling give an antiferromagnetic coupling between -5 and -10 cm^{-1} .

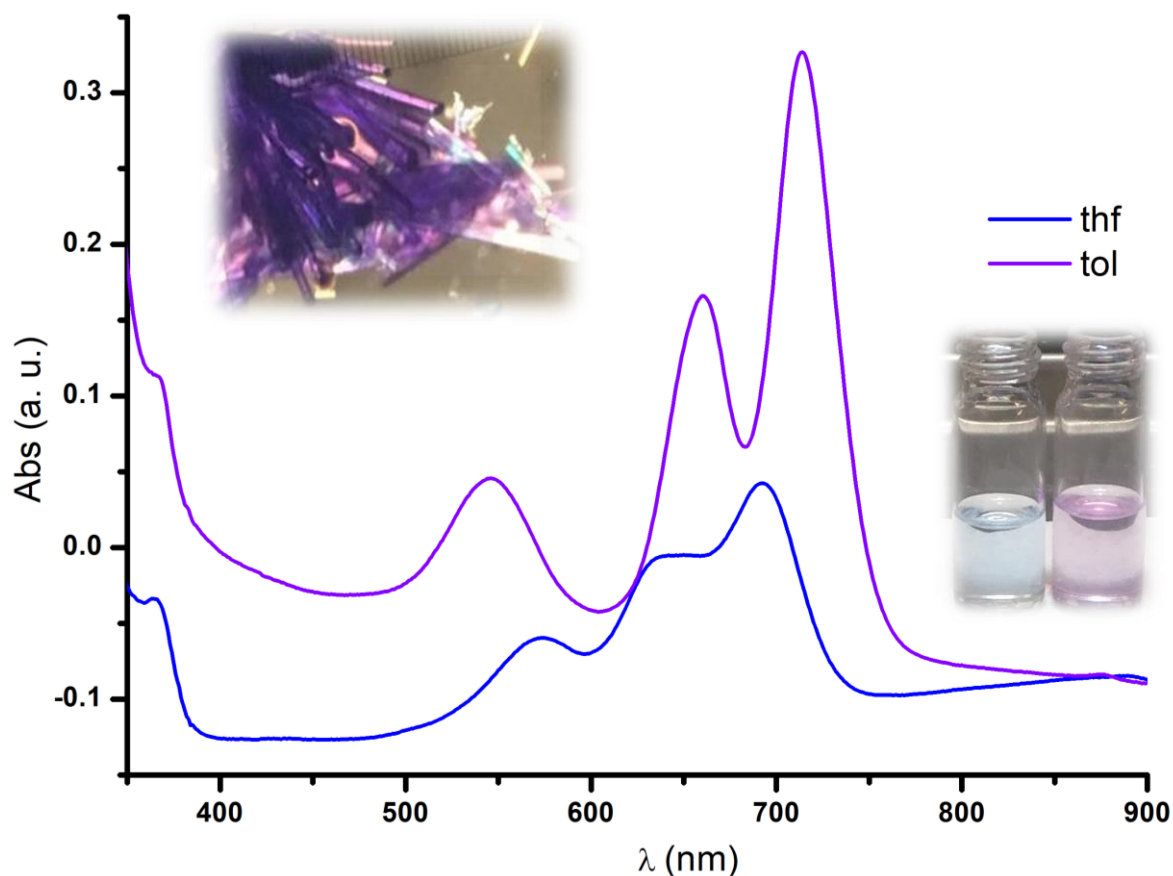


Figure 4.2.18.5. UV-vis spectra of $[[(\text{Ph}_2(\text{S}(\text{N}^i\text{Bu})_2)_2\text{Cl})\text{Co}(\mu^2\text{-Cl}_2)\text{Co}\{\text{Cl}(\text{Ph}_2(\text{S}(\text{N}^i\text{Bu})_2)_2)\}]_2(\text{C}_7\text{H}_8)]$ in THF and toluene. Picture of the solutions (left is in THF and right is in toluene) and picture of the crystals under the microscope.

The compound $[[(\text{Ph}_2(\text{S}(\text{N}^i\text{Bu})_2)_2\text{Cl})\text{Co}(\mu^2\text{-Cl}_2)\text{Co}\{\text{Cl}(\text{Ph}_2(\text{S}(\text{N}^i\text{Bu})_2)_2)\}]_2(\text{C}_7\text{H}_8)]$ presents solvatochromism: the purple crystals can be dissolved in either THF or toluene. In toluene, the solution remains purple, while the THF solution turns light blue.

Conclusion for ditopic SN based compounds:

The magnetic characterization of the three previous compounds shows the potential underlying in the ditopic SN ligands towards the design and synthesis of novel multinuclear SMMs. Although the magnetic characterization is challenging, the three presented compounds present interesting magnetic properties, even under zero field. In order to circumvent crystallization issues, the use of the $-\text{SiMe}_3$ substituted sulfur diimine ($\text{S}(\text{N}(\text{SiMe}_3)_2)_2$) as starting material for the ligands is recommended.

4.2.19. $M(\text{Mebox})_2$ complexes ($M = \text{Mn, Fe, Co, Ni}$)

General procedure. In an Argon-filled glovebox, a solution of the deprotonated ligand in THF was added dropwise to a stirring suspension of $M\text{Cl}_2$ in THF at room temperature. The obtained mixture was let to stir overnight, then filtered and the solvent was reduced to 1mL. Crystals were obtained by slow evaporation of pentane in the THF solution at -35°C .

$\text{Mn}(\text{Mebox})_2(\text{THF})_2$ Isolated 17.5 mg in crystalline yield (48%) from the reaction of KMebox (2eq, 50mg, 0.13mmol) with MnCl_2 (1eq, 8.33mg, 0.06mmol). Block-shaped yellow crystals suitable for X-ray analysis were obtained after 48h. IR(neat): 3054w, 2926w, 2323w, 1810w, 1528s, 1374s, 1239s, 1060s, 996s, 810s, 740s, 656m, 541m; ^1H NMR (500 MHz, THF-d^8 , ppm) δ -7.69 (bs), 11.56 (bs), 37.24 (bs). ^{13}C NMR was unsuccessful due to strong paramagnetism. Anal. Calc. for $\text{C}_{34}\text{H}_{26}\text{MnN}_4\text{O}_4$ ($M=609.49\text{g/mol}^{-1}$, without THF molecules): C, 66.99; H, 4.30; N, 9.19. Found: C, 67.24; H, 4.53; N, 9.16. LIFDI-MS (m/z , THF): 609.2g/mol

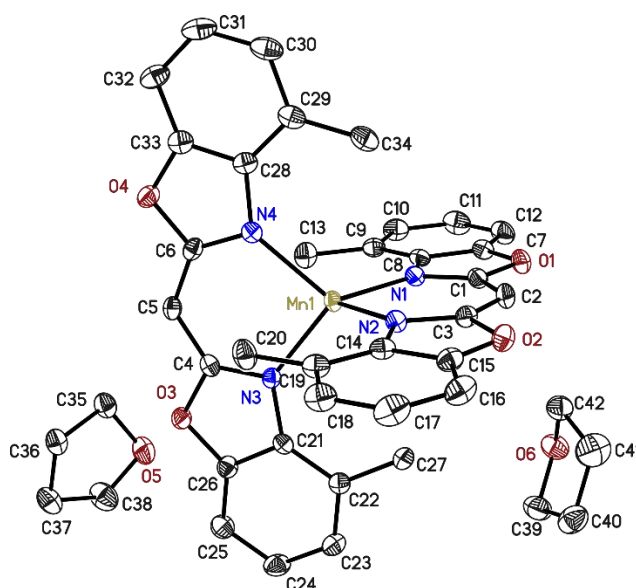


Figure 4.2.19. Molecular structure of $\text{Mn}(\text{Mebox})_2(\text{THF})_2$. The asymmetric unit contains one complex molecule and two THF molecules without any disorder.

Structure code	$\text{Mn}(\text{Mebox})_2(\text{THF})_2$	CCDC Number	2095989
Empirical Formula	$\text{C}_{42}\text{H}_{42}\text{MnN}_4\text{O}_6$	μ [mm^{-1}]	0.419
Formula weight [g mol^{-1}]	753.73	F(000)	790
Sample temperature [K]	100(2)	θ range [$^\circ$]	1.367 to 28.401
Wavelength [\AA]	0.71073	Reflections collected	89253
Crystal System	Triclinic	Unique Reflections	9072
Space group	$P\bar{1}$	R_{int}	0.0677
Unit cell dimensions [\AA]	$a = 9.886(19)$ $\alpha = 88.59(2)$	Completeness to θ_{max} [%]	100
	$b = 12.349(2)$ $\beta = 88.40(2)$	restraints/parameter	0 / 482
	$c = 14.910(3)$ $\gamma = 87.21(2)$	GooF	1.016
Volume [\AA^3]	1817.0(6)	R1 (all data)	0.0344
Z	2	wR2 (all data)	0.0896
Crystal dimensions [mm]	0.278 0.237 0.103	max. diff. peak / hole [$\text{e}\text{\AA}^{-3}$]	0.381 and -0.374
Crystal shape and color	Yellow blocks		

Magnetic characterization of $\text{Mn}(\text{Mebox})_2$.

The dc data is given at the end of the series in order to compare all parent complexes with each other.

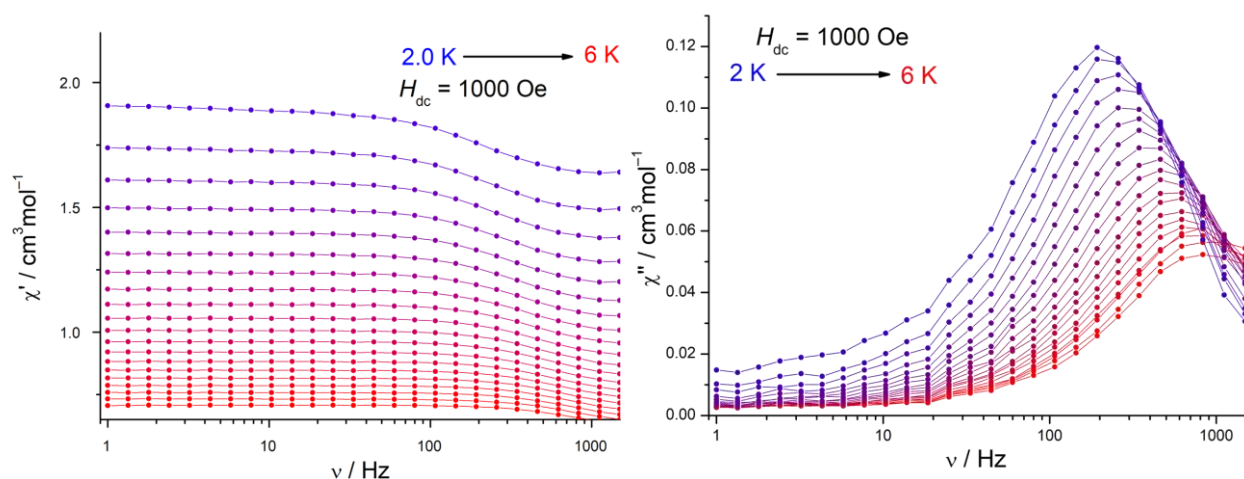


Figure 4.2.19.1. ac susceptibility data at 1000 Oe. Maxima are visible up to 6K. Lines are guide for the eyes.

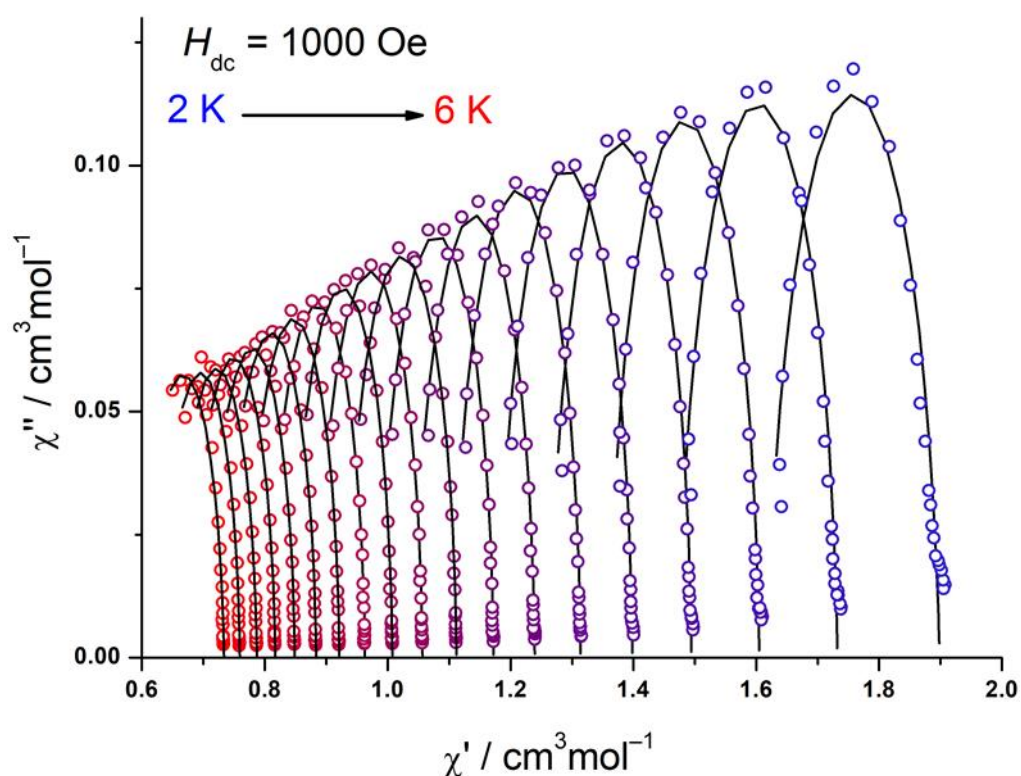


Figure 4.2.19.2. Corresponding Cole-Cole plot. Lines are fits to the curves. The curves disposition in successive arcs suggests that a process different than Orbach is taking place.

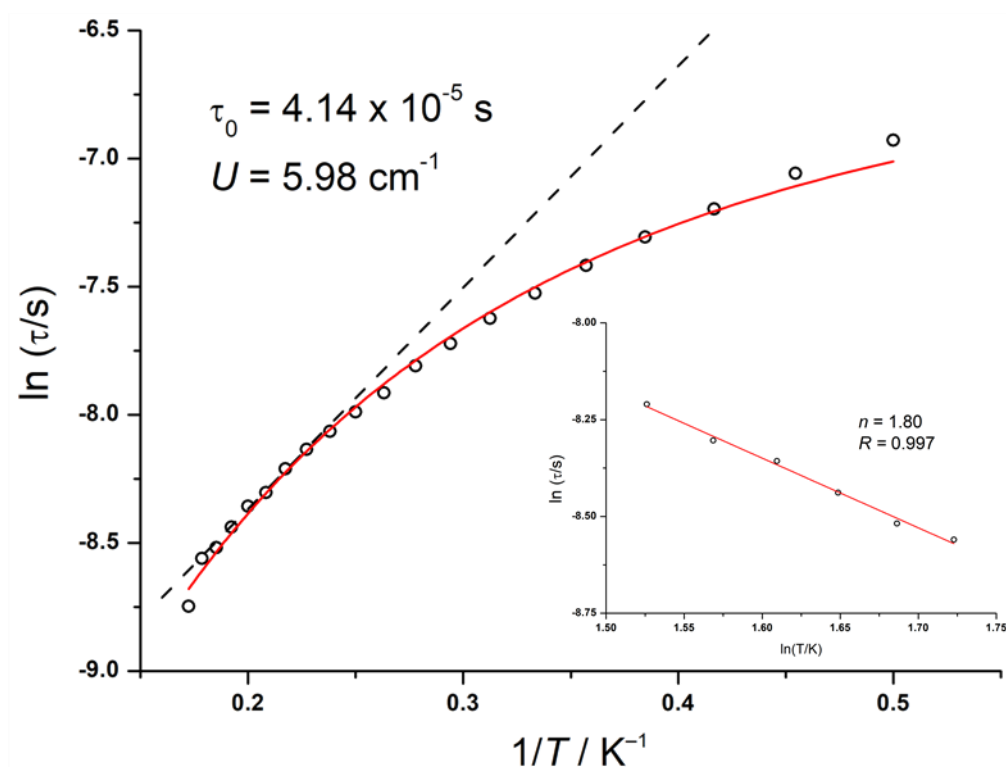


Figure 4.2.19.3. Arrhenius plot and power law plot. Plotting $\ln(\tau)$ vs $\ln(T)$ gives access to the Raman parameter $n = 1.80$, which is relatively close to 2 and may speak for a phonon bottleneck process.

This means that the present compound is not a SMM but that the observable slow relaxation is due to the phonon bottleneck process.

Fe(Mebox)₂(THF)₂: Isolated 25.6 mg in crystalline yield (70%) from the reaction of KMebox (2eq, 50mg, 0.13mmol) with FeCl₂ (1eq, 8.33mg, 0.06mmol). Block orange-red crystals suitable for X-ray analysis were obtained after 48h. Drying for several hours the crystalline material and recrystallizing it by the same procedure yields **Fe(Mebox)₂**. IR(neat): 3055w, 2950w, 2330w, 1810w, 1630m, 1540s, 1375s, 1221s, 976s, 740s, 656s, 528s; ¹H NMR (500 MHz, THF-d⁸, ppm) δ - 33.85 (bs, 1H, H1), - 15.35 (s, 2H, H), 8.95 (s, 2H, H), 41.03 (s, 2H, H), 49.55 (bs, 6H, CH₃); ¹³C NMR (75 MHz, THF-d⁸, ppm) δ 47.20 (s, 1C), 51.71 (s, 1C), 118.36 (s, 1C) 176.16 (s, 1C) 244.50 (s, 1C) 301.99 (s, 1C) 364.19 (s, 1C) 624.52 (s, 1C) 628.55 (s, 1C). Anal. Calc. for C₃₄H₂₆FeN₄O₄ (M=610.4g/mol⁻¹): C, 66.90; H, 4.29; N, 9.18. Found: C, 65.48; H, 4.49; N, 9.02; LIFDI-MS (m/z, THF): 610.2g/mol.

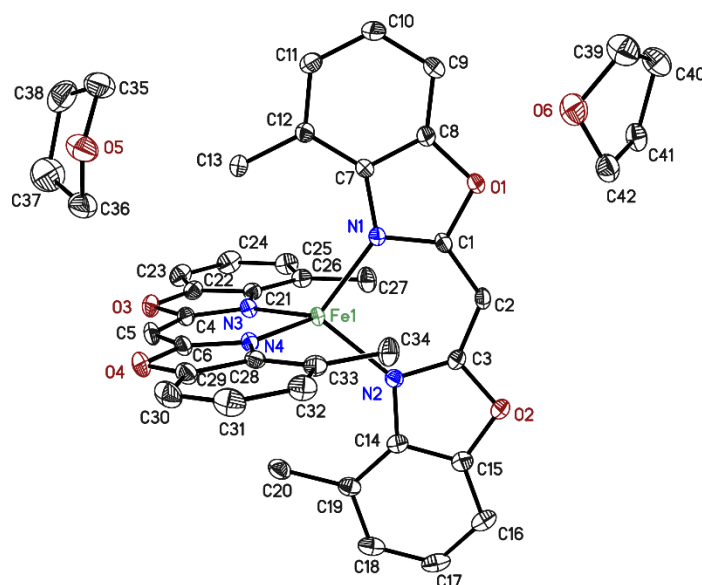


Figure 4.2.20. Molecular structure of **Fe(Mebox)₂(THF)₂**. The asymmetric unit contains one complex molecule and two THF molecules without any disorder. This structure is isostructural to **Mn(Mebox)₂(THF)₂**.

Structure code	Fe(Mebox) ₂ (THF) ₂	CCDC Number	2095990
Empirical Formula	C ₄₂ H ₄₂ FeN ₄ O ₆	μ [mm ⁻¹]	0.474
Formula weight [g mol ⁻¹]	754.64	F(000)	792
Sample temperature [K]	100(2)	θ range [°]	1.37 to 30.95
Wavelength [Å]	0.71073	Reflections collected	150736
Crystal System	Triclinic	Unique Reflections	11341
Space group	<i>P</i> $\bar{1}$	R _{int}	0.0414
Unit cell dimensions [Å]	<i>a</i> = 9.930(4)	Completeness to θ_{\max} [%]	98.9
	α = 88.59(2)	restraints/parameter	0 / 482
	<i>b</i> = 12.250(2)	GooF	1.065
Volume [Å ³]	β = 88.09(2)	R1 (all data)	0.0439
	<i>c</i> = 14.847(6)	wR2 (all data)	0.0879
Z	γ = 87.26(2)	max. diff. peak / hole [eÅ ⁻³]	0.570 and -0.371
Crystal dimensions [mm]	0.442 0.268 0.196		
Crystal shape and color	Red-orange blocks		

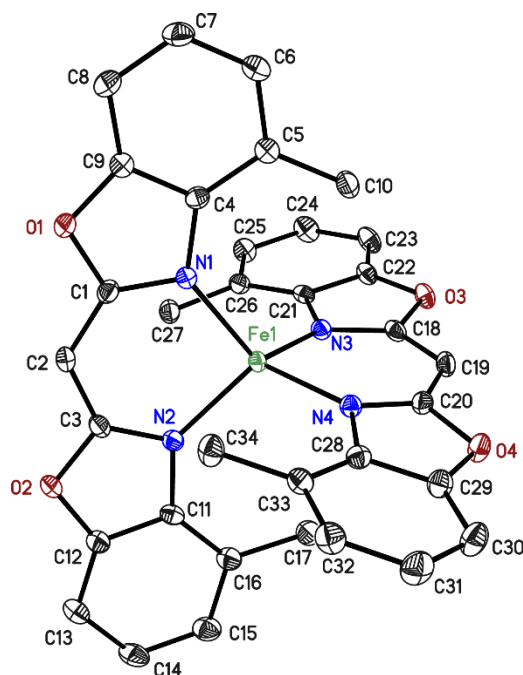


Figure 4.2.21. Molecular structure of $\text{Fe}(\text{Mebox})_2$. The asymmetric unit contains one complex molecule, without any disorder nor solvent molecule.

Structure code	$\text{Fe}(\text{Mebox})_2$	CCDC Number	2095991
Empirical Formula	$\text{C}_{34}\text{H}_{26}\text{FeN}_4\text{O}_4$	μ [mm^{-1}]	0.580
Formula weight [g mol^{-1}]	610.44	F(000)	1264
Sample temperature [K]	100(2)	θ range [$^\circ$]	1.826 to 28.350
Wavelength [\AA]	0.71073	Reflections collected	54594
Crystal System	Monoclinic	Unique Reflections	7045
Space group	$P2_1/n$	R_{int}	0.0271
Unit cell dimensions [\AA]	$a = 11.23(10)$	Completeness to θ_{max} [%]	100
	$b = 14.937(2)$ $\beta = 93.65(2)$	restraints/parameter	0 / 392
	$c = 16.803(3)$	GooF	1.027
Volume [\AA^3]	2830.1(7)	R1 (all data)	0.0306
Z	4	wR2 (all data)	0.0719
Crystal dimensions [mm]	0.408 0.323 0.262	max. diff. peak / hole [$\text{e}\text{\AA}^{-3}$]	0.367 and -0.294
Crystal shape and color	Red-orange blocks		

Co(Mebox)₂: Isolated 27.6 mg in crystalline yield (75%) from the reaction of KMebox (2eq, 50mg, 0.13mmol) with CoCl₂ (1eq, 8.33mg, 0.06mmol). Block orange-red crystals suitable for X-ray analysis were obtained after 48h. IR(neat): 3067w, 2939w, 2336w, 1810w, 1630m, 1547s, 1368s, 1227s, 976s, 810s, 733s, 656s, 528s; ¹H NMR (500 MHz, THF-d⁸, ppm) δ -38.61 (bs, 1H, H1), -29.32 (s, 2H, H), 5.48 (s, 2H, H), 43.72 (bs, 6H, H), 53.08 (s, 2H, H); ¹³C NMR (75 MHz, THF-d⁸, ppm) δ 5.71 (s, 1C), 27.85 (s, 1C), 260.54 (s, 1C) 261.80 (s, 1C) 310.38 (s, 1C) 365.95 (s, 1C) 450.75 (s, 1C) 586.56 (s, 1C) 748.57 (s, 1C). Anal. Calc. for C₃₄H₂₆CoN₄O₄ (M=613.48g/mol⁻¹): C, 66.56; H, 4.27; N, 9.13. Found: C, 65.76; H, 4.70; N, 8.87. LIFDI-MS (m/z, THF): 613.2 g/mol.

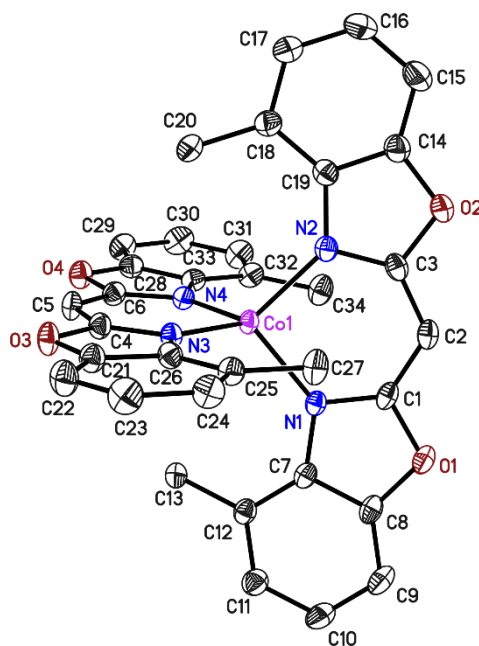


Figure 4.2.21: Molecular structure of Co(Mebox)₂. The asymmetric unit contains one complex molecule, without any disorder nor solvent molecule.

Structure code	Co(Mebox) ₂	CCDC Number	2095992
Empirical Formula	C ₃₄ H ₂₆ CoN ₄ O ₄	μ [mm ⁻¹]	0.660
Formula weight [g mol ⁻¹]	613.52	F(000)	1268
Sample temperature [K]	100(2)	θ range [°]	1.824 to 30.772
Wavelength [Å]	0.71073	Reflections collected	98624
Crystal System	Monoclinic	Unique Reflections	8715
Space group	P2 ₁ /n	R _{int}	0.0635
Unit cell dimensions [Å]	$a = 11.17(17)$	Completeness to θ_{\max} [%]	100
	$b = 14.946(2)$	restraints/parameter	0 / 392
	$c = 16.818(3)$	GooF	1.100
Volume [Å ³]	2803.0(7)	R1 (all data)	0.0398
Z	4	wR2 (all data)	0.0951
Crystal dimensions [mm]	0.183 0.160 0.108	max. diff. peak / hole [eÅ ⁻³]	0.468 and -0.498
Crystal shape and color	Red blocks		

Magnetic characterization of Co(Mebox)₂:

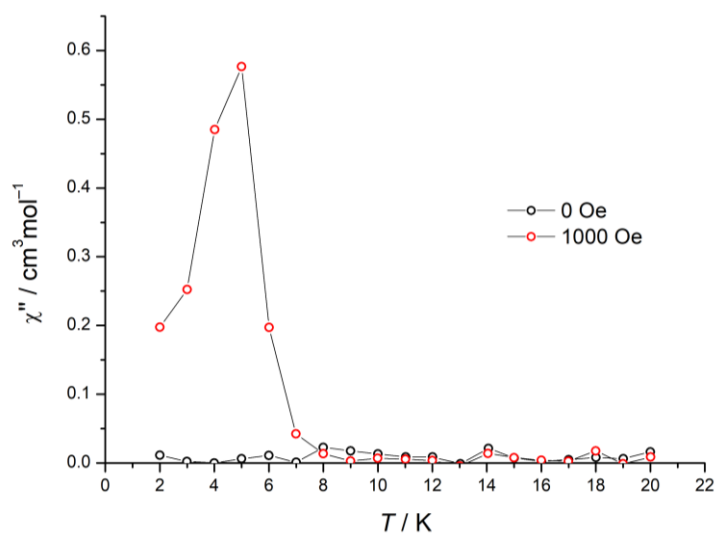


Figure 4.2.21.1. Temperature dependency of the out-of-phase signal of the ac susceptibility at 0 and 1000 Oe. A maxima is clearly achieved around 4.5K under 1000 Oe while no slow magnetic relaxation is detected without applied field.

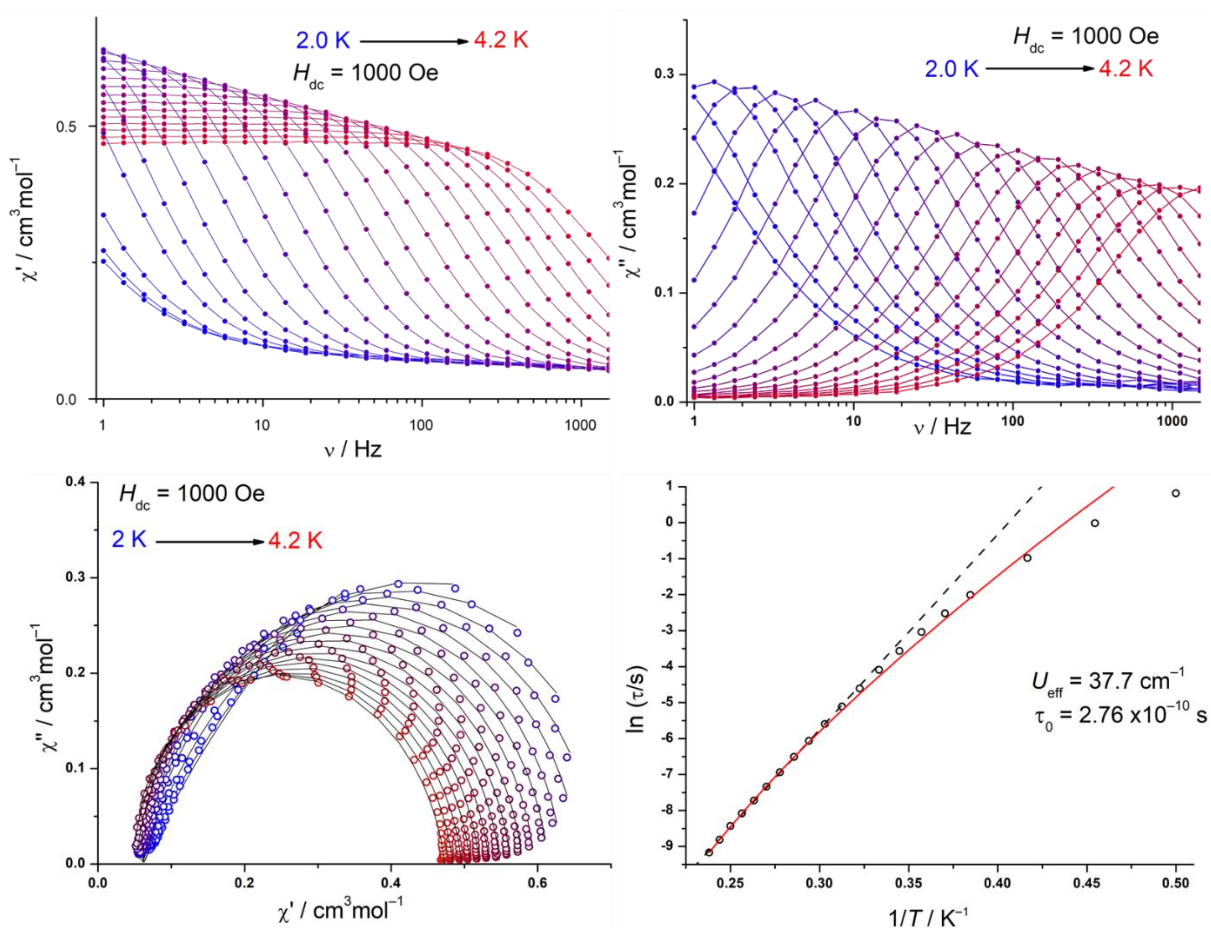


Figure 4.2.21.2. ac susceptibility data for Co(Mebox)₂. (top) In and out-of-phase signals of the ac susceptibility under 1000 Oe. Lines are guide for the eyes. (bottom) Corresponding Cole-Cole plot and Arrhenius plot. Solid lines are fits to the curves.

Ni(Mebox)₂ Isolated 22.6 mg in crystalline yield (28%) from the reaction of KMebox (2eq, 200mg, 0.26mmol) with Ni(acac)₂ (1eq, 33.4mg, 0.13mmol). Block deep-blue crystals suitable for X-ray analysis were obtained after 1w. . IR(neat): 3035w, 2901w, 2348w, 1810w, 1630m, 1534s, 1368s, 1252s, 1208s, 1002s, 810s, 740s, 547m, 502m; ¹H NMR (500 MHz, THF-d⁸, ppm) δ - 121.93 (bs, 1H, H1), - 14.38 (s, 2H, H), 19.50 (s, 2H, H), 41.03 (s, 2H, H), 42.26 (bs, 6H, CH₃); ¹³C NMR (75 MHz, THF-d⁸, ppm) δ - 381.35 (s, 1C), - 105.17 (s, 1C), - 3.21 (s, 1C) 117.72 (s, 1C) 291.19 (s, 1C) 292.44 (s, 1C) 359.58 (s, 1C) 442.38 (s, 1C) 572.78 (s, 1C). Anal. Calc. for C₃₄H₂₆NiN₄O₄ (M=613.3g/mol⁻¹): C, 66.59; H, 4.27; N, 9.14. Found: C, 65.92; H, 4.23; N, 9.05; LIFDI-MS (m/z, THF): 613.2 g/mol.

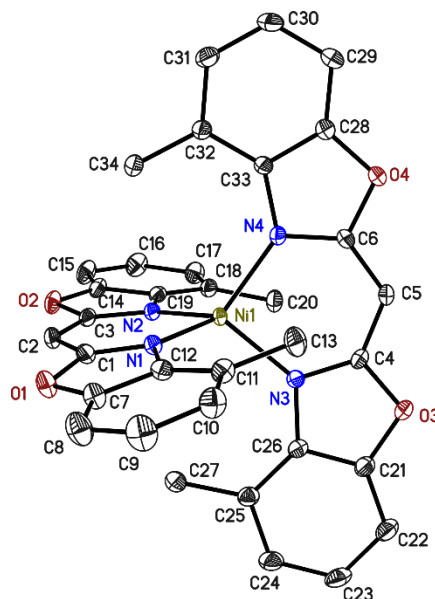


Figure 4.2.22. Molecular structure of **Ni(Mebox)₂** The asymmetric unit contains one complex molecule, without any disorder nor solvent molecule.

Structures **Fe(Mebox)₂** , **Co(Mebox)₂** and **Ni(Mebox)₂** are isostructural.

Structure code	Ni(Mebox) ₂	CCDC Number	2095993
Empirical Formula	C ₃₄ H ₂₆ NiN ₄ O ₄	μ [mm ⁻¹]	0.731
Formula weight [g mol ⁻¹]	613.30	F(000)	1272
Sample temperature [K]	100(2)	θ range [°]	1.82 to 30.68
Wavelength [Å]	0.71073	Reflections collected	85549
Crystal System	Monoclinic	Unique Reflections	8720
Space group	<i>P</i> 2 ₁ / <i>n</i>	<i>R</i> _{int}	0.0426
	<i>a</i> = 11.262(4)	Completeness to θ_{max} [%]	99.0
Unit cell dimensions [Å]	<i>b</i> = 14.937(6) β = 93.70(9)	restraints/parameter	0 / 392
	<i>c</i> = 16.914(6)	GooF	1.104
Volume [Å ³]	2839.4(18)	<i>R</i> 1 (all data)	0.0397
<i>Z</i>	4	<i>wR</i> 2 (all data)	0.0973
Crystal dimensions [mm]	0.350 0.247 0.198	max. diff. peak / hole [eÅ ⁻³]	0.466 and -0.569
Crystal shape and color	Deep blue blocks		

Series **a** for $M(\text{Box})_2$; series **b** for $M(\text{Mebox})_2$; **1-4** for Mn-Ni

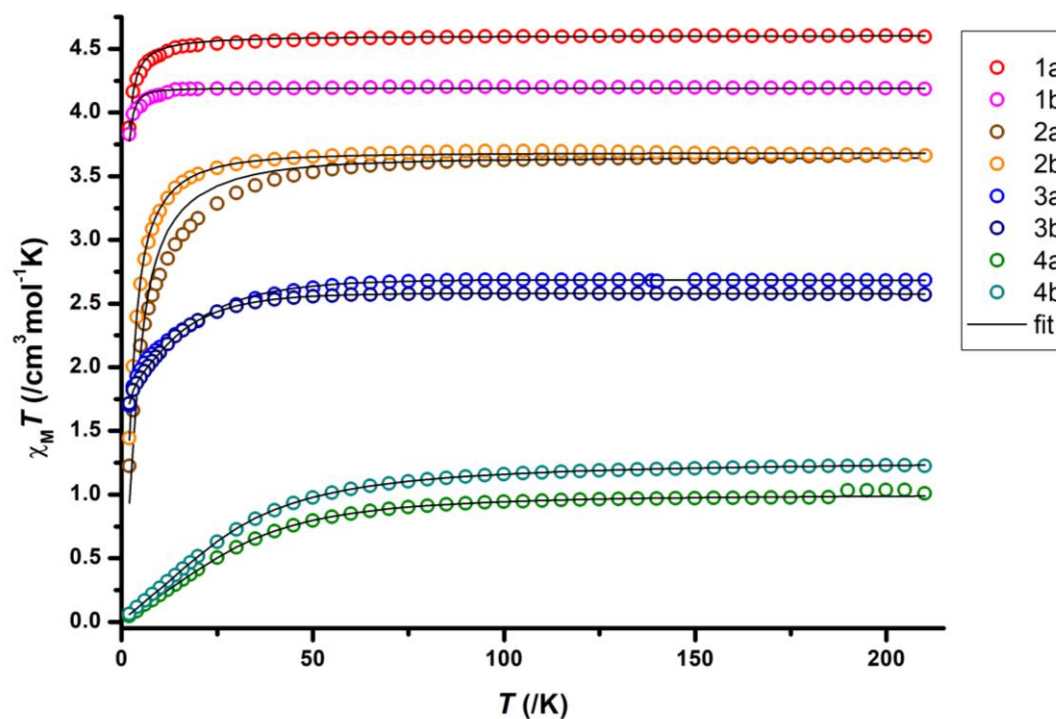


Figure 4.2.22.1. Dc susceptibility data for all $M(\text{Mebox})_2$ complexes and the parent $M(\text{Box})_2$ complexes ($M=\text{Mn, Fe, Co, Ni}$) (see D. Lüert's PhD thesis).²³⁶

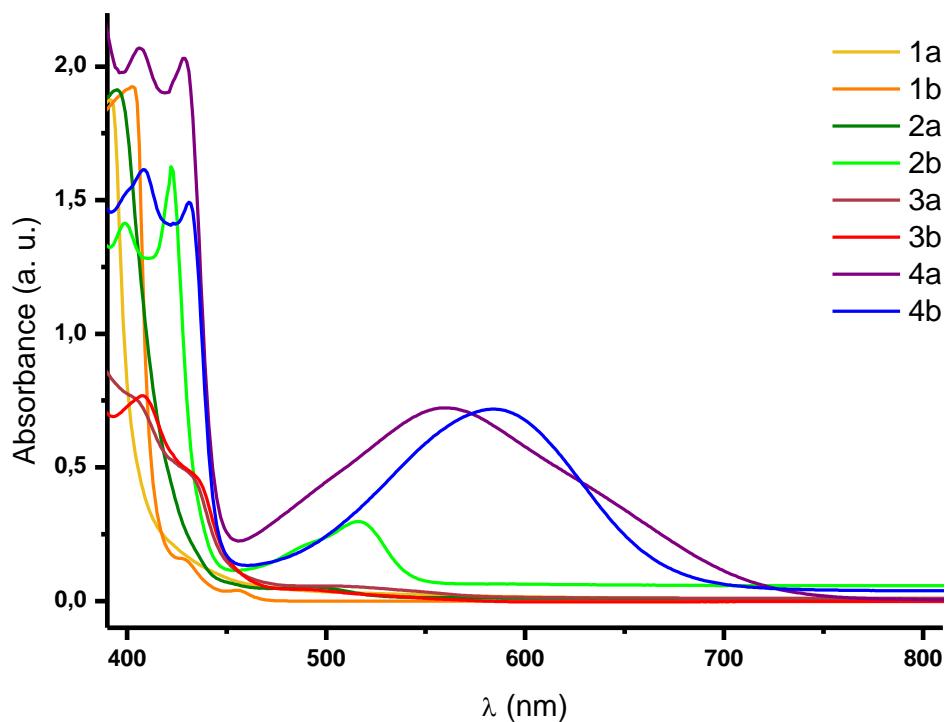


Figure 4.2.22.2. UV-vis spectra for all $M(\text{Mebox})_2$ and $M(\text{Box})_2$ complexes

CASSCF-NEVPT2 calculations:

Table 4.2.22.1. Magnetic parameters for **Co(Mebox)₂** as determined from CASSCF-NEVPT2 calculations. The parent compound Co(Box)₂ is shown here for comparison.

Compound	D (cm ⁻¹)	E/D	$g_{x, y, z}$	ΔE ($d_{xy}, d_{x^2-y^2}$) (cm ⁻¹)
Co(Box) ₂	-43	0.12	2.07, 2.21, 2.64	1 348
Co(MeBox) ₂	-27	0.02	2.13, 2.14, 2.45	2 358

The 3d orbital splitting for **Co(Box)₂** is more promising for SMM properties. However, the huge E/D value shows the presence of transverse anisotropy. The analysis of the ac data gives similar results.

Magnetic details:

Table 4.2.22.2. Experimental magnetic parameters for all **M(Mebox)₂** and **M(Box)₂** complexes

Compound	D (cm ⁻¹)	E/D	$g_{x, y, z}$	U_{eff} (cm ⁻¹)	τ_0 (s)
Mn(Box) ₂	0.0	0	2.05	–	–
Mn(MeBox) ₂	0.5	0	1.96	5.2	4.14 x 10 ⁻⁵
Fe(Box) ₂	10.6	0	2.20	–	–
Fe(MeBox) ₂	6.8	0	2.20	–	–
Co(Box) ₂	-25.0	0	2.27, 2.27, 2.58	18.8	4.61 x 10 ⁻⁶
Co(MeBox) ₂	-18.4	0.02	2.28, 2.20 2.50	10.3	2.76 x 10 ⁻¹⁰
Ni(Box) ₂	67.5	0	2.00	–	–
Ni(MeBox) ₂	54.1	0	1.95, 1.95, 3.14	–	–

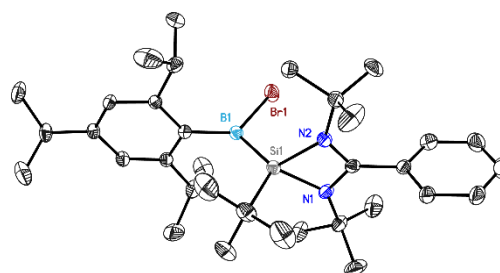
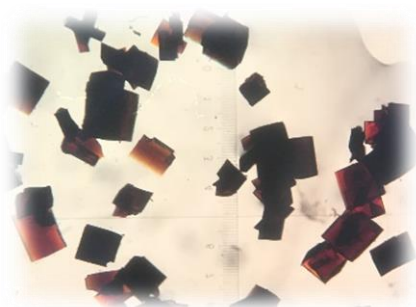
Conclusion for M(RBox)₂ (R=H, Me) complexes:

This series of transition metal complexes has the following advantages:

- they possess several optical and magnetic properties,
- the obtained complexes are highly stable in the solid state against potential oxidation,
- the obtained crystals are of significant sizes, which enables advanced crystallographic experiments (charge density, polarized neutron diffraction...),
- the box ligand is a well-known tunable platform, which is ideal to study electronic and steric effects of various substituents. This can be further exploit with lanthanides as well.

They represent novel compounds that are suitable for benchmarking studies.

Annex 1: Crystallography service



In this section, I would like to thank Prof. Dr. h.c. mult. Dr. rer. nat. em. Herbert W. Roesky and his postdoctoral fellow Dr. Mohd Nazish for the opportunity they gave me to contribute to their research through crystallographic analyses.

Note:

Some of the presented crystal structures have already been published in peer-reviewed publications and can be found online in the references below.

Publications:

Publication **I** for NS_1-4

Publication **V** for NS_7-8 (a, b, c)

Publication **XI** for NS_14

Publication **XII** for NS_11-12

Summary of following crystal structures:

Structures from Dr. Nazish Mohd (Roesky group)

Probing the coordination of heavy main group elements with ligands containing phosphane-silylene donor groups

- Crystal structure of NS_1 CCDC# 1994258
- Crystal structure of NS_2 CCDC# 1994261
- Crystal structure of NS_3 CCDC# 1994263
- Crystal structure of NS_4 CCDC# 1994265
- Crystal structure of NS_5
- Crystal structure of NS_6

Stable boron-silicon compounds and their radicals

- Crystal structure of NS_7 CCDC# 2069375
- Crystal structure of NS_8 (a, b, c) CCDC# 2069376-7 (two datasets)
- Crystal structure of NS_9
- Crystal structure of NS_10
- Crystal structure of NS_11 CCDC#2120410
- Crystal structure of NS_12 CCDC#2120409

Sb-Si-Si-Sb radical species

- Crystal structure of NS_13

Silaimine compound

- Crystal structure of NS_14 CCDC# 2067320

Selenium and alkali-metal containing compounds

- Crystal structure of NS_15
- Crystal structure of NS_16
- Crystal structure of NS_17

Crystal structure of NS_1: $\text{PhC}(\text{N}^t\text{Bu})_2\text{SiSeC}_6\text{H}_4\text{PPh}_2$

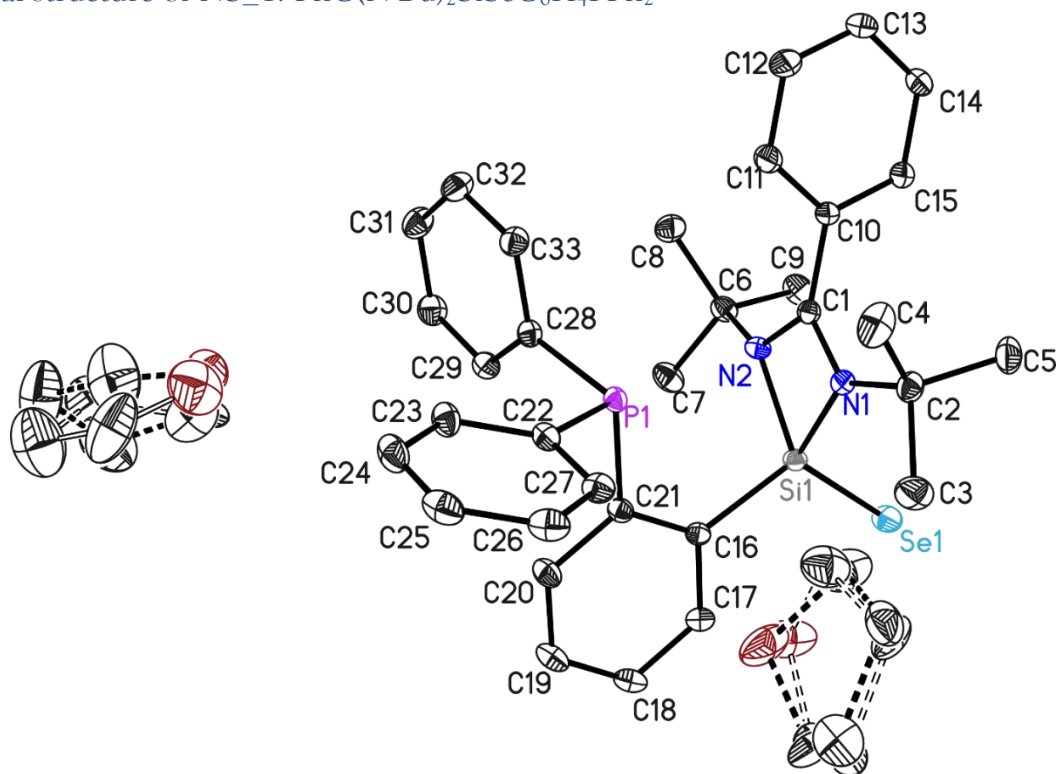


Figure 5.1: Molecular structure of NS_1 with thermal ellipsoids at 50% probability level. It consists of two fragments, one complex molecule and one and a half THF solvent molecules. The hydrogen atoms are omitted for clarity. The phosphane silylene ligand binds the selenium atom through the silicon donor atom only.

The THF molecules are disordered in two and four positions, from which two were related a crystallographic two-fold axis. Both were refined with distance restraints and restraints for the anisotropic displacement parameters. The occupancy of the major components refined to 0.50(2) and 0.346(7), respectively.

Structure code	NS_1	CCDC Number	1994258
Empirical Formula	$\text{C}_{39}\text{H}_{49}\text{N}_2\text{O}_{1.50}\text{PSeSi}$	μ [mm^{-1}]	1.141
Formula weight [g mol^{-1}]	707.82	$F(000)$	2976
Sample temperature [K]	100(2)	θ range [$^\circ$]	1.178 to 30.543
Wavelength [\AA]	0.71073	Reflections collected	121654
Crystal System	Monoclinic	Unique Reflections	10844
Space group	$C2/c$	R_{int}	0.0270
	$a = 36.923(8)$	Completeness to θ_{max} [%]	100
Unit cell dimensions [\AA]	$b = 10.143(2)$ $\beta = 110.6(2)$	restraints/parameters	464 / 531
	$c = 20.797(4)$	GooF	1.060
Volume [\AA^3]	7293(3)	R1 (all data)	0.0256
Z	8	wR2 (all data)	0.0699
Crystal dimensions [mm]	0.384 x 0.383 x 0.287	max. diff. peak / hole [$\text{e}\text{\AA}^{-3}$]	0.424 and -0.577

Crystal shape and color	Colorless blocks
-------------------------	------------------

Crystal structure of NS_2: $\text{PhC}(\text{N}^t\text{Bu})_2\text{SiZnCl}_2\text{C}_6\text{H}_4\text{PPh}_2$

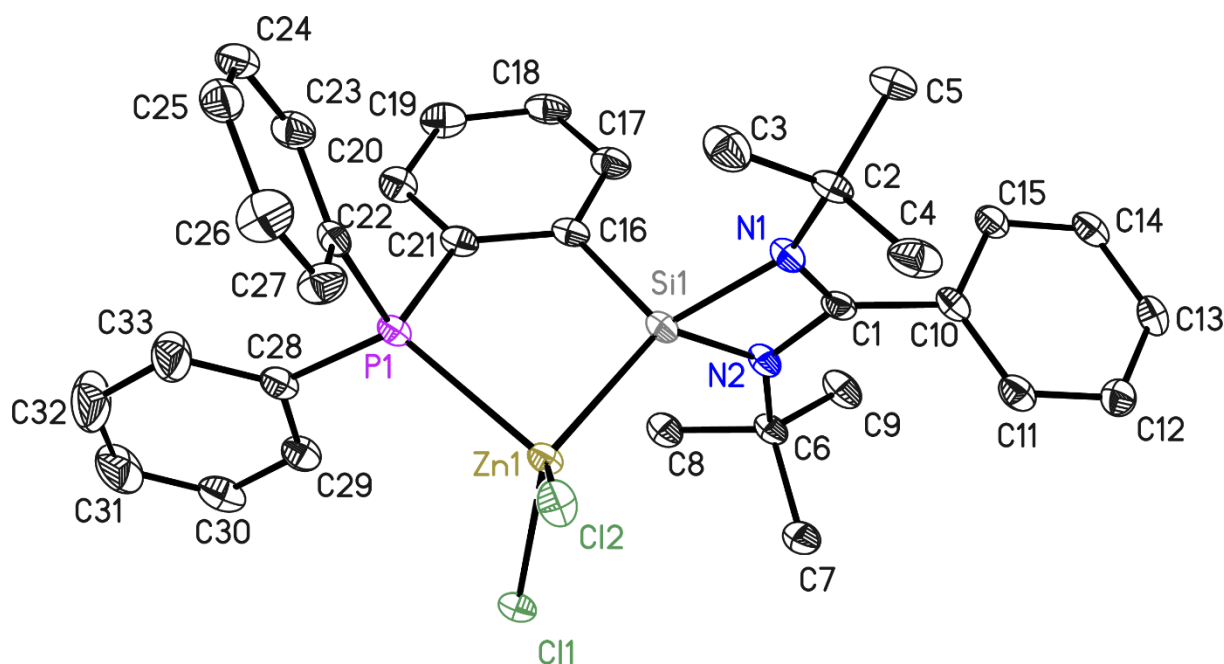


Figure 5.2: Molecular structure of NS_2 with thermal ellipsoids at 50% probability level. The hydrogen atoms are omitted for clarity. Both silicon and phosphorus donor atoms are involved in metal coordination.

Structure code	NS_2	CCDC Number	1994261
Empirical Formula	$\text{C}_{33}\text{H}_{37}\text{Cl}_2\text{N}_2\text{PSiZn}$	μ [mm^{-1}]	1.035
Formula weight [g mol^{-1}]	656.97	$F(000)$	1368
Sample temperature [K]	100(2)	θ range [$^\circ$]	2.260 to 26.815
Wavelength [\AA]	0.71073	Reflections collected	57492
Crystal System	Monoclinic	Unique Reflections	6795
Space group	$P2_1/c$	R_{int}	0.07460
	$a = 17.348(3)$	Completeness to θ_{max} [%]	99.9
Unit cell dimensions [\AA]	$b = 10.356(2)$ $\beta = 113.7(2)$	restraints/parameters	0 / 367
	$c = 19.683(7)$	GooF	1.038
Volume [\AA^3]	3237.9(15)	R1 (all data)	0.0337
Z	4	wR2 (all data)	0.0793
Crystal dimensions [mm]	0.302 x 0.128 x 0.042	max. diff. peak / hole [$\text{e}\text{\AA}^{-3}$]	0.403 and -0.395
Crystal shape and color	Colorless blocks		

Crystal structure of NS_3: $\text{PhC}(\text{N}^t\text{Bu})_2\text{SiAlCl}_3\text{C}_6\text{H}_4\text{PPh}_2$

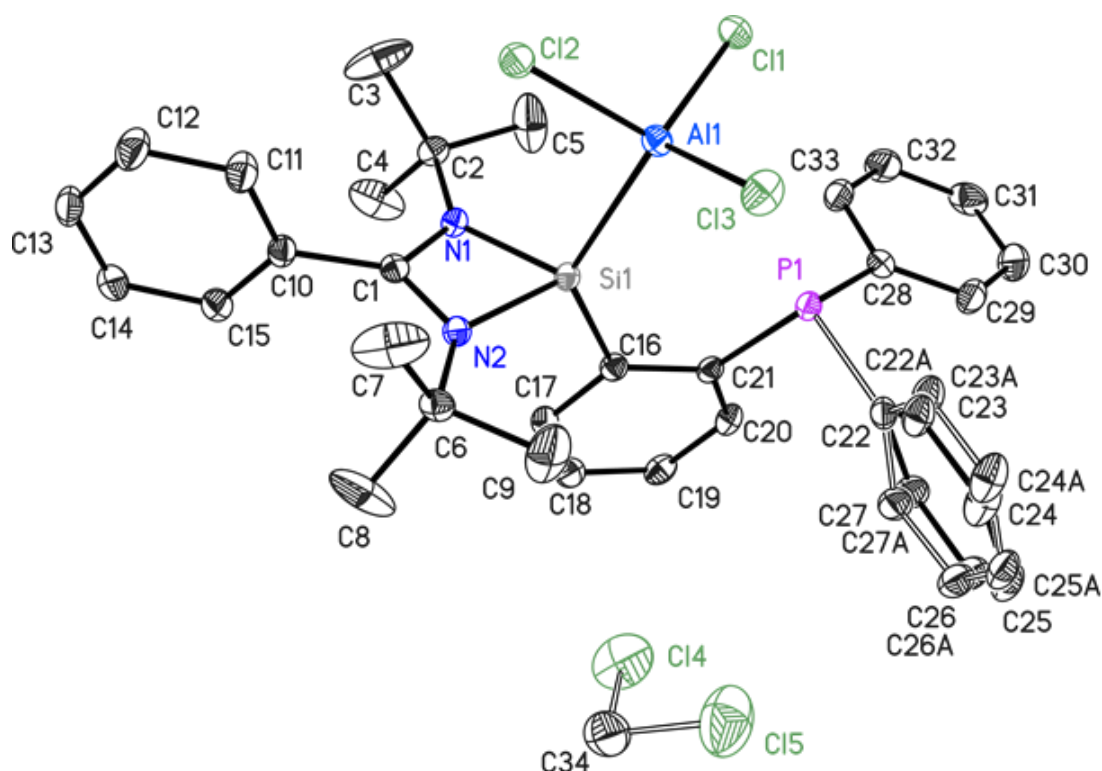


Figure 5.3: Molecular structure of NS_3 with thermal ellipsoids at 50% probability level. It consists of two fragments, one complex molecule and half a DCM solvent molecule on a special position. The hydrogen atoms are omitted for clarity. The silicon atom is coordinating the aluminium atom while the phosphorus atom points towards it, indicating a weak interaction.

One phenyl ring and the DCM molecule are disordered. For the refinement of the DCM molecule, distance restraints and restraints for the anisotropic displacement parameters were used. The occupancy of the main position of the phenyl ring refined to 0.79(2).

Structure code	NS_3	CCDC Number	1994263
Empirical Formula	$\text{C}_{33.5}\text{H}_{38}\text{AlCl}_4\text{N}_2\text{PSi}$	μ [mm^{-1}]	0.473
Formula weight [g mol^{-1}]	696.5	F(000)	1452
Sample temperature [K]	100(2)	θ range [$^\circ$]	1.82 to 26.42
Wavelength [\AA]	0.71073	Reflections collected	76991
Crystal System	Monoclinic	Unique Reflections	7136
Space group	$P2_1/c$	R_{int}	0.0352
	$a = 9.089(2)$	Completeness to θ_{max} [%]	100
Unit cell dimensions [\AA]	$b = 17.068(2)$ $\beta = 95.11(2)$	restraints/parameters	377 / 419
	$c = 22.497(3)$	GooF	1.025
Volume [\AA^3]	3476.1(10)	R1 (all data)	0.0326
Z	4	wR2 (all data)	0.0722
Crystal dimensions [mm]	0.281 x 0.223 x 0.113	max. diff. peak / hole [$\text{e}\text{\AA}^{-3}$]	0.343 and -0.275
Crystal shape and color	Colorless blocks		

Crystal structure of NS_4: $\text{PhC}(\text{N}^t\text{Bu})_2\text{SiGaCl}_3\text{C}_6\text{H}_4\text{PPh}_2$

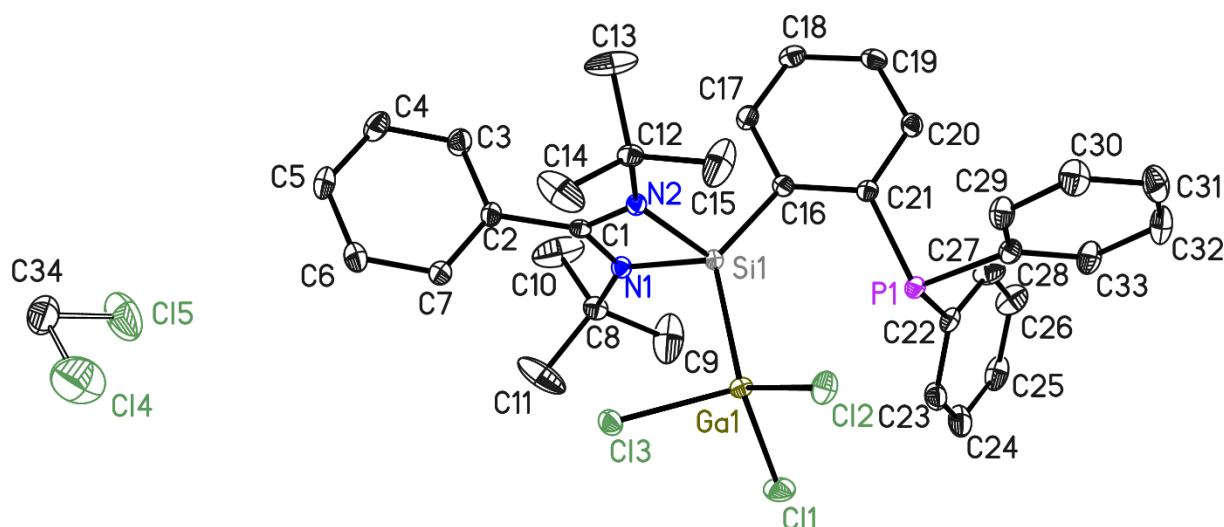


Figure 5.4: Molecular structure of NS_4 with thermal ellipsoids at 50% probability level. It consists of two fragments, one complex molecule and one DCM solvent molecule (disordered on a special position). The hydrogen atoms are omitted for clarity. The silicon atom is coordinating the gallium atom while the phosphorus atom points towards it, indicating a weak interaction

For the refinement of the DCM molecule, distance restraints and restraints for the anisotropic displacement parameters were used.

Structures NS_3 and NS_4 are isostructural.

Structure code	NS_4	CCDC Number	1994265
Empirical Formula	$\text{C}_{33.5}\text{H}_{38}\text{GaCl}_4\text{N}_2\text{PSi}$	μ [mm^{-1}]	1.210
Formula weight [g mol^{-1}]	739.24	F(000)	1524
Sample temperature [K]	100(2)	θ range [$^\circ$]	1.50 to 26.39
Wavelength [\AA]	0.71073	Reflections collected	57981
Crystal System	Monoclinic	Unique Reflections	7096
Space group	$P2_1/c$	R_{int}	0.0331
	$a = 9.034(2)$	Completeness to θ_{max} [%]	99.9
Unit cell dimensions [\AA]	$b = 17.084(2)$ $\beta = 95.28(2)$	restraints/parameters	20 / 403
	$c = 22.542(3)$	GooF	1.065
Volume [\AA^3]	3464.3(10)	R1 (all data)	0.0237
Z	4	wR2 (all data)	0.0579
Crystal dimensions [mm]	0.528 x 0.463 x 0.332	max. diff. peak / hole [$\text{e}\text{\AA}^{-3}$]	0.391 and -0.295
Crystal shape and color	Colorless blocks		

Crystal structure of NS_5: $[\{\text{PhC}(\text{N}^i\text{Bu})_2\text{SiF}_2(\text{C}_6\text{H}_4\text{PPh}_2)_2\text{Ag}\}\{\text{AlCl}_4\}]$

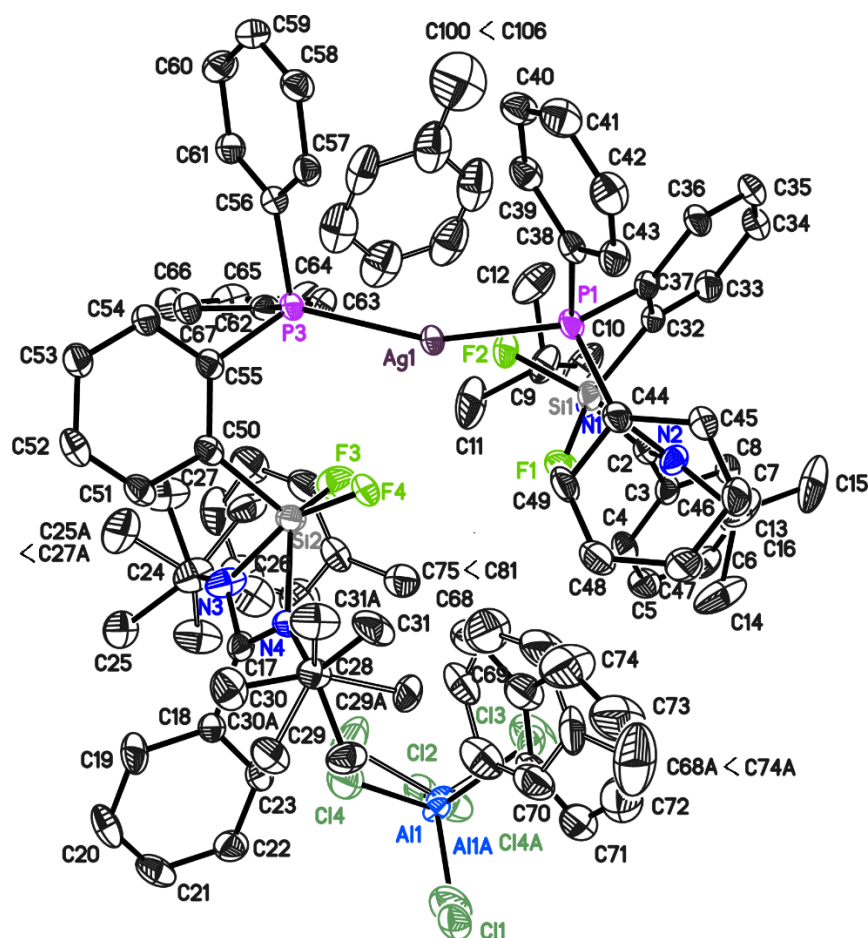


Figure 5.5: Crystal structure of NS_5. Hydrogens are omitted for clarity. Thermal ellipsoids are represented at the 50% probability level. The asymmetric unit contains one complex molecule composed of two fragments and three toluene molecules.

Structure code	NS_5	CCDC Number	/
Empirical Formula	$\text{C}_{40}\text{H}_{44.9}\text{Ag}_{0.5}\text{Al}_{0.5}\text{Cl}_2\text{F}_2\text{N}_2\text{PSi}$	μ [mm^{-1}]	0.531
Formula weight [g mol^{-1}]	789.06	F(000)	3279
Sample temperature [K]	100(2)	θ range [$^\circ$]	1.479 to 26.422
Wavelength [\AA]	0.71073	Reflections collected	146476
Crystal System	Monoclinic	Unique Reflections	16046
Space group	$P2_1/c$	R_{int}	0.1034
Unit cell dimensions [\AA]	$a = 13.773(2)$	Completeness to θ_{max} [%]	100
	$b = 13.57(19)$ $\beta = 91.80(3)$	restraints/parameters	952 / 1129
	$c = 41.898(6)$	GooF	1.026
Volume [\AA^3]	7828.0(19)	R1 (all data)	0.0516
Z	8	wR2 (all data)	0.1437
Crystal dimensions [mm]	0.188 x 0.164 x 0.153	max. diff. peak / hole [$\text{e}\text{\AA}^{-3}$]	1.580 and -1.114
Crystal shape and color	Colorless blocks		

Crystal structure of NS_6: $\text{PhC}(\text{N}^t\text{Bu})_2\text{SiP}(\text{Tip})\text{C}_6\text{H}_4\text{PPh}_2$

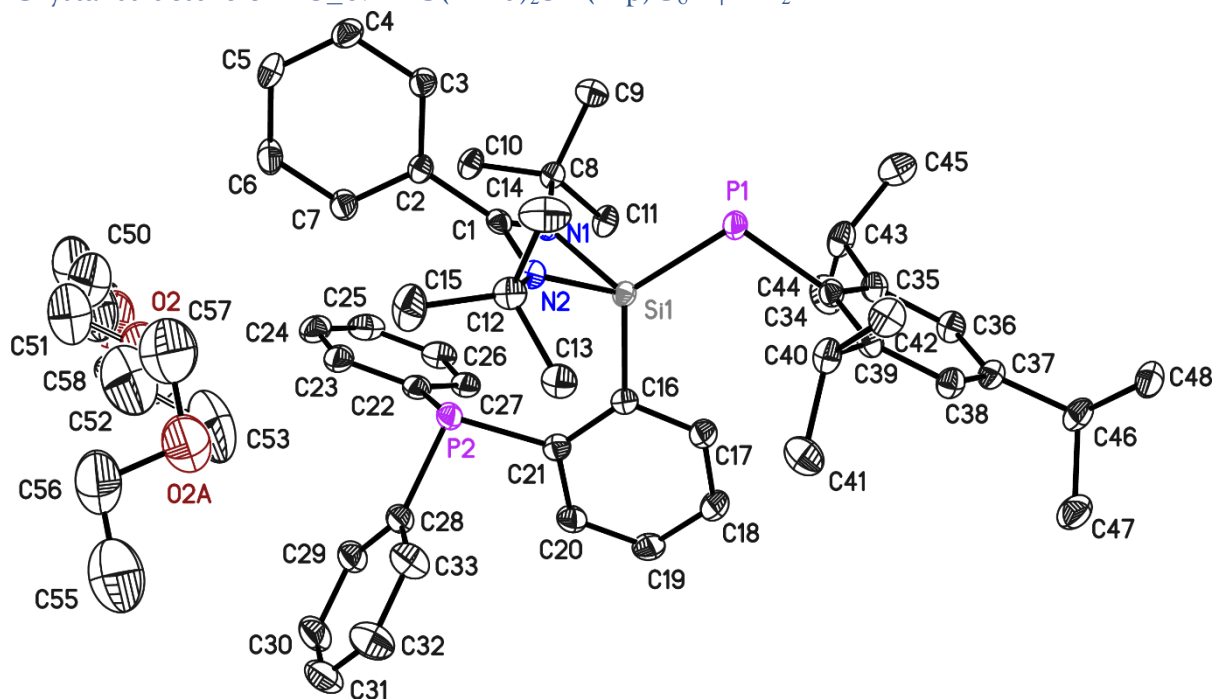


Figure 5.6: Crystal structure of NS_6. Hydrogens are omitted for clarity. The thermal ellipsoids are represented at the 50% probability level. The asymmetric unit contains one complex molecule and one disordered ether molecule.

Structure code	NS_6	CCDC Number	/
Empirical Formula	$\text{C}_{53.10}\text{H}_{71.95}\text{N}_2\text{O}_{1.27}\text{P}_2\text{Si}$	μ [mm^{-1}]	0.147
Formula weight [g mol^{-1}]	848.65	F(000)	917
Sample temperature [K]	100(2)	θ range [°]	1.119 to 27.066
Wavelength [Å]	0.71073	Reflections collected	118963
Crystal System	Triclinic	Unique Reflections	11161
Space group	$P\bar{1}$	R_{int}	0.0990
Unit cell dimensions [Å]	$a=10.3137(14)$ $\alpha=86.436(2)$	Completeness to θ_{max} [%]	100
	$b=13.9512(18)$ $\beta=113.7(2)$	restraints/parameters	243 / 602
Volume [Å ³]	$c=18.865(2)$ $\gamma=76.474(2)$	GooF	1.045
	2546.1(6)	R1 (all data)	0.0410
Z	2	wR2 (all data)	0.1179
Crystal dimensions [mm]	0.282 x 0.266 x 0.190	max. diff. peak / hole [eÅ^{-3}]	0.395 and -0.701
Crystal shape and color	Colorless blocks		

Crystal structure of NS_7: $\text{PhC}(\text{N}^t\text{Bu})_2\text{Si}^t(\text{Bu})^* - \text{B}(\text{Br})\text{Tip}$

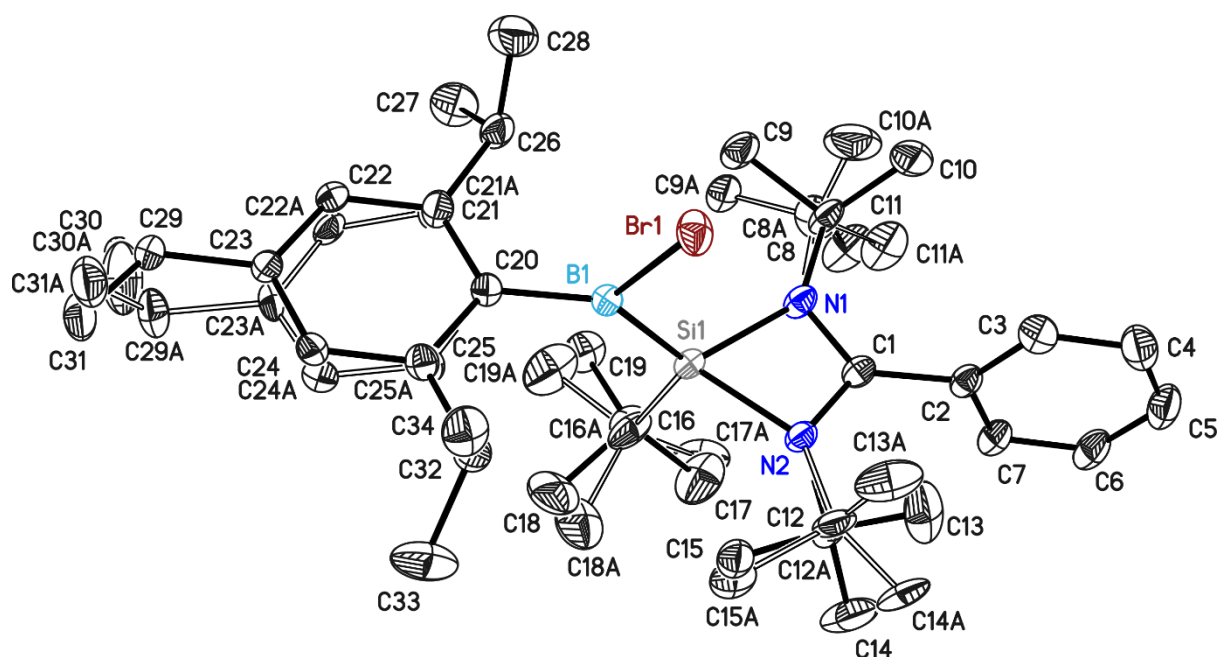


Figure 5.7: Molecular structure of NS_7. The asymmetric unit consists of one complex molecule. Light grey, baby blue, black, blue and dark red represent silicon, boron, carbon, nitrogen and bromine atoms, respectively. The hydrogen atoms are omitted for clarity.

The tert-butyl groups and the Tip ligand are disordered. The disorders were treated with distance and anisotropic displacement parameter restraints. The occupancies of the major positions were refined to 0.811(5), 0.814(7), 0.625(15), and 0.797(5), respectively.

Structure code	NS_7	CCDC Number	2069375
Empirical Formula	$\text{C}_{34}\text{H}_{55}\text{BBrN}_2\text{Si}$	μ [mm^{-1}]	1.253
Formula weight [g mol^{-1}]	610.61	F(000)	654
Sample temperature [K]	100(2)	θ range [$^\circ$]	1.999 to 28.590
Wavelength [\AA]	0.71073	Reflections collected	67574
Crystal System	Triclinic	Unique Reflections	8740
Space group	$P\bar{1}$	R_{int}	0.0255
Unit cell dimensions [\AA]	$a = 9.526(2)$ $\alpha = 81.14(2)$	Completeness to θ_{max} [%]	99.9
	$b = 10.332(2)$ $\beta = 89.09(3)$	restraints/parameters	1244 / 539
	$c = 17.731(3)$ $\gamma = 86.07(2)$	GooF	1.053
Volume [\AA^3]	1720.2(6)	R1 (all data)	0.0307
Z	2	wR2 (all data)	0.0712
Crystal dimensions [mm]	0.350 x 0.240 x 0.230	max. diff. peak / hole [$\text{e}\text{\AA}^{-3}$]	0.516 and -0.374
Crystal shape and color	Dark red-orange blocks		

Crystal structure of NS_8: $\text{PhC}(\text{N}^i\text{Bu})_2\text{Si}(\text{HMDS})^+ \cdot \text{B}(\text{Br})\text{Tip}$

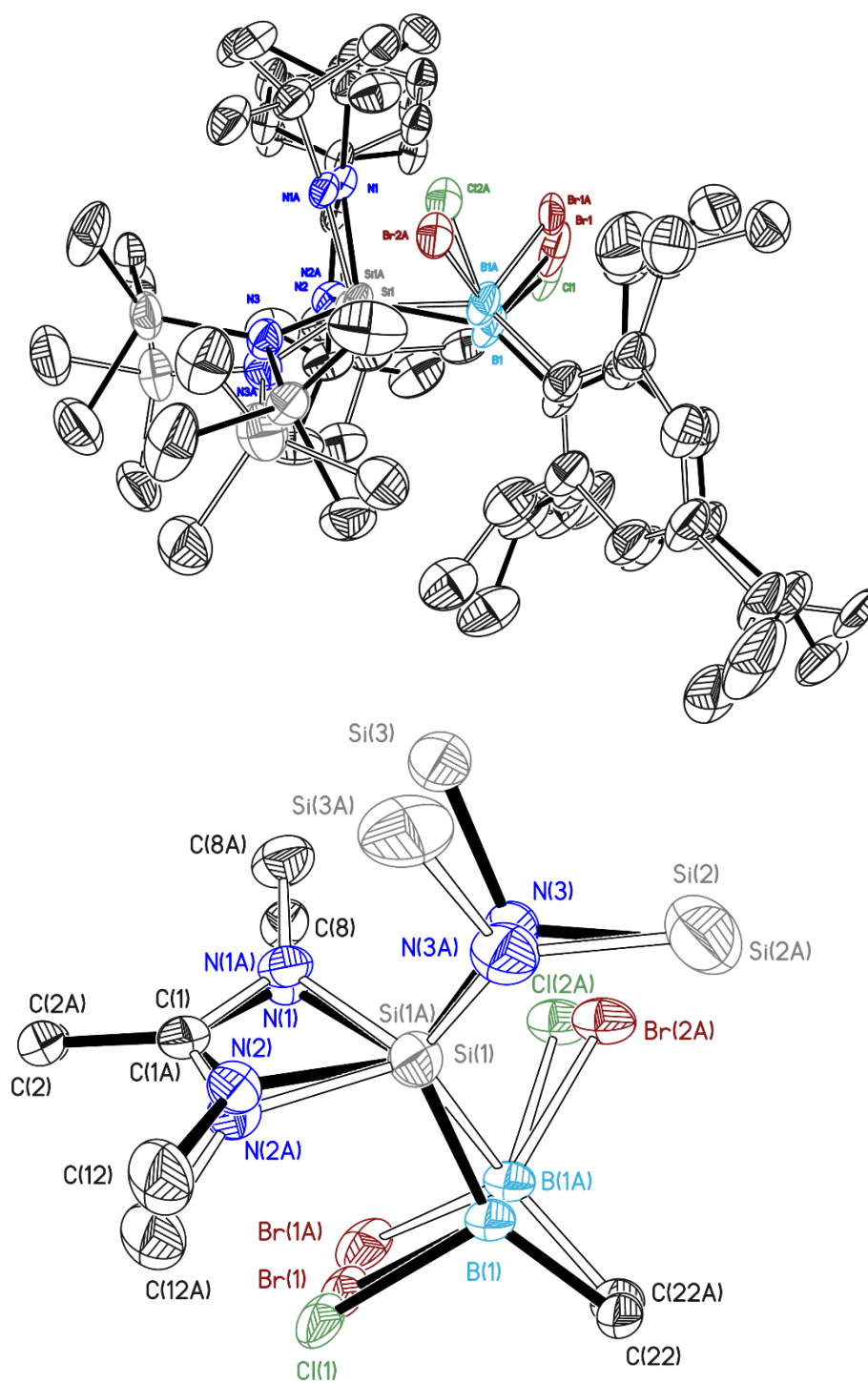


Figure 5.8: Molecular structure of NS_8 with all disorders (a, b, c), with thermal ellipsoids at 50% probability level. It consists of one complex molecule. The hydrogen atoms are omitted for clarity. A more detailed view zooming on the Si-B bond is shown for better clarity (bottom).

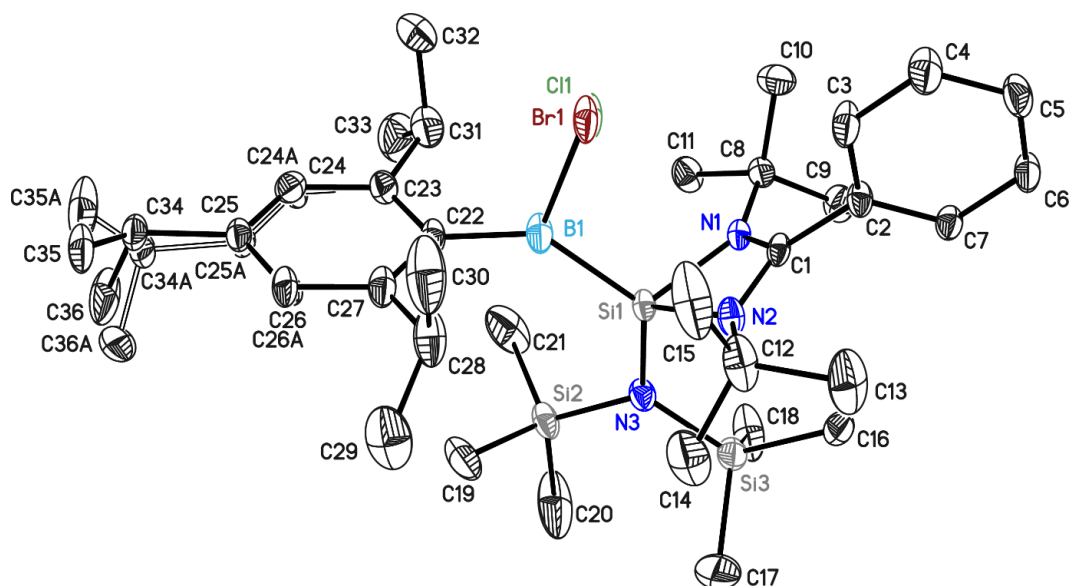


Figure 5.9: Molecular structure of NS_8 a/b with thermal ellipsoids at 50% probability level. Hydrogen atoms are omitted for clarity.

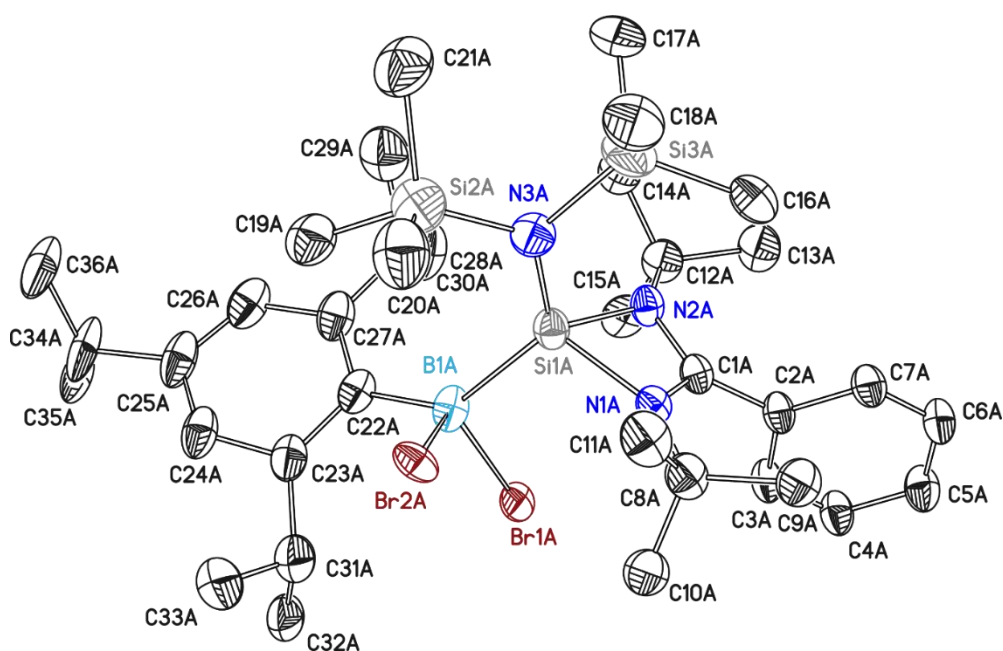


Figure 5.10: Molecular structure of NS_8 c with thermal ellipsoids at 50% probability level. Hydrogen atoms are omitted for clarity.

The isopropyl group on the Tip ligand is disordered. The disorder was treated with distance and anisotropic displacement parameter restraints. The occupancy of the major positions of the Tip ligand refined to 0.609(7). The Br/Cl disorder is in agreement with the LIFDI-MS results. The chlorine is probably coming from the starting material. The occupancy of the Cl atom refined to 0.167(2). However, the B-Cl distance refined with 1.970(8) Å for the second data set and even 2.121(17) Å for the first data set, which are much longer values than the ones calculated by theory. This indicates that the Br/Cl positions are not well resolved.

Structure code	NS_8_first dataset	CCDC Number	2069376
Empirical Formula	C ₃₆ H ₆₄ BBr _{1.09} Cl _{0.10} N ₃ Si ₃	μ [mm ⁻¹]	1.230
Formula weight [g mol ⁻¹]	706.42	F(000)	776
Sample temperature [K]	100(2)	θ range [°]	2.040 to 28.452
Wavelength [Å]	0.71073	Reflections collected	120593
Crystal System	Triclinic	Unique Reflections	10107
Space group	$P\bar{1}$	R _{int}	0.0590
Unit cell dimensions [Å]	$a = 10.148(2)$ $\alpha = 87.80(4)$	Completeness to θ_{\max} [%]	100
	$b = 12.679(3)$ $\beta = 83.69(4)$	restraints/parameters	2779 / 832
	$c = 15.951(3)$ $\gamma = 81.51(4)$	GooF	1.035
Volume [Å ³]	2017.1(8)	R1 (all data)	0.0693
Z	2	wR2 (all data)	0.1033
Crystal dimensions [mm]	0.359 x 0.211 x 0.184	max. diff. peak / hole [eÅ ⁻³]	0.455 and -0.345
Crystal shape and color	Dark red-orange blocks		

Structure code	NS_8_second dataset	CCDC Number	2069377
Empirical Formula	C ₃₆ H ₆₄ BBr _{0.83} Cl _{0.17} N ₃ Si ₃	μ [mm ⁻¹]	0.983
Formula weight [g mol ⁻¹]	706.42	F(000)	760
Sample temperature [K]	100(2)	θ range [°]	1.631 to 28.474
Wavelength [Å]	0.71073	Reflections collected	127493
Crystal System	Triclinic	Unique Reflections	10126
Space group	$P\bar{1}$	R _{int}	0.0761
Unit cell dimensions [Å]	$a = 10.137(2)$ $\alpha = 88.12(4)$	Completeness to θ_{\max} [%]	100
	$b = 12.623(3)$ $\beta = 83.67(4)$	restraints/parameters	323 / 472
	$c = 15.990(3)$ $\gamma = 81.64(4)$	GooF	1.075
Volume [Å ³]	2011.7(8)	R1 (all data)	0.0444
Z	2	wR2 (all data)	0.1048
Crystal dimensions [mm]	0.359 x 0.211 x 0.184	max. diff. peak / hole [eÅ ⁻³]	0.866 and -0.910
Crystal shape and color	Dark red-orange blocks		

Crystal structure of NS_9: $\text{PhC}(\text{N}^t\text{Bu})_2\text{Si}(\text{NMe}_2)^{\bullet}-\text{B}(\text{Br})\text{Tip}$

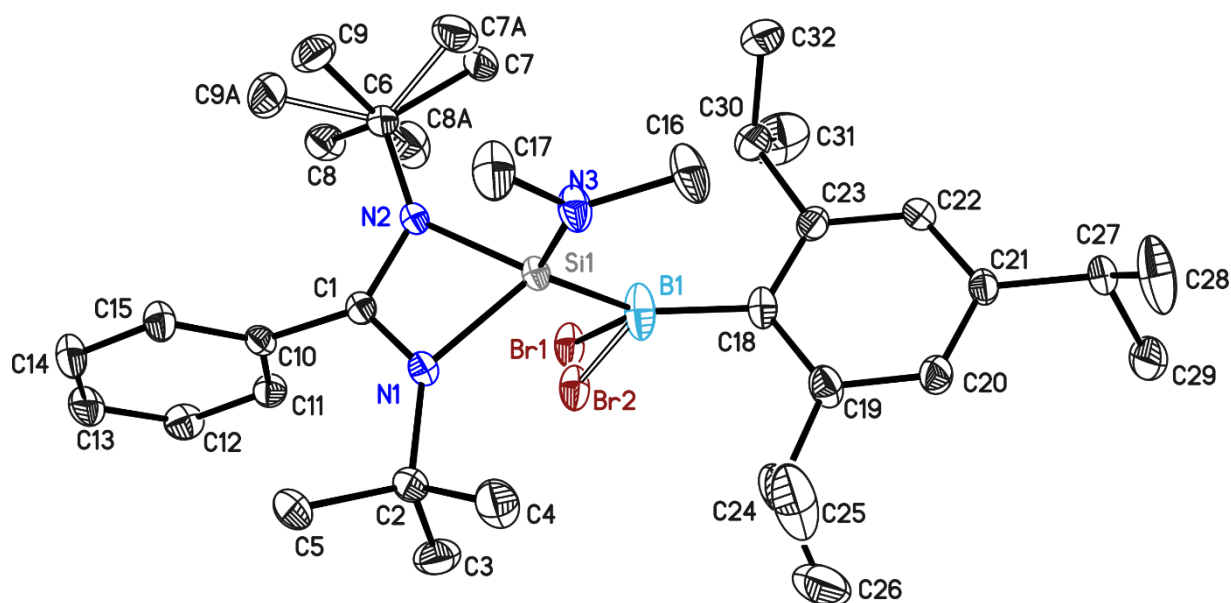


Figure 5.11: Crystal structure of NS_9. Hydrogens are omitted for clarity. Thermal ellipsoids are represented at the 50% probability level. The asymmetric unit contains one complex molecule. The bromine atom and one t Bu group were found disordered. The compound is EPR-active.

Structure NS_9 is similar to NS_7 and NS_8 (also a radical species) and varies only due to the substituent on the silicon atom.

Structure code	NS_8	CCDC Number	/
Empirical Formula	$\text{C}_{32}\text{H}_{52}\text{BBrN}_3\text{Si}$	μ [mm^{-1}]	1.263
Formula weight [g mol^{-1}]	597.57	F(000)	1263
Sample temperature [K]	100(2)	θ range [$^\circ$]	1.686 to 28.423
Wavelength [\AA]	0.71073	Reflections collected	133165
Crystal System	Monoclinic	Unique Reflections	8564
Space group	$P2_1/n$	R_{int}	0.0498
	$a=11.0999(8)$	Completeness to θ_{max} [%]	99.9
Unit cell dimensions [\AA]	$b=14.8915(11)$ $\beta=102.589(2)$	restraints/parameters	145 / 398
	$c=21.1549(15)$	GooF	1.487
Volume [\AA^3]	3412.7(4)	R1 (all data)	0.0415
Z	4	wR2 (all data)	0.0877
Crystal dimensions [mm]	0.359 x 0.337 x 0.201	max. diff. peak / hole [$\text{e}\text{\AA}^{-3}$]	0.406 and -0.354
Crystal shape and color	Red blocks		

Crystal structure of NS_10: PhC(NⁱBu)₂Si(NⁱBu)-B(Br₂)Tip

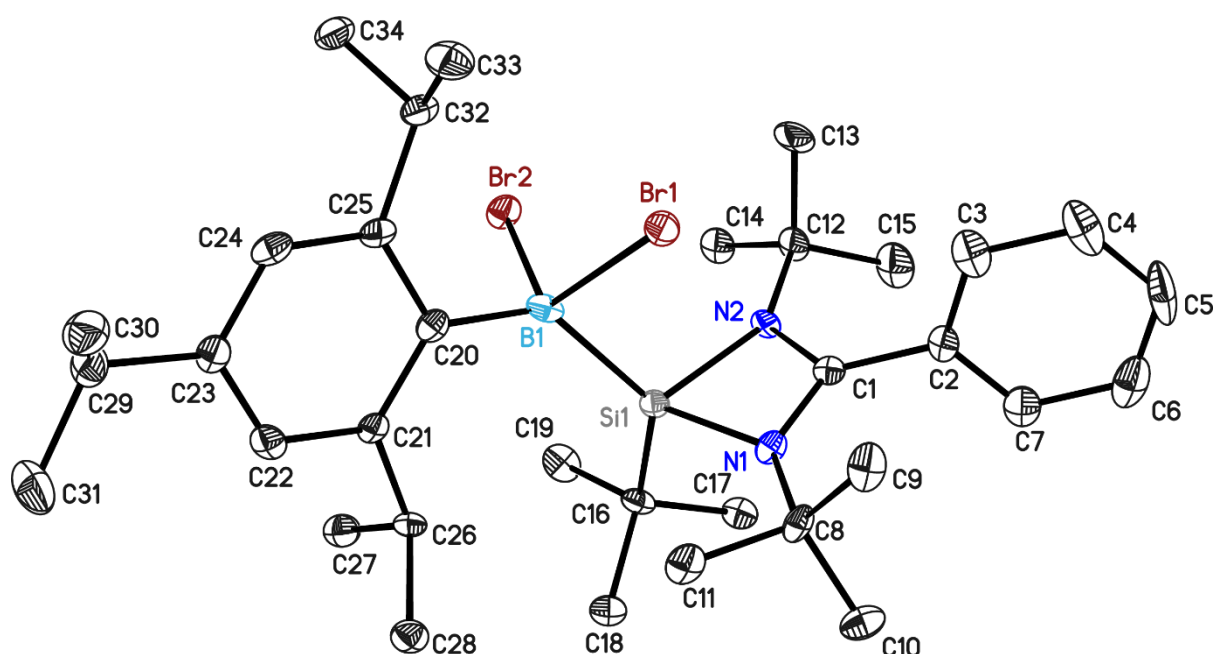


Figure 5.12: Crystal Structure of NS_10. The asymmetric unit contains one complex molecule. This compound was isolated during the work-up of reactions giving NS_7.

Structure code	NS_10	CCDC Number	/
Empirical Formula	C ₃₄ H ₅₅ BBr ₂ N ₂ Si	μ [mm ⁻¹]	2.409
Formula weight [g mol ⁻¹]	690.52	F(000)	1448
Sample temperature [K]	100(2)	θ range [°]	1.510 to 26.481
Wavelength [Å]	0.71073	Reflections collected	24265
Crystal System	Monoclinic	Unique Reflections	6805
Space group	<i>P</i> 2 ₁ / <i>n</i>	<i>R</i> _{int}	0.1416
	<i>a</i> =16.0881(19)	Completeness to θ_{\max} [%]	97.1
Unit cell dimensions [Å]	<i>b</i> =12.4827(13) β =105.962(5)	restraints/parameters	0 / 376
	<i>c</i> =17.868(2)	GooF	0.918
Volume [Å ³]	3450.0(7)	<i>R</i> 1 (all data)	0.0499
<i>Z</i>	4	<i>wR</i> 2 (all data)	0.1198
Crystal dimensions [mm]	0.100 x 0.100 x 0.100	max. diff. peak / hole [eÅ ⁻³]	1.849 and - 1.270
Crystal shape and color	Colorless blocks		

Crystal structure of NS_11: $\text{PhC}(\text{N}^t\text{Bu})_2\text{SiB}(\text{Tip})\text{C}_6\text{H}_4\text{PPh}_2$

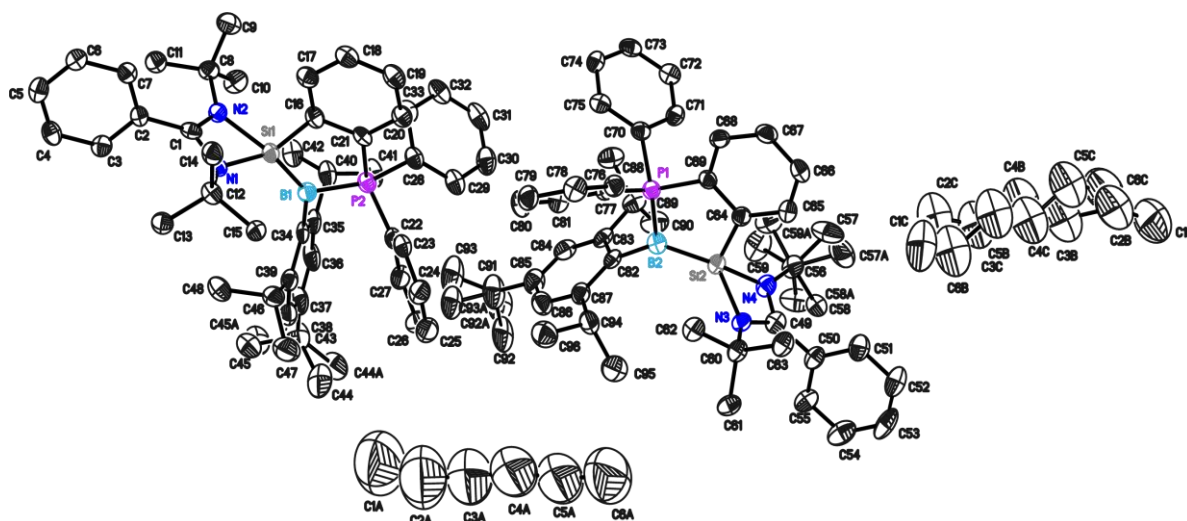


Figure 5.13: Molecular structure of NS_11. Hydrogens are omitted for clarity. The thermal ellipsoids are represented at the 50% probability level. The asymmetric unit contains two complex molecules and two hexane molecules, which are disordered and badly resolved. Additional disorder can be refined on the complex molecules as well.

Structure code	NS_11	CCDC Number	2120410
Empirical Formula	$\text{C}_{54}\text{H}_{72.5}\text{BN}_2\text{PSi}$	μ [mm^{-1}]	0.116
Formula weight [g mol^{-1}]	819.51	F(000)	1778
Sample temperature [K]	100(2)	θ range [$^\circ$]	0.763 to 25.154
Wavelength [\AA]	0.71073	Reflections collected	198926
Crystal System	Triclinic	Unique Reflections	17513
Space group	$P\bar{1}$	R_{int}	0.2837
Unit cell dimensions [\AA]	$a = 10.415(3)$ $\alpha = 104.60(2)$	Completeness to θ_{max} [%]	99.0
	$b = 18.086(5)$ $\beta = 90.81(2)$	restraints/parameters	687 / 1218
Volume [\AA^3]	$c = 27.627(7)$ $\gamma = 101.09(3)$	GooF	1.031
	4931(2)	R1 (all data)	0.1834
Z	4	wR2 (all data)	0.2450
Crystal dimensions [mm]	0.100 x 0.100 x 0.100	max. diff. peak / hole [$\text{e}\text{\AA}^{-3}$]	0.511 and -0.605
Crystal shape and color	Red needles		

Crystal structure of NS_12: $\text{PhC}(\text{N}^t\text{Bu})_2\text{SiB}(\text{Tip})\text{C}_6\text{H}_4\text{PPh}_2\text{Br}$

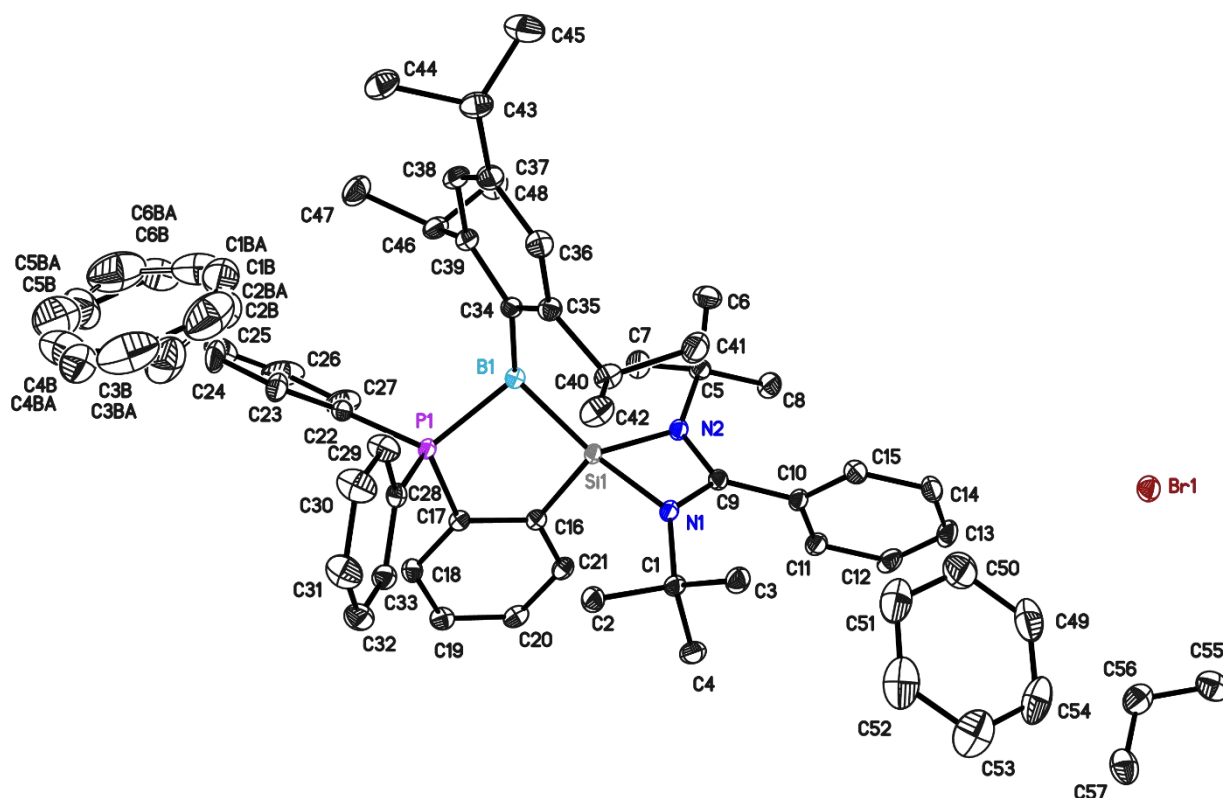


Figure 5.14: Crystal structure of NS_12. The asymmetric unit contains one complex molecule and two and a half benzene molecules. The compound is EPR active.

Structure code	NS_12	CCDC Number	2120409
Empirical Formula	$\text{C}_{63}\text{H}_{75}\text{BrBrN}_2\text{SiP}$	μ [mm^{-1}]	0.821
Formula weight [g mol^{-1}]	1010.03	F(000)	2144
Sample temperature [K]	100(2)	θ range [$^\circ$]	1.234 to 30.710
Wavelength [\AA]	0.71073	Reflections collected	191682
Crystal System	Monoclinic	Unique Reflections	17422
Space group	$P2_1/c$	R_{int}	0.0543
Unit cell dimensions [\AA]	$a=17.7776(7)$	Completeness to θ_{max} [%]	100
	$b=15.2236(6)$ $\beta=111.865(2)$	restraints/parameters	0 / 689
Volume [\AA^3]	$c=22.3727(8)$	GooF	1.019
	5619.4(4)	R1 (all data)	0.0509
Z	4	wR2 (all data)	0.0917
Crystal dimensions [mm]	0.629 x 0.332 x 0.214	max. diff. peak / hole [$\text{e}\text{\AA}^{-3}$]	1.071 and -0.335
Crystal shape and color	Red blocks		

Crystal structure of NS_13: $\text{PhC}(\text{N}^t\text{Bu})_2\text{TipSbSi-SiSbTip}(\text{N}^t\text{Bu})_2\text{CPh}$

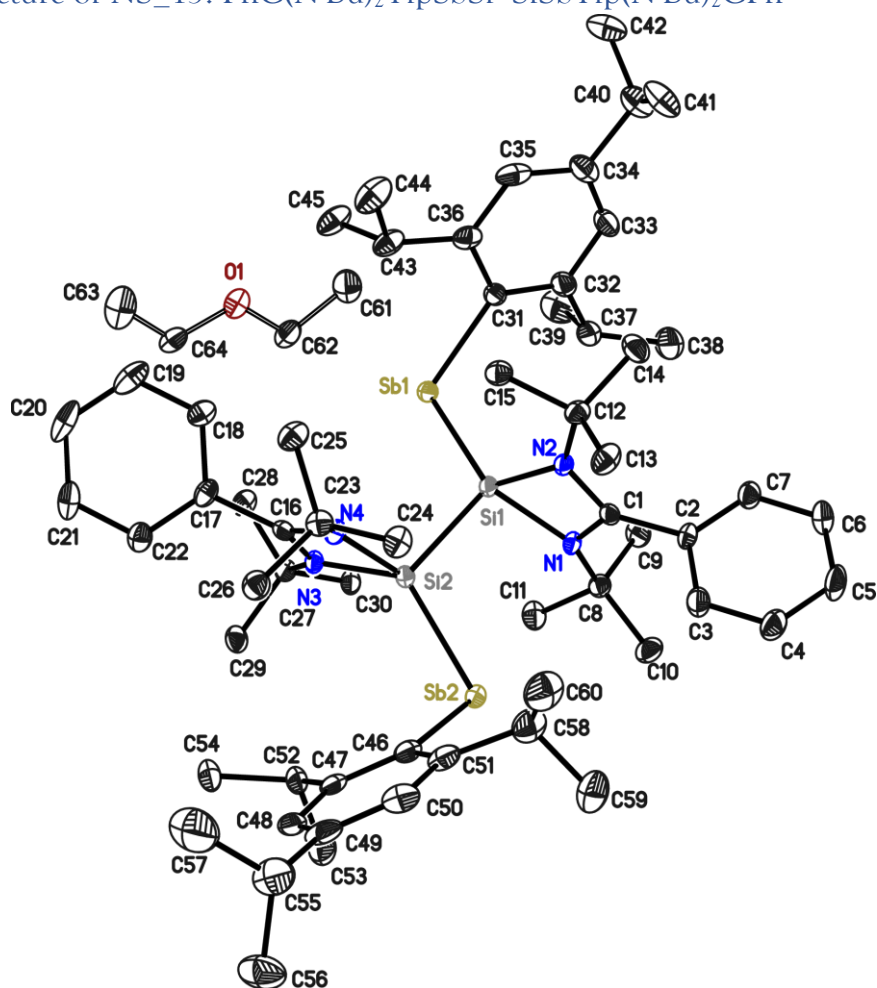


Figure 5.15: Crystal structure of NS_13. Hydrogens are omitted for clarity. Thermal ellipsoids are represented at the 50% probability level. The asymmetric unit contains one complex molecule featuring a Sb-Si-Si-Sb zig-zag unit. The compound is a radical species and represents the first Sb-Si-Si-Sb bridged compound.

Structure code	NS_13 (twin)	CCDC Number	/
Empirical Formula	$\text{C}_{62}\text{H}_{97}\text{Sb}_2\text{O}_{0.5}\text{N}_4\text{Si}_2$	μ [mm^{-1}]	0.925
Formula weight [g mol^{-1}]	1206.11	F(000)	2524
Sample temperature [K]	100(2)	θ range [$^\circ$]	1.189 to 29.770
Wavelength [\AA]	0.71073	Reflections collected	175058
Crystal System	Monoclinic	Unique Reflections	13261
Space group	$P2_1/c$	R_{int}	0.0827
	$a = 17.933(3)$	Completeness to θ_{max} [%]	99.9
Unit cell dimensions [\AA]	$b = 10.375(2)$ $\beta = 91.62(2)$	restraints/parameters	48 / 687
	$c = 34.259(4)$	GooF	1.021
Volume [\AA^3]	6371.5(18)	R1 (all data)	0.0970
Z	4	wR2 (all data)	0.2707
Crystal dimensions [mm]	0.100 x 0.115 x 0.229	max. diff. peak / hole [$\text{e}\text{\AA}^{-3}$]	0.956 and -0.813
Crystal shape and color	Red-orange blocks		

Crystal structure of NS_14: $\text{PhC}(\text{N}^t\text{Bu})_2\text{Si}(\text{HMDS})(\text{N}^t\text{Bu})\text{Si}(\text{N}^t\text{Bu})_2\text{CPh}$

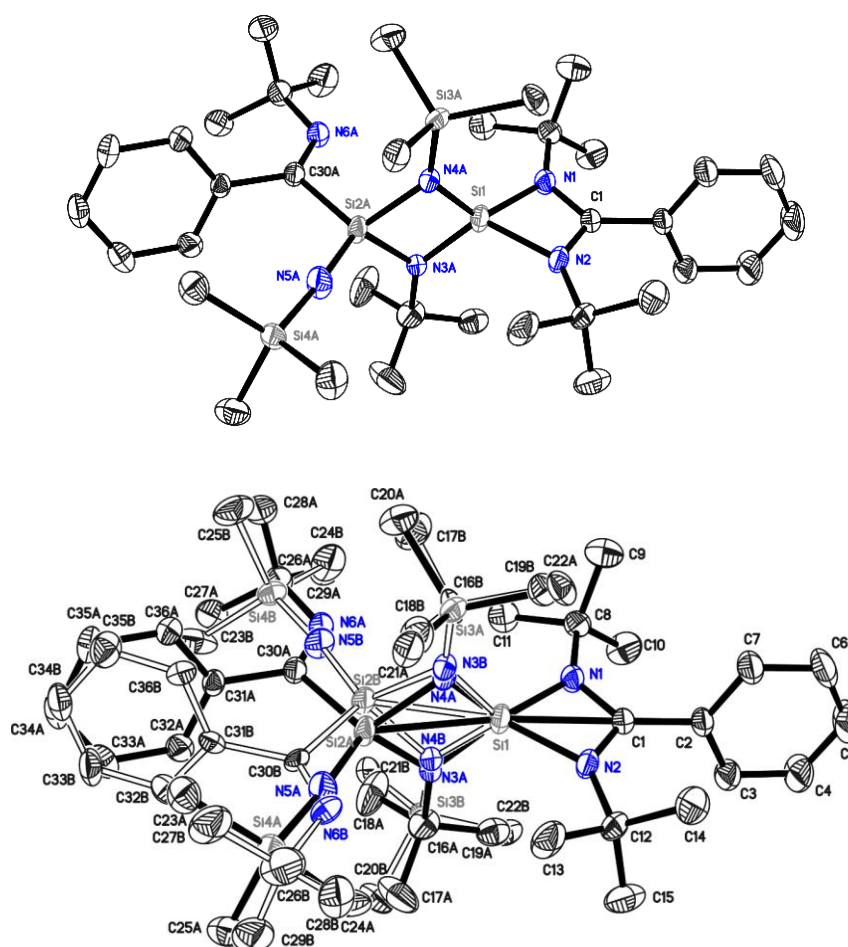


Figure 5.16: Crystal structure of NS_14 (structure solution with P. Niklas Ruth). The main component is depicted on top.

The structure is highly disordered due to ligand scrambling during the reaction. While one amidinate ligand survived during the synthesis, the second one underwent a rearrangement resulting in the two present positions and the $^t\text{Bu}/\text{SiMe}_3$ disorders.

Structure code	NS_14	CCDC Number	2067320
Empirical Formula	$\text{C}_{36}\text{H}_{64}\text{N}_6\text{Si}_4$	μ [mm^{-1}]	0.176
Formula weight [g mol^{-1}]	693.29	F(000)	1512
Sample temperature [K]	100(2)	θ range [$^\circ$]	1.803 to 29.155
Wavelength [\AA]	0.71073	Reflections collected	85318
Crystal System	Monoclinic	Unique Reflections	11096
Space group	Cc	R_{int}	0.0345
Unit cell dimensions [\AA]	$a = 11.985(2)$	Completeness to θ_{max} [%]	100
	$b = 22.595(3)$ $\beta = 94.22(2)$	restraints/parameters	1644 / 652
	$c = 15.218(2)$	GooF	1.035
Volume [\AA^3]	4109.9(10)	R1 (all data)	0.039
Z	4	wR2 (all data)	0.0927
Crystal dimensions [mm]	0.421 x 0.401 x 0.222	max. diff. peak / hole [$\text{e}\text{\AA}^{-3}$]	0.370 and -0.196
Crystal shape and color	Colorless plates		

Crystal structure of NS_15: $\text{PhC}(\text{N}^t\text{Bu})_2\text{Si}^t(\text{Bu})\text{Se}/\text{PhC}(\text{HN}^t\text{Bu})_2\text{Br}$

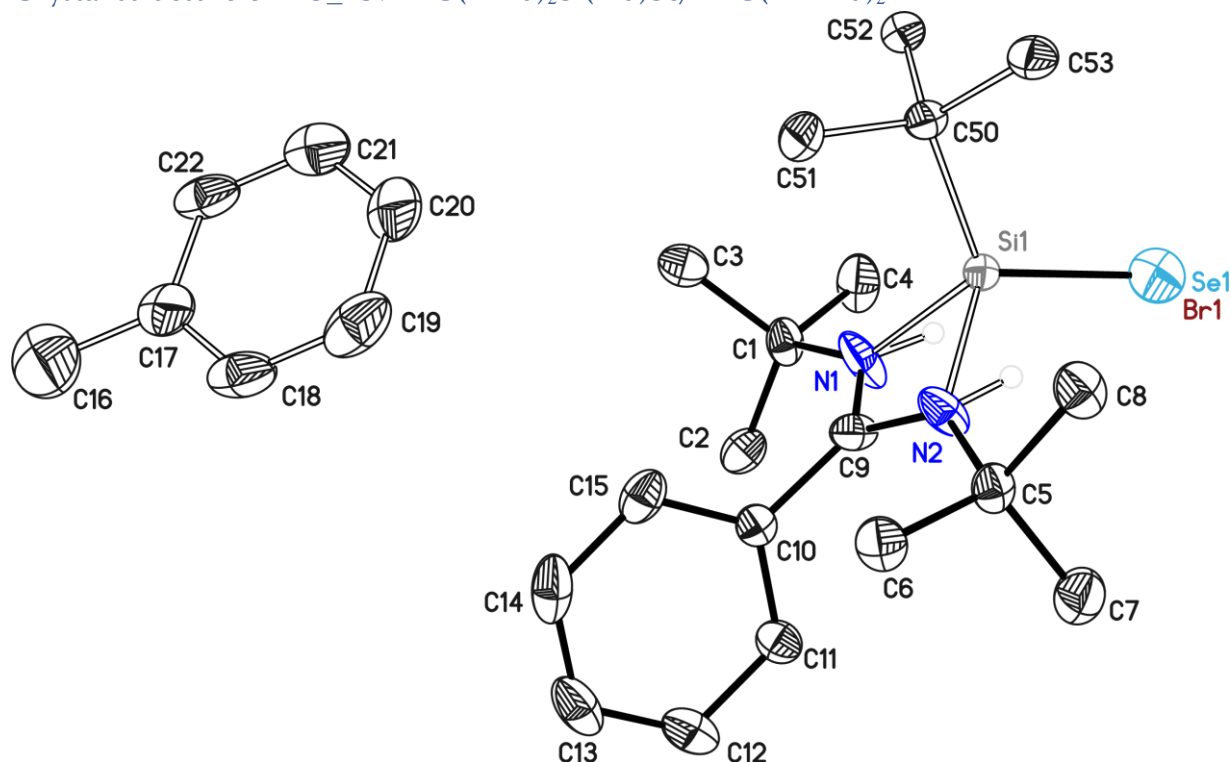


Figure 5.17: Crystal structure of NS_15. All hydrogen atoms but the ones on N1 and N2 are omitted for clarity. The asymmetric unit contains one toluene molecule and one disordered complex molecule (either the protonated amidinate or the silylene coordinated to either a selenium or a bromine atom).

Structure code	NS_16	CCDC Number	/
Empirical Formula	$\text{C}_{20.5}\text{H}_{32.5}\text{N}_2\text{Br}_{0.5}\text{Se}_{0.5}\text{Si}_{0.5}$	μ [mm^{-1}]	1.894
Formula weight [g mol^{-1}]	400.46	F(000)	1688
Sample temperature [K]	100(2)	θ range [$^\circ$]	1.585 to 26.410
Wavelength [\AA]	0.71073	Reflections collected	42766
Crystal System	Monoclinic	Unique Reflections	4330
Space group	C2/c	R_{int}	0.0356
	$a = 30.533(3)$	Completeness to θ_{max} [%]	100
Unit cell dimensions [\AA]	$b = 8.760(2)$ $\beta = 122.67(2)$	restraints/parameters	117 / 295
	$c = 18.766(2)$	GooF	1.052
Volume [\AA^3]	4225.2(14)	R1 (all data)	0.0268
Z	8	wR2 (all data)	0.0499
Crystal dimensions [mm]	0.350 x 0.236 x 0.122	max. diff. peak / hole [$\text{e}\text{\AA}^{-3}$]	0.272 and -0.289
Crystal shape and color	Colorless blocks		

Crystal structure of NS_16: $\text{PhC}(\text{N}^t\text{Bu})_2\text{Si}(\text{PTip})_2\text{K}(\text{Et}_2\text{O})_2$

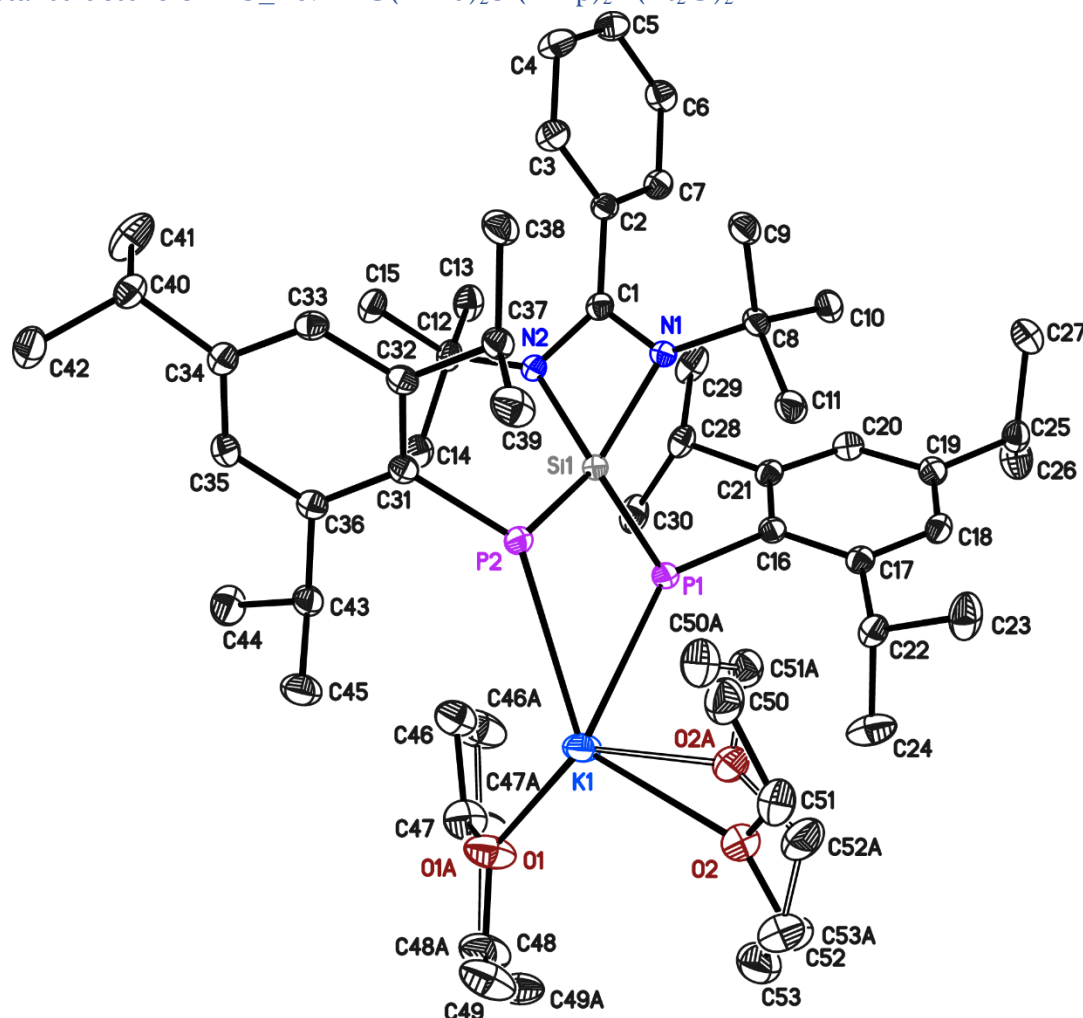


Figure 5.18: Crystal structure of NS_16. Hydrogens are omitted for clarity. Thermal ellipsoids are represented at the 50% probability level. The asymmetric unit contains one complex molecule. The ether substituents on the potassium were found to be disordered.

Structure code	NS_16	CCDC Number	/
Empirical Formula	$\text{C}_{53}\text{H}_{89}\text{KN}_2\text{O}_2\text{P}_2\text{Si}$	μ [mm^{-1}]	0.218
Formula weight [g mol^{-1}]	915.39	F(000)	1000
Sample temperature [K]	100(2)	θ range [$^\circ$]	1.755 to 28.424
Wavelength [\AA]	0.71073	Reflections collected	98547
Crystal System	Triclinic	Unique Reflections	13605
Space group	$P\bar{1}$	R_{int}	0.0682
Unit cell dimensions [\AA]	$a = 10.689(3)$ $\alpha = 74.09(2)$	Completeness to θ_{max} [%]	100
	$b = 12.842(3)$ $\beta = 87.80(2)$	restraints/parameters	420 / 668
	$c = 21.852(3)$ $\gamma = 69.97(2)$	GooF	1.000
Volume [\AA^3]	2705.1(11)	R1 (all data)	0.0346
Z	2	wR2 (all data)	0.0918
Crystal dimensions [mm]	0.465 x 0.251 x 0.198	max. diff. peak / hole [$\text{e}\text{\AA}^{-3}$]	0.378 and -0.248
Crystal shape and color	Colorless blocks		

Crystal structure of NS_17 : (PhC(N^tBu)₂Si)₂Li₂I(N^tBu)₂PhC

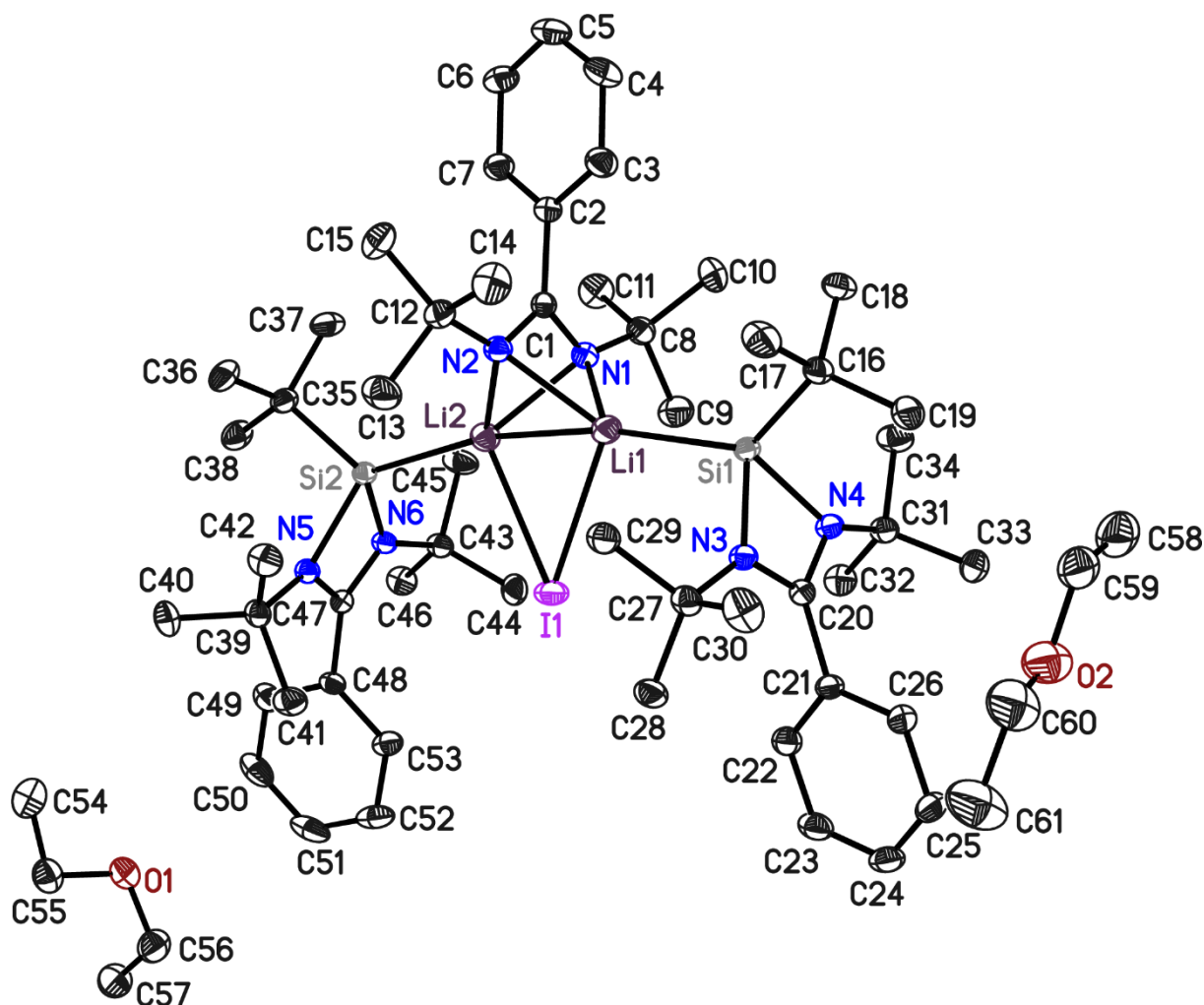


Figure 5.19: Crystal structure of NS_17. The asymmetric unit contains one complex molecule and two ether molecules.

Structure code	NS_17	CCDC Number	/
Empirical Formula	C ₆₁ H ₁₀₇ IN ₆ O ₂ Li ₂ Si ₂	μ [mm ⁻¹]	0.554
Formula weight [g mol ⁻¹]	1153.48	F(000)	2472
Sample temperature [K]	100(2)	θ range [°]	1.809 to 33.654
Wavelength [Å]	0.71073	Reflections collected	296106
Crystal System	Monoclinic	Unique Reflections	25265
Space group	P2 ₁ /n	R _{int}	0.0323
	<i>a</i> =22.1702(16)	Completeness to θ_{\max} [%]	99.9
Unit cell dimensions [Å]	<i>b</i> =13.8892(9) β =113.773(2)	restraints/parameters	0 / 695
	<i>c</i> =23.8253(15)	GooF	1.027
Volume [Å ³]	6713.9(8)	R1 (all data)	0.0619
Z	4	wR2 (all data)	0.0887
Crystal dimensions [mm]	0.410 x 0.342 x 0.274	max. diff. peak / hole [eÅ ⁻³]	1.146 and -0.686
Crystal shape and color	Yellow blocks		

Annex 2: Magnetometry service



In this section, I would like to thank several people:

- Dr. Serhiy Demeshko for his help and constant advice.
- Prof. Dr. h. c. mult. Dr. rer. nat. em. Herbert W. Roesky and his postdoctoral fellow Dr. M. Nazish for the opportunity they gave me to contribute to their research through magnetic characterization of some of their compounds.
- My fellow PhD candidates for always providing new complexes and challenging me to further improve my knowledge and skills in magnetochemistry.

Note: For some compounds, further details are available in the corresponding articles published in peer-reviewed journals, as indicated below.

Publications:

Publication **III** for **JJ_1-2**

Publication **V** for **NS_7**

Publication **XIII** for **DL_1**

Summary of the following magnetic data:

- **JK_K3** (Johannes Kretsch, AK Stalke)
- **NS_7** (Dr. Mohd Nasizh, AK Roesky)
- **JJ_1** (Jochen Jung, AK Stalke)
- **JJ_2** (Jochen Jung, AK Stalke)
- **DL_1** (Daniel Lüert, AK Stalke)

JK_K₃: K(B^{zh}H₂BoxCH)_n(THF)₂K@18-crown-6

Synthesis of JK_K₃ (obtained as a dark red crystalline powder), as described in previously published literature²³⁷.

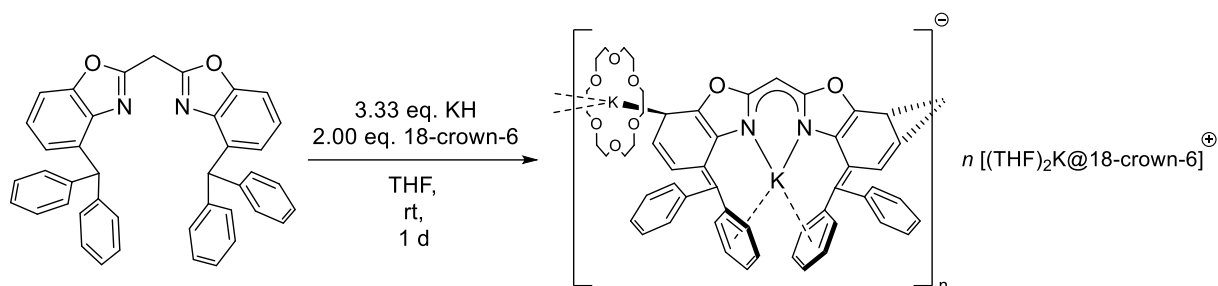


Figure 5.1: Synthesis route to JK_K₃

Magnetic characterization of JK_K₃:

Motivation: elucidation of the magnetic status of the complex (diamagnetic or mono-radical/bi-radical). The complex was found to be diamagnetic, as visible in the following picture.

Crystalline material was crushed and charged in gelatin caps and covered with Fomblin oil Y45 to avoid potential crystallite reorientation. The assembled sample was inserted in a plastic straw and brought to the SQUID instrument (MPMS XL equipped with a 5T magnet) in a Schlenk tube under argon. The temperature dependence of the product of the magnetic susceptibility and the temperature was measured from 300K to 2K under an external applied field $H=5000$ Oe. The obtained data was fitted with the program *JulX* (v. 1.16) written by E. Bill. The best fit was obtained with the following parameters: $g=2$ (fixed), $TIP = 303.8 \cdot 10^{-6}$ emu (variable) and 1.4% magnetic impurities ($S=1/2$; denoted PI on **Figure 5.2**).

The product $\chi_M T$ was found almost constant with the temperature and close to zero, clearly indicative of a diamagnetic species.

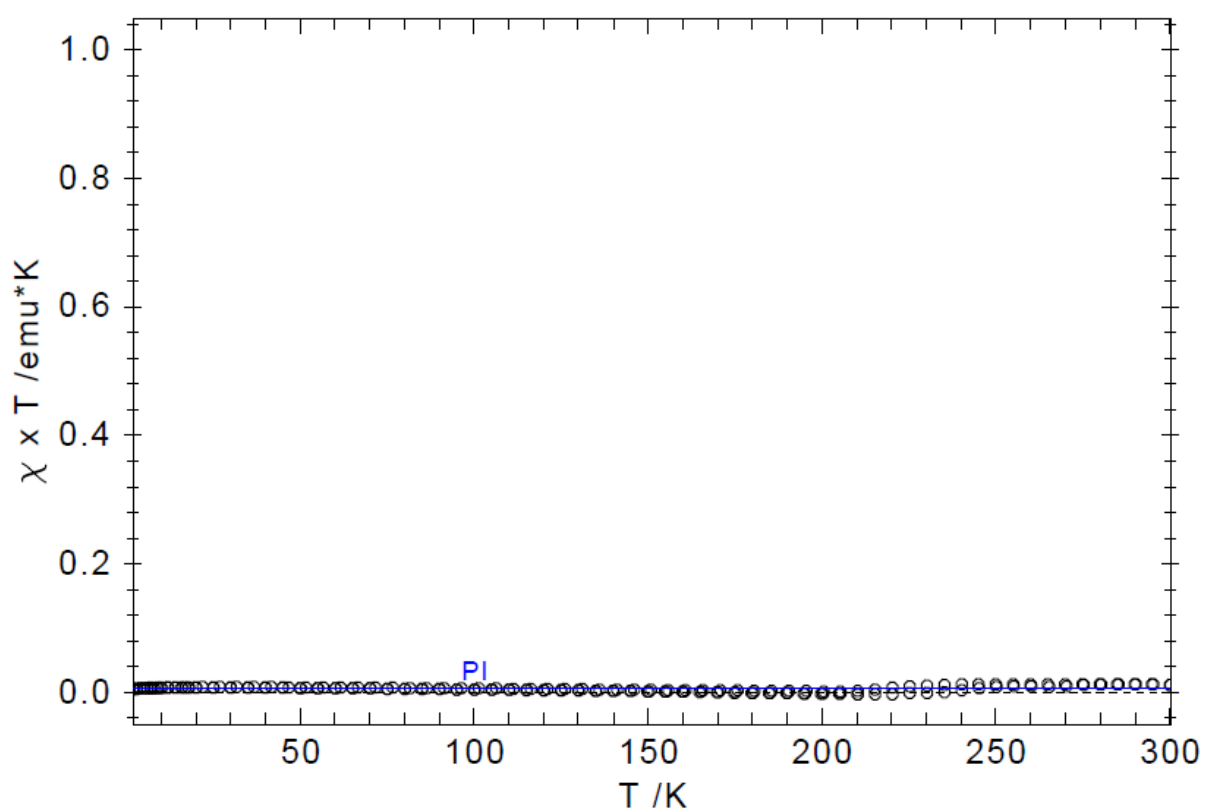


Figure 5.2: Temperature dependence of the product $\chi_M T$ from 300K to 2K under 5000 Oe dc field for **JK_K₃**. The small increase observed around 210-250K is due to the Fomblin oil transition from frozen to liquid.

NS_7: $\text{PhC}(\text{N}^t\text{Bu})_2\text{Si}^t(\text{Bu})^*-\text{B}(\text{Br})\text{Tip}$

Synthesis reported in Publication V.

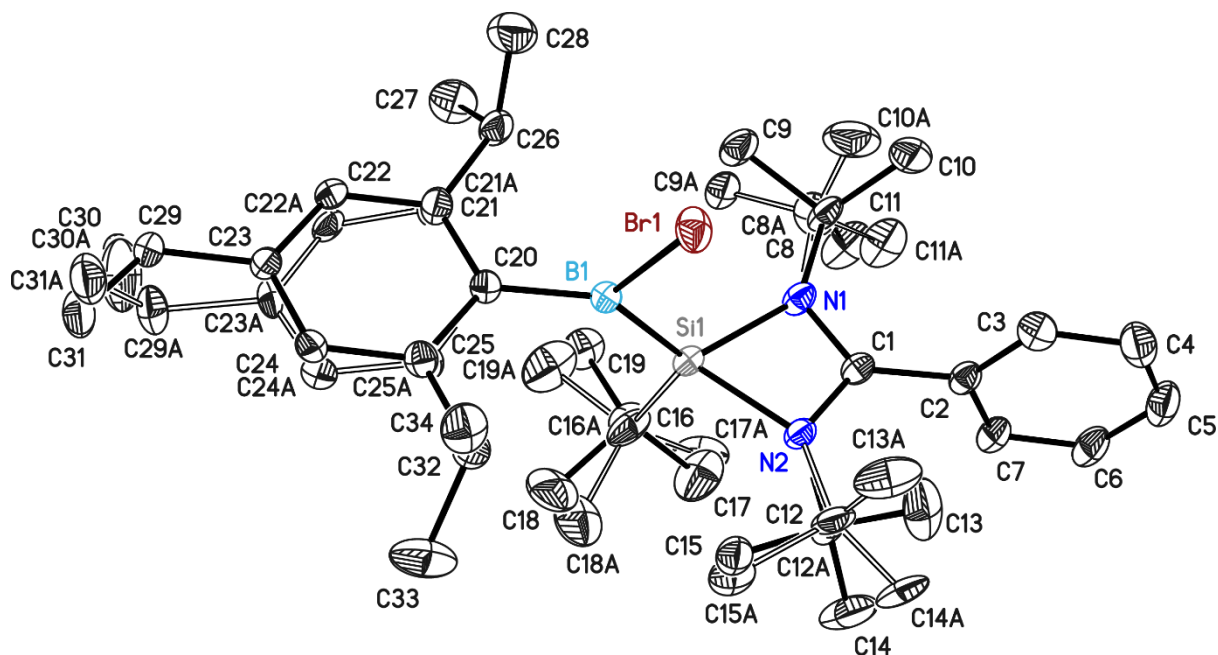


Figure 5.3: Crystal structure of NS_7. The boron atom is bounded to the silicon atom, to a bromide atom and to a negatively charged Tip ligand. (see annex1)

Magnetic characterization of NS_7:

Motivation:

- previous observation of the paramagnetic character of the molecule through EPR (by Dr. A. C. Stückl)
- further DFT calculations to determine the energy values of the SOMO orbitals.

Therefore, an additional check of the paramagnetic character of NS_7 was performed through a dc measurement on the SQUID magnetometer. The sample NS_7 was found paramagnetic.

Crystalline material was crushed and charged in gelatin caps. No oil was used since the expected spin was $\frac{1}{2}$. The assembled sample was inserted in a plastic straw and brought to the SQUID instrument (MPMS XL equipped with a 5T magnet) in a Schlenk tube under Argon. The temperature dependence of the product of the magnetic susceptibility and the temperature was measured from 200K to 2K under an external applied field $H=5000$ Oe. The obtained data was fitted with the program *JulX* (v. 1.16) written by E. Bill.²³² The best fit was obtained with the following parameters: $g=2$ (fixed), $\text{TIP} = 123.9 \cdot 10^{-6}$ emu (variable), Weiss Temperature $T_W = -0.528$ K and 23% diamagnetic impurities ($S=0$).

The product $\chi_M T$ showed a constant value of approx. 0.285 emuK until 40 K, thereafter, drastically dropping to 0.228 emuK. The value at low temperatures is not as close to zero as it should be, which can be explained by the 23% diamagnetic impurities found during fitting. Nevertheless, the curve shape is undoubtedly confirming the paramagnetic character of NS_7.

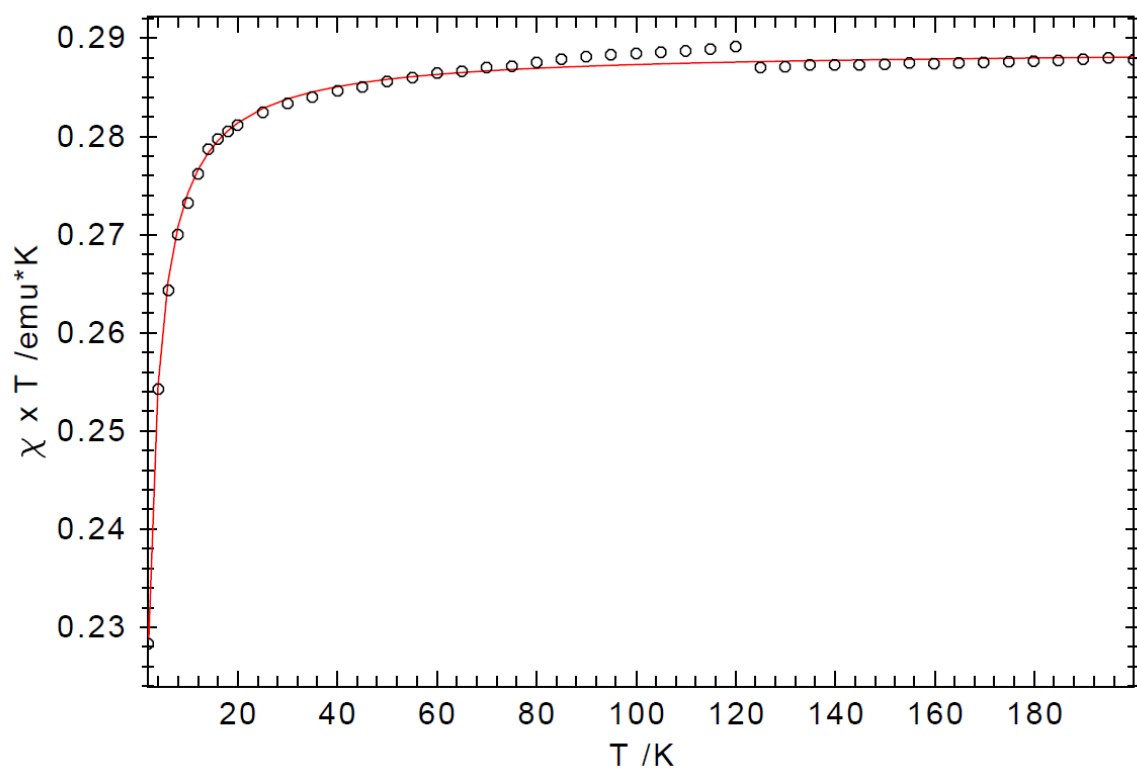


Figure 5.4: Temperature dependence of the product $\chi_M T$ from 200K to 2K under 5000 Oe dc field for NS_7.

JJ_1: $[\text{Cl}_2\text{Mn}(\text{N}^t\text{Bu})_2\text{S}^t\text{BuN})_2\text{Mn}\{\text{ClLi}(\text{THF})_3\}_2]$

Synthesis, structure and magnetism reported in **Publication III**.

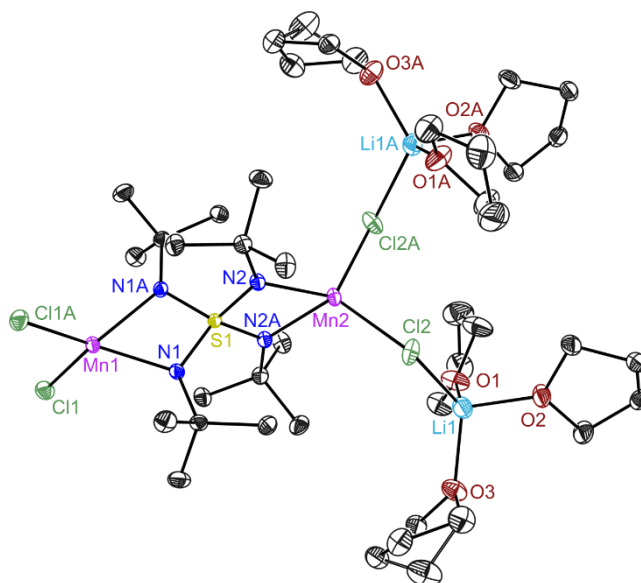


Figure 5.5 : Crystal structure of **JJ_1**: The ligand **L₄** is coordinating two asymmetric manganese paramagnetic centers. One is further coordinated by two chlorine atoms, while the second one possesses two single chlorine bridges each coordinating a lithium atom with three THF molecules.

Magnetic characterization:

The motivation for magnetic investigation is described in **Publication III**. The main goal is to determine the magnetic exchange coupling between the two manganese centers and access whether or not the different ligand environments can induce enough asymmetry for interesting magnetic properties.

Crystalline material was crushed and charged in gelatin caps with Fomblin Y45 oil. The assembled sample was inserted in a plastic straw and brought to the SQUID instrument (MPMS XL equipped with a 5T magnet) in a Schlenk tube under Argon. The temperature dependence of the product of the magnetic susceptibility and the temperature was measured from 200K to 2K under an external applied field $H=5000$ Oe. The obtained data was fitted with the program *Jul-2s* written by E. Bill.²³² The obtained fitting parameters are $g = 2.0$ (fixed); $D = 0$ cm^{-1} ; $J = -1.0$ cm^{-1} , $\text{TIP} = 1805 \times 10^{-6}$ $\text{cm}^3\text{mol}^{-1}$ and $\text{PI} = 13.6\%$ (the high impurity percentage is due to solvent loss and was proofed by elemental analysis, as described in the **publication III**).

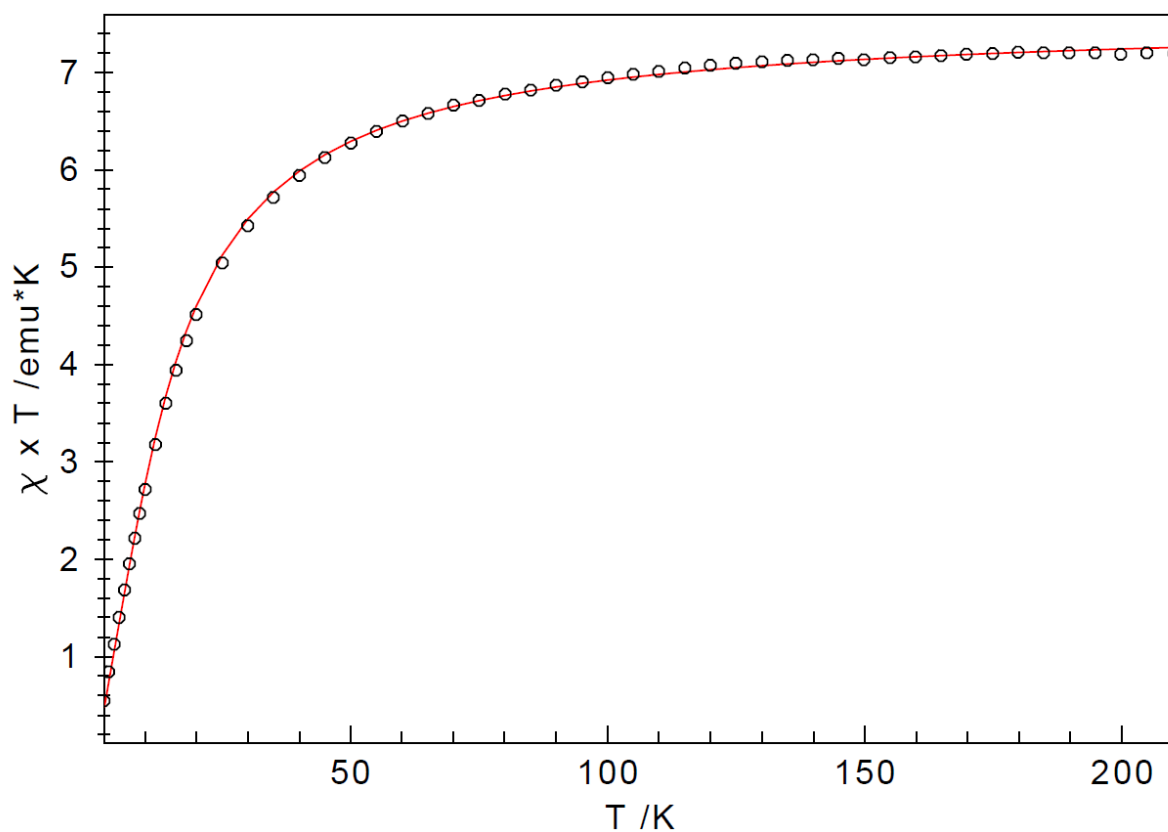


Figure 5.6: Temperature dependence of the product $\chi_M T$ from 200K to 2K under 5000 Oe dc field for **JJ_1**.

An antiferromagnetic coupling of $J = -1.0 \text{ cm}^{-1}$ was found between the two manganese centers.

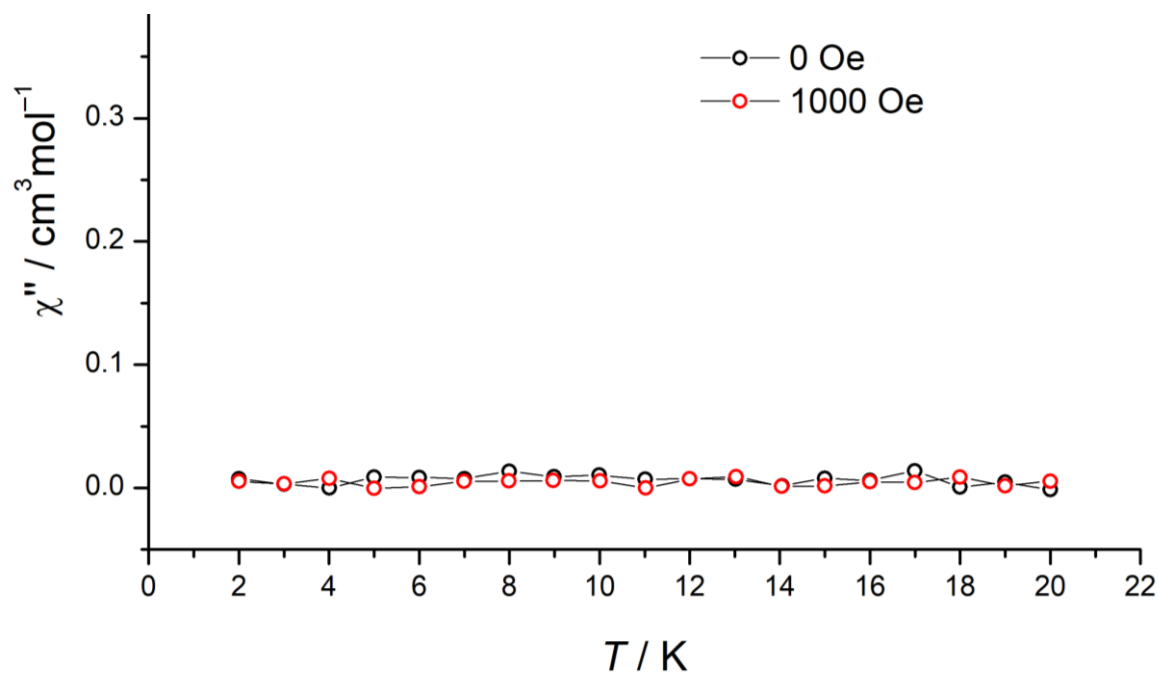


Figure 5.7: Temperature dependency of the out-of-phase signal of the ac susceptibility in **JJ_1**

SMM behavior was not detected in **JJ_1**, even under applied field.

JJ_2: [(acac)Co(NⁱBu)₂S(^tBuN)₂Co(acac)]

Synthesis, structure and magnetism reported in **Publication III**.

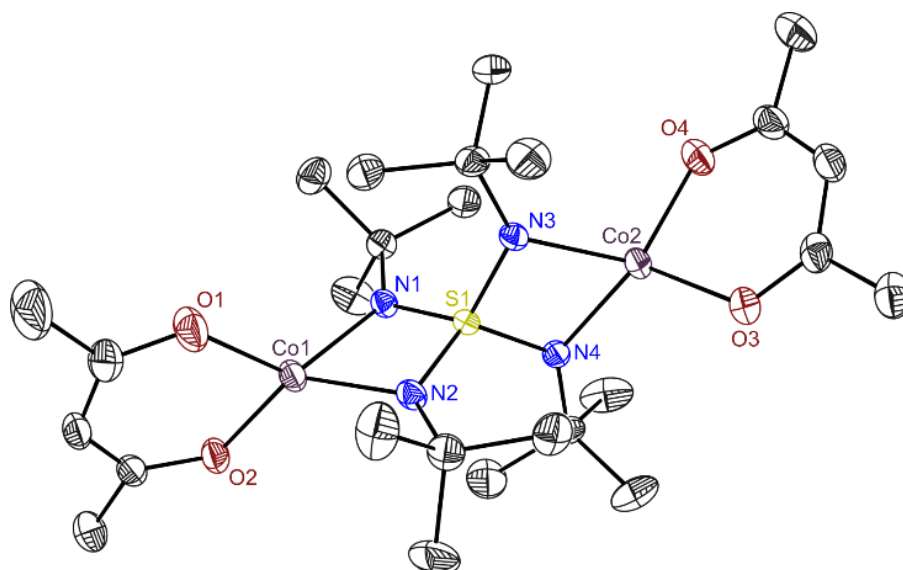


Figure 5.8: Crystal structure of **JJ_2**: The ligand **L₄** is coordinating two cobalt paramagnetic centers. These are further coordinated by a standard ‘acac’ ligand (from the starting material).

Magnetic characterization:

Motivation: Magnetic investigation was motivated by the same reasons than for **JJ_1**.

Crystalline material was crushed and charged in gelatin caps with Fomblin Y45 oil. The assembled sample was inserted in a plastic straw and brought to the SQUID instrument (MPMS XL equipped with a 5T magnet) in a Schlenk tube under Argon. The temperature dependence of the product of the magnetic susceptibility and the temperature was measured from 200K to 2K under an external applied field $H=5000$ Oe. The initial temperature-dependent susceptibility measurement for **JJ_2** showed a high temperature $\chi_M T$ value of $5.1 \text{ cm}^3 \text{ mol}^{-1} \text{ K}$. This value is larger than the spin-only value expected for two independent cobalt ions with $S = 3/2$ ($3.75 \text{ cm}^3 \text{ mol}^{-1} \text{ K}$), but consistent with a sizable contribution of unquenched orbital angular momentum, common for Co(II). $\chi_M T$ decreases upon cooling, reaching $0.31 \text{ cm}^3 \text{ mol}^{-1} \text{ K}$ at 5 K. This behavior strongly suggests that the spins of the Co(II) couple antiferromagnetically. Experimental $\chi_M T$ versus T data in the whole temperature range was modelled by using the simulation package julX for exchange coupled systems. The best fit to the data gives $J = -6.1 \text{ cm}^{-1}$ (based on the spin Hamiltonian $\hat{H} = -2JS_1S_2$) with $g = 2.59$, $D = -56.9 \text{ cm}^{-1}$ and $\text{TIP} = 244 \times 10^{-6} \text{ emu mol}^{-1}$.

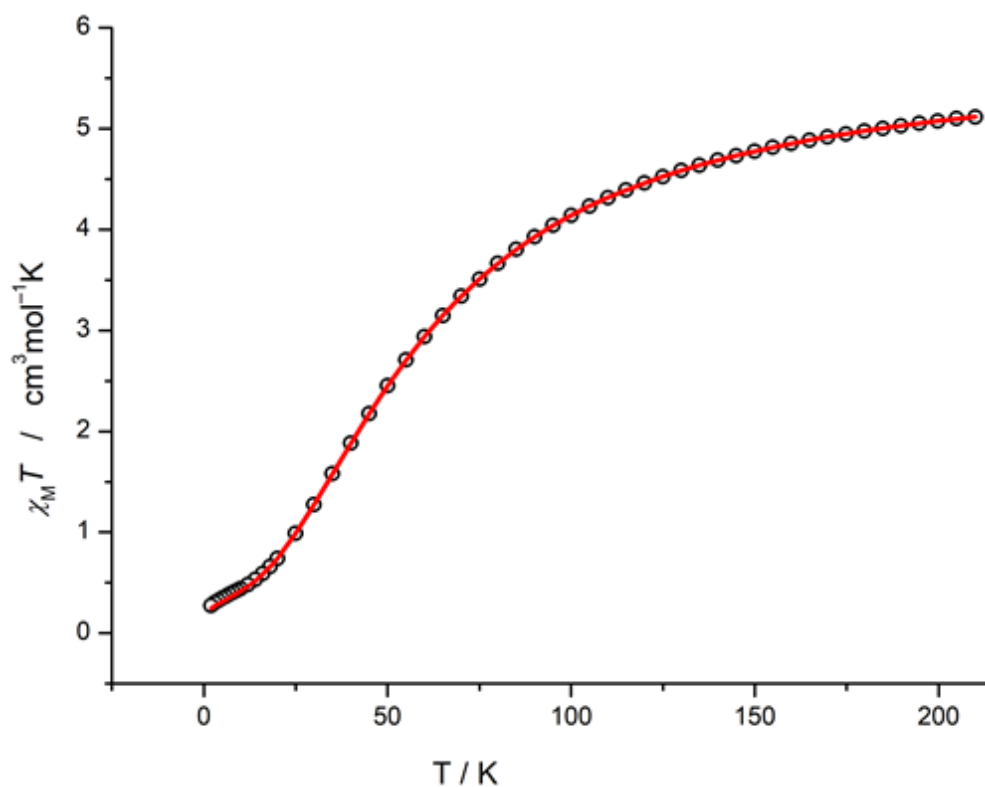


Figure 5.9: Temperature dependency of the product $\chi_M T$ from 200K to 2K under 5000 Oe dc field for JJ_2.

JJ_2 possesses an appreciable antiferromagnetic exchange coupling between the two cobalt centres of $J = -6.1 \text{ cm}^{-1}$. Like in JJ_1, no SMM behaviour was shown.

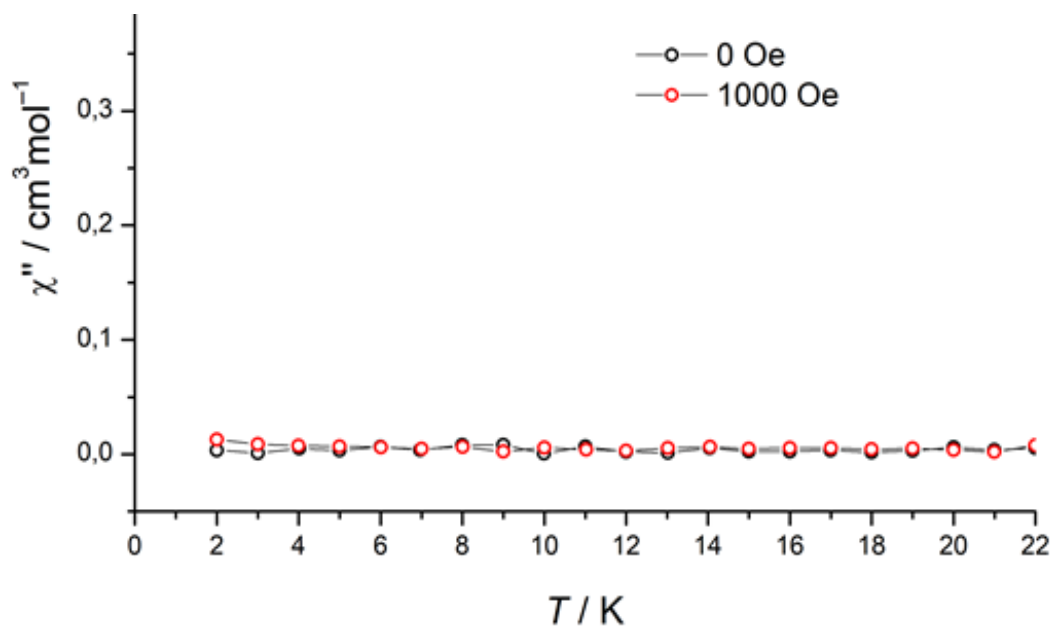


Figure 5.10: Temperature dependency of the out-of-phase signal of the ac susceptibility in JJ_2

DL_1: $\{(\text{MeBox})_2\text{Gd}(\mu^2\text{-Cl}_2)\text{Gd}(\text{Mebox})_2\}$

The synthesis of the compound is reported in D. Lüert's PhD thesis.²³⁶

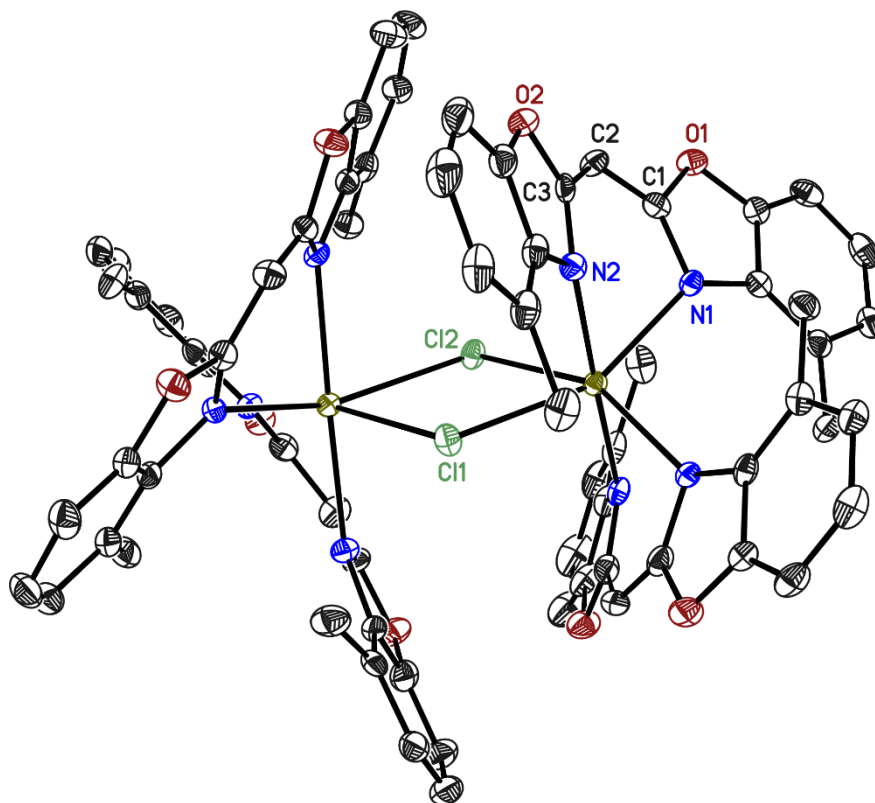


Figure 5.11. Crystal structure of $\{(\text{MeBox})_2\text{M}(\mu^2\text{-Cl}_2)\text{M}(\text{Mebox})_2\}$ ($\text{M} = \text{Gd}, \text{Dy}$). The metal ion is represented in yellow brown. Hydrogens are omitted for clarity. Thermal ellipsoids are shown to the 50% probability level.

Motivation: Several lanthanide complexes containing box ligand derivatives were magnetically investigated and the dysprosium and terbium analogs showed promising results. Amongst them, binuclear complexes were obtained. In order to quantify the magnetic exchange coupling strength, the gadolinium analogs were synthesized, and a dc measurement was performed to extract the coupling strength. Fitting was performed with the program PHI developed by N. F. Chilton, with the help of S. Demeshko.

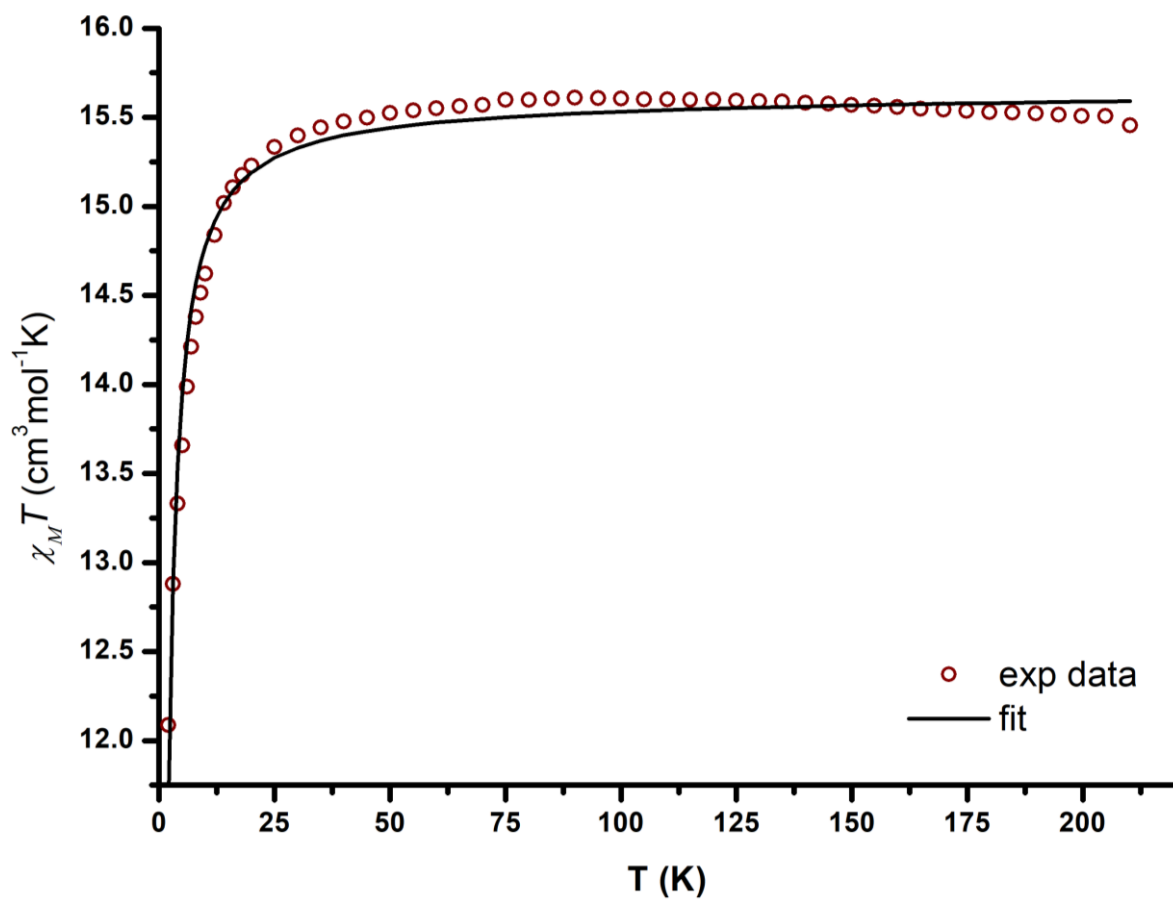


Figure 5.12. Temperature dependency of the product $\chi_M T$ from 200K to 2K under 1000 Oe dc field for DL_1. The black line represents fit to the data.

The coupling between the two Gd ions is found to be -0.035 cm^{-1}

Bibliography

- (1) Sharma, B. D.; Donohue, J. The crystal and molecular structure of sulfur nitride, S₄N₄. *Acta Crystallogr. Sec. A* **1963**, *16* (9), 891–897. DOI: 10.1107/s0365110x63002401.
- (2) Goehring, M. Über den Schwefelstickstoff N₄S₄. *Chem. Ber.* **1947**, *80* (2), 110–122. DOI: 10.1002/cber.19470800204.
- (3) Goehring, M. Sulphur nitride and its derivatives. *Q. Rev. Chem. Soc.* **1956**, *10* (4), 437–450.
- (4) Goehring, M.; Ebert, J. Ein chemischer Beweis für Mesomerie bei Tetraschwefeltetranitrid. *Z. Naturforsch. B* **1955**, *10* (5). DOI: 10.1515/znb-1955-0501.
- (5) Greene, R. L.; Street, G. B.; Suter, L. J. Superconductivity in Polysulfur Nitride (SN)_x. *Phys. Rev. Lett.* **1975**, *34* (10), 577–579. DOI: 10.1103/PhysRevLett.34.577.
- (6) Street, G. B.; Greene, R. L. Preparation and Properties of (SN)_x. *IBM J. Res. & Dev.* **1977**, *21* (2), 99–110. DOI: 10.1147/rd.212.0099.
- (7) Becke-Goehring, V. M. Über Schwefel-Stickstoff-Verbindungen. In *Progress in Inorganic Chemistry*; John Wiley & Sons, Inc., **2007**; pp 207–234. DOI: 10.1002/9780470166024.ch3.
- (8) Goehring, M.; Weis, G. Über ein Di-imid der schwefligen Säure. *Angew. Chem.* **1956**, *68* (21), 678. DOI: 10.1002/ange.19560682106.
- (9) Clemens, D. H.; Bell, A. J.; O'Brien, J. L. Synthesis of stable aliphatic sulfur diimines. *Tetrahedron Lett* **1965**, *6* (20), 1487–1489. DOI: 10.1016/S0040-4039(00)90094-7.
- (10) Glemser, O.; Wegener, J. Tris(N-trimethylsilylimido)sulfur and Bis(N-trimethylsilylimido)sulfur Difluoride. *Angew. Chem. Int. Ed.* **1970**, *9* (4), 309. DOI: 10.1002/anie.197003091.
- (11) Lidy, W.; Sundermeyer, W.; Verbeek, W. Reaktionen des Bis-trimethylsilyl-schwefeldiimids zur Darstellung neuer Schwefel-Stickstoff-Verbindungen. *Z Anorg Allg Chem* **1974**, *406* (2-3), 228–234. DOI: 10.1002/zaac.19744060215.
- (12) Mews, R.; Glemser, O. Reactions of sulfur difluoride imides and sulfur dichloride imides. *Inorg. Chem.* **1972**, *11* (10), 2521–2525. DOI: 10.1021/ic50116a046.
- (13) Glemser, O.; Mews, R. Chemistry of Thiazyl Fluoride(NSF) and Thiazyl Trifluoride(NSF₃): A Quarter Century of Sulfur-Nitrogen-Fluorine Chemistry. *Angew. Chem. Int. Ed.* **1980**, *19* (11), 883–899. DOI: 10.1002/anie.198008831.
- (14) Fleischer, R.; Freitag, S.; Pauer, F.; Stalke, D. [S(N^tBu)₃]²⁻ – A Cap-Shaped Dianion, Isoelectronic with the Sulfite Ion and Oxidizable to a Stable Radical Anion. *Angew. Chem. Int. Ed.*, **1996**, *35*, 204–206. DOI: 10.1002/anie.199602041.
- (15) Fleischer, R.; Rothenberger, A.; Stalke, D. S(N^tBu)₄²⁻ a dianion isoelectronic to SO₄²⁻ and the related MeS(N^tBu)₃⁻, *Angew. Chem. Int. Ed.*, **1997**, *36*, 1105–1107. DOI:10.1002/anie.199711051.
- (16) Fleischer, R.; Stalke, D. A new route to sulfur polyimido anions S(NR)_n^{m-}: reactivity and coordination behavior. *Coord. Chem. Rev.* **1998**, *176*, 431–450. DOI: 10.1016/s0010-8545(98)00130-1.
- (17) Fleischer, R.; Freitag, S.; Stalke, D. Oxidation of [Li₄{(NBu^t)₃S}₂]: a new route to sulfur triimides. *J. Chem. Soc., Dalton Trans.* **1998**, 193–197. DOI: 10.1039/a707085c.
- (18) Leusser, D.; Henn, J.; Kocher, N.; Engels, B.; Stalke, D. S=N versus S⁺-N⁻: An Experimental and Theoretical Charge Density Study. *J. Am. Chem. Soc.* **2004**, *126* (6), 1781–1793. DOI: 10.1021/ja038941.

- (19) Deuerlein, S.; Leusser, D.; Flierler, U.; Ott, H.; Stalke, D. [(thf)Li₂{H₂CS(N^tBu)₂}]₂: Synthesis, Polymorphism, and Experimental Charge Density to Elucidate the Bonding Properties of a Lithium Sulfur Ylide. *Organometallics* **2008**, *27* (10), 2306–2315. DOI: 10.1021/om800046n.
- (20) Leusser, D.; Walfort, B.; Stalke, D. Charge-Density Study of Methane Di(triimido)sulfonic Acid H₂C{S(N^tBu)₂(NH^tBu)}₂—the NR Analogue of H₂C{S(O)₂(OH)}₂. *Angew. Chem. Int. Ed.* **2002**, *41* (12), 2079. DOI:10.1002/1521-3773(20020617)41:12<2079:aid-anie2079>3.0.CO;2-l.
- (21) Jung, J.; Münch, A.; Herbst-Irmer, R.; Stalke, D. Tetraimido Sulfuric Acid H₂S(N^tBu)₄ - Valence Isoelectronic to H₂SO₄. *Angew. Chem. Int. Ed.* **2021**, *60* (11), 5679–5682 DOI: 10.1002/anie.202014426.
- (22) Leusser, D.; Henn, J.; Kocher, N.; Engels, B.; Stalke, D. S=N versus S⁺-N⁻: An Experimental and Theoretical Charge Density Study. *J. Am. Chem. Soc.* **2004**, *126* (6), 1781–1793. DOI : 10.1021/ja038941%2B
- (23) Stalke, D. Polyimido sulphur anions S(NR)^{mm-}: Free radicals and coordination behaviour. *Proc. Indian Acad. Sci. (Chem. Sci.)* **2000**, *112* (3), 155–170.
- (24) Stalke, D. Polyimido sulfur anions and ylides. *Chem. Commun.* **2012**, *48* (77), 9559–9573. DOI: 10.1039/c2cc33221c.
- (25) Selinka, C.; Stalke, D. Novel Asymmetrical Dianionic Polyimido-Sulfur(IV)-Ylides. *Z. Naturforsch. B* **2003**, *58b*, 291–298. DOI:10.1515/znb-2003-0407
- (26) Selinka, C.; Stalke, D. Heteroaromatic-Substituted Mono- and Bis(triimidosulfonates). *Eur. J. Inorg. Chem.* **2003** (18), 3376–3382. DOI:10.1002/ejic.200300194
- (27) Selinka, C.; Deuerlein, S.; Häuser, T.; Stalke, D. Heteroaromatic substituted diimidosulfinates. *Inorg. Chim. Acta* **2004**, *357* (6), 1873–1880. DOI:10.1016/j.ica.2003.12.002
- (28) Walfort, B.; Bertermann, R.; Stalke, D. A new class of dianionic sulfur-ylides: alkylenediazasulfites. *Chem. Eur. J.* **2001**, *7* (7), 1424–1430. DOI: 10.1002/1521-3765%2820010401%297%3A7<1424%3A%3AAID-CHEM1424>3.0.CO%3B2-5
- (29) Walfort, B.; Leedham, A. P.; Russell, C. R.; Stalke, D. Triimidosulfonic acid and organometallic triimidosulfonates: S⁺-N⁻ versus S=N bonding. *Inorg. Chem.* **2001**, *40* (22), 5668–5674. DOI:10.1021/ic0105009
- (30) Walfort, B.; Pandey, S. K.; Stalke, D. The inverse podant [Li₃(NBu^t)₃S]]⁺ stabilises a single ethylene oxide OCHNCH₂ anion as a high- and low-temperature polymorph of [(thf)₃Li₃(OCHNCH₂){(NBu^t)₃S}]. *Chem. Commun.* **2001**, 1640–1641. DOI: 10.1039/b105429p.
- (31) Meyer, J. T. E.; Schulz, T.; Pandey, S. K.; Stalke, D. New Chelating Ligands Based on S-Organosulfur diimides. *Inorg. Chem.* **2010**, *49* (6), 2743–2749. DOI: 10.1021/ic902071m.
- (32) Meinholz, M. M.; Stalke, D. Enhancing N, P, S-Janus Head Tripod Ligands by Oxidation. *Z. Anorg. Allg. Chem.* **2011**, *637* (14-15), 2233–2238. DOI: 10.1002/zaac.201100285.
- (33) Meinholz, M. M.; Pandey, S. K.; Deuerlein, S. M.; Stalke, D. Access to new Janus head ligands: linking sulfur diimides and phosphanes for hemilabile tripodal scorpionates. *Dalton Trans.* **2011**, *40* (8), 1662–1671. DOI: 10.1039/C0DT00665C
- (34) Roesky, H. W.; Grünhagen, A.; Edelmann, F. T.; Noltemeyer, M. N,N'-Di(t-butyl)-S-ferrocenylsulfonic Acid Imidoamide - a New Ligand for the Synthesis of Metal Complexes. *Z. Naturforsch. B* **1989**, *44* (11), 1365–1368. DOI: 10.1515/znb-1989-1107.

- (35) Schulz, T.; Deuerlein, S.; Stalke, D. Magnesium Diimidosulfinates-Conformational Studies in the Solid State and in Solution. *Eur. J. Inorg. Chem.* **2010**, 2178–2184. DOI: 10.1002/ejic.201000045.
- (36) Schulz, T.; Stalke, D. Magnesium Triimidosulfonates from Grignard Reagents. *Eur. J. Inorg. Chem.* **2010**, 2185–2192. DOI: 10.1002/ejic.201000046.
- (37) Schulz, T.; Stalke, D. Lithium and Aluminum Anthracenyldiimidosulfinates. *Z. Naturforsch. B* **2010**, 701–710. DOI:10.1515/znb-2010-0606
- (38) Walfort, B.; Lameyer, L.; Weiss, W.; Herbst-Irmer, R.; Bertermann, R.; Rocha, J.; Stalke, D. $[(\text{MeLi})_4(\text{dem})_{1.5}]_1$ and $[(\text{thf})_3\text{Li}_3\text{Me}\{(\text{N}^i\text{Bu})_3\text{S}\}]$: How to Reduce Aggregation of Parent Methyllithium. *Chem. Eur. J.* **2001**, 7 (7), 1417. DOI: 10.1002/1521-3765(20010401)7:7<1417::AID-CHEM1417>3.0.CO
- (39) Meinholz, M. M.; Stalke, D. Monoanionic N,P,S-Janus Head Tripods in s-Block Metal Coordination. *Eur. J. Inorg. Chem.* **2011**, 2011 (29), 4578–4584. DOI: 10.1002/ejic.201100658.
- (40) Fleischer, R.; Stalke, D. Syntheses and Structures of Main Group Metal Complexes of the $\text{S}(\text{N}^i\text{Bu})_3^{2-}$ Dianion, an Inorganic Y-Conjugated Tripod. *Organomet.* **1998**, 17, 832–838. DOI: 10.1021/om970909z.
- (41) Walfort, B.; Auth, T.; Degel, B.; Helten, H.; Stalke, D. Copper and Silver Triimidosulfites: $\text{S}(\text{N}^i\text{Bu})_3^{2-}$ -Bicapped M_3 -Triangles Connected via Lithium Halide Ladders or Fragments Thereof. *Organomet.* **2002**, 21 (11), 2208–2214. DOI: 10.1021/om020032q.
- (42) Carl, E.; Demeshko, S.; Meyer, F.; Stalke, D. Triimidosulfonates as Acute Bite-Angle Chelates: Slow Relaxation of the Magnetization in Zero Field and Hysteresis Loop of a Co(II) Complex. *Chem. Eur. J.* **2015**, 21 (28), 10109–10115. DOI: 10.1002/chem.201406083.
- (43) Bayram, M.; Bläser, D.; Wölper, C.; Schulz, S. Synthesis and X-ray Crystal Structure of Diimidosulfinate Transition Metal Complexes. *Organomet.* **2015**, 34 (13), 3421–3427. DOI: 10.1021/acs.organomet.5b00407.
- (44) Fleischer, R.; Walfort, B.; Gbureck, A.; Scholz, P.; Kiefer, W.; Stalke, D. Raman Spectroscopic Investigation and Coordination Behavior of the Polyimido SVI Anions $[\text{RS}(\text{NR})_3]^-$ and $[\text{S}(\text{NR})_4]^{2-}$. *Chem. Eur. J.* **1998**, 4 (11), 2266–2274. DOI: 10.1002/(sici)1521-3765(19981102)4:11<2266::aid-chem2266>3.0.co;2-4.
- (45) Gao, Q.; Xiu, Y.; Li, G.-D.; Chen, J.-S. Sensor material based on occluded trisulfur anionic radicals for convenient detection of trace amounts of water molecules. *J Mater Chem* **2010**, 20 (16), 3307. DOI: 10.1039/b925233a.
- (46) Jung, J.; Legendre, C. M.; Herbst-Irmer, R.; Stalke, D. Exchange Coupling in Binuclear Manganese and Cobalt Complexes with the Tetraimido Sulfate Anion $[\text{S}(\text{N}^i\text{Bu})_4]^{2-}$. *Inorg. Chem.* **2021**, 60 (2), 967–972. DOI: 10.1021/acs.inorgchem.0c03085.
- (47) Gaita-Ariño, A.; Luis, F.; Hill, S.; Coronado, E. Molecular spins for quantum computation. *Nat Chem* **2019**, 11 (4), 301–309. DOI: 10.1038/s41557-019-0232-y.
- (48) Marin, R.; Brunet, G.; Murugesu, M. Shining New Light on Multifunctional Lanthanide Single-Molecule Magnets. *Angew. Chem. Int. Ed.* **2021**, 60 (4), 1728–1746. DOI:10.1002/anie.201910299.
- (49) Ungur, L.; Chibotaru, L. F. Strategies toward High-Temperature Lanthanide-Based Single-Molecule Magnets. *Inorg. Chem.* **2016**, 55 (20), 10043–10056. DOI:10.1021/acs.inorgchem.6b01353.

- (50) Winpenny, R., Ed. *Single-Molecule Magnets and Related Phenomena*; Springer Berlin Heidelberg, 2006.
- (51) Coronado, E. Molecular magnetism: from chemical design to spin control in molecules, materials and devices. *Nat Rev Mater* **2020**, 5 (2), 87–104. DOI: 10.1038/s41578-019-0146-8.
- (52) Bogani, L.; Wernsdorfer, W. Molecular spintronics using single-molecule magnets. *Nat. Mater.* **2008**, 7 (3), 179. DOI: 10.1038/nmat2133
- (53) Christou, G.; Gatteschi, D.; Hendrickson, D. N.; Sessoli, R. Single-molecule-magnets. *MRS Bulletin* **2000**, 25 (11), 66–71. DOI: 10.1557/mrs2000.226
- (54) Mannini, M.; Bonacchi, D.; Zobbi, L.; Piras, F. M.; Speets, E. A.; Caneschi, A.; Cornia, A.; Magnani, A.; Ravoo, B. J.; Reinhoudt, D. N.; Sessoli, R.; Gatteschi, D. Advances in single-molecule magnet surface patterning through microcontact printing. *Nano Letters* **2005**, 5 (7), 1435–1438. DOI: 10.1021/nl0508016.
- (55) Fleischer, R.; Stalke, D. A new route to sulfur polyimido anions $S(NR)^{nm-}$: Reactivity and coordination behavior. *Coord. Chem. Rev.* **1998**, 176 (1), 431–450. DOI: 10.1016/S0010-8545(98)00130-1.
- (56) Meinholz, M. M.; Pandey, S. K.; Deuerlein, S. M.; Stalke, D. Access to new Janus head ligands: linking sulfur diimides and phosphanes for hemilabile tripodal scorpionates. *Dalton Trans.* **2011**, 40 (8), 1662–1671. DOI: 10.1039/c0dt00665c.
- (57) Carl, E.; Stalke, D. Polyimido Sulfur(VI) Phosphanyl Ligand in Metal Complexation. *Chem. Eur. J.* **2014**, 20 (48), 15849–15854. DOI: 10.1002/chem.201404860.
- (58) Thomas Schulz; David-Raphael Dauer; Dietmar Stalke. π -Spacer-coupled Diimidosulfonates. *Z. Naturforsch. B* **607** (6), 711–718. DOI: 10.1515/znb-2010-0607
- (59) Cremllyn, R. J. W. *An introduction to organosulfur chemistry*; Wiley, 1996.
- (60) Fleischer, R.; Freitag, S.; Pauer, F.; Stalke, D. $[S(N^iBu)_3]^{2-}$ —A Cap-Shaped Dianion, Isoelectronic with the Sulfite Ion and Oxidizable to a Stable Radical Anion. *Angew. Chem. Int. Ed.* **1996**, 35 (2), 204–206. DOI: 10.1002/anie.199602041.
- (61) Steiner, T. Lengthening of the N–H bond in N–H \cdots N hydrogen bonds. Preliminary structural data and implications of the bond valence concept. *J. Chem. Soc., Chem. Commun.* **1995** (13), 1331–1332. DOI: 10.1039/C39950001331.
- (62) Martinez, C. R.; Iverson, B. L. Rethinking the term “pi-stacking”. *Chem. Sci.* **2012**, 3 (7), 2191. DOI: 10.1039/c2sc20045g.
- (63) La Rie, E. R. de; Michelin, A.; Ngako, M.; Del Federico, E.; Del Grosso, C. Photo-catalytic degradation of binding media of ultramarine blue containing paint layers: A new perspective on the phenomenon of “ultramarine disease” in paintings. *Polym. Degrad. Stab.* **2017**, 144, 43–52. DOI: 10.1016/j.polymdegradstab.2017.08.002.
- (64) Chivers, T.; Elder, P. J. W. Ubiquitous trisulfur radical anion: fundamentals and applications in materials science, electrochemistry, analytical chemistry and geochemistry. *Chem. Soc. Rev.* **2013**, 42 (14), 5996–6005. DOI: 10.1039/c3cs60119f.
- (65) Meyer, B. Elemental sulfur. *Chem. Rev* **1976**, 76 (3), 367–388. DOI:10.1021/cr60301a003.
- (66) Armstrong, A.; Chivers, T.; Parvez, M.; Boéré, R. T. Stable Cubic Phosphorus-Containing Radicals. *Angew. Chem. Int. Ed.* **2004**, 43 (4), 502–505. DOI: 10.1002/anie.200353108.
- (67) Brask, J. K.; Chivers, T.; McGarvey, B.; Schatte, G.; Sung, R.; Boéré, R. T. ESR Investigations of the Radicals $\{Li_3E((N^iBu)_3)_2\}^*$ (E = S, Se) and the Radical Anions $SO_x\{(N^iBu)_3\}_x^*$ (x = 1, 2). *Inorg. Chem.* **1998**, 37 (18), 4633–4636. DOI: 10.1021/ic9803560.

- (68) Chivers, T.; Parvez, M.; Schatte, G. Preparation and Structure of $\text{Li}_2\{\text{Se}(\text{N}^t\text{Bu})_3\}_2$, Containing the Novel $\text{Se}(\text{N}^t\text{Bu})_3\}^{2-}$ Anion. *Inorg. Chem.* **1996**, *35* (14), 4094–4095. DOI: 10.1021/ic960307s.
- (69) Konu, J.; Chivers, T. Stable Radicals of the Heavy p-Block Elements. In *Stable radicals: Fundamentals and applied aspects of odd-electron compounds*; Hicks, R. G., Ed.; Wiley-Blackwell, 2010; pp 381–406. DOI: 10.1002/9780470666975.ch10.
- (70) Chivers, T.; Gao, X.; Parvez, M. A $\text{Te}_2\text{N}_6\text{Li}_4$ Cage Containing the Tris(tert-butylimido)tellurite Dianion. *Angew. Chem. Int. Ed.* **1995**, *34* (22), 2549–2551. DOI: 10.1002/anie.199525491.
- (71) Lis, T. Preparation, structure, and magnetic properties of a dodecanuclear mixed-valence manganese carboxylate. *Acta Crystallogr. Sec. B* **1980**, *36* (9), 2042–2046. DOI: 10.1107/S0567740880007893.
- (72) Kahn, O. *Molecular magnetism*; Wiley-VCH, 1993.
- (73) Clemente-León, M.; Coronado, E.; Gómez-García, C. J.; López-Jordà, M.; Camón, A.; Repollés, A.; Luis, F. Insertion of a single-molecule magnet inside a ferromagnetic lattice based on a 3D bimetallic oxalate network: towards molecular analogues of permanent magnets. *Chem. - Eur. J.* **2014**, *20* (6), 1669–1676. DOI: 10.1002/chem.201303044.
- (74) Croat, J. J.; Herbst, J. F.; Lee, R. W.; Pinkerton, F. E. Pr-Fe and Nd-Fe-based materials: A new class of high-performance permanent magnets. *J. Appl. Phys.* **1984**, *55* (6), 2078–2082. DOI: 10.1063/1.333571.
- (75) Lee, S. Magnetic quantum dots and magnetic edge states. *Phys. Rep.* **2004**, *394* (1), 1–40. DOI: 10.1016/j.physrep.2003.11.004.
- (76) Atzori, M.; Sessoli, R. The Second Quantum Revolution: Role and Challenges of Molecular Chemistry. *J. Am. Chem. Soc.* **2019**, *141* (29), 11339–11352. DOI: 10.1021/jacs.9b00984.
- (77) Bogani, L.; Wernsdorfer, W. Molecular spintronics using single-molecule magnets. *Nat Mater* **2008**, *7* (3), 179–186. DOI: 10.1038/nmat2133.
- (78) Sanvito, S. Molecular spintronics. *Chem. Soc. Rev.* **2011**, *40* (6), 3336–3355. DOI: 10.1039/c1cs15047b.
- (79) Raman, K. V.; Kamerbeek, A. M.; Mukherjee, A.; Atodiressei, N.; Sen, T. K.; Lazić, P.; Caciuc, V.; Michel, R.; Stalke, D.; Mandal, S. K.; Blügel, S.; Münzenberg, M.; Moodera, J. S. Interface-engineered templates for molecular spin memory devices. *Nature* **2013**, *493* (7433), 509–513. DOI: 10.1038/nature11719.
- (80) Aromí, G.; Brechin, E. K. Synthesis of 3d Metallic Single-Molecule Magnets. In *Single-Molecule Magnets and Related Phenomena*; Winpenny, R., Ed.; Springer Berlin Heidelberg, **2006**; pp 1–67. DOI: 10.1007/430_022.
- (81) Craig, G. A.; Murrie, M. 3d single-ion magnets. *Chem. Soc. Rev.* **2015**, *44* (8), 2135–2147. DOI: 10.1039/c4cs00439f.
- (82) Cui, Y.; Wu, Y.; Li, Y.; Liu, R.; Dong, X.; Wang, Y. Pressure-induced changes in the magnetic properties of the single crystal of Mn_3 single-molecule magnet. *Sci. China Phys. Mech. Astron.* **2014**, *57* (7), 1299–1303. DOI: 10.1007/s11433-014-5493-2.
- (83) Ruiz, D.; Sun, Z.; Albela, B.; Folting, K.; Ribas, J.; Christou, G.; Hendrickson, D. N. Single-Molecule Magnets: Different Rates of Resonant Magnetization Tunneling in Mn_{12}

- Complexes. *Angew. Chem. Int. Ed.* **1998**, 37 (3), 300–302. DOI: 10.1002/(sici)1521-3773(19980216)37:3<300:aid-anie300>3.0.co;2-c.
- (84) Chen, W.-P.; Singleton, J.; Qin, L.; Camón, A.; Engelhardt, L.; Luis, F.; Winpenny, R. E. P.; Zheng, Y.-Z. Quantum Monte Carlo simulations of a giant {Ni₂₁Gd₂₀} cage with a S = 91 spin ground state. *Nat Commun* **2018**, 9 (1), 2107. DOI: 10.1038/s41467-018-04547-4.
- (85) Ako, A. M.; Hewitt, I. J.; Mereacre, V.; Clérac, R.; Wernsdorfer, W.; Anson, C. E.; Powell, A. K. A Ferromagnetically Coupled Mn₁₉ Aggregate with a Record S=83/2 Ground Spin State. *Angew. Chem. Int. Ed.* **2006**, 118 (30), 4926–4929. DOI: 10.1002/anie.200601467.
- (86) Neese, F.; Pantazis, D. A. What is not required to make a single molecule magnet. *Faraday Discuss.* **2011**, 148, 229–38; discussion 299–314. DOI: 10.1039/c005256f.
- (87) Pedersen, K. S.; Dreiser, J.; Weihe, H.; Sibille, R.; Johannesen, H. V.; Sørensen, M. A.; Nielsen, B. E.; Sigrist, M.; Mutka, H.; Rols, S.; Bendix, J.; Piligkos, S. Design of Single-Molecule Magnets: Insufficiency of the Anisotropy Barrier as the Sole Criterion. *Inorg. Chem.* **2015**, 54 (15), 7600–7606. DOI: 10.1021/acs.inorgchem.5b01209.
- (88) Rinehart, J. D.; Long, J. R. Exploiting single-ion anisotropy in the design of f-element single-molecule magnets. *Chem. Sci.* **2011**, 2 (11), 2078. DOI: 10.1039/c1sc00513h.
- (89) Waldmann, O. A criterion for the anisotropy barrier in single-molecule magnets. *Inorg. Chem.* **2007**, 46 (24), 10035–10037. DOI: 10.1021/ic701365t.
- (90) Cucinotta, G.; Perfetti, M.; Luzon, J.; Etienne, M.; Car, P.-E.; Caneschi, A.; Calvez, G.; Bernot, K.; Sessoli, R. Magnetic Anisotropy in a Dysprosium/DOTA Single-Molecule Magnet: Beyond Simple Magneto-Structural Correlations. *Angew. Chem. Int. Ed.* **2012**, 124 (7), 1606–1610. DOI: 10.1002/anie.201107453.
- (91) Rinehart, J. D.; Long, J. R. Exploiting single-ion anisotropy in the design of f-element single-molecule magnets. *Chem. Sci.* **2011**, 2 (11), 2078. DOI: 10.1039/c1sc00513h.
- (92) Vaidya, S.; Tewary, S.; Singh, S. K.; Langley, S. K.; Murray, K. S.; Lan, Y.; Wernsdorfer, W.; Rajaraman, G.; Shanmugam, M. What Controls the Sign and Magnitude of Magnetic Anisotropy in Tetrahedral Cobalt(II) Single-Ion Magnets? *Inorg. Chem.* **2016**, 55 (19), 9564–9578. DOI: 10.1021/acs.inorgchem.6b01073.
- (93) Gomez-Coca, S.; Cremades, E.; Aliaga-Alcalde, N.; Ruiz, E. Mononuclear single-molecule magnets: tailoring the magnetic anisotropy of first-row transition-metal complexes. *J. Am. Chem. Soc.* **2013**, 135 (18), 7010–7018. DOI: 10.1021/ja4015138.
- (94) Deng, Y.-F.; Han, T.; Yin, B.; Zheng, Y.-Z. On balancing the QTM and the direct relaxation processes in single-ion magnets – the importance of symmetry control. *Inorg. Chem. Front.* **2017**, 4 (7), 1141–1148. DOI: 10.1039/C7QI00135E.
- (95) Chilton, N. F. Design criteria for high-temperature single-molecule magnets. *Inorg. Chem.* **2015**, 54 (5), 2097–2099. DOI: 10.1021/acs.inorgchem.5b00089.
- (96) Ishikawa, N.; Sugita, M.; Ishikawa, T.; Koshihara, S.-Y.; Kaizu, Y. Lanthanide double-decker complexes functioning as magnets at the single-molecular level. *J. Am. Chem. Soc.* **2003**, 125 (29), 8694–8695. DOI: 10.1021/ja029629n.
- (97) Ishikawa, N.; Sugita, M.; Ishikawa, T.; Koshihara, S.-Y.; Kaizu, Y. Mononuclear Lanthanide Complexes with a Long Magnetization Relaxation Time at High Temperatures: A New Category of Magnets at the Single-Molecular Level. *J. Phys. Chem. B* **2004**, 108 (31), 11265–11271. DOI: 10.1021/jp0376065.

- (98) Locht, I. L. M.; Kvashnin, Y. O.; Rodrigues, D. C. M.; Pereiro, M.; Bergman, A.; Bergqvist, L.; Lichtenstein, A. I.; Katsnelson, M. I.; Delin, A.; Klautau, A. B.; Johansson, B.; Di Marco, I.; Eriksson, O. Standard model of the rare earths analyzed from the Hubbard I approximation. *Phys. Rev. B* **2016**, *94* (8). DOI: 10.1103/PhysRevB.94.085137.
- (99) Strnat, K.; Hoffer, G.; Olson, J.; Ostertag, W.; Becker, J. J. A Family of New Cobalt-Base Permanent Magnet Materials. *J. Appl. Phys.* **1967**, *38* (3), 1001–1002. DOI:10.1063/1.1709459.
- (100) Sagawa, M.; Fujimura, S.; Togawa, N.; Yamamoto, H.; Matsuura, Y. New material for permanent magnets on a base of Nd and Fe (invited). *J. Appl. Phys.* **1984**, *55* (6), 2083–2087. DOI: 10.1063/1.333572.
- (101) Raymond, K. N.; Pierre, V. C. Next generation, high relaxivity gadolinium MRI agents. *Bioconj. Chem.* **2005**, *16* (1), 3–8. DOI: 10.1021/bc049817y.
- (102) Chilton, N. F.; Goodwin, C. A. P.; Mills, D. P.; Winpenny, R. E. P. The first near-linear bis(amide) f-block complex: a blueprint for a high temperature single molecule magnet. *Chem. Commun.* **2015**, *51* (1), 101–103. DOI: 10.1039/c4cc08312a.
- (103) Guo, F.-S.; Day, B. M.; Chen, Y.-C.; Tong, M.-L.; Mansikkamäki, A.; Layfield, R. A. A Dysprosium Metallocene Single-Molecule Magnet Functioning at the Axial Limit. *Angew. Chem. Int. Ed.* **2017**, *129* (38), 11603–11607. DOI: 10.1002/anie.201705426.
- (104) Guo, F.-S.; Day, B. M.; Chen, Y.-C.; Tong, M.-L.; Mansikkamäki, A.; Layfield, R. A. Magnetic hysteresis up to 80 kelvin in a dysprosium metallocene single-molecule magnet. *Science* **2018**, *362* (6421), 1400–1403. DOI: 10.1126/science.aav0652.
- (105) Woodruff, D. N.; Winpenny, R. E. P.; Layfield, R. A. Lanthanide single-molecule magnets. *Chem. Rev.* **2013**, *113* (7), 5110–5148. DOI: 10.1021/cr400018q.
- (106) Sessoli, R.; Tsai, H. L.; Schake, A. R.; Wang, S.; Vincent, J. B.; Folting, K.; Gatteschi, D.; Christou, G.; Hendrickson, D. N. High-spin molecules:[Mn₁₂O₁₂(O₂CR)₁₆(H₂O)₄]. *J. Am. Chem. Soc.* **1993**, *115* (5), 1804–1816. DOI: 10.1021/ja00058a027.
- (107) Camarero, J. & Coronado, E. Molecular vs. inorganic spintronics: the role of molecular materials and single molecules. *J. Mater. Chem.* **2009**, *19*, 1678–1684, 1678.
- (108) Rinehart, J. D.; Fang, M.; Evans, W. J.; Long, J. R. A N₂³⁻ radical-bridged terbium complex exhibiting magnetic hysteresis at 14 K. *J. Am. Chem. Soc.* **2011**, *133* (36), 14236–14239. DOI: 10.1021/ja206286h.
- (109) Harriman, K. L. M.; Brosmer, J. L.; Ungur, L.; Diaconescu, P. L.; Murugesu, M. Pursuit of Record Breaking Energy Barriers: A Study of Magnetic Axiality in Diamide Ligated Dy(III) Single-Molecule Magnets. *J. Am. Chem. Soc.* **2017**, *139* (4), 1420–1423. DOI: 10.1021/jacs.6b12374.
- (110) Goodwin, C. A. P.; Ortu, F.; Reta, D.; Chilton, N. F.; Mills, D. P. Molecular magnetic hysteresis at 60 kelvin in dysprosocenium. *Nature* **2017**, *548* (7668), 439–442. DOI: 10.1038/nature23447.
- (111) Chen, Y.-C.; Liu, J.-L.; Lan, Y.; Zhong, Z.-Q.; Mansikkamäki, A.; Ungur, L.; Li, Q.-W.; Jia, J.-H.; Chibotaru, L. F.; Han, J.-B.; Wernsdorfer, W.; Chen, X.-M.; Tong, M.-L. Dynamic Magnetic and Optical Insight into a High Performance Pentagonal Bipyramidal Dy(III) Single-Ion Magnet. *Chem.*, **2017**, *23* (24), 5708–5715. DOI: 10.1002/chem.201606029.
- (112) Mattocks, J. A.; Cotruvo, J. A. Biological, biomolecular, and bio-inspired strategies for detection, extraction, and separations of lanthanides and actinides. *Chem. Soc. Rev.* **2020**, *49* (22), 8315–8334. DOI: 10.1039/d0cs00653j.

- (113) Bunting, P. C.; Atanasov, M.; Damgaard-Møller, E.; Perfetti, M.; Crassee, I.; Orlita, M.; Overgaard, J.; van Slageren, J.; Neese, F.; Long, J. R. A linear cobalt(II) complex with maximal orbital angular momentum from a non-Aufbau ground state. *Science* **2018**, *362* (6421). DOI: 10.1126/science.aat7319.
- (114) Damgaard-Møller, E.; Krause, L.; Tolborg, K.; Macetti, G.; Genoni, A.; Overgaard, J. Quantification of the Magnetic Anisotropy of a Single-Molecule Magnet from Experimental Electron Density. *Angew. Chem. Int. Ed.* **2020** (59), 21203–21209. DOI:10.1002/anie.202007856.
- (115) Zadrozny, J. M.; Atanasov, M.; Bryan, A. M.; Lin, C.-Y.; Rekker, B. D.; Power, P. P.; Neese, F.; Long, J. R. Slow magnetization dynamics in a series of two-coordinate iron(ii) complexes. *Chem. Sci.* **2013**, *4* (1), 125–138. DOI: 10.1039/C2SC20801F.
- (116) Zadrozny, J. M.; Liu, J.; Piro, N. A.; Chang, C. J.; Hill, S.; Long, J. R. Slow magnetic relaxation in a pseudotetrahedral cobalt(II) complex with easy-plane anisotropy. *Chem. Commun.* **2012**, *48* (33), 3927–3929. DOI: 10.1039/c2cc16430b.
- (117) Fataftah, M. S.; Zadrozny, J. M.; Rogers, D. M.; Freedman, D. E. A mononuclear transition metal single-molecule magnet in a nuclear spin-free ligand environment. *Inorg. Chem.* **2014**, *53* (19), 10716–10721. DOI: 10.1021/ic501906z.
- (118) Zadrozny, J. M.; Long, J. R. Slow magnetic relaxation at zero field in the tetrahedral complex Co(SPh)₄2-. *J. Am. Chem. Soc.* **2011**, *133* (51), 20732–20734. DOI:10.1021/ja2100142.
- (119) Zadrozny, J. M.; Xiao, D. J.; Atanasov, M.; Long, G. J.; Grandjean, F.; Neese, F.; Long, J. R. Magnetic blocking in a linear iron(I) complex. *Nat Chem* **2013**, *5* (7), 577–581. DOI: 10.1038/nchem.1630.
- (120) Bill, E. Single-molecule magnets: Iron lines up. *Nat Chem* **2013**, *5* (7), 556–557. DOI: 10.1038/nchem.1687.
- (121) Sarkar, A.; Dey, S.; Rajaraman, G. Role of Coordination Number and Geometry in Controlling the Magnetic Anisotropy in FeII, CoII, and NiII Single-Ion Magnets. *Chem. - Eur. J.* **2020** (26), 14036–14058. DOI: 10.1002/chem.202003211.
- (122) Guo, F.-S.; Bar, A. K.; Layfield, R. A. Main Group Chemistry at the Interface with Molecular Magnetism. *Chem. Rev.* **2019**, *119* (14), 8479–8505. DOI:10.1021/acs.chemrev.9b00103.
- (123) Sarkar, A.; Tewary, S.; Sinkar, S.; Rajaraman, G. Magnetic Anisotropy in CoII X₄ (X=O, S, Se) Single-Ion Magnets: Role of Structural Distortions versus Heavy Atom Effect. *Chem. - Asian J.* **2019**, *14* (24), 4696–4704. DOI: 10.1002/asia.201901140.
- (124) Thiel, A. M.; Damgaard-Møller, E.; Overgaard, J. High-Pressure Crystallography as a Guide in the Design of Single-Molecule Magnets. *Inorg. Chem.* **2020**, *59* (3), 1682–1691. DOI: 10.1021/acs.inorgchem.9b02794.
- (125) Jeon, I.-R.; Park, J. G.; Xiao, D. J.; Harris, T. D. An azophenine radical-bridged Fe₂ single-molecule magnet with record magnetic exchange coupling. *J. Am. Chem. Soc.* **2013**, *135* (45), 16845–16848. DOI: 10.1021/ja409927v.
- (126) Thorarinsdottir, A. E.; Björnsson, R.; Harris, T. D. Insensitivity of Magnetic Coupling to Ligand Substitution in a Series of Tetraoxolene Radical-Bridged Fe₂ Complexes. *Inorg. Chem.* **2020**, *59* (7), 4634–4649. DOI: 10.1021/acs.inorgchem.9b03736.

- (127) Demir, S.; Nippe, M.; Gonzalez, M. I.; Long, J. R. Exchange coupling and magnetic blocking in dilanthanide complexes bridged by the multi-electron redox-active ligand 2,3,5,6-tetra(2-pyridyl)pyrazine. *Chem. Sci.* **2014**, *5* (12), 4701–4711. DOI: 10.1039/C4SC02154A.
- (128) Karunadasa, H. I.; Arquero, K. D.; Berben, L. A.; Long, J. R. Enhancing the magnetic anisotropy of cyano-ligated chromium(II) and chromium(III) complexes via heavy halide ligand effects. *Inorg. Chem.* **2010**, *49* (11), 4738–4740. DOI: 10.1021/ic1002995.
- (129) Lan, W.; Zhou, Z.; Li, J.; Dou, Y.; Hao, X.; Yang, L.; Liu, H.; Li, D.; Liu, Q.; Zhang, D. A cyanide-bridged FeIII-MnII heterobimetallic one-dimensional coordination polymer: synthesis, crystal structure, experimental and theoretical magnetism investigation. *Acta Crystallogr.* **2019**, *75*, 1475–1481. DOI: 10.1107/S2053229619013172.
- (130) Pugh, T.; Vieru, V.; Chibotaru, L. F.; Layfield, R. A. Magneto-structural correlations in arsenic- and selenium-ligated dysprosium single-molecule magnets. *Chem. Sci.* **2016**, *7* (3), 2128–2137. DOI: 10.1039/c5sc03755g.
- (131) Pugh, T.; Chilton, N. F.; Layfield, R. A. Antimony-ligated dysprosium single-molecule magnets as catalysts for stibine dehydrocoupling. *Chem. Sci.* **2017**, *8* (3), 2073–2080. DOI: 10.1039/c6sc04465d.
- (132) Zhu, Y.-Y.; Zhang, Y.-Q.; Yin, T.-T.; Gao, C.; Wang, B.-W.; Gao, S. A Family of Co(II)Co(III)₃ Single-Ion Magnets with Zero-Field Slow Magnetic Relaxation: Fine Tuning of Energy Barrier by Remote Substituent and Counter Cation. *Inorg. Chem.* **2015**, *54* (11), 5475–5486. DOI: 10.1021/acs.inorgchem.5b00526.
- (133) Nguyen, T. N.; Wernsdorfer, W.; Abboud, K. A.; Christou, G. A supramolecular aggregate of four exchange-biased single-molecule magnets. *J. Am. Chem. Soc.* **2011**, *133* (51), 20688–20691. DOI: 10.1021/ja2087344.
- (134) Cosquer, G.; Shen, Y.; Almeida, M.; Yamashita, M. Conducting single-molecule magnet materials. *Dalton Trans.* **2018**, *47* (23), 7616–7627. DOI: 10.1039/c8dt01015c.
- (135) Cavallini, M.; Facchini, M.; Albonetti, C.; Biscarini, F. Single molecule magnets: from thin films to nano-patterns. *Phys. Chem. Chem. Phys.* **2008**, *10* (6), 784–793. DOI: 10.1039/b711677b.
- (136) Clemente-Juan, J. M.; Coronado, E.; Gaita-Ariño, A. Magnetic polyoxometalates: from molecular magnetism to molecular spintronics and quantum computing. *Chem. Soc. Rev.* **2012**, *41* (22), 7464–7478. DOI: 10.1039/c2cs35205b.
- (137) Bender, C. M.; Wu, T. T. Analytic Structure of Energy Levels in a Field-Theory Model. *Phys Rev Lett* **1968**, *21* (6), 406–409. DOI: 10.1103/PhysRevLett.21.406.
- (138) Sessoli, R.; Gatteschi, D.; Caneschi, A.; Novak, M. A. Magnetic bistability in a metal-ion cluster. *Nature* **1993**, *365* (6442), 141–143. DOI: 10.1038/365141a0.
- (139) H. A. Kramers. Théorie générale de la rotation paramagnétique dans les cristaux. *Proc. K. Ned. Akad. Wet.*, 1930, 959–972.
- (140) Cucinotta, G.; Poggini, L.; Pedrini, A.; Bertani, F.; Cristiani, N.; Torelli, M.; Graziosi, P.; Cimatti, I.; Cortigiani, B.; Otero, E.; Ohresser, P.; Saintavit, P.; Dediu, A.; Dalcanale, E.; Sessoli, R.; Mannini, M. Tuning of a Vertical Spin Valve with a Monolayer of Single Molecule Magnets. *Adv. Funct. Mater.* **2017**, *27* (42), 1703600. DOI: 10.1002/adfm.201703600.
- (141) Mannini, M.; Pineider, F.; Danieli, C.; Totti, F.; Sorace, L.; Saintavit, P.; Arrio, M.-A.; Otero, E.; Joly, L.; Cezar, J. C.; Cornia, A.; Sessoli, R. Quantum tunnelling of the

- magnetization in a monolayer of oriented single-molecule magnets. *Nature* **2010**, *468* (7322), 417–421. DOI: 10.1038/nature09478.
- (142) Mannini, M.; Bertani, F.; Tudisco, C.; Malavolti, L.; Poggini, L.; Misztal, K.; Menozzi, D.; Motta, A.; Otero, E.; Ohresser, P.; Saintavit, P.; Condorelli, G. G.; Dalcanale, E.; Sessoli, R. Magnetic behaviour of TbPc₂ single-molecule magnets chemically grafted on silicon surface. *Nat Commun* **2014**, *5* (1), 4582. DOI: 10.1038/ncomms5582.
- (143) Cervetti, C.; Rettori, A.; Pini, M. G.; Cornia, A.; Repollés, A.; Luis, F.; Dressel, M.; Rauschenbach, S.; Kern, K.; Burghard, M.; Bogani, L. The classical and quantum dynamics of molecular spins on graphene. *Nat Mater* **2016**, *15* (2), 164–168. DOI: 10.1038/nmat4490.
- (144) Prins, F.; Monrabal-Capilla, M.; Osorio, E. A.; Coronado, E.; van der Zant, H. S. J. Room-temperature electrical addressing of a bistable spin-crossover molecular system. *Adv. Mat.* **2011**, *23* (13), 1545–1549. DOI: 10.1002/adma.201003821.
- (145) Bogani, L.; Wernsdorfer, W. Molecular spintronics using single-molecule magnets. *Nat Mater* **2008**, *7* (3), 179–186. DOI: 10.1038/nmat2133.
- (146) Mitcov, D.; Pedersen, A. H.; Ceccato, M.; Gelardi, R. M.; Hassenkam, T.; Konstantatos, A.; Reinholdt, A.; Sørensen, M. A.; Thulstrup, P. W.; Vinum, M. G.; Wilhelm, F.; Rogalev, A.; Wernsdorfer, W.; Brechin, E. K.; Piligkos, S. Molecular multifunctionality preservation upon surface deposition for a chiral single-molecule magnet. *Chem. Sci.* **2019**, *10* (10), 3065–3073. DOI: 10.1039/c8sc04917c.
- (147) Vincent, R.; Klyatskaya, S.; Ruben, M.; Wernsdorfer, W.; Balestro, F. Electronic read-out of a single nuclear spin using a molecular spin transistor. *Nature* **2012**, *488* (7411), 357–360. DOI: 10.1038/nature11341.
- (148) Sessoli, R.; Gatteschi, D.; Caneschi, A.; Novak, M. A. Magnetic bistability in a metal-ion cluster. *Nature* **1993**, *365* (6442), 141–143. DOI: 10.1038/365141a0.
- (149) Spin-lattice relaxation in rare-earth salts: field dependence of the two-phonon process. *Proc. R. Soc. Lond. A* **1961**, *264* (1319), 485–495. DOI: 10.1098/rspa.1961.0212.
- (150) Shrivastava, K. N. Theory of Spin–Lattice Relaxation. *Phys. Stat. Sol. B*, **1983**, *117* (2), 437–458. DOI: 10.1002/pssb.2221170202.
- (151) Orbach, R. On the Theory of Spin-Lattice Relaxation in Paramagnetic Salts. *Proc. Phys. Soc.* **1961**, *77* (4), 821–826. DOI: 10.1088/0370-1328/77/4/301.
- (152) Orbach, R. Spin-Lattice Relaxation in Rare-Earth Salts. *Proc. Math. Phys. Eng. Sci. A* **1961**, *264* (1319), 458–484. DOI: 10.1098/rspa.1961.0211.
- (153) Lunghi, A.; Totti, F.; Sessoli, R.; Sanvito, S. The role of anharmonic phonons in under-barrier spin relaxation of single molecule magnets. *Nat Commun* **2017**, *8* (1), 14620. DOI: 10.1038/ncomms14620.
- (154) E. Damgaard-Møller. E. Damgaard-Møller, PhD. thesis, Aarhus University, Aarhus, Denmark, 2020.
- (155) Standley, K. J. *Electron spin relaxation phenomena in solids*; Springer US, **1969**. DOI: 10.1007/978-1-4899-6539-4.
- (156) Raman, C. V. A new radiation. *Indian J. Phys.* **1928**, *2*, 387–398.
- (157) Thomas, L.; Lionti, F.; Ballou, R.; Gatteschi, D.; Sessoli, R.; Barbara, B. Macroscopic quantum tunnelling of magnetization in a single crystal of nanomagnets. *Nature* **1996**, *383* (6596), 145–147. DOI: 10.1038/383145a0.

- (158) Wu, T.; Zhai, Y.-Q.; Deng, Y.-F.; Chen, W.-P.; Zhang, T.; Zheng, Y.-Z. Correlating magnetic anisotropy with the subtle coordination geometry variation of a series of cobalt(ii)-sulfonamide complexes. *Dalton Trans.* **2019**, 48 (41), 15419–15426. DOI: 10.1039/c9dt01296f.
- (159) Suturina, E. A.; Maganas, D.; Bill, E.; Atanasov, M.; Neese, F. Magneto-Structural Correlations in a Series of Pseudotetrahedral Co(II)(XR)₄²⁻ Single Molecule Magnets: An ab Initio Ligand Field Study. *Inorg. Chem.* **2015**, 54 (20), 9948–9961. DOI:10.1021/acs.inorgchem.5b01706.
- (160) Feng, M.; Tong, M.-L. Single Ion Magnets from 3d to 5f: Developments and Strategies. *Chem. - Eur. J.* **2018**, 24 (30), 7574–7594. DOI: 10.1002/chem.201705761.
- (161) Frost, J. M.; Harriman, K. L. M.; Murugesu, M. The rise of 3-d single-ion magnets in molecular magnetism: towards materials from molecules? *Chem. Sci.* **2016**, 7 (4), 2470–2491. DOI: 10.1039/c5sc03224e.
- (162) Pedersen, K. S.; Bendix, J.; Clérac, R. Single-molecule magnet engineering: building-block approaches. *Chem. Commun.* **2014**, 50 (34), 4396–4415. DOI: 10.1039/c4cc00339j.
- (163) Atanasov, M.; Ganyushin, D.; Sivalingam, K.; Neese, F. A Modern First-Principles View on Ligand Field Theory Through the Eyes of Correlated Multireference Wavefunctions. In *Molecular electronic structures of transition metal complexes*; Mingos, D. M. P., Day, P., Dahl, J. P., Eds.; Structure and Bonding, 142-143; Springer, **2012**; 149–220. DOI:10.1007/430_2011_57.
- (164) Figgis, B. N.; Hitchman, M. A. *Ligand field theory and its applications*; Special topics in inorganic chemistry; Wiley-VCH, **2000**.
- (165) Liu, J.-L.; Chen, Y.-C.; Tong, M.-L. Symmetry strategies for high performance lanthanide-based single-molecule magnets. *Chem. Soc. Rev.* **2018**, 47 (7), 2431–2453. DOI:10.1039/c7cs00266a.
- (166) Le Roy, J. J.; Ungur, L.; Korobkov, I.; Chibotaru, L. F.; Murugesu, M. Coupling strategies to enhance single-molecule magnet properties of erbium-cyclooctatetraenyl complexes. *J. Am. Chem. Soc.* **2014**, 136 (22), 8003–8010. DOI: 10.1021/ja5022552.
- (167) Lin, P.-H.; Smythe, N. C.; Gorelsky, S. I.; Maguire, S.; Henson, N. J.; Korobkov, I.; Scott, B. L.; Gordon, J. C.; Baker, R. T.; Murugesu, M. Importance of out-of-state spin-orbit coupling for slow magnetic relaxation in mononuclear Fe(II) complexes. *J. Am. Chem. Soc.* **2011**, 133 (40), 15806–15809. DOI: 10.1021/ja203845x.
- (168) Pugh, T.; Tuna, F.; Ungur, L.; Collison, D.; McInnes, E. J. L.; Chibotaru, L. F.; Layfield, R. A. Influencing the properties of dysprosium single-molecule magnets with phosphorus donor ligands. *Nat. Commun.* **2015**, 6, 7492. DOI: 10.1038/ncomms8492.
- (169) Pearson, T. J.; Fataftah, M. S.; Freedman, D. E. Enhancement of magnetic anisotropy in a Mn-Bi heterobimetallic complex. *Chem. Commun.* **2016**, 52 (76), 11394–11397. DOI: 10.1039/c6cc06369a.
- (170) F. Neese. ORCA:An *ab initio*, DFT and semiempirical SCF-MO package.
- (171) Neese, F. The ORCA program system. *Wiley Interdiscip. Rev. Comput. Mol. Sci.* **2012**, 2 (1), 73–78. DOI: 10.1002/wcms.81.
- (172) Chilton, N. F.; Collison, D.; McInnes, E. J. L.; Winpenny, R. E. P.; Soncini, A. An electrostatic model for the determination of magnetic anisotropy in dysprosium complexes. *Nat Commun* **2013**, 4 (1), 2551. DOI: 10.1038/ncomms3551.
- (173) Randall McClain, K.; Gould, C. A.; Chakarawet, K.; Teat, S. J.; Groshens, T. J.; Long, J. R.; Harvey, B. G. High-temperature magnetic blocking and magneto-structural correlations in a

series of dysprosium(iii) metallocenium single-molecule magnets. *Chem. Sci.* **2018**, *9* (45), 8492–8503. DOI: 10.1039/c8sc03907k.

(174) Day, B. M.; Guo, F.-S.; Layfield, R. A. Cyclopentadienyl Ligands in Lanthanide Single-Molecule Magnets: One Ring To Rule Them All? *Acc. Chem. Res.* **2018**, *51* (8), 1880–1889. DOI: 10.1021/acs.accounts.8b00270.

(175) Hilgar, J. D.; Bernbeck, M. G.; Rinehart, J. D. Million-fold Relaxation Time Enhancement across a Series of Phosphino-Supported Erbium Single-Molecule Magnets. *J. Am. Chem. Soc.* **2019**, *141* (5), 1913–1917. DOI: 10.1021/jacs.8b13514.

(176) Meihaus, K. R.; Long, J. R. Magnetic blocking at 10 K and a dipolar-mediated avalanche in salts of the bis(η^8 -cyclooctatetraenide) complex $\text{Er}(\text{COT})^2$. *Journal of the American Chemical Society* **2013**, *135* (47), 17952–17957. DOI: 10.1021/ja4094814.

(177) Chen, S.-M.; Xiong, J.; Zhang, Y.-Q.; Yuan, Q.; Wang, B.-W.; Gao, S. A soft phosphorus atom to « harden » an erbium(iii) single-ion magnet. *Chem. Sci.* **2018**, *9* (38), 7540–7545. DOI: 10.1039/c8sc01626g.

(178) Gould, C. A.; McClain, K. R.; Yu, J. M.; Groshens, T. J.; Furche, F.; Harvey, B. G.; Long, J. R. Synthesis and Magnetism of Neutral, Linear Metallocene Complexes of Terbium(II) and Dysprosium(II). *J. Am. Chem. Soc.* **2019**, *141* (33), 12967–12973. DOI: 10.1021/jacs.9b05816.

(179) Guo, F.-S.; Day, B. M.; Chen, Y.-C.; Tong, M.-L.; Mansikkamäki, A.; Layfield, R. A. A Dysprosium Metallocene Single-Molecule Magnet Functioning at the Axial Limit. *Angew. Chem. Int. Ed.* **2017**, *56* (38), 11445–11449. DOI: 10.1002/anie.201705426.

(180) Demir, S.; Zadrozny, J. M.; Long, J. R. Large spin-relaxation barriers for the low-symmetry organolanthanide complexes $\text{Cp}^*_2 \text{Ln}(\text{BPh}_4)$ (Cp^* =pentamethylcyclopentadienyl; $\text{Ln}=\text{Tb}, \text{Dy}$). *Chem. - Eur. J.* **2014**, *20* (31), 9524–9529. DOI: 10.1002/chem.201403751.

(181) Demir, S.; Boshart, M. D.; Corbey, J. F.; Woen, D. H.; Gonzalez, M. I.; Ziller, J. W.; Meihaus, K. R.; Long, J. R.; Evans, W. J. Slow Magnetic Relaxation in a Dysprosium Ammonia Metallocene Complex. *Inorg. Chem.* **2017**, *56* (24), 15049–15056. DOI: 10.1021/acs.inorgchem.7b02390.

(182) Meng, Y.-S.; Zhang, Y.-Q.; Wang, Z.-M.; Wang, B.-W.; Gao, S. Weak Ligand-Field Effect from Ancillary Ligands on Enhancing Single-Ion Magnet Performance. *Chem. - Eur. J.* **2016**, *22* (36), 12724–12731. DOI: 10.1002/chem.201601934.

(183) Evans, P.; Reta, D.; Goodwin, C. A. P.; Ortu, F.; Chilton, N. F.; Mills, D. P. A double-dysprosocenium single-molecule magnet bound together with neutral ligands. *Chem. Commun.* **2020**, *56* (42), 5677–5680. DOI: 10.1039/c9cc08945d.

(184) Goodwin, C. A. P. Blocking like it's hot: a synthetic chemists' path to high-temperature lanthanide single molecule magnets. *Dalton Trans.* **2020**, *49* (41), 14320–14337. DOI: 10.1039/d0dt01904f.

(185) Christina M. Legendre, Selvan Demir. unpublished results, **2017-2019**.

(186) J. Jung, C. M. Legendre, S. Demeshko, R. Herbst-Irmer, D. Stalke. *Inorg. Chem.*, under revision, **2021**.

(187) Han, T.; Giansiracusa, M. J.; Li, Z.-H.; Ding, Y.-S.; Chilton, N. F.; Winpenny, R. E. P.; Zheng, Y.-Z. Exchange-Biasing in a Dinuclear Dysprosium(III) Single-Molecule Magnet with a Large Energy Barrier for Magnetisation Reversal. *Chem. - Eur. J.* **2020**, *26* (30), 6773–6777. DOI: 10.1002/chem.202000719.

- (188) Durrant, J. P.; Tang, J.; Mansikkamäki, A.; Layfield, R. A. Enhanced single-molecule magnetism in dysprosium complexes of a pristine cyclobutadienyl ligand. *Chem. Commun.* **2020**, 56 (34), 4708–4711. DOI: 10.1039/D0CC01722A.
- (189) Zhu, Z.; Zhang, Y.-Q.; Li, X.-L.; Guo, M.; Lu, J.; Liu, S.; Layfield, R. A.; Tang, J. Tuning Magnetic Relaxation in Square-Pyramidal Dysprosium Single-Molecule Magnets using Apical Alkoxide Ligands. *CCS Chem.* **2021**, 1–27. DOI: 10.31635/ccschem.021.202000715.
- (190) He, M.; Guo, F.-S.; Tang, J.; Mansikkamäki, A.; Layfield, R. A. Fulvalene as a platform for the synthesis of a dimetallic dysprosocenium single-molecule magnet. *Chem. Sci.* **2020**, 11 (22), 5745–5752. DOI: 10.1039/d0sc02033h.
- (191) Matussek, J.; Herbst-Irmer, R.; Objartel, I.; Stalke, D. Transition metal complexes containing the $S(N^tBu)_4^{2-}$ tetraimidosulfate dianion. *Dalton Trans.* **2014**, 43 (42), 15944–15949. DOI: 10.1039/c4dt01995d.
- (192) Zhang, P.; Guo, Y.-N.; Tang, J. Recent advances in dysprosium-based single molecule magnets: Structural overview and synthetic strategies. *Coord. Chem. Rev.* **2013**, 257 (11-12), 1728–1763. DOI: 10.1016/j.ccr.2013.01.012.
- (193) Guo, Y.-N.; Xu, G.-F.; Guo, Y.; Tang, J. Relaxation dynamics of dysprosium(III) single molecule magnets. *Dalton Trans.* **2011**, 40 (39), 9953–9963. DOI: 10.1039/c1dt10474h.
- (194) Ishikawa, N.; Sugita, M.; Ishikawa, T.; Koshihara, S.-Y.; Kaizu, Y. Mononuclear Lanthanide Complexes with a Long Magnetization Relaxation Time at High Temperatures: A New Category of Magnets at the Single-Molecular Level. *J. Phys. Chem. B* **2004**, 108 (31), 11265–11271. DOI: 10.1021/jp0376065.
- (195) Reta, D.; Chilton, N. F. Uncertainty estimates for magnetic relaxation times and magnetic relaxation parameters. *Phys. Chem. Chem. Phys.* **2019**, 21 (42), 23567–23575. DOI: 10.1039/c9cp04301b.
- (196) J. Jung. *PhD thesis*, **2021**.
- (197) Boča, R.; Miklovič, J.; Titiš, J. Simple mononuclear cobalt(II) complex: a single-molecule magnet showing two slow relaxation processes. *Inorg. Chem.* **2014**, 53 (5), 2367–2369. DOI: 10.1021/ic5000638.
- (198) Zadrozny, J. M.; Telser, J.; Long, J. R. Slow magnetic relaxation in the tetrahedral cobalt(II) complexes $[Co(EPh)_4]^{2-}$ (EO, S, Se). *Polyhedron* **2013**, 64, 209–217. DOI: 10.1016/j.poly.2013.04.008.
- (199) Rechkemmer, Y.; Breitgoff, F. D.; van der Meer, M.; Atanasov, M.; Hakl, M.; Orlita, M.; Neugebauer, P.; Neese, F.; Sarkar, B.; van Slageren, J. A four-coordinate cobalt(II) single-ion magnet with coercivity and a very high energy barrier. *Nat Commun* **2016**, 7 (1), 10467. DOI: 10.1038/ncomms10467.
- (200) Tripathi, S.; Vaidya, S.; Ansari, K. U.; Ahmed, N.; Rivière, E.; Spillecke, L.; Koo, C.; Klingeler, R.; Mallah, T.; Rajaraman, G.; Shanmugam, M. Influence of a Counteranion on the Zero-Field Splitting of Tetrahedral Cobalt(II) Thiourea Complexes. *Inorg. Chem.* **2019**, 58 (14), 9085–9100. DOI: 10.1021/acs.inorgchem.9b00632.
- (201) Vaidya, S.; Shukla, P.; Tripathi, S.; Rivière, E.; Mallah, T.; Rajaraman, G.; Shanmugam, M. Substituted versus Naked Thiourea Ligand Containing Pseudotetrahedral Cobalt(II) Complexes: A Comparative Study on Its Magnetization Relaxation Dynamics Phenomenon. *Inorg. Chem.* **2018**, 57 (6), 3371–3386. DOI: 10.1021/acs.inorgchem.8b00160.

- (202) Albold, U.; Bamberger, H.; Hallmen, P. P.; van Slageren, J.; Sarkar, B. Strong Exchange Couplings Drastically Slow Down Magnetization Relaxation in an Air-Stable Cobalt(II)-Radical Single-Molecule Magnet (SMM). *Angew. Chem. Int. Ed.* **2019**, *58* (29), 9802–9806. DOI: 10.1002/anie.201904645.
- (203) Deng, Y.-F.; Wang, Z.; Ouyang, Z.-W.; Yin, B.; Zheng, Z.; Zheng, Y.-Z. Large Easy-Plane Magnetic Anisotropy in a Three-Coordinate Cobalt(II) Complex $\text{Li}(\text{THF})_4\text{Co}(\text{NPh}_2)_3$. *Chem. - Eur. J.* **2016**, *22* (42), 14821–14825. DOI: 10.1002/chem.201603238.
- (204) Eichhöfer, A.; Lan, Y.; Mereacre, V.; Bodenstein, T.; Weigend, F. Slow magnetic relaxation in trigonal-planar mononuclear Fe(II) and Co(II) bis(trimethylsilyl)amido complexes—a comparative study. *Inorg. Chem.* **2014**, *53* (4), 1962–1974. DOI: 10.1021/ic401677j.
- (205) Inoshita, T.; Sakaki, H. Electron-phonon interaction and the so-called phonon bottleneck effect in semiconductor quantum dots. *Phys. B: Cond. Mat.* **1996**, *227* (1-4), 373–377. DOI: 10.1016/0921-4526(96)00445-0.
- (206) Suturina, E. A.; Nehrkorn, J.; Zadrozny, J. M.; Liu, J.; Atanasov, M.; Weyhermüller, T.; Maganas, D.; Hill, S.; Schnegg, A.; Bill, E.; Long, J. R.; Neese, F. Magneto-Structural Correlations in Pseudotetrahedral Forms of the $\text{Co}(\text{SPh})_4^{2-}$ Complex Probed by Magnetometry, MCD Spectroscopy, Advanced EPR Techniques, and ab Initio Electronic Structure Calculations. *Inorg. Chem.* **2017**, *56* (5), 3102–3118. DOI: 10.1021/acs.inorgchem.7b00097.
- (207) Ostrovsky, S. Magnetostructural study of four-coordinated Co(II) complexes with mixed ligand surrounding. *Polyhedron* **2021**, *194*, 114936. DOI: 10.1016/j.poly.2020.114936.
- (208) Prescimone, A.; Sanchez-Benitez, J.; Kamenev, K. V.; Moggach, S. A.; Lennie, A. R.; Warren, J. E.; Murrie, M.; Parsons, S.; Brechin, E. K. High pressure effects on a trimetallic Mn(II/III) SMM. *Dalton Trans.* **2009** (36), 7390–7395. DOI: 10.1039/b908718d.
- (209) Craig, G. A.; Sarkar, A.; Woodall, C. H.; Hay, M. A.; Marriott, K. E. R.; Kamenev, K. V.; Moggach, S. A.; Brechin, E. K.; Parsons, S.; Rajaraman, G.; Murrie, M. Probing the origin of the giant magnetic anisotropy in trigonal bipyramidal Ni(II) under high pressure. *Chem. Sci.* **2018**, *9* (6), 1551–1559. DOI: 10.1039/c7sc04460g.
- (210) Ziegenbalg, S.; Hornig, D.; Görls, H.; Plass, W. Cobalt(II)-Based Single-Ion Magnets with Distorted Pseudotetrahedral N2O2 Coordination: Experimental and Theoretical Investigations. *Inorg. Chem.* **2016**, *55* (8), 4047–4058. DOI: 10.1021/acs.inorgchem.6b00373.
- (211) Neese, F. Software update: the ORCA program system, version 4.0. *Wiley Interdiscip. Rev. Comput. Mol. Sci.* **2018**, *8* (1). DOI: 10.1002/wcms.1327.
- (212) Dance, I. G. Synthesis, crystal structure, and properties of the hexa(μ -benzenethiolato)tetra(benzenethiolatocobaltate(II)) dianion, the prototype cobalt(II)-thiolate molecular cluster. *J. Am. Chem. Soc.* **1979**, *101* (21), 6264–6273. DOI: 10.1021/ja00515a018.
- (213) Fedotova, Y. V.; Kornev, A. N.; Sushev, V. V.; Kursky, Y. A.; Mushtina, T. G.; Makarenko, N. P.; Fukin, G. K.; Abakumov, G. A.; Zakharov, L. N.; Rheingold, A. L. Phosphinohydrazines and phosphinohydrazides $\text{M}(\text{-NR-NR-PPh}_2)_n$ of some transition and main group metals: synthesis and characterization. *J. Organomet. Chem.* **2004**, *689* (19), 3060–3074. DOI: 10.1016/j.jorganchem.2004.06.056.
- (214) Franz, K. J.; Singh, N.; Spingler, B.; Lippard, S. J. Aminotroponimines as ligands for potential metal-based nitric oxide sensors. *Inorg. Chem.* **2000**, *39* (18), 4081–4092. DOI: 10.1021/ic000344q.

- (215) Jesse, K. A.; Filatov, A. S.; Xie, J.; Anderson, J. S. Neocuproine as a Redox-Active Ligand Platform on Iron and Cobalt. *Inorg. Chem.* **2019**, *58* (14), 9057–9066. DOI: 10.1021/acs.inorgchem.9b00531.
- (216) Kalutarage, L. C.; Heeg, M. J.; Martin, P. D.; Saly, M. J.; Kuiper, D. S.; Winter, C. H. Volatility and high thermal stability in mid-to-late first-row transition-metal complexes containing 1,2,5-triazapentadienyl ligands. *Inorg. Chem.* **2013**, *52* (3), 1182–1184. DOI: 10.1021/ic302787z.
- (217) Li, Z.; Lee, D. K.; Coulter, M.; Rodriguez, L. N. J.; Gordon, R. G. Synthesis and characterization of volatile liquid cobalt amidinates. *Dalton Trans.* **2008** (19), 2592–2597. DOI: 10.1039/b800712h.
- (218) Schmidt, J. A. R.; Arnold, J. First-row transition metal complexes of sterically-hindered amidinates. *J. Chem. Soc., Dalton Trans.* **2002** (18), 3454–3461. DOI: 10.1039/b202737m.
- (219) Zhou, M.-S.; Huang, S.-P.; Weng, L.-H.; Sun, W.-H.; Liu, D.-S. Synthesis and crystal structures of novel β -diketiminato-lithium, iron, cobalt, nickel, zirconium complexes and their catalytical behaviors in polymerization of ethylene. *J. Organomet. Chem.* **2003**, *665* (1-2), 237–245. DOI: 10.1016/S0022-328X(02)02139-3.
- (220) Dmitry Piryazev. CSD Communication, **2017** (CCDC database)
- (221) Lim, B. S.; Rahtu, A.; Park, J.-S.; Gordon, R. G. Synthesis and characterization of volatile, thermally stable, reactive transition metal amidinates. *Inorg. Chem.* **2003**, *42* (24), 7951–7958. DOI: 10.1021/ic0345424.
- (222) Prashanth, B.; Singh, S. Bulky iminophosphonamines for N–P–N coordination: Synthesis and structural characterization of lithium iminophosphonamides and homoleptic bis-chelates of Co(II), Ni(II) and Cu(II). *J. Chem. Sci.* **2015**, *127* (2), 315–325. DOI: 10.1007/s12039-015-0769-2.
- (223) Zhang, Y.; Du, L.; Liu, X.; Ding, Y. Synthesis, characterization, and thermal properties of cobalt(ii) compounds with guanidinate ligands. *New J. Chem.* **2018**, *42* (11), 9110–9115. DOI: 10.1039/C8NJ01232F.
- (224) Bruker AXS Inc. SAINT v8.30C, **2013**.
- (225) Sheldrick, G. M. SADABS, **2014**.
- (226) Sheldrick, G. M. TWINABS 1.05 in SAINTPLUS v6/6.0; WI, USA, **2000**.
- (227) Sheldrick, G. M. XPREP in SHELXTL 2014/2, **2014**.
- (228) Bruker AXS Inc. SHELXTL, **2000**.
- (229) Sheldrick, G. M. XP in SHELXTL 6.10: XP in SHELXTL 6.10; WI, USA, **2000**.
- (230) Pennington, W. T. DIAMOND – Visual Crystal Structure Information System. *J. Appl. Cryst.* **1999**, *32* (5), 1028–1029. DOI: 10.1107/S0021889899011486.
- (231) OriginLab Corporation. Origin(Pro), **2021**.
- (232) Bill, E. *JulX-2s*, **2013**.
- (233) Chilton, N. F.; Anderson, R. P.; Turner, L. D.; Soncini, A.; Murray, K. S. PHI: a powerful new program for the analysis of anisotropic monomeric and exchange-coupled polynuclear d- and f-block complexes. *J. Comput. Chem.* **2013**, *34* (13), 1164–1175. DOI: 10.1002/jcc.23234.
- (234) Hanwell, M. D.; Curtis, D. E.; Lonie, D. C.; Vandermeersch, T.; Zurek, E.; Hutchison, G. R. Avogadro: an advanced semantic chemical editor, visualization, and analysis platform. *J. Cheminform* **2012**, *4* (1), 17. DOI: 10.1186/1758-2946-4-17.

- (235) Chemcraft. *Chemcraft - graphical software for visualization of quantum chemistry computations*.
<https://www.chemcraftprog.com/>.
- (236) D. Lüert. *PhD thesis*, 2022.
- (237) Kretsch, J.; Kreyenschmidt, A.; Herbst-Irmer, R.; Stalke, D. Alkali metal complexes based on bisheterocyclomethanide ligands. *Dalton Trans.* 2018, 47 (36), 12606–12612. DOI: 10.1039/c8dt01678j.